# Photoactivated Click Chemistry for Labelling of DNA and Chemotherapeutics in Cells

Zur Erlangung des akademischen Grades einer

DOKTORIN DER NATURWISSENSCHAFTEN
(Dr. rer. nat.)
von der KIT-Fakultät für Chemie und Biowissenschaften
des Karlsruher Instituts für Technologie (KIT)

vorgelegte

Dissertation

von

**M. Sc. Lisa Maria Rieger**
aus Rickenbach

Karlsruhe, Oktober 2024

Dekan: Prof. Dr. Martin Bastmeyer
Referent: Prof. Dr. Hans-Achim Wagenknecht
Korreferentin: Prof. Dr. Ute Schepers

Tag der mündlichen Prüfung: 12.12.2024

*Meiner Familie*

Die vorliegende Arbeit wurde im Zeitraum von Dezember 2021 bis Dezember 2024 unter der Betreuung von Prof. Dr. Hans-Achim Wagenknecht am Karlsruher Institut für Technologie (KIT) durchgeführt.

# Eidesstattliche Erklärung

Ich versichere hiermit, dass ich die vorliegende Arbeit selbstständig verfasst und keine anderen als die angegebenen Quellen und Hilfsmittel verwendet habe. Wörtlich oder inhaltlich übernommene Stellen sind als solche gekennzeichnet und die Satzung des Karlsruher Instituts für Technologie (KIT) zur Sicherung guter wissenschaftlicher Praxis wurde in der jeweilis gültigen Fassung beachtet.

Des Weiteren erkläre ich, dass ich mich derzeit in keinem weiteren laufenden Promotionsverfahren befinde und auch keine vorausgegangenen Promotionsversuche unternommen habe.

30. Oktober 2024

Lisa M. Rieger Datum

# Kurzfassung

In den letzten Jahren hat die fluoreszenzbasierte Markierung von Biomolekülen in lebenden Zellen erheblich an Bedeutung gewonnen, um tiefere Einblicke in komplexe biologische Prozesse zu ermöglichen. Ein besonders leistungsfähiger Ansatz hierfür sind bioorthogonale Reaktionen, die seit zwei Jahrzehnten entwickelt werden und selektive, störungsfreie Markierungen von Biomolekülen wie Proteinen und Nukleinsäuren erlauben. Die Kombination solcher bioorthogonaler Markierungstechniken mit Chemotherapeutika ermöglicht es, deren Interaktionen und Wirkmechanismen auf molekularer Ebene präzise zu verfolgen. Dies ist besonders wertvoll für die Untersuchung von Krebsmedikamenten, die die DNA-Replikation hemmen, somit die Zellteilung unterbrechen und anschließend zum Zelltod führen. Mithilfe bioorthogonaler Markierungen lassen sich die Interaktionen dieser Substanzen mit der DNA in Echtzeit visualisieren, wodurch neue Einblicke in ihre Effekte auf zelluläre Prozesse gewonnen werden können.

Diese Arbeit gliedert sich in drei Teile. Im ersten Teil wird eine lichtgesteuerte bioorthogonale Markierungsmethode - die sogenannte "Photoclick Reaktion" - untersucht und weiterentwickelt. Hierbei werden tetrazolbasierte Reaktanden so modifiziert, dass die Reaktion durch Belichtung mit sichtbarem Licht (> 405 nm) ausgelöst werden kann. Neben der bathochromen Verschiebung der Anregungswellenlänge verbessern diese Modifikationen auch die Wasserlöslichkeit der Reaktanden, was die Visualisierung des gewünschten Biomoleküls in lebenden biologischen Systemen weiter optimiert. Die Reaktion findet zwischen Tetrazolen als Farbstoffen und 2'-Desoxynukleosiden statt, die durch die Zelle in die eigene DNA eingebaut werden. Die Reaktivität der Tetrazole wurde mit UV/Vis-Spektroskopie und HPLC-Analyse charakterisiert und erfolgreich auf HeLa-Zellen übertragen.

Der zweite Teil der Arbeit widmet sich der Entwicklung und Visualisierung photoaktivierbarer Chemotherapeutika, die im inaktiven Zustand (dunkel) nicht toxisch sind. Erst durch Lichtaktivierung wird ein Teil des Moleküls abgespalten, wodurch das Krebsmedikament aktiviert und somit toxisch wird. Da diese Moleküle von Natur aus nicht fluoreszent sind, werden sie zur zellulären Untersuchung zunächst durch die kupferkatalysierte Azid-Alkin-Cycloaddition bioorthogonal markiert, um eine Visualisierung in Echtzeit und damit einhergehend die Verfolgung der Wirkung zu ermöglichen. Dies erfolgt durch Untersuchung der aktivierten Krebsmedikamente in verschiedenen Aktivierungs- und Inkubationszeiten sowie der Analyse ihrer zellulären Zielorganelle mithilfe der Immunfluoreszenz.

Im dritten Teil dieser Arbeit wird die Methode auf Chemotherapeutika ausgeweitet, die in die DNA interkalieren und dadurch die Replikation beeinflussen. Durch die Kombination der im ersten und zweiten Teil entwickelten Ansätze wird die DNA-Replikation in der Zelle beobachtet und der Zeitpunkt erfasst, ab dem die Synthese neuer DNA gehemmt wird. Hierzu wird ein 2'-Desoxynukleosid gleichzeitig mit dem Chemotherapeutikum in den Zellen inkubiert und anhand bioorthogonaler Reaktionen die neu replizierte DNA visualisiert, um das Wirkungsspektrum des Chemotherapeutikums und seine Effekte auf zelluläre Systeme detailliert zu analysieren.

Diese Arbeit leistet somit einen bedeutenden Beitrag zur Entwicklung innovativer Markierungstechniken und zur präzisen Untersuchung von Chemotherapeutika, die die DNA-Replikation in Krebszellen beeinflussen und bietet wichtige Perspektiven für neue therapeutische Ansätze.

# Table of Contents

# List of Figures

# List of Tables

# List of Abbreviations

| | |
|---|---|
| ° C | Degree Celcius |
| µJ | Micro Joule |
| µL | Micro Liter |
| µM | Micro Molar |
| 1-MCP | 1-Methylcyclopropene |
| 1MLCT | Singlet metal-to-ligand-charge-transfer state |
| 3MC | Triplet excited state |
| 3-MCP | 3-Methylcyclopropene |
| 3MLCT | Triplet-metal-to-ligand-charge-transfer state |
| Å | Angstrom |
| AAS | Atomic Absorption Spectroscopy |
| AB | Antibody |
| $Ac_2O$ | Acetic anhydride |
| AcOH | Acetic acid |
| BARAC | Biarylazacyclooctynes |
| BCN | Bicyclononyne |
| Bp | Basepairs |
| Bpy | 2,2'-bipyridine |
| BSA | Bovine Serum Albumin |
| $CDCl_3$ | Chloroform |
| CP | Cyclopropene |
| CTR1 | Copper transporter 1 |
| Cu | Copper |
| CuAAC | Copper-Catalysed Azide Alkyne Cycloaddition |
| Cy3 | Cyanine 3 |
| DA | Diels-Alder |
| DFT | Density Functional Theory |
| DIBO | Dibenzocyclooctyne |
| DIFO | Difluorocyclooctyne |

| | |
|---|---|
| DMEM | Dulbecco’s Modified Eagle Medium |
| DMF | *N*,*N*-Dimethylformamide |
| DMSO | Dimethylsulfoxide |
| DNA | Deoxyribonucleic Acid |
| DOX | Doxorubicin |
| $EC_{50}$ | Effective Concentration 50 |
| EDC-HCl | *N*-(3-Dimethylaminopropyl)-*N’*-Ethylcarbodiimide Hydrochloride |
| ER | Endoplasmic Reticulum |
| ERA | Electron-rich alkene cycloadditions |
| ESI | Electrospray Ionization |
| $ET_3N$ | Triethylamine |
| EtOAc | Ethyl acetate |
| EtOH | Ethanol |
| FCS | Fetal Calf Serum |
| FDA | Food and Drug Administration |
| GM | Glutamax |
| GS | Ground state |
| $H_2O$ | Water |
| $H_2SO_4$ | Sulfuric Acid |
| $HBF_4$ | Hydrogen tetrafluoroborate |
| HCl | Hydrochloride |
| Hmte | Hydroxy-2-methyl-2-[(3,5-dimethyl-phenyl)imino]ethyl]benzene |
| $HNO_3$ | Nitric Acid |
| HOMO | Highest Occupied Molecular Orbital |
| HPLC | High Performance Liquid Chromatography |
| HRCS AAS | High-Resolution Continuum Source Atomic Absorption Spectroscopy |
| HRMS | High-Resolution Mass Spectrometry |
| IEDDA | Inverse Electron-Demand Diels-Alder Cycloaddition |
| i-biq | 3,3'-biisoquinoline |
| i-Hdiqa | di(isoquinolin-3-yl)amine |

| | |
|---|---|
| $K_2CO_3$ | Potassium Carbonate |
| LC-MS | Liquid Chromatography Coupled Mass Spectrometry |
| LED | Light Emitting Diode |
| LUMO | Lowest Unoccupied Molecular Orbital |
| MC | Excited state |
| MeCN | Acetonitrile |
| MeOH | Methanol |
| MgSO4 | Magnesiumsulfate |
| MHz | Megahertz |
| min | Minutes |
| mL | Milli Liter |
| mM | Milli Molar |
| MTT | 3-(4,5-dimethylthiazol-2-yl)-2,5-diphenyltetrazolium bromide |
| MW Marker | Molecular Weight Marker |
| NaBF4 | Sodiumtetrafluoroborate |
| NaCl | Sodiumchloride |
| NaOH | Sodiumhydroxide |
| NB | Norbornenes |
| n-Hex | n-Hexane |
| NHS | N-Hydroxysuccinimide |
| NITEC | Nitrile imine-mediated tetrazole-ene cycloaddition |
| nm | Nanometer |
| NMR | Nuclear Magnetic Resonanze |
| o.n. | Over night |
| P/S | Penicillin/Streptomycin |
| PACT | Photoactivated Chemotherapy |
| PBS | Phosphate-Buffered Saline |
| Pd/C | Palladium on carbon |
| PDD | Photodynamic Diagnosis |
| PDT | Photodynamic Therapy |
| PEG | Polyethylene Glykol |

| | |
|---|---|
| PFA | Paraformaldehyde |
| PI | Photoindex |
| PPG | Photolabile protecting group |
| PQ-ERA | Phenanthrenequinone-electron-rich alkene cycloadditions |
| PS | Photosubstitution |
| PTT | Photothermal therapy |
| r. t. | Room temperature |
| Retro-DA | Retro-Diels-Alder |
| RNA | Ribonucleic Acid |
| ROS | Reactive Oxygen Species |
| RP-HPLC | Reversed-Phase High-Performance Liquid Chromatography |
| s | Seconds |
| Sec AB | Secondary antibody |
| SL | Staudinger ligation |
| SnCL2 | Tin(II) chloride |
| SPAAC | Strain-promoted azide-alkyne cycloaddition |
| SPH | Spiro[2.3]hex-1-ene |
| SRB | Sulforhodamine B |
| TBDMS | Tert-Butyldimethylsilyl |
| TCO | Trans-cyclooctene |
| THF | Tetrahydrofuran |
| THPTA | triaryl hydrazinotriazine |
| TMS | Trimethylsilane |
| Tpy | Terpyridine |
| UV | Ultraviolet |
| VdU | Vinyl-desoxyuridine |
| Vis | Visible |
| λ | Wavelength |

# I. General Introduction

The targeted initiation of chemical reactions through external triggers represents an innovative strategy in organic chemistry, enabling precise control over the reactivity and selectivity of compounds.[1] Such triggers include physical stimuli, like light or temperature, or chemical activators, as applied in antibody-drug conjugates (ADCs).[2-4]

However, thermal triggers present certain limitations: heat diffuses throughout the medium, making precise spatial control challenging. Once the temperature is elevated, it becomes difficult to stop the reaction with temporal precision, resulting in thermal triggers to be nearly impractical for use in biological systems. In contrast, photochemical triggers offer both spatial and temporal control (schematically shown in Figure 1). With precise irradiation, reactions can be selectively initiated in specific regions, while unexposed areas remain unaffected. Moreover, the reaction can be activated at a precise moment and immediately stopped by switching off the light source.

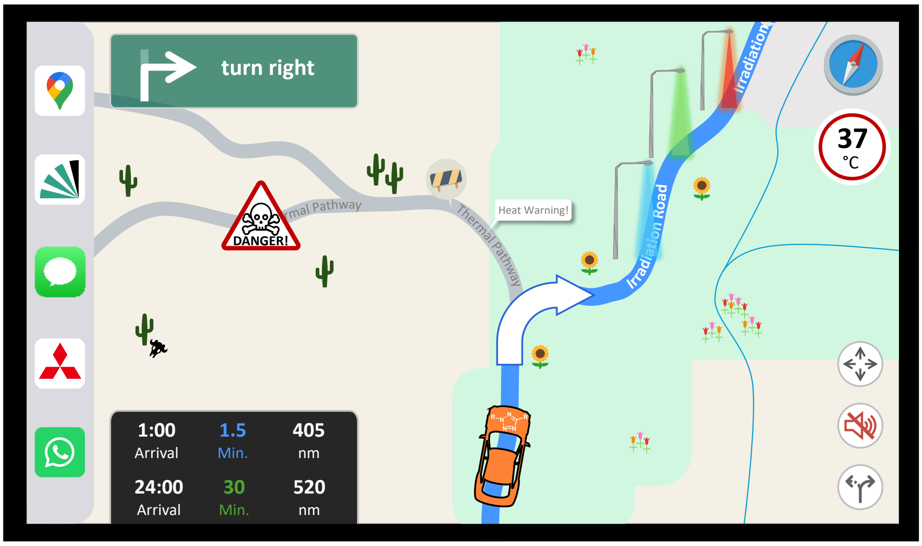

Figure 1. Schematic representation of various externally triggered reactions.

This distinct controllability is particularly relevant to this work, as it allows reactions to be precisely initiated in specific cell regions or tissue layers and controlled with exact timing. Due to the cytotoxicity of UV light, it is important to focus on using visible light as a trigger.

Thus, this research explores the concept of photochemical activation to fully harness the potential for spatially and temporally regulated chemical modifications in biological systems by studying the only click reaction activated by light in the visible range.

This work is divided into three parts. The first part investigates and further develops a light-controlled bioorthogonal labelling method, known as the "photoclick reaction". In this process, tetrazole-based reactants are modified that the reaction can be triggered using visible light (above 405 nm). Besides shifting the activation wavelength and therefore labelling reaction to the visible light range, the herein introduced modifications further enhance the water solubility of the tetrazoles, allowing a potential application in living biological systems. The reaction occurs between tetrazoles as dyes and 2'- deoxynucleosides, which are incorporated into the cellular DNA. The reactivity of the tetrazoles was characterized using UV/Vis spectroscopy and HPLC analysis and was successfully implemented in HeLa cells.

The second part of the work focuses on the development of photoactivatable chemotherapeutics that are non-toxic in their inactive state (in the dark). Only upon light activation, a molecular ligand is cleaved, leading to controlled cell death. Since these molecules are non-emissive, they are initially bioorthogonally labelled using the copper-catalyzed azide-alkyne cycloaddition for cellular studies and visualization to gain insights in their site of action. Various activation and incubation times are examined to investigate the mode of action of the activated substances, and their cellular target organelle is analyzed using immunofluorescence.

In the third part of this work, the method is extended to chemotherapeutics that influence DNA replication. Generally, many chemotherapeutics are known to inhibit the nucleic acid synthesis of cells to suppress the growth of the tumour tissue.[5] As a result, the DNA replication as a prerequisite for an organism to grow and regenerate is brought into the focus of scientific attention to combine the approaches developed in the first and second parts. DNA replication in the cell is observed, and the point at which the biosynthesis of new DNA is inhibited is recorded. For this purpose, a 2'-deoxynucleoside is incubated with the chemotherapeutic agents, and the DNA replication is followed using bioorthogonal reactions to analyze the mode of action of chemotherapeutics and their effects on cellular systems in detail.

# II. Theoretical Background

## 1 Bioorthogonal Reactions

The term “bioorthogonal chemistry“ was introduced by the group of Bertozzi in the early 2000s.[6-8] Since then, bioorthogonal reactions are defined as those that can occur within a cell or living systems without interfering or disrupting biological processes. The goal of this concept is to label biomolecules chemoselectively and thus study them in their natural environment and functions.

The implementation of bioorthogonal reactions occurs in a two-step pathway. First, in the so-called metabolic incorporation step, a building block - for example a 2’-desoxy-nucleoside - modified with a chemical reporter of interest, is added to the biological system. The chemical reporter is ideally not present in the investigated system. This modified building block is metabolically incorporated into the genomic DNA. If the metabolic incorporation is not possible, an unnatural biosynthetic pathway such as DNA transfection can be used (Figure 2 left).[9]

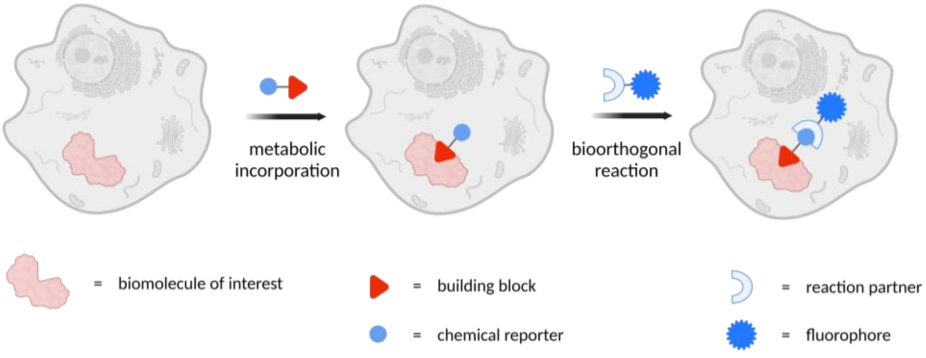

Figure 2. Schematic representation of the two-step pathway of bioorthogonal reactions. First, the metabolic incorporation, a building block (red triangle) modified with a chemical reporter (light blue circle) is metabolically incorporated and binds to the biomolecule of interest (light red protein). Second, the bioorthogonal reaction, the reaction partner (light blue hemicircle) which is coupled with a fluorophore (dark blue circle) covalently binds to the chemical reporter.

In the second step, known as bioorthogonal labelling step, the respective reaction partner with the complementary chemical functionality to the modified 2’-desoxynucleoside is added into the system and binds covalently to the chemical reporter. The reaction partner

is functionalized with a fluorescent tag (chromophore), allowing the visualization of the biomolecule of interest (Figure 2 right). [10]
To meet the criteria of bioorthogonality, several requirements must be fulfilled: i) reactants and products need to be non-toxic and stable in the cellular environment,[6] ii) functional groups need to react selectively with their counterparts without causing undesired side reactions with other biomolecules present in the investigated biological compartment, presuming that the natural properties and biochemical processes within a cell are not or only minimally disrupted, iii) the selective reactants must react under physiological conditions (neutral pH, physiological temperature, aqueous medium), [6, 11-12] iv) bioorthogonal reactions need to be rapid and provide high-second order rate constants, to avoid poor solubility and the toxicity of the reagents.[6, 12-13]

At this point, it needs to be noted, that the two-step reaction minimizes the effects of disturbing the natural structure of the biomolecule. In the first step the only unknown part for the cell is the small functionalization which can be easily tolerated by the kinases in the cells. The second step can be chosen from a library of different bioorthogonal labelling reactions, which one is the best for the visualization of the biomolecule of interest.[14] Additionally, bioorthogonal reactions are versatile enough to label different types of biomolecules, like nucleic acids, glycans, small metabolites and proteins.[12, 15-16]

In the past two decades, numerous reactions that meet these criteria have been developed and opened multiple opportunities to study the biological processes in biological systems. In particular the Staudinger ligation (SL),[17] the copper-catalyzed azide-alkyne cycloaddition (CuAAC),[18] strain-promoted azide-alkyne cycloaddition (SPAAC),[19] inverse electron-demand Diels-Alder cycloadditions (IEDDA), [15] and the photoclick reaction[20-21] gained popularity. Typically, the bioorthogonal reactions follow second-order kinetics, due to the two reactive species involved.[22]

Figure 3A gives an overview of bioorthogonal reactions. SL, initially described by *Hermann Staudinger* in 1919 was the first reaction introducing azides as functional groups and requiring triphenylphosphines as reaction partners to receive primary amines. This laid the foundation for subsequent bioorthogonal reactions (Figure 3, yellow) and resulted in *Staudinger* being the eponym for this reaction.[17, 23] It took almost 80 years, until *Bertozzi et al.* discovered the reaction between azides and triarylphosphines in what became known as the bioorthogonal SL. This reaction enabled the labelling of glycoconjugates on cell surfaces in 2000 with high selectivity under physiological conditions. [23-24] The major drawbacks of the SL are the toxicity of triphenylphosphines and the slow reaction kinetics, as shown in Figure 3B. This was improved by the CuAAC (Figure 3, green). It employes azides and terminal alkynes and was first introduced as a bioorthogonal reaction in 2002 by *Sharpless*[25] and *Meldal* [26] using cu-catalysis, but it was already known since 1960 by *Huisgen* using thermal methods to activate.[27] Negative drawback of the CuAAC is already introduced with the name, it needs Cu (I) species for successful reaction of the reactants, which is cytotoxic for biological systems.[28] This was changed by the SPAAC (Figure 3, rosé), which was developed as bioorthogonal reaction by *Bertozzi* and coworkers,[29] being a copper-free labelling method with strained alkynes, like cyclooctyne as really reactive reaction partner. Those are known as explosive from literature in 1953.[30-31] The general reaction between azide and cyclooctine is known since 1961 from *Wittig* and *Krebs*.[32]

Unfortunately, SPAAC lags behind CuAAC due to its low reaction rate constants, resulting in a lower reaction speed (Figure 3B).[12] Even with the most reactive cyclooctynes, its rate is still too low for certain biological processes.[33] Fast reaction kinetics are provided by the IEDDA (Figure 3, red) and photoclick reaction (Figure 3, blue) due to the small gap of energy between the LUMO of the diene and HOMO of the dienophile and highly reactive nitrile imine, generated in situ by light. Additionally, the photoclick reaction offers spatial and temporal control over the ligation and visualization process, being the only bioorthogonal reaction, enabling the on-demand and remote labelling of biological processes in highly dynamic systems while maintaining equally fast reaction kinetics.

Regarding the relevance to this work, the beforehand briefly mentioned advantages and disadvantages of the azide alkye cycloadditions (CuAAC and SPAAC), IEDDA and photoclick reaction are described in more detail in the following chapters.

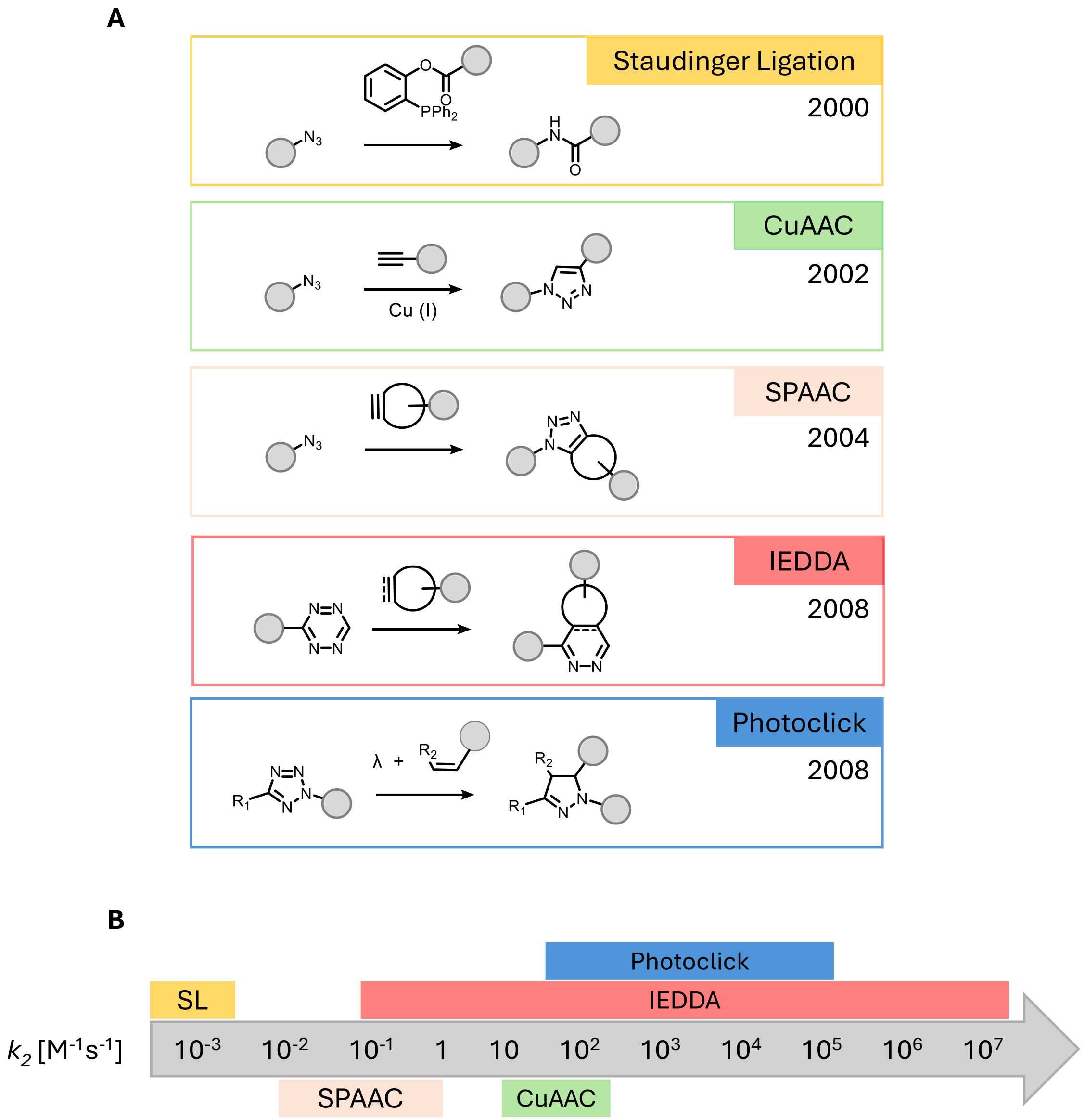

Figure 3. A: Overview of bioorthogonal reactions in their time-order: Staudinger ligation (2000, yellow), CuAAC (2002, green), SPAAC (2004, rosé), IEDDA (2008, red) and Photoclick (2008, blue); B: Overview over the labelling methods and their range of reaction rates $k_2$.[19]

## 1.1 Azide Alkyne Cycloadditions

Albeit the CuAAC (Figure 3A, green) is one of the fastest bioorthogonal labelling methods (up to $k_2 = 200\ M^{-1}s^{-1}$)[19] and was the reaction between azides and alkynes was first introduced in the 1960s by *Huisgen* (Figure 4).[27, 34] Along with the need of high temperatures and low reaction rates, the uncatalyzed reaction resulted in two different regioisomers (1,4- and 1,5-isomers, Figure 4), rendering it unsuitable as a bioorthogonal reaction. *Sharpless* and *Meldal* independently introduced Cu(I) as catalyst and thus made it applicable bioorthogonal reactions,[25-26, 35-37] which not only significantly improved the regioselectivity (1,4-isomer only) due to the six-membered copper metallacyle but also led to faster reaction rate constants. CuAAC counts as one of the fastest bioorthogonal labelling methods. Compared to SL, the CuAAC reaction is 25 times faster (Figure 3, green) and can be performed at ambient temperatures. [6, 25-26] Taking the criteria for bioorthogonal reactions into account, the used reactants, azides and terminal alkynes, are not existing in living organisms and sufficiently stable under physiological conditions.[38-39] Up-to-now, the CuAAC found widespread application in organic chemistry,[38] drug development,[40] material science,[41] as well in labelling of various biomolecules as nucleic acids,[42] glycans,[43] proteins,[44] lipids,[45] anticancer complexes.[46-47] Even though CuAAC labelling in live cell has been reported,[48-49] most of the visualization experiments were conducted in fixed cells due to the cytotoxicity of Cu(I) and Cu(II) ions.[50] Both, Cu(I) and Cu(II) can lead to the formation of reactive oxygen species (ROS),[51-52] that are cytotoxic by interrupting normal cellular function or damaging the DNA resulting in different diseases, such as Alzheimer’s and *Parkinson’s* disease.[53]

To reduce the use of toxic reagents novel Cu(I)-stabilizing ligands (e.g. tris((1-hydroxy-propyl-1H-1,2,3-triazol-4-yl)methyl)amine (THPTA)) were developed, with the aim to prevent the oxidation of Cu(I) to Cu(II). It was assumed to reduce DNA damage and toxicity in cells, while improving water solubility and thereby enhancing the reaction rate constants.[54-55] Despite these improvements, the CuAAC is still not entirely applicable in living cells, due to the toxicity of the Cu-species and the huge stabilization agent which is slowing down the reaction due to bad permeabilization properties.

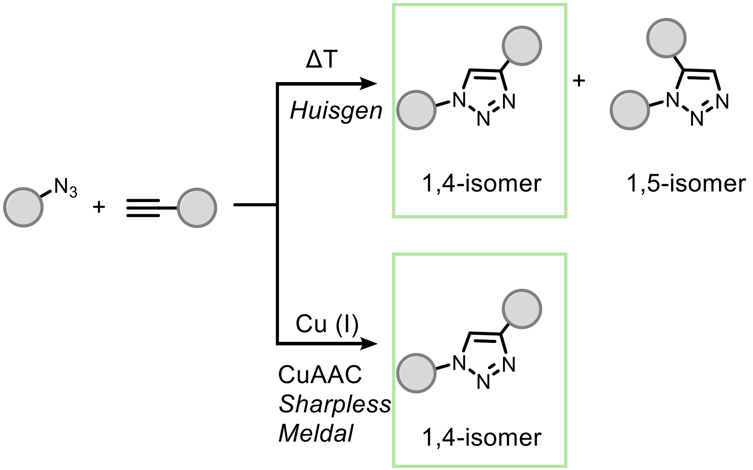

Figure 4. Schematic drawing of the two cycloadditions using alkynes and azides. Top: Cycloaddition by *Huisgen* et al., requiring high temperatures and long reaction times, generating two reaction products. Bottom: CuAAC employing Cu(I) as catalysts, selectively leading to one reaction product, introduced from *Sharpless* and *Meldal*.

In order to reduce ROS formation, potentially leading to DNA damage, and to make bioorthogonal reactions more applicable *in vivo*, the metal-free labelling method was developed and called SPAAC (Figure 3 rosé). Here, the alkyne or alkene substrates are under ring tension. In 2004 *Bertozzi et al*. reported the first reaction between azides and strained-alkynes in the biological environment (called "first generation SPAAC") with a modified sugar for glycan labelling.[29] Removing the copper-catalyst and changing to ring tension slowed down the reaction 10000 to 20000 times, and therefore comprised the $k_2$ to 0.01 to 0.02 $M^{-1}s^{-1}$ (Figure 3, rosé).[29] To improve the reaction coefficients, a second generation SPAAC with higher reaction coefficients was introduced some years later. Despite the modifications of the reactants with fluorides (DIFO),[30, 56-57] aromatic systems (DIBO)[58] and heteroatoms (BARAC) [59] , the SPAAC is still 200 times slower than CuAAC.[30] These compounds are a combination of a strained cyclooctyne core with electron-withdrawing substituents, condensed aromatic rings, and/or heteroatoms. While the increased ring strain enhances reactivity, the higher lipophilicity and steric hindrance reduce the application of SPAAC in aqueous and living systems by undesired side effects. The steric limitations were overcome by the introduction of bicyclo[6.1.0]non-4-yn (BCN) in 2010 from *van Delft et al.*, applying SPAAC-labelling in live cells, e.g. in HeLa cells, zebrafish and mice.[60-61] This strained moiety was either attached to a biomolecule[9] or coupled to a fluorescent dye. [62]

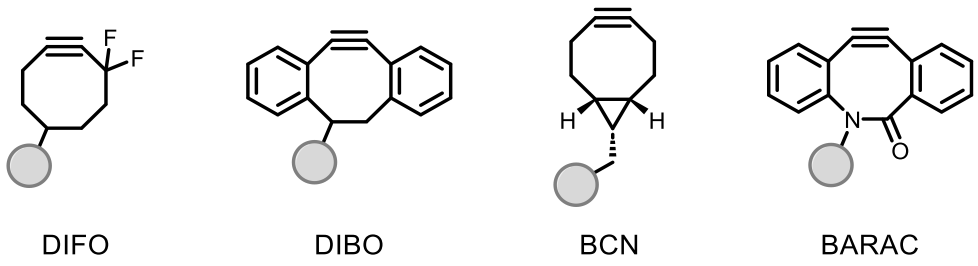

Figure 5: Examples of stained cyclooctyne derivatives for SPAAC from less reactive to most reactive (left to right): Difluorocyclooctyne (DIFO), dibenzylcyclooctyne (DIBO), bicyclononyne (BCN) and biarylazacyclooctynes (BARAC).

The biggest limitation of the SPAAC is the low reaction rate constant[63] and the low stability of the strained alkynes.[12, 33] An acceleration (Figure 3B) was achieved through developing the IEDDA reaction (Figure 3, red), which will be explained in the following chapter.

## 1.2 IEDDA

The IEDDA reaction (Figure 3, red), where 1,2,4,5-tetrazines react with electron-deficient alkenes, was added to the library of bioorthogonal reactions in 2008 by the groups of *Fox* and *Hilderbrand*.[64-65] They modified the Diels-Alder cycloaddition reaction, presented by *Otto Diels* and *Kurt Alder* almost a century ago.[66] The Diels-Alder reaction is one of the most used synthetic tools for forming carbon-carbon bonds. Mechanistically, the Diels-Alder (DA) reaction, as well as the IEDDA reaction are [4+2]-cycloadditions of a conjugated diene (4 π-electron system) with a dienophile (2π-electrons system).

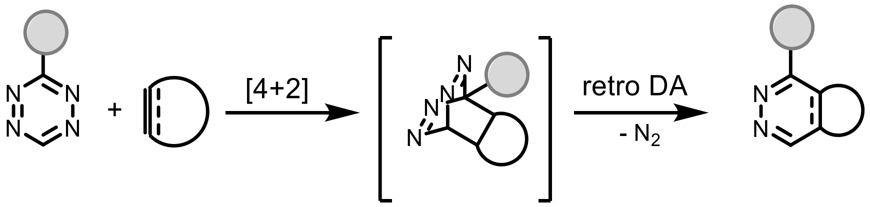

Figure 6. General reaction mechanism of the IEDDA reaction between 1,2,4,5-tetrazines with a dienophile.

Cycloadditions in general are reactions, that involve the reorganization of π-electrons and formation of two new σ-bonds,[67] resulting in a ring as product (Figure 6). Depending on the two initial reaction partners and their number of π-electrons, the name and numbers are different (e.g. [2+2], [4+2] or [4+4]).[68] Major differences in both methods are the energetic positions of the involved frontier molecular orbitals and are displayed in Figure 7. In the Diels-Alder reaction with normal electron demand, the highest occupied molecular orbital (HOMO) of the diene and the lowest unoccupied molecular orbital (LUMO) of the dienophile react with each other. For the IEDDA, the LUMO of the diene is reacting with the HOMO of the dienophile (Figure 7).[69] In a Diels-Alder reaction, the conjugated diene carries electron-donating groups, while the dienophile is substituted with electron-withdrawing groups. In contrast, for the IEDDA reaction, the roles are reversed.

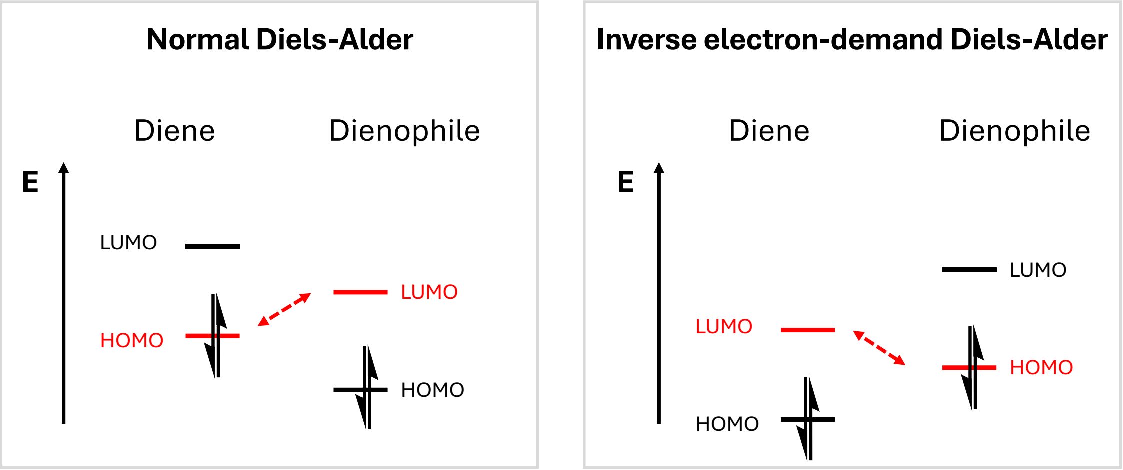

Figure 7. Interacting molecular orbitals in a normal Diels-Alder reaction (left) and IEDDA (right).[70]

Both, the Diels-Alder reaction and the IEDDA reaction seem well-suited for bioorthogonal reactions: they can take place in aqueous environments as well as under physiological conditions, and they show high yields and high chemoselectivity. This high chemoselectivity allows for the use of low reactant concentrations minimizing toxicity and limiting interference for cellular systems. In the case of the IEDDA reaction, which utilizes 1,2,4,5-tetrazines, the reaction is driven by nitrogen extrusion. This not only makes the reaction irreversible but also results in a single side product, which is nitrogen.

Most common used dienophiles for the IEDDA are vinylated-compounds,[69] norbornenes (NB),[71-72] cyclopropenes (CP),[73] bicyclononynes (BCN)[74] and trans-cyclooctenes (TCOs)[75] in combination with 1,2,4,5-tetrazines as dienes (Figure 8).

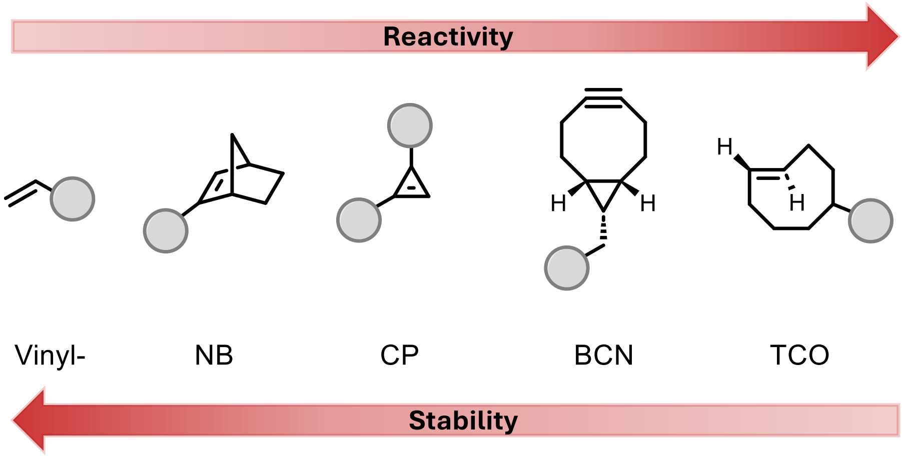

Figure 8. Overview of the most important dienophiles for a bioorthogonal IEDDA reaction in terms of reactivity and stability.

The reactivity increases from vinylated-compounds ($k_2 = 10^{-3}$ bis $10^{-2}\,M^{-1}s^{-1}$)[69, 76] to TCOs ($k_2 = 10^{6}\,M^{-1}s^{-1}$)[69, 75] as the most reactive known reaction partner for tetrazines (Figure 3B). However, higher reaction rate constants often comprise the stability of the starting materials, making higher reactivity less advantageous, especially in living systems where stability is essential to avoid unwanted side reactions and ensure controlled, specific interactions.[77]

In biological systems, it is crucial not only to achieve high reaction rates constants and high stability, but also to be able to monitor the reaction using a confocal microscope.[78] As a result, performing the bioorthogonal reactions with fluorogenic tetrazines has gained significant research interest in the past years. A key feature of tetrazines is their ability to quench fluorophores, rendering them ideal for the utilization as fluorogenic probes when combined with fluorescence.[79] Upon reacting with their respective reaction partner (electron-rich alkene), the fluorescence of these tetrazines is activated, offering a significant advantage for the *in vivo* experiments. Since only the reacted tetrazines become fluorescent, additional washing steps are unnecessary.[9, 80-81] This significantly improves the signal-to-noise ratio compared to conventional tetrazines.[82-83] The fluorescent tetrazines were further improved for nucleic acids by *Geng et al*., named as “two-factor fluorogenicity of cyanine-styryl dyes”.[9, 84] This concept encompasses two aspects: firstly, the quenching effect followed by an increase in tetrazine fluorescence, and secondly, an additional boost in fluorescence due to restricted rotation of the dye after intercalation into the DNA, shown in Figure 9.[84]

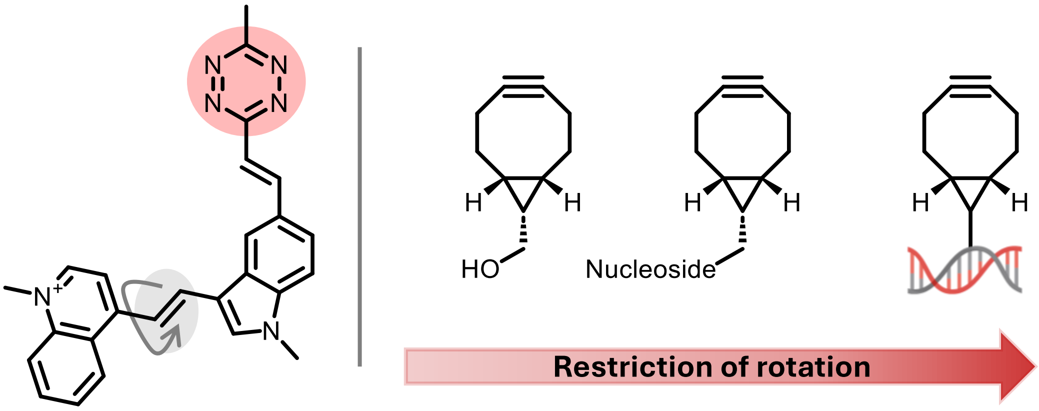

Figure 9. Two-factor fluorogenicity of a tetrazine-modified cyanine-styryl dye (left side). Tetrazine mojety (red), reacts as quencher for the cyanine-styryl dye. Additionally, the rotation restriction of the dye (grey) is increasing from reacting with a BCN-OH to BCN incubated into DNA (right side).

Today, the IEDDA reaction is the most widely used bioorthogonal click reaction due to all the mentioned advantages while featuring significantly higher reaction rate constants $k_2 = 10^7\ M^{-1}s^{-1}$ (Figure 3B) than that of CuAAC.

In conclusion, both the CuAAC and SPAAC bear certain disadvantages (i.e. cytotoxicity and slow reaction kinetics) that have been significantly improved by the IEDDA. However, none of the three previously introduced bioorthogonal labelling (or ligation) reactions offer spatial and temporal control over the visualization process and the timing of the reaction.

A potential solution involves the utilization of light as an external trigger to initiate the reaction. [85] This approach enables precise control over both spatial and temporal parameters through the application of light.[21, 86] The photoclick reaction (Figure 3A, blue) utilizes this concept, enabling controlled activation of a bioorthogonal reaction with high specificity and accuracy.[20] Given the high relevance to the current work, light-induced bioorthogonal reactions will be discussed in further detail in the next chapter.

## 1.3 Light-induced Bioorthogonal Reactions

Currently, there are four different photoactivatable bioorthogonal reactions. To simplify their distinction, they are classified “type 1-4”.[86-87] Type 1 refers to a click reaction, in which both reaction partners are activated, either by photocatalysis or photoinitiators. An example of a type 1 reaction is the “photoinitiated azide-alkyne click reaction”. Herein, it is possible to generate the Cu(I) species in situ by activation with light. This allows for spatiotemporal control of the CuAAC reaction. A specific example is the indirect photoreduction, where copper ions are generated by triggering the intramolecular electron transfer from the π-system of the ligand to the metal ion, whereas the Cu(II) is converted to Cu(I) and the ligand becomes a ligand radical.[88] The advantage of this method is that it eliminates the need for a stabilizing agent like sodium ascorbate, thereby reducing toxicity. However, a significant drawback of type 1 is the need of UV-light to activate the photocatalyst and to receive the radicals.[88-89]

The more commonly used type 2 reaction describes the classical click reaction that is activated by the cleavage of a covalent bond upon exposure to light from a photolabile protecting group (PPG).[90] In this context the PPGs, also known as photocages, can mask the thiol click functionality in thiol-Michael additions. Once activated, the thiol is photochemically released, allowing the thiol-ene click reaction to proceed as usual.[90] One drawback of this approach is, that the cleaved PPG stays as side product in the reaction mixture. An example is the ortho-nitrobenzyl[91] which has limitations, such as the need of high-energy ultraviolet (UV) light and the production of toxic and strongly light absorbing byproduct of the reaction.[92] Type 3 is referred to the photoclick or nitrile imine-mediated tetrazole-ene cycloaddition (NITEC) reaction.[85] This type will be used in the thesis and will be explained more detailed *vide infra*.

Type 4 involves 9,10-phenanthrenequinone-electron-rich alkene cycloadditions (PQ-ERA) which are known since the 1940s by *Schönberg*.[93] Herein, the PQ is excited and reacts with electron-rich alkenes (ERA), such as sytrenes or triphenyl ethylene.[93] Until 2018, a strong mercury lamp was used, leading to the formation of an excited state that underwent internal conversion to the triplet state. This process resulted in reaction time exceeding several days, which was a significant disadvantage.

Nonetheless, from 2018 on *Zhang* and colleagues, along with the *Feringa* research group advanced the PQ-ERA methodology, enabling the use of high-energy violet or blue light.[94-95]

As explained, type 3 known as the photoclick or NITEC reaction is used in this work due to its high potential for application in living systems. This reaction produces only a small byproduct, the $N_2$ gas, and research is on-going to shift activation into the visible light range. Generally, a molecule gets irreversibly photoactivated while generating reactive intermediates. The reaction described by *Huisgen et al.*, involves a 1,3-dipolar cycloaddition of a nitrile imine generated from 2,5-substituted diaryltetrazoles by release of $N_2$ upon UV light irradiation.[27, 96] This reaction required high temperatures (150 °C) or UV light (from a high pressure mercury lamp) to obtain the desired product.[96-98] In 2008, *Lin et al.*[99-100] transformed the reaction to one of the most intriguing bioorthogonal reactions due to its spatiotemporal control.

The generated nitrile imine immediately undergoes a 1,3-dipolar cycloaddition with dipolarophiles (e.g. alkenes) leading to the five-membered pyrazoline as photoclick product (Figure 10).[100]

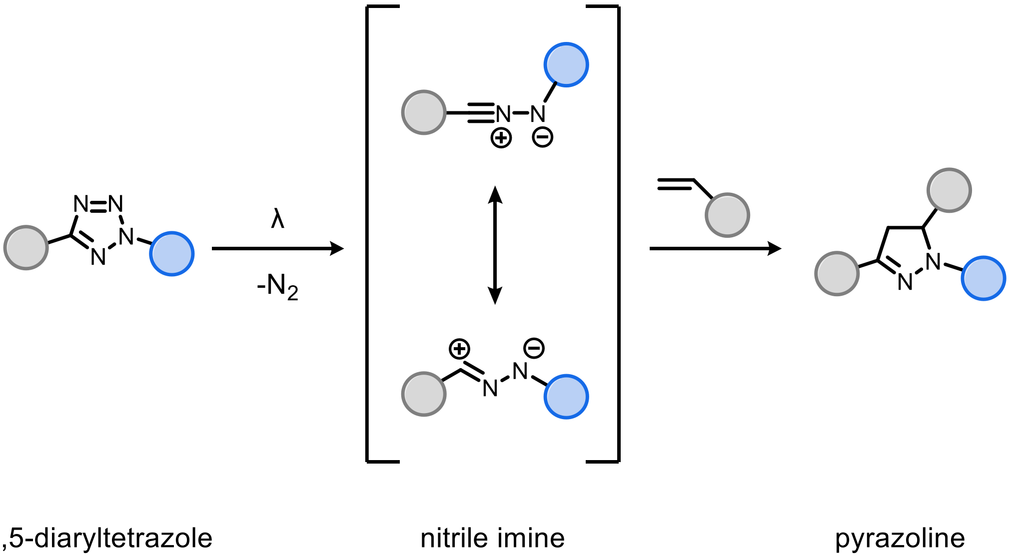

Figure 10. Two-step reaction mechanism of the nitrile imine photoclick reaction: After activating the 2,5-diaryltetrazole with a specific wavelength of light, nitrogen is eliminated to generate a highly reactive nitrile imine which reacts with an alkene and results in the pyrazoline product.

In addition to its photoactivation, the photoclick reaction is characterized by its high reaction rate constants. Depending on the reaction partners and conditions, rate constants in the range of $k_2 = 10^5$ $M^{-1}s^{-1}$ are realized (Figure 3B, blue). Since the photoclick reaction can be divided into two distinct steps – the generation of the nitrile imine and reaction with the nucleophile, two different rate constants should be considered. The kinetics of the first step, the photolysis of the tetrazole, depends on various factors, such as the light source, its intensity, and the so-called inner filter effect of the reaction solution. The inner filter effect refers to the attenuation of light intensity within the sample due to absorption by molecules at the sample's surface, resulting in uneven irradiation throughout the solution. This effect is strongly dependent on the concentration of the sample. At high reactant concentrations the light cannot penetrate deeply into the sample, resulting in a prolonged light exposure of some reactants to generate the nitrile imine. Consequently, this first step of photolysis can be slowed down by technical means. The second step in the photoclick reaction is assumed to be significantly faster, as the highly reactive nitrile imine rapidly reacts with various possible partners.[101] Therefore, the design and synthesis of the tetrazoles are the most crucial aspects in the photoclick reaction to enhance the reaction rate.

Thus, in 2008, *Lin*'s research group pioneered the photoclick reaction and synthesized various methyl benzoate-functionalized diaryltetrazoles and activated them using a handheld UV lamp ($\lambda$ = 302 nm).[102] Additionally, they successfully labelled tetrazole-modified proteins in cell lysate and *E. coli*, making the first instance of bioorthogonal labelling in cells using light activation.[99-100, 103] Various modified tetrazoles were synthesized (e.g. terthiophenes or naphthalene groups), all activated with UV light of $\lambda$ = 365 nm,[104-105] which is a significant improvement in comparison to the previously used $\lambda$ = 302 nm altough it still falls within the UV range of light.

An important limiting factor is the chemoselectivity of the reactants. The highly reactive nitrile imine shows cross-reactivity with different moieties that are present in cellular environments, like water, amines, thiols and carboxylic acids (Figure 11).[85, 106-107]

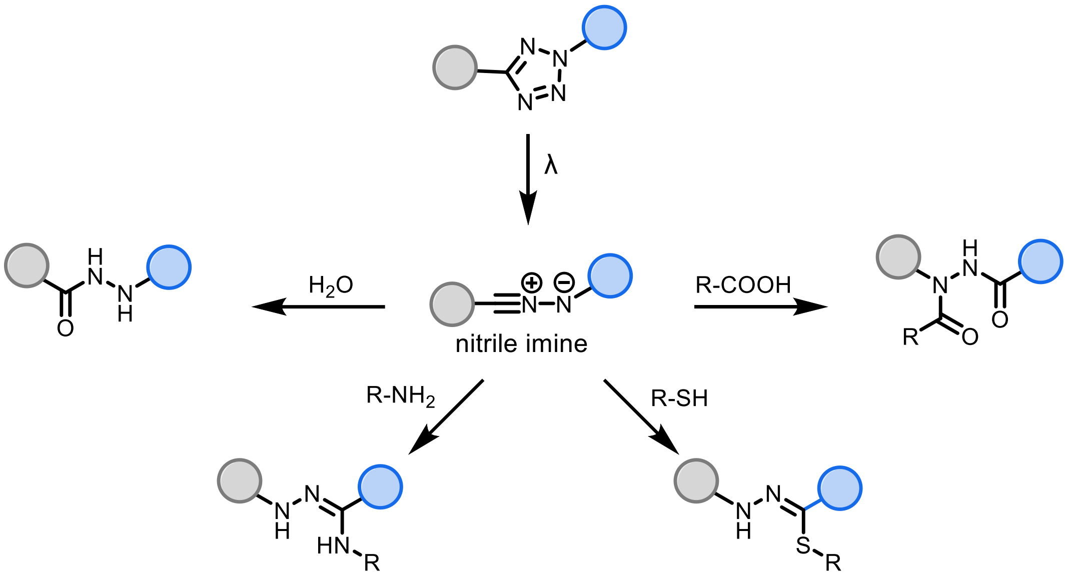

Figure 11. Overview for the side-reactions of the nitrile imine with moieties present in cellular environments: water, amines, thioles and carboxylic acids.

To prevent these undesired side reactions, three different approaches are currently pursued: i) protection of the nitrile imine from a nucleophilic attack through static and electrostatic effects by introducing two trifluoromethyl groups, each carrying a partial negative charge. This was introduced by *Yu et al.* in 2020.[108] ii) sterically demanding groups near the nitrile imine can shield it, thereby preventing the possibility of a nucleophilic attack.[109] iii) Using intercalating agents on one side of the tetrazol, that are close to the reacting side in the nucleic acids and therefore decrease side reactions.[101]

All above explained tetrazoles and methods were mostly used for protein labelling[109-112] but rarely for nucleic acids. Around one decade ago, *Wagenknecht* and coworkers were the first group, who expanded the research from proteins to oligonucleotides. A DNA builiding block bearing a diaryltetrazole moiety was incorporated into a DNA strand. The labelling of the tetrazole-modified DNA strand was realized exploiting a sulfo-Cy3 maleimide dye that reacted with the generated nitrile imine after irradiation with a $\lambda = 365$ nm LED. [113] This method was further improved by *Wagenknecht et al.* and applied for RNA labelling.[114]

It is a significant advancement that the photoclick reaction has already been successfully carried out on DNA and RNA; however, the main drawbacks are the wavelengths used for irradiation, which range between 305 and 400 nm, which can be harmful to living cells,[115] and therefore is the limiting factor of current light-induced bioorthogonal reactions. Additionally, high energy light has only low tissue penetration, and therefore visible-light activated tetrazoles are more desirable for the usage in living organisms.[116] With the knowledge that the different modified tetrazoles (Figure 13) applied on living systems need to be activated with low energy, the synthesis of the 2,5-diaryltetrazoles plays a crucial role. Different methods for the synthesis were already studied in 1901 by the groups of *Hantzsch* and *Vagt*.[117] As of today, two different methods are used for the synthesis of 2,5-modified tetrazoles. Although the first synthetic approaches were already studied more than one century ago by *Kakehi et al.* in 1976 via hydrazones,[118] while the second method was introduced in 2015 by *Liu et al*. using amidines. [85, 119]

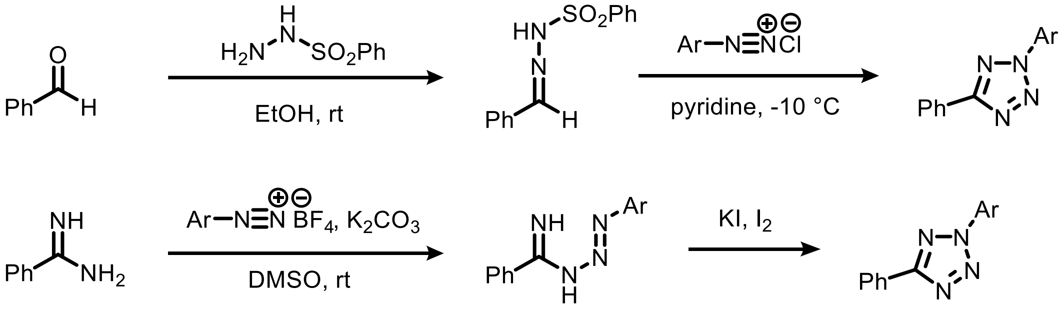

Figure 12. Different synthetic pathways to synthesize tetrazoles. Top: tetrazole synthesis after *Kakehi et al.* using a hydrazone moiety; bottom: tetrazole synthesis after *Liu et al.* using amidines.

Tetrazole synthesis using hydrazones offers several advantages over the method using amidines. Hydrazone-based synthesis generally operates under milder conditions, allowing for a wider range of substrates and often leading to higher yields due to reduced side reactions. Hydrazones are also typically more stable and easier to handle compared to amidine salts. Overall, these factors make the hydrazone method a more efficient and versatile approach for tetrazole synthesis. This is why most tetrazoles known are synthesized with the *Kakehi* method.[21-22]

One new idea, resulting in visible light irradiation, was the usage of a two naphthyl substituents tetrazole which can be activated with a two-photon femtosecond laser system at 700 nm. With this method it was possible to perform the reaction in live cells.[111] Drawbacks herefore is the femtosecond laser system that is needed. *Barner-Kowollik* and coworkers used a *N*,*N*-dimethyl-aminopyrene aryl tetrazole [120] which was used in polymer chemistry and was activated with green light ($\lambda$ = 515 nm).[121] The problem in this tetrazole system is the water solubility, which makes the tetrazole unusable in living systems. All discussed tetrazoles are presented in Figure 13. From top to bottom, the excitation wavelength increases, resulting in less cellular toxicity and better tissue penetration because of light. The tetrazole that can be excited at 700 nm was stimulated using a femtosecond-laser and the other tetrazoles excited at lower wavelengths were performed with LEDs. The laser setup is more difficult and more expensive to use than LEDs, which makes it not applicable to every lab.

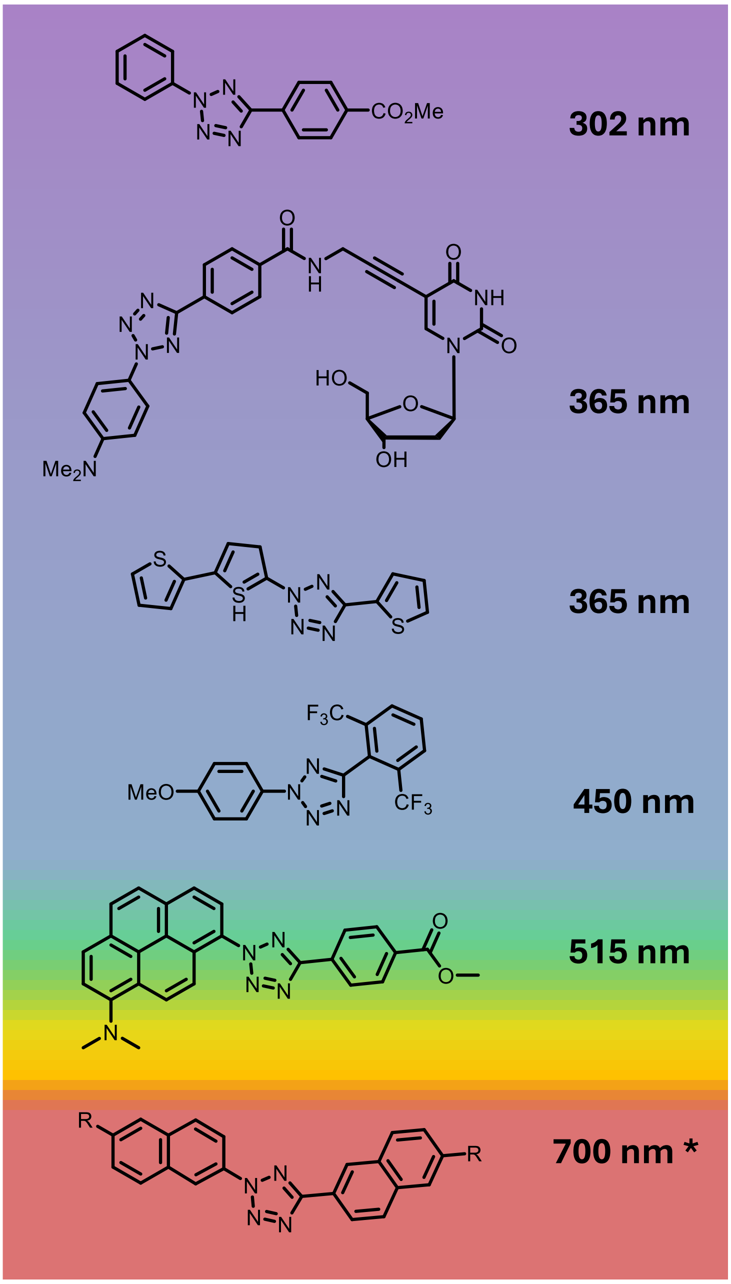

Figure 13. An overview of known tetrazoles used in photoclick reactions along with their excitation wavelengths, ranging from short to long wavelengths. The tetrazole excitable at 700 nm was activated *via* two-photon excitation using a femtosecond laser.

What further enhances the appeal of the photoclick reaction is its combination with another bioorthogonal reaction, enabling spatiotemporal control in comparison to conventional methods. In combination it could be possible to image at a certain time point (though photoclick) and apply therapy or get more insights for diagnosis of drugs. These approaches will be explored in more detail in the following chapter.

# 2 Dual Bioorthogonal Labelling

To fully understand living systems, it is often insufficient to track only a single organelle, reaction, process, or small molecule. It is essential to observe interactions between, for example, proteins, oligonucleotides, or even drugs and DNA. By employing multiple chemical reporters, it becomes possible to monitor molecular dynamics within living systems. This approach has significant applications in cancer therapy, where diagnosis and treatment must often be tracked simultaneously.[122-126] In such applications, using more than one bioorthogonal reaction within the same system is feasible.[127] However, careful consideration must be given to the selection of these reactions to avoid undesired side reactions. Several different combinations are already well-known. One straightforward approach is to combine two bioorthogonal reactions that utilize the same chemical reporters.

For instance, this can be achieved with CuAAC and SPAAC reactions using strained alkynes. If the experimental setup allows for sequential execution of these reactions, this method should present no significant issues. However, in a one-pot reaction, complete chemoselectivity cannot be guaranteed, leading to potential cross-reactivity and the formation of side products.[128] Selecting two reactions with different mechanisms of bioorthogonality is the most direct approach to achieving reliable dual bioorthogonality. A recent publication by the *Burley* group shows, that the combination of CuAAC and SPAAC is feasible due to the controlled modulation of the copper-glutathione ratio.[129] This ratio serves as an activator for CuAAC, as it regulates the oxidation state of the copper catalyst. This new discovery is of significant scientific interest. It offers an additional mean of control: not only light as an external trigger but also the precise concentration of glutathione. This approach could potentially expand the versatility and selectivity of CuAAC reactions by fine-tuning the reaction environment based on glutathione levels.[129]

Approaches to dual labelling are often more complex and typically involve computational modeling prior to *in vitro* and *in vivo* applications. For instance, *Houk et al.* investigated the activation energy for using cyclopropenes and sydnones versus azides, leading to the subsequent implementation of SPAAC with sydnones in combination with IEDDA.[130] This was validated both theoretically and experimentally in the labelling of two proteins.

As discussed in the CuAAC and IEDDA chapters above, both reactions are based on cycloaddition mechanisms and involve alkynes. However, the alkynes used in CuAAC exhibit HOMOs of lower energy, whereas IEDDA favors alkynes with HOMOs of high energy. This distinction has allowed CuAAC and IEDDA reactions to serve as mutually orthogonal bioorthogonal reactions for several years. With this method it was possible for *Jaschke et al.* to dually label DNA *in vivo*.[131]

Sterically hindered groups can be strategically employed to modulate reaction specificity.[132] For instance, *Hilderbrand et al*. developed a system integrating SPAAC and IEDDA by utilizing a sterically hindered cyclooctyne.[133] This steric hindrance effectively slows down the undesired side reaction between tetrazines and cyclooctynes, reducing it to a negligible level relative to the intended reaction. *Hilderbrand*'s approach has already been successfully applied *in vivo* in mice, enabling fluorescence-guided tumor resection.[123]

Recent work by *Seul et al.* has developed a dual strategy that combines steric hindrance and activation via an external trigger, specifically employing photoclick chemistry.[134] In this approach, two distinct cyclopropenes (CPs) are incorporated into cellular DNA either *in vitro* or within living cells through metabolic labelling facilitated by the SNT-transporter. 1-Methylcyclopropenes (1-MCP) are potent candidates for IEDDA reactions; however, methyl substitution at the 3-position of CP introduces significant steric hindrance in the transition state, effectively impeding the IEDDA reaction, shown in Figure 14.[135-136] Interestingly, these 3-substituted CPs (3-MCPs) undergo rapid photoclick reactions with nitrile imines if activated by a carboxy group.[137] The study demonstrates dual bioorthogonal and orthogonal labelling of genomic DNA through metabolic incorporation of both 1-MCP and 3-MCP, each conjugated to different 2′-deoxynucleosides. This innovative approach provides a versatile tool not only for genomic DNA labelling but also for potential applications in labelling cellular RNA or therapeutic oligonucleotides delivered into cells, enabling multiplexed bioorthogonal and orthogonal reactions.[134]

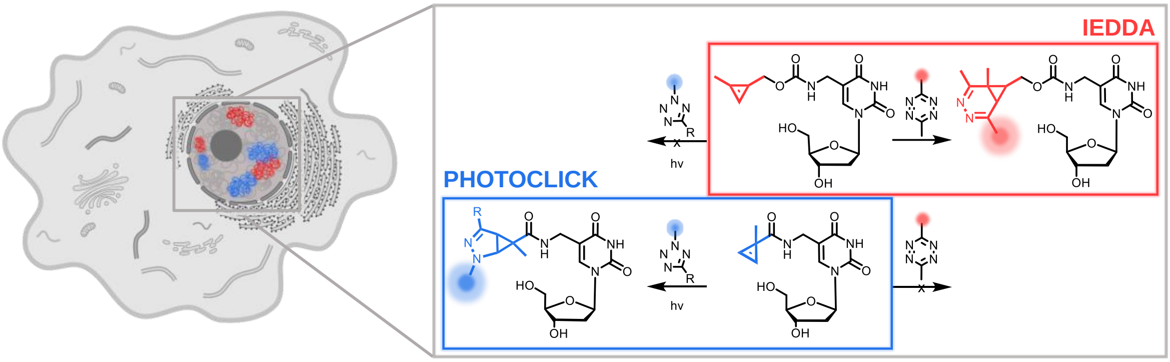

Figure 14. Dual bioorthogonal and orthogonal labelling of DNA through the combined use of IEDDA and photoclick reactions, facilitated by the incorporation of isomeric methylcyclopropenes (1-MCP and 3-MCP) as 2′-deoxyuridine modifications.[134] Adopted with permission from *Seul et al*., *Angew. Chem. Int. Ed*., **2024**, *63*, e202403044. Copyright 2024 John Wiley and Sons.[1]

---

[1] N. Seul, D. Lamade, P. Stoychev, M. Mijic, R. T. Michenfelder, L. Rieger, P. Geng, H. A. Wagenknecht, *Angew. Chem. Int. Ed. Engl.* **2024**, *63*, e202403044

# 3 Photoactivated Chemotherapy

Despite all the efforts, cancer is today still one of the deadliest diseases worldwide. In 2022, worldwide cancer cases rose to 20 mio, with cancer-related deaths inceasting up to 10 mio.[138] The golden standard in cancer treatments included removal of the tumor by surgery, and/or systemic therapy (chemotherapy, hormonal treatmens and targeted biological therapies) to eliminate the tumor and its metastasis.[139] Commonly used chemotherapeutic agents in chemotherapy are doxorubicin (DOX),[140] paclitaxel,[141] S-crizotinig[142] or cisplatin.[143-144] The Pt(II) containing cisplatin was approved by the FDA in 1978 for the clinics.[145] Up to date, the success of cisplatin continues as its still the most applied chemotherapeutic worldwide. The most recognized mode-of-action of cisplatin involves several key steps: i) cellular uptake by passive diffusion or with the help of an active transporter e.g. copper transporter 1 (CTR1), ii) hydrolysis of the chlorido ligand(s) and formation of a mono or bis-aqua intermediate, and iii) binding of the intermediate aqua complexes to DNA via coordination to N7 of the purine bases (Figure 15).[146]

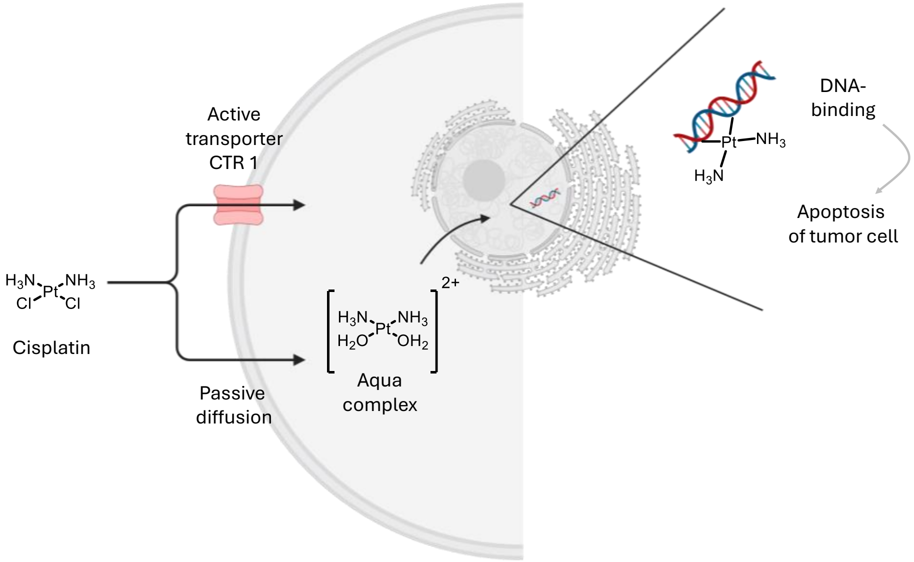

Figure 15. Mode-of-action of cisplatin. Cisplatin is taken up by the cell either through passive diffusion or via active transporter (e.g. CTR1); hydroloysis of the chloride ligands, forming the aqua complex; binding to DNA; killing the cell.

As a result, DNA damage occurs triggering apoptosis of cells. Some tumor cells, however, are resistant to cisplatin treatment. In addition, cisplatin treatment is frequently associated with several side effects, that can limit its therapeutic efficacy.[147]

Second generation Pt(II) derivatives led to lower toxicity but also with a reduction in effectiveness. Nevertheless, the discovery of cisplatin paved the way for more transition metal complex in bioinorganic application. One of these metals that draw attention in the field of oncology is ruthenium. NAMI-A,[148] KP1339[148] also known as BOLD-100[149] as well as TLD1433[150] are Ru-based complexes that had been or are still under clinical investigations. KP1339/BOLD-100 is the second-generation drug of NAMI-A which was the first ever Ru-based drug applied to humans but failed in clinical phase II developed by *Keppler et al.* (Figure 16, left). Currently it is under clinical investigation for the treatment of colon cancer.[151-152] Its mode-of-action relies on the activation of the complex leading to formation of the Ru(II) species with labile Ru-Cl bonds. In cellular systems, the complex interacts with DNA, leading to DNA unwinding and slight bending, ultimately inducing apoptosis via intrinsic (mitochondrial) pathway.[152] Another complex that reached humans is TLD1433 from the *McFarland* lab. Different to KP1339 and cisplatin, TLD1433 is a photosensitizer (PS) used in photodynamic therapy (PDT). In PDT, the drug acts as prodrug and remains inert in the dark. Upon exposure to light, the PDT compound produces reactive oxygen species that cause localized cytotoxicity in the tumor, providing both spatial and temporal control over the treatment. TLD1433 has entered clinical trials for the treatment of bladder cancer using green light activation and successfully completed Phase 1.[153] Harmful side effects in this method are long lasting photosensitivity of patients receiving PDT treatment.[154]

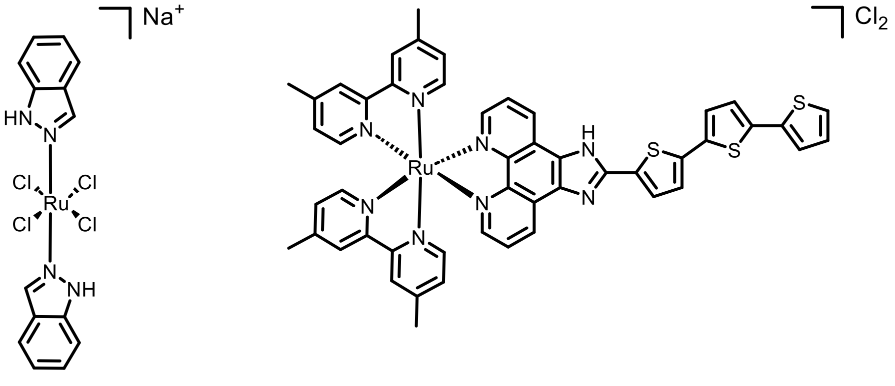

**KP1339** **TLD1433**

Figure 16. Chemical structures of two examples for cancer treatment with metal-complexes. KP1339 is activated through reduction (left), TLD1433 is a photosensitizer and is activated with light of a specific wavelength.

These light-activated prodrugs can be classified into three categories: photodynamic therapy (PDT), photoactivated chemotherapy (PACT), and photothermal therapy (PTT). PDT generates reactive oxygen species to induce cell death, PACT activates prodrugs to release cytotoxic agents, and PTT uses heat generated by light to destroy cancer cells.[155-156]

Albeit PACT and PDT are both activated by light, their energy transfer processes are different and can be explained by the Jablonski Diagram displayed in (Figure 17). Firstly, PDT and PACT agents follow the same pathway: excitation of an electron occurs from their ground state (GS) into the singlet metal-to-ligand-charge-transfer state($^1$MLCT), that reaches via intersystem crossing the triplet MLCT state ($^3$MLCT). At this point, the pathways diverge. In PDT type I, the $^3$MLCT reacts with substrates like biomolecules or $O_2$ through electron transfer leading to the production of superoxide radical anions ($O_2^{\cdot -}$ ), dihydrogen peroxide ($H_2O_2$), or hydroxyl radicals ($OH^{\cdot}$), forming reactive oxygen species (ROS). In PDT type II, the photosensitizer (PDT molecule) transfers energy from the triplet excited state to molecular oxygen ($^3O_2$) generating highly reactive singlet oxygen ($^1O_2$), which induces oxidative damage in cells.

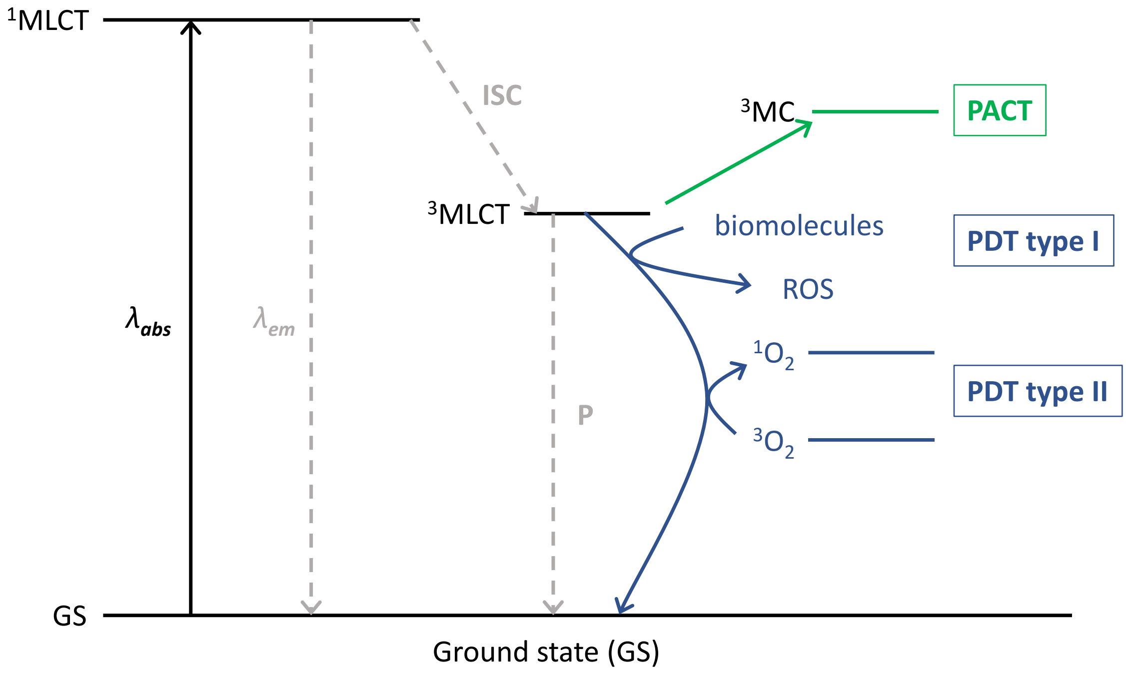

Figure 17. Jablonski diagram for two classes of light-activated prodrugs; PDT type I + II (blue) and PACT (green).

Both methods initially follow the same procedural steps in clinical application. The patient, diagnosed with a tumor, receives an injection of a prodrug specific to either photodynamic therapy (PDT) or photoactivated chemotherapy (PACT). After a predetermined incubation period, spatially and temporally controlled light activation of the prodrug within the tumor site is performed. This activation triggers a therapeutic response, leading to a reduction in tumor size, with the potential for complete tumor eradication in optimal cases (Figure 18).

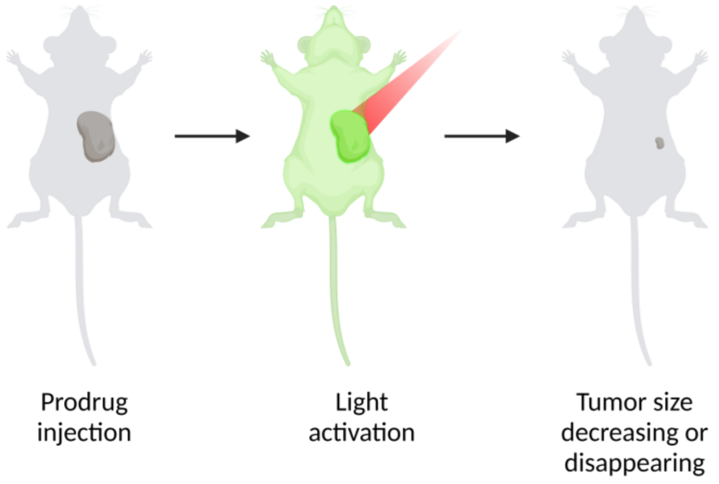

Figure 18. Prodrug is applied to the patient (mice) with a tumor (dark grey). In the next step the tumor (now green) is activated by light (red beam) of a specific wavelength, leading to reduction of the tumor with potential for complete tumor elimination.

A limitation of the PDT is its dependency on molecular oxygen, in the light-irradiated tumor region. Therefore, in some tumors, that are known for being hypoxic tumors (solid tumors: e.g. glioblastomas), the molecular oxygen concentration is low, PDT is ineffective and alternative treatments are required.[157]

For PACT the pathway diverges from the $^3$MLCT state (Figure 17, green pathway). If the metal-centered triplet excited state ($^3$MC) lies close enough in energy to the $^3$MLCT, it can be thermally promoted.[155-156] This promotion to the $^3$MC state leads to an elongation of ruthenium-ligand bond, which results in the cleavage of the ligand from the metal center and subsequently photosubstituted by solvent molecules.

Because of the existing drawbacks in PDT which are side effects like erythema, pain, burns, edema, itching, desquamation, and pustular formation, the interest in PACT agents is higher than ever.[158] Given the use of PACT agents in this work, the theoretical background of this class of light-activated chemotherapeutics will be further elaborated. The discussion will delve into the underlying mechanisms of photoactivation, the unique properties of PACT compounds, and their specific applications in targeted cancer therapy.

## 3.1 PACT

The first PACT prodrugs from the *Sadler* group demonstrated an activation meachnism for their Pt(IV) compounds, which is different from the previously explained mechanism for Ru(II) complexes.[159] Pt(IV) is reduced by light to Pt(II), which is unstable and is capable of interacting with biomolecules. Ultimately, these complexes can bind to e.g. DNA or other relevant biomolecules. In 2003, *Etchenique et al.* published the first Ru(II) polypyridyl PACT agent working by photosubstitution.[160] In this example, the photo-released ligand is the biological relevant component and the Ru(II) polypyridyl complex acts as photocages. Since then, a plethora of studies e.g. by *Salder* (proposed the term "photoactivated chemotherapy" in 2009[161]), *Balzani*,[162] *McMillin*,[163] *Meyer*[164] took place in order to gain deeper understanding on the reaction mechanism and the refinement of the design of these molecules. In additional, these studies were performed the elucidate whether the biological activity comes from the photoreleased ligand or the metal complex. Some examples for PACT agents are shown in Figure 19B.

In order to be a sufficient PACT agent, it must be inert or only active in high concentrations in the dark (photocaged, called prodrug), while upon light activation a ligand is liberated (uncaged, called photoproduct). As displayed in Figure 19A, three possibilities are given: First: the photoproduct is an inhibitor which active moiety is blocked via the bonding to the photocage, second: the Ru-based complex is biological relevant and the ligand cages the complex, or third: both the Ru-based complex and the ligand are biological active and upon separation they achieve a synergistic effect.[5]

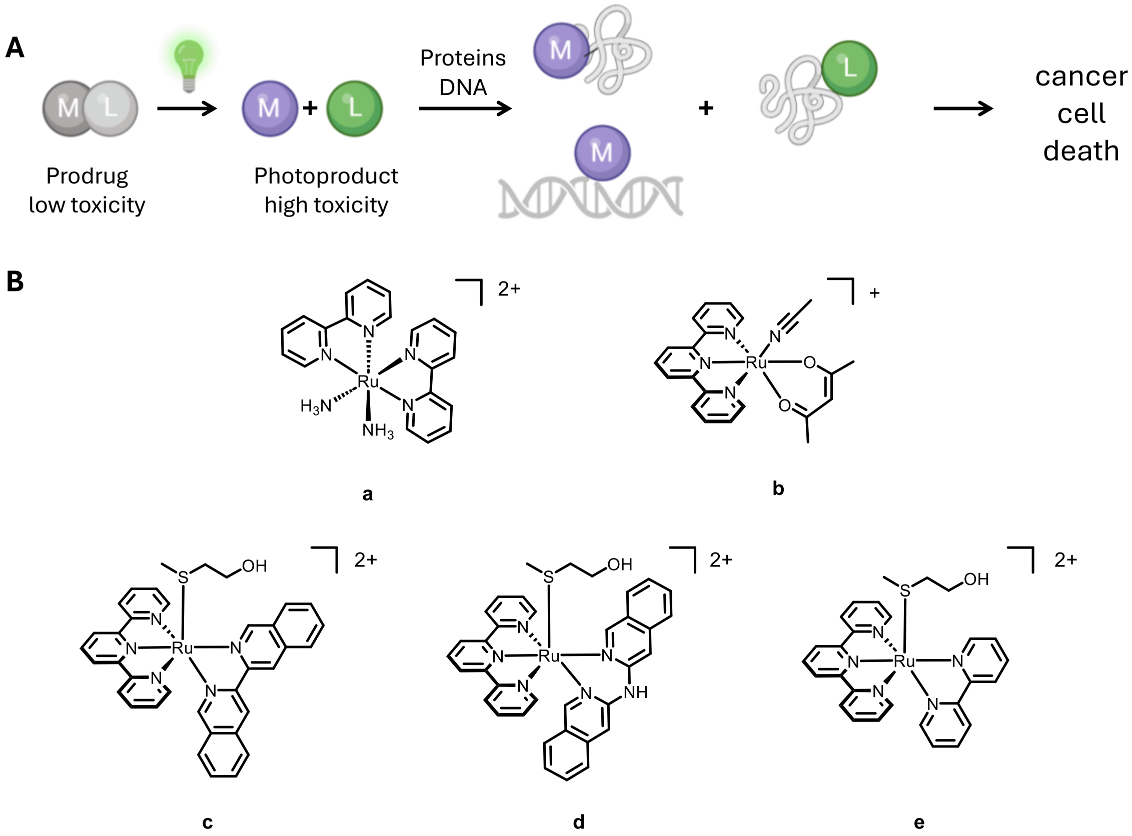

Figure 19. **A** is the general mechanism behind the PACT. First the prodrug, which is inert and low toxic in dark gets photoactivated by light resulting in the photoproduct with high toxicity. Afterwards either the metal or the ligand reacts with proteins or DNA and therefore causes cancer cell death. **B** exemplary PACT agents: **a** and **b** are from different groups[165-166]; **c**, **d** and **e** are activatable with green light, 520 nm.[8, 167]

To understand a drug's mechanism in biological systems and identify its potential intracellular targets, it is crucial to utilise emissive drugs that can be easily monitored under a confocal microscope. There are clinically approved drugs (e.g. doxorubicine) or tested compounds (e.g. TLD1433) that are naturally emissive, but many drugs lack this property. A common method to visualize non-emissive drugs is to use organic fluorophore moieties and link them covalently.[168] The first example of this method was published by the group of *Molenaar*,[169] where they followed a cisplatin derivative covalently bound to an emissive carboxylfluorescein diacetate moiety. Hereafter, several groups investigated fluorophore-labelled drug derivatives.[170-173] While the use of large dyes raises questions about how they modify the biodistribution and biological properties of the drug in comparison to the unmodified version. Therefore, it remains unclear whether the attached moiety drastically changes the lipophilicity of the drug, potentially reducing cellular uptake and distribution within the cell.[147, 174]

## 3.2 Labelling of Chemotherapeutics

The primary challenge associated with the labelling approach described above for chemotherapeutic agents lies in the alteration of the molecular properties. The addition of a fluorophore can significantly modify the molecule's characteristics, leading to a potentially different intracellular distribution when labelling experiments are conducted without the fluorescent dye. Consequently, it became necessary to explore alternative methods for tracking non-emissive PACT agents without relying on fluorescent labelling.

To identify the target of a prodrug, it needs to be isolated and analyzed after binding to a specfic target. The pull-down method was developed for this purpose.[175] Originally developed to identify the protein-protein interactions, this method can also be adapted to study the interaction of the metal-based drugs with proteins. As an example, *Hartinger et al.* published in 2015, the first experiments involving metallodrugs in the pull down method.[176] They investigated the targets of RAPTA-C, which is an organometallic Ru(II) compound, that inhibits processes related to metastasis *in vitro*, shown in Figure 20.

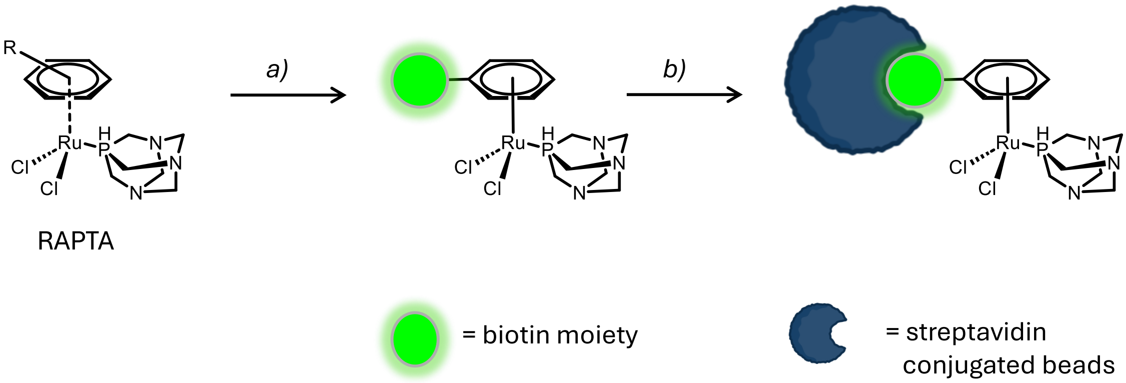

Figure 20. Drug derivative RAPTA by *Hartinger* group.[176] *a*) functionalization with a biotin moiety.; b) immobilization of the biotin moiety with RAPTA onto streptavidin conjugated beads. Afterwards, the drug conjugate is incubated with cell lysate and metal-protein adducts were isolated from the unbound proteins. These isolated adducts were measured in HRMS.

The complex was functionalized with a biotin moiety, which facilites the immobilization of the drug onto streptavidin-conjugated beads. Following immobilization, the drug conjugate was incubated with human cancer cell lysate, and metal-protein adducts were subsequently isolated from unbound proteins via centrifugation. In this particular experiment, high-resolution mass spectrometry (HRMS) identified 15 distinct cancer-associated target proteins.[176]

While using the biotin moiety, the chemical properties of the drug massively changed, which might also result in the change of the biological properties (e.g. cellular uptake and distribution).

Therefore, *DeRose et al.* synthesized azide-functionalized cisplatin derivatives for CuAAC and used these for the pull-down experiment. They confirmed the interaction of the complexes with gel electrophoresis[177] and they could determine the successful binding of the Pt-protein by affinitiy purification.[178] As explained previously, for CuAAC either an azide or an alkyne as functional groups is required. With this knowledge in hand, combining both, the pull-down and the CuAAC, the experiment is structured as shown in Figure 21. For the azidoplatin (A), *S. cerecisiae* were treated with compound A and afterwards the proteins extracted, and in A1 labelled though CuAAC-reaction with biotin-steptavidin, or in A2 with a fluorescent tag, both is implemented on a modified alkyne as reaction partner.[178] For the gold (III) NHS agent (B), the situation is somewhat different. B contains a photoactivatable group (an azirine), which is cleaved upon activation by light (with $N_2$ as the leaving group). After cleavage, the gold complex reacts with proteins in the treated HeLa cells. Subsequently, either an azido-biotin-streptavidin (B1) or an azido-fluorophore (B2) is used for labelling. When B1 is used, further analysis is performed with the pull-down/MS assay. In the case of B2, the cells are imaged to observe the targets.[179]

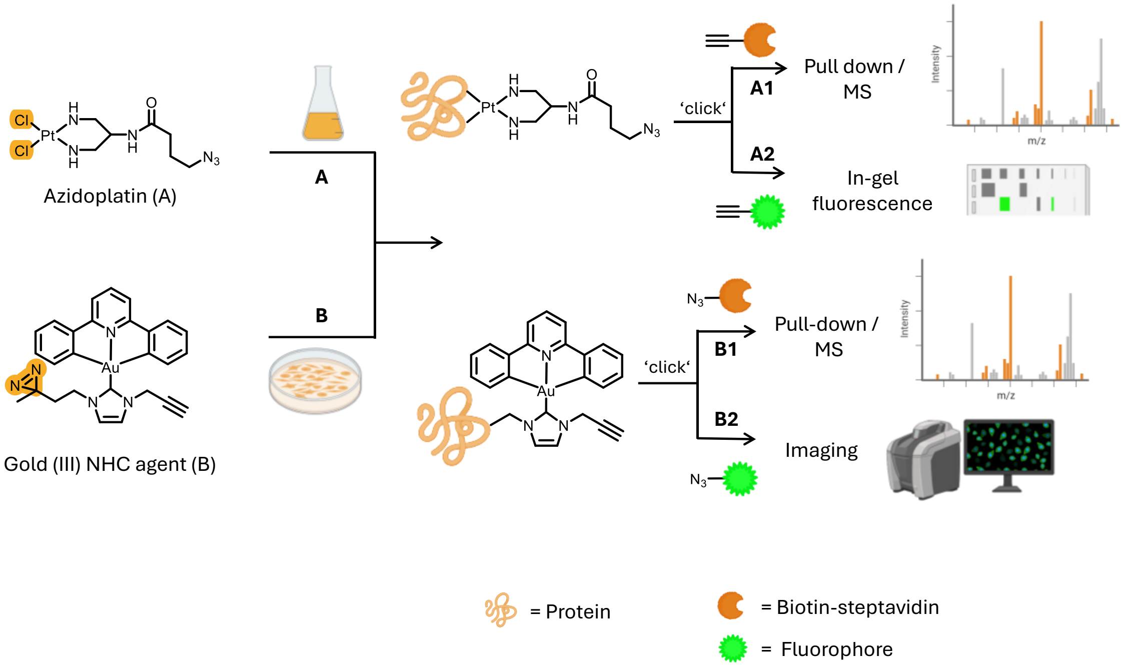

Figure 21. Drugs of pull-down experiments of A (*DeRose et al.)* and B (*Che et al.)* For both methods, labelling via MS (A1+B1) or fluorescence experiments (A2+B2) CuAAC was used and combined with the pull-down method.

In addition, *Bierbach et al.* started with a method based on minimal modification of the drug, a "click-handle", as shown above, but for a post labelling of the drug after cell fixation by the CuAAC. Herein, cellular uptake and distribution are minimally affected.[180] As the groups of *DeRose*,[181] *Che*[179, 182] and *Griffith*[46] used the click chemistry for labelling of their complexes, all of them used the CuAAC reaction (Figure 3, green). Their original molecule gets modified with the smallest handle possible, in this case either an alkyne or an azide. This modification is so minor that it does not alter the biological activity of the complex. After this small modification the cells were treated with the drug, fixed and the CuAAC reaction was performed. All the groups employed a costaining method, to ensure accurate localization within the cell (e.g. by immunostaining or different tracker), as shown in Figure 22. These results are imaged *via* confocal microscopy.

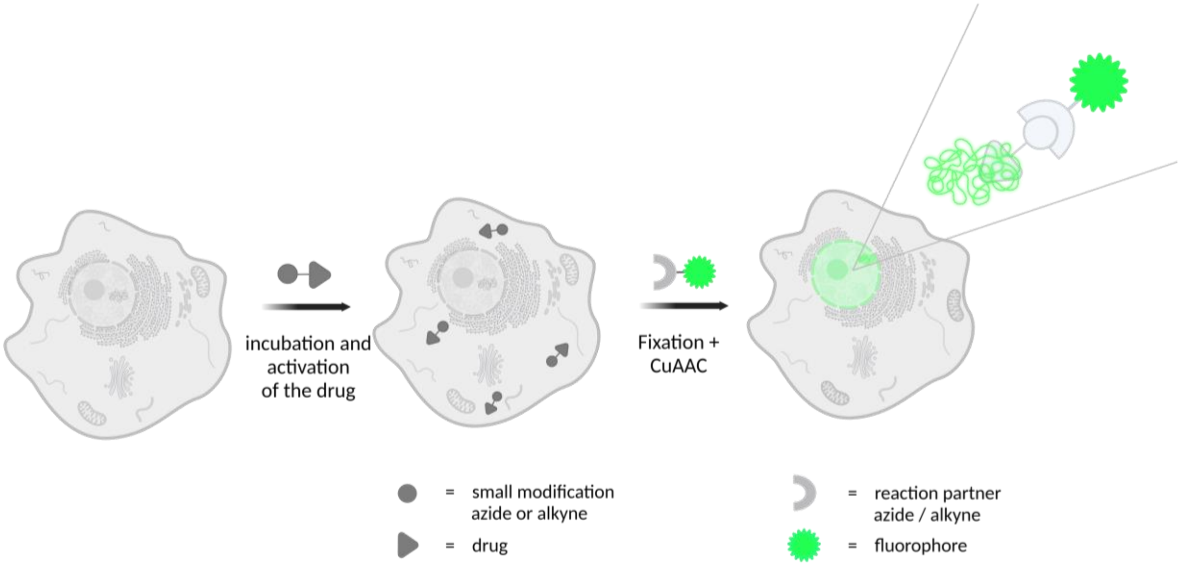

Figure 22. Experimental procedure of the localization experiments of *DeRose* and *Che* for Pt (II) and Au (III) chemotherapy agents. First the drug (dark grey) gets incubated and activated in the cell. After a specific incubation period, the complex is distributed throughout the cell and gradually accumulates in the target organelles. In the next step, during fixation and permeabilization, the unbound complex is washed out of the cells. Consequently, only the bound complexes with their modifications are labeled in the following CuAAC reaction (green fluorophore is bound to the reaction partner). In this example, the complex accumulates in the nucleus by binding to DNA, allowing it to be detected in the final imaging step.

# III. Metabolic Labelling of DNA in Cells by means of the Photoclick Reaction triggered by Visible Light

Fluorescent labelling of biomolecules in the cellular environment has become increasingly significant in the past years. As described above in section II.1, bioorthogonal labelling methods are powerful tools for this purpose. Well-known reactions such as CuAAC, IEDDA, and SPAAC are widely used, yet they all share a common limitation: the lack of precise spatio-temporal control. This control can only be achieved by using light as an external trigger. As a result, photoclick reactions have gained increasing interest. A key challenge in these reactions is the excitation wavelength, as most known reactions are triggered by UV light at wavelengths below 400 nm. The use of UV light presents inherent disadvantages, including safety risks, cell damage, and resulting cell toxicity.[183]

In order to address these challenges, the objective of this project was to develop new tetrazoles that can be activated by visible light while minimizing potential side reactions of the photoclick reaction, as described in section II.1.3. Pyrene and xanthone modifications were chosen as substituents for the tetrazoles, enabling excitation at wavelengths above 400 nm through their extensive aromatic systems, which also impart their fluorescent properties. Additionally, the tetrazole is expected to be stabilized by $\pi$-$\pi$ interactions of the aromatic groups within the DNA helix, thereby reducing undesired side reactions. The conversion of the tetrazole to the pyrazoline and pyrazole could potentially induce a change in fluorescence colour due to alterations in photochemical properties while releasing nitrogen. This is very useful for the application in living systems when imaging DNA and makes it possible to see when the reaction has taken place and where the product is located.

The photoclick reaction of the developed tetrazoles should then be investigated with different modified nucleosides and functional groups using UV/Vis and fluorescence spectroscopy as well as reversed-phase high-performance liquid chromatography (RP-HPLC). Ultimately, the optimized reaction setup will be applied to label genomic DNA in HeLa cells, employing metabolic incorporation to introduce a modified nucleoside into the DNA, followed by photoclick labelling of the nucleoside (Figure 23).[1]

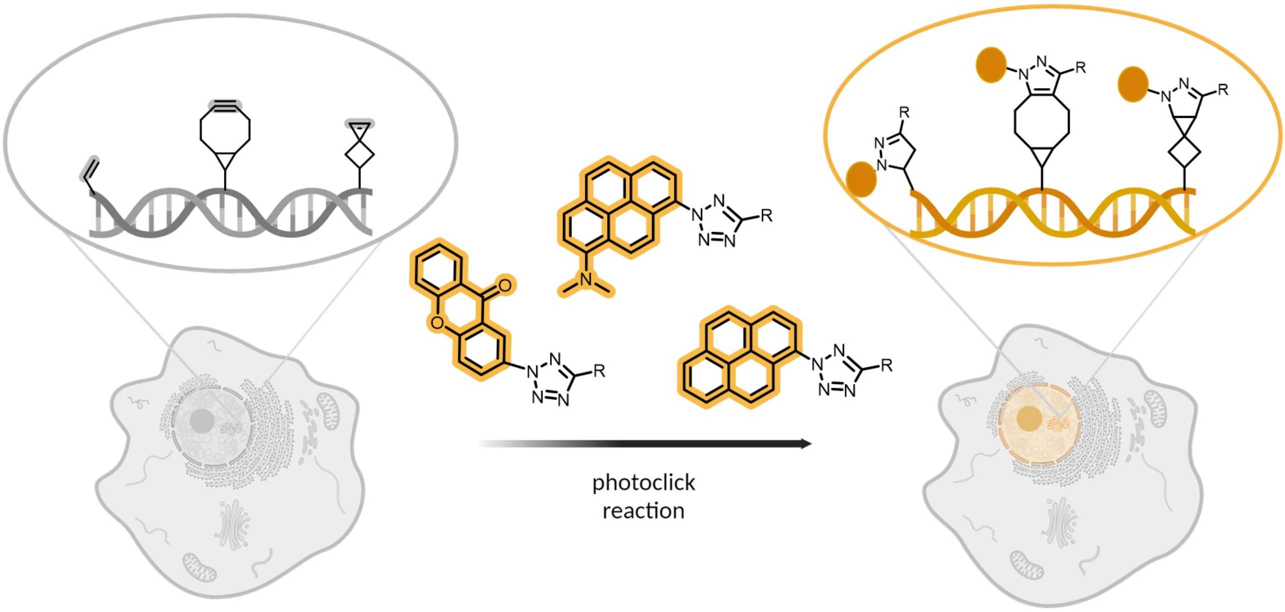

Figure 23. Bioorthogonal labelling by means of the photoclick reaction of DNA after metabolic incorporation of different nucleosides into genomic DNA. Usage of different fluorogenic tetrazoles, triggered with visible light. R = benzoic acid methyl ester.

---

[1] Parts of this chapter and the corresponding supporting information have been published already:

"Metabolic labelling of DNA in cells by means of the "photoclick" reaction triggered by visible light", L. Rieger, B. Pfeuffer and H.-A. Wagenknecht, *RSC Chem. Biol.*, **2023**, *4*, 1037-1042; DOI: 10.1039/D3CB00150D.

# 1 Modular Design of tetrazoles

In general, the core structure was constructed following the procedures developed by the *Wagenknecht* and *Barner-Kowollik* groups,[121, 184] with the following considerations. The tetrazoles should be excited by irradiation at wavelengths above λ = 400 nm. Therefore, a xanthone derivative was coupled to the nitrogen in the 2-position of the tetrazole (counting starts from the first nitrogen left of the carbon counterclockwise). Additionally, pyrene and dimethylamino-modified pyrene were coupled to the same position Figure 24. It was previously shown that the additional dimethylamino substituent, according to *Kamm et al.*, causes a bathochromic shift in the excitation wavelength.[121] These changes demonstrate the straightforward synthetic modularity of this tetrazole design. In addition, the carbon in the 5-position of the tetrazole can also be modularised to improve the solubility of the highly non-polar pyrene tetrazoles in polar solvents, thus enabling their use in living systems, which will be discussed in detail in the next chapter.

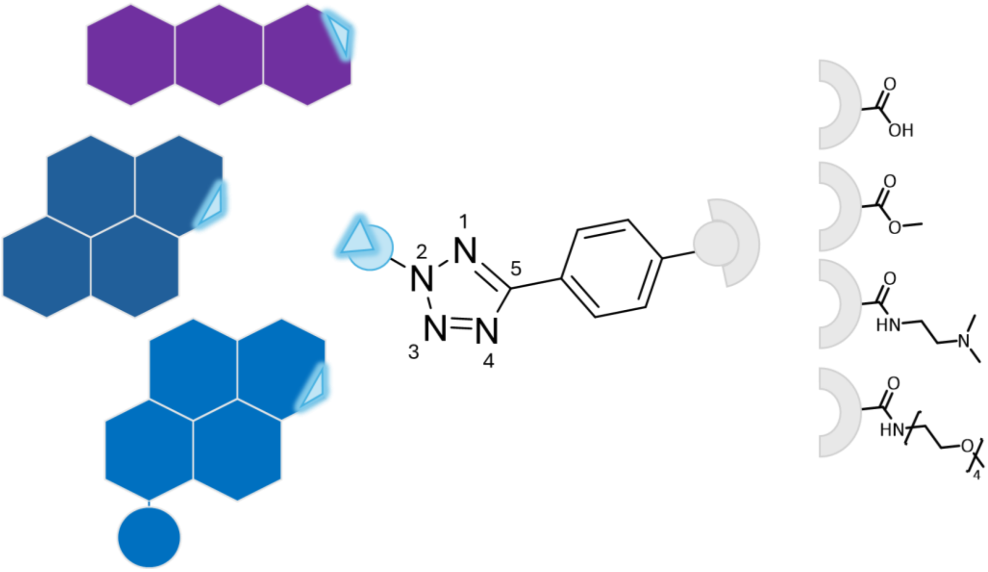

Figure 24. General overview of the synthetic core structure of the different tetrazoles synthesized in this work. In 2-position of the tetrazole an aromatic system is coupled to the nitrogen. In 5-position, a second modularity is given though coupling different moieties modified in the para position.

In this study, the synthesis was initiated from the aromatic system as the starting material, using three different chromophores as basic structures. In the subsequent step of the synthetic pathway, the carboxylic ester was utilized to achieve the formation of the tetrazole.

Following ring closure, the solubility of the resulting tetrazoles was modulated by introducing various functional groups, such as amines or polyethylene glycol chains. The resulting target molecules **1-6** are illustrated in Figure 25. These were synthesized, characterized and analyzed as the target compounds for this research project.

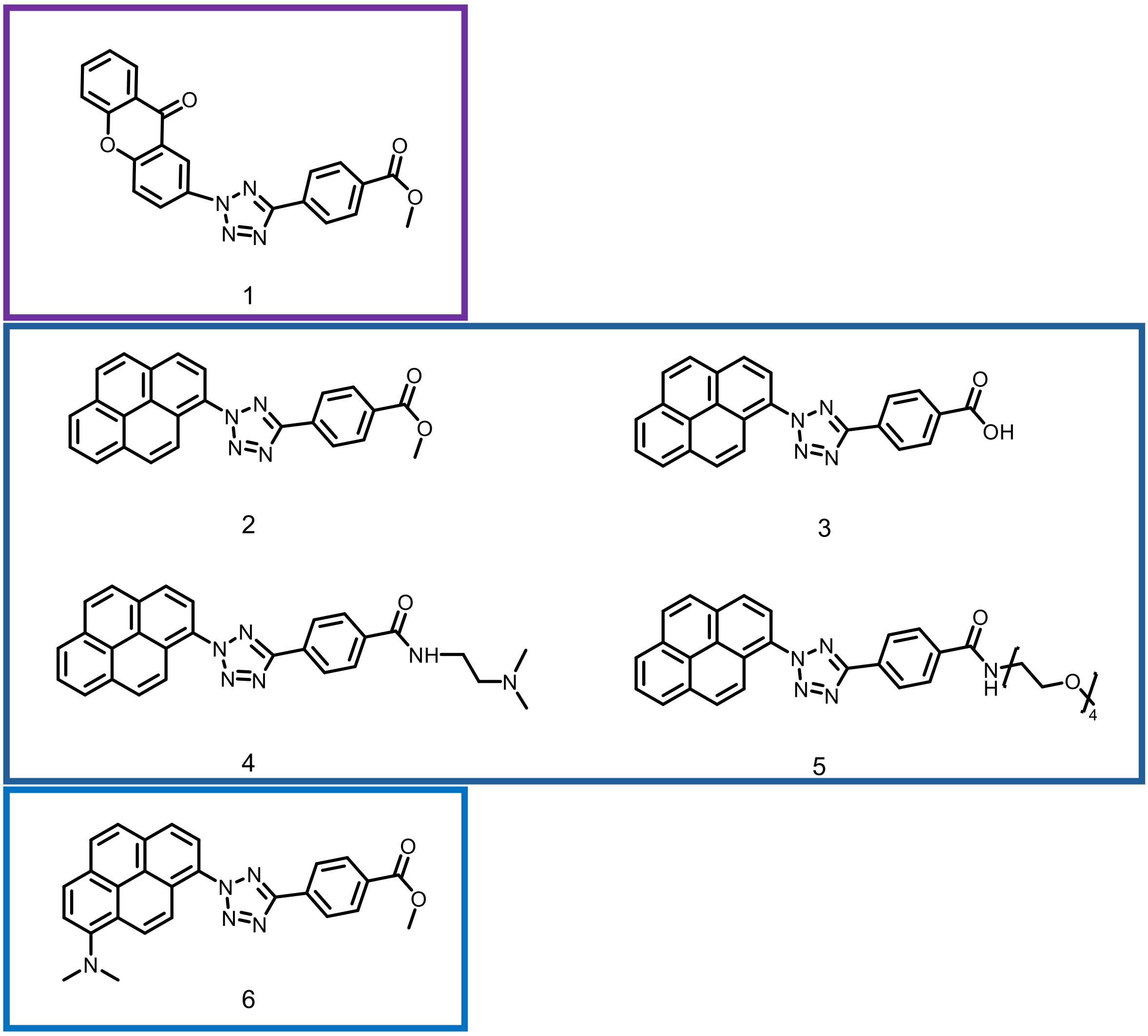

Figure 25. Tetrazoles **1-6** that were synthesized and characterized in the photoclick reaction for the labelling of nucleic acids.

## 1.1 Synthesis of tetrazoles 1 - 3

In order to couple the aromatic moiety of the tetrazole to the benzylic moiety through a ring forming reaction, it is necessary that both parts of the molecule contain specific functional groups. Typically, an amine is attached to the aromatic moiety, which is then converted *in situ* to a diazonium salt prior to ring formation.[118]

Since 1-pyrenyl-amine **10** is commercially available, no further preliminary reactions were necessary for the synthesis of the tetrazoles **2-5**. In contrast, the precursor molecule **9** for the synthesis of the the xanthone tetrazole **1** required a nitration of xanthone **7**,[185] followed by the reduction of the nitro group of **8** to the amine **9** (Figure 26).[186] During the nitration, multiple substitutions and the resulting formation of different isomers was effectively prevented by using only 0.5 equivalents of nitrating acid. Following the nitration (Figure 26 step ***a***), the nitrated xanthone **8** was neutralized, washed, dried, and used directly in the subsequent reaction (Figure 26 step ***b***).

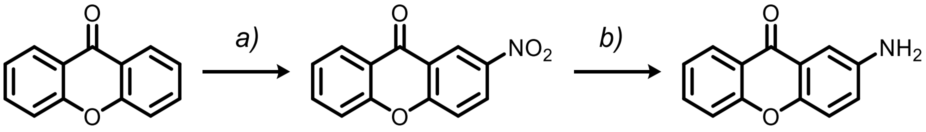

**7** **8** **9**

Figure 26. Synthesis of the aminated xanthone **9**. a) $H_2SO_4/HNO_3$, $H_2SO_4$, 0 °C, 1.5 h; b) $SnCl_2 \cdot 2\ H_2O$, EtOH, 85 °C, 10 h, 12% over two steps.

For the synthesis of tetrazole **6**, which contains an additional dimethylamino group, the commercially available 1-pyrenyl-amine (**10**) needs to be protected with a methyl group to prevent the formation of two diazonium salts. Following methylation (***a***), the dimethylated pyrenyl-amine **11** was nitrated (***b***), and the nitro group of **12** was subsequently reduced (***c***) to yield the free amine **13** (Figure 27). The nitration step resulted in different pyrene regioisomers; however, as demonstrated by *Kamm et al.*, these isomers could be separated, allowing the selective use of the 1,8-isomer in the subsequent steps.[187]

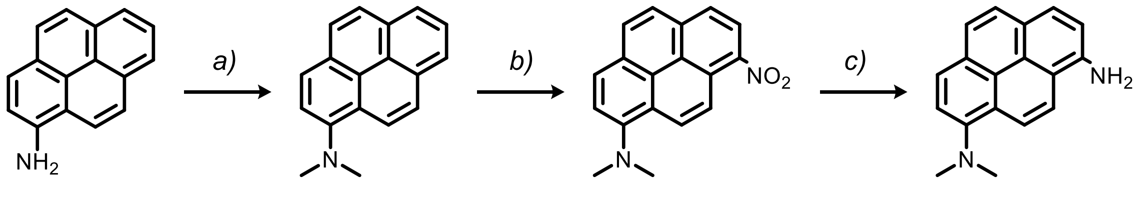

**10** **11** **12** **13**

Figure 27. Synthesis of the dimethylated-pyrene-amine **13**. a) Methyliodid, $K_2CO_3$, DMF, 120 °C, 2 h, 90%; b) $HNO_3$, AcOH, $Ac_2O$, r. t., 3 h, 51%; c) $H_2$, Pd/C, EtOAc, r. t., 30 min, 91%.

The amino-modified aromatic components **9**, **10** and **13** can undergo tetrazole formation according to the method described by *Kakehi et al.* (section 1.3).[118] As a coupling partner, hydrazone **16** was synthesized for easy modular exchange of the benzylic residues. The synthesis of **16** was achieved through a reaction between methyl 4-formylbenzoate (**14**) and benzenesulfohydrazide (**15**) in ethanol at 45 °C (Figure 28).

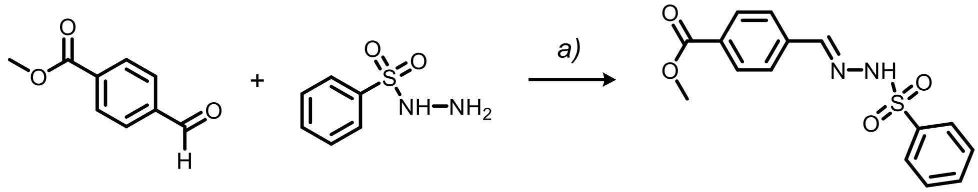

**14** **15** **16**

Figure 28. Synthesis of the hydrazone **16**. a) EtOH, 45 °C, 1 h, 95%.

The final tetrazole formation for all tetrazoles **1, 2** and **6** was carried out in a comparable manner. The aromatic moiety was diazotized using either sodium tetrafluoroborate / tetrafluoroboric acid or hydrochloric acid and sodium nitrite. The diazonium salts react with **16**, dissolved in pyridine, at various temperatures in situ as shown in Figure 29.

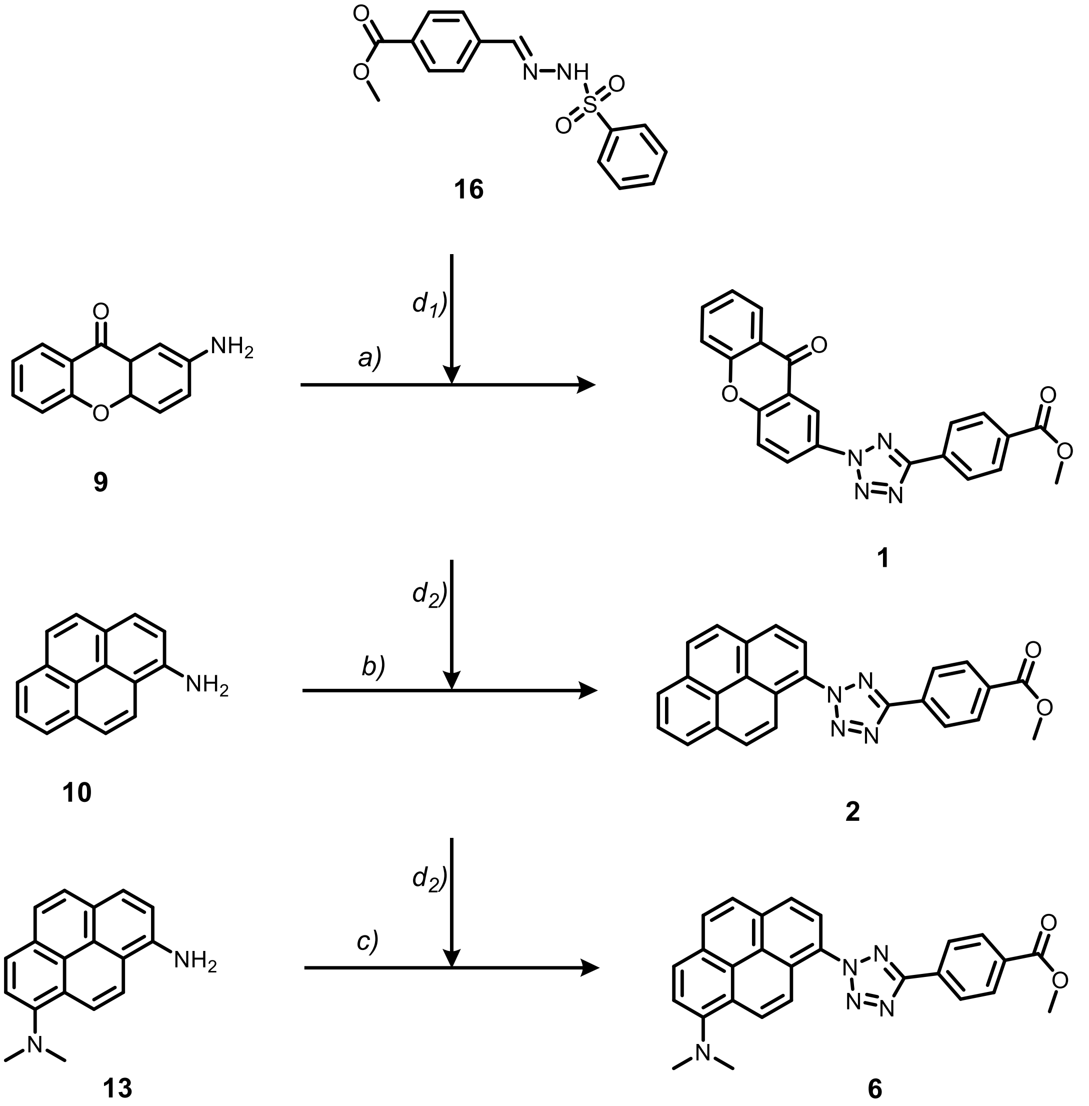

Figure 29. Synthesis of **1**, **2** and **6**. a) sodium nitrate, HCl, EtOH/$H_2O$, 0 °C, 20 min; b) sodium nitrate, $NaBF_4$/$HBF_4$ (50%), -10 °C, 30 min; c) sodium nitrate, HCl, EtOH/$H_2O$, 0 °C, 20 min; $d_1$) diazoniumsalt, hyrazone (**16**), pyridine, -30 °C to r. t., over night; $d_2$) diazoniumsalt, hyrazone (**16**), pyridine, 0 °C to r. t., over night.

## 1.2 Characterization by Optical Spectroscopy

After the synthesis, tetrazoles **1**, **2** and **6** were characterized by UV/Vis spectroscopy to confirm that one of the essential criteria - the activation of the molecules with visible light - was met.

Figure 30, **1**, shown in purple, has an absorption range between 210 nm and 360 nm. There are two maxima within this range. The first maximum, up to 300 nm, shows three smaller bands with an extinction coefficient of $5 \cdot 10^4$ $M^{-1}cm^{-1}$. A bathochromic shift shows a small shoulder up to 360 nm but with a significantly lower extinction coefficient ($\varepsilon_{350nm} = 0.6 \cdot 10^4$ $M^{-1}cm^{-1}$).

For tetrazole **2**, a broader absorption range is observed with three maxima between 210 nm and 410 nm. The most interesting maximum for tetrazole **2** is the one with the largest bathochromic shift at $\lambda_{max}$ = 343 nm, which has an extinction coefficient of $\varepsilon_{343nm} = 2.3 \cdot 10^4$ $M^{-1}cm^{-1}$.

Tetrazole **6** also displays three maxima. Although these maxima have lower extinction values compared to tetrazole **2**, they are characterized by significantly broader absorption peaks. The most important, bathochromically shifted maximum occurs between $\lambda_{max}$ = 375 nm and $\lambda_{max}$ = 405 nm, with two local maxima showing an extinction coefficient of $\varepsilon_{405nm} = 1.9 \cdot 10^4$ $M^{-1}cm^{-1}$.

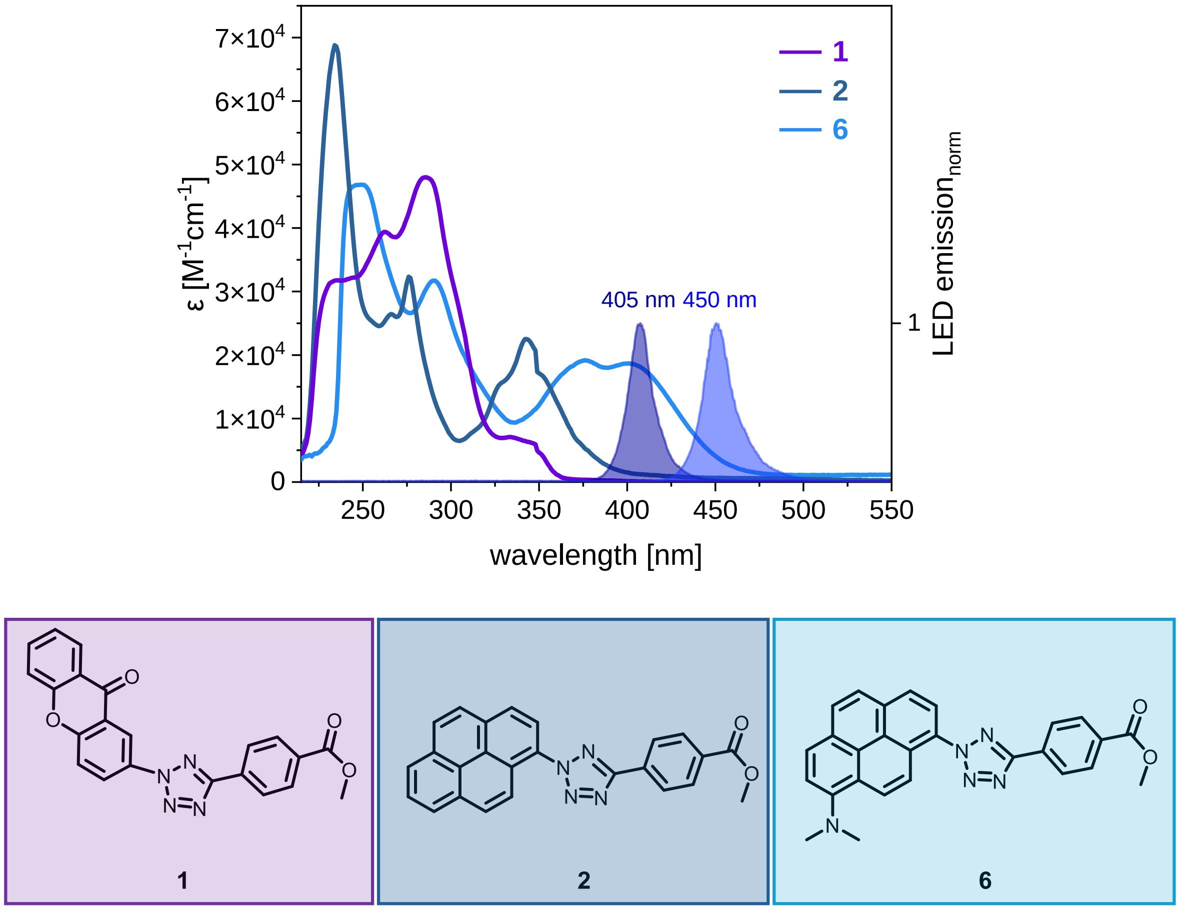

Figure 30. UV/Vis absorbance of **1**, **2** and **6** in comparison with the normalized emission of the 405 nm and 450 nm LED.

Since the goal is to excite the tetrazoles as far as possible within the visible light spectrum, the most bathochromically shifted maximum is always considered. Upon examining the different spectra of the tetrazoles, tetrazole **1** does not show any absorption in the visible light range and, therefore, cannot be excited above 365 nm. Consequently, the xanthone derivative **1** is not used in the subsequent proof-of-principle experiments. Tetrazole **2**, on the other hand, can be excited in this region, because its absorbance extends up to $\lambda = 430$ nm. Consequently, tetrazole **2** can still be excited by the most commonly used 405 nm LED. Tetrazole **6** has an even more bathochromically shifted maximum, so it can be excited with both the 405 nm and the 450 nm LEDs.

## 2 *In vitro* Experiments

In the following experiments, the photoclick reaction was performed with tetrazoles **2** and **6**. Therefore, a small library of reactive counterparts shown in Figure 31, including methylmaleimide (**17**) as an unstrained alkene, spiro[2.3]hex-1-ene (SPH, **18**) as a strained alkene, and BCN (**19**) as a strained alkyne, as well as the corresponding modified nucleosides, 5-vinyl-2'-deoxyuridine (VdU, **20**), the SPH-modified uridine **21** and the BCN-modified uridine **22**, were used, to evaluate the general reaction and kinetics by their reaction rates. The general scheme of the photoclick reaction of **2** and **6** with **17-22** and forming the products **23-28** and **29-34** respectively, is shown in Figure 31.

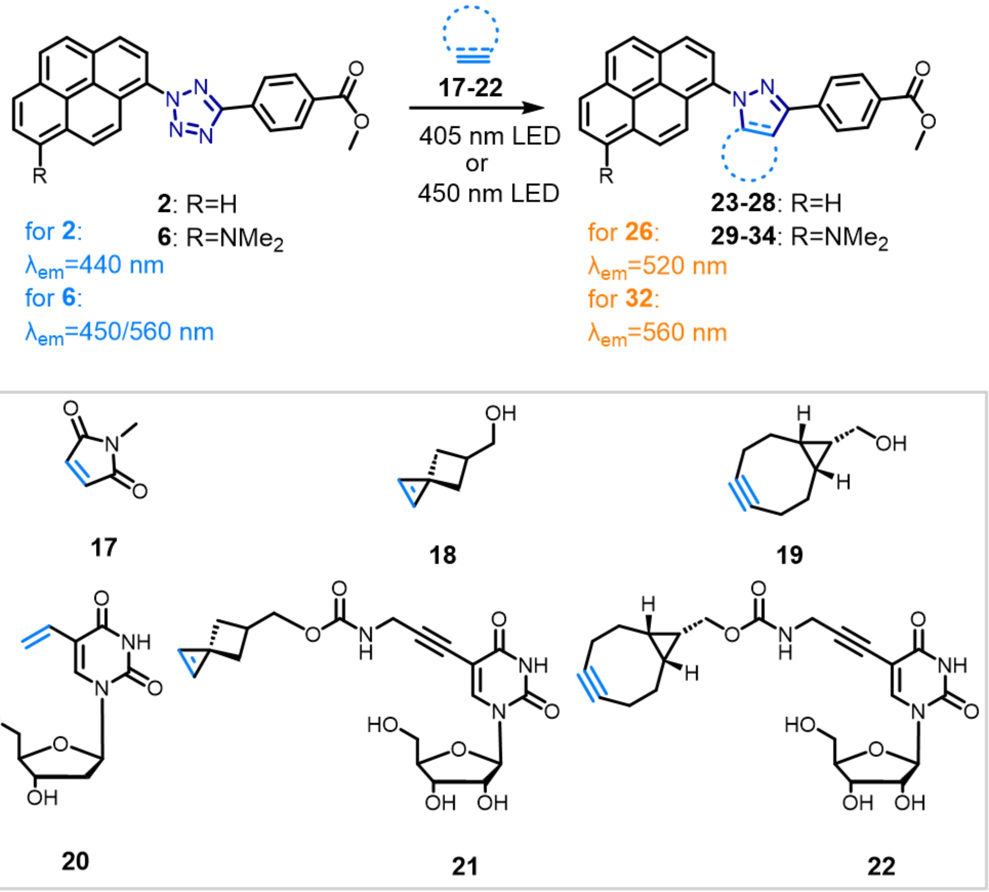

Figure 31. Photoclick reaction between **2** and **6** and **17-22** yielding in **23-28** and **29-34**.

Due to the poor solubility of the tetrazoles **2** and **6**, all proof-of-principle experiments were performed and monitored in MeCN and irradiated by a 405 nm or 450 nm LED.

## 2.1 UV/Vis and Fluorescence Experiments

A tenfold excess of the dienophile (c = 250 µM) compared to the tetrazole (c = 25 µM) was used to monitor the reaction via UV/Vis and fluorescence spectroscopy. In addition, a $\lambda$ = 405 nm LED was used for excitation of both tetrazoles to allow direct comparison. For tetrazole **2**, exposure times were set to 0-600 s, while for tetrazole **6** exposure times of up to 100 min were required. The following chapter focuses only on the reaction of **2** with **20** (VdU) to give product **26** as well as **6** with **20** (VdU) to give product **32**. The spectra of the remaining reactions are given in the supporting information.

During the photoinduced reaction of **2** with **20**, the characteristic maximum in the absorbance spectra (Figure 32, left) at $\lambda$ = 342 nm of the starting material decreases with increasing irradiation time and a new band is formed that is shifted to a wavelength of $\lambda$ = 400 nm. These changes are visible after 5 s of irradiation. After another 10 s, this band shifts to the final maximum at $\lambda$ = 453 nm. According to the isosbestic point at $\lambda$ = 375 nm, the reaction seems to be completed after 60 s without any obvious intermediates. This shows that after the extrusion of nitrogen, the nitril imine is an extremely short-lived intermediate reacting immediately with **20**. In the irradiation time range from 60 to 600 s, the isosbestic point at $\lambda$ = 375 nm shifts bathochromically, indicating a second reaction. To further investigate this reaction, control experiments were performed in which the samples were irradiated for only up to 60 s and the UV/Vis spectra were measured continuously at the same intervals, but not irradiated that long. This clearly shows that the band of the first product does not shift further into the visible without further irradiation of the reaction mixture. (Figure A 1) This confirms that the second reaction also appears to be light-induced. Based on the mass spectrometry analysis (given in the SI), the second step involves a light-induced dehydrogenation of the pyrazoline **26a** to the pyrazole in the final product **26b**. Throughout the reaction, a red shift in the fluorescence was observed, shifting the maximum from $\lambda_{max}$ = 440 nm (**2**) to $\lambda_{max}$ = 520 nm (**26a**/**26b**) (Figure 32 right). This shift was clearly visible in the cuvettes, by a colour change from blue to yellow-green (Figure 32, bottom). Excitation spectra (Figure A 2) and 3D fluorescence data (Figure A 3), indicate that the pyrene is responsible for the fluorescence band at 440 nm in tetrazole **2** in the reaction mixture, which is excited at 320-360 nm, whereas the fluorescence observed in product **26** originates from the pyrazole chromophore, excited at 380-420 nm.

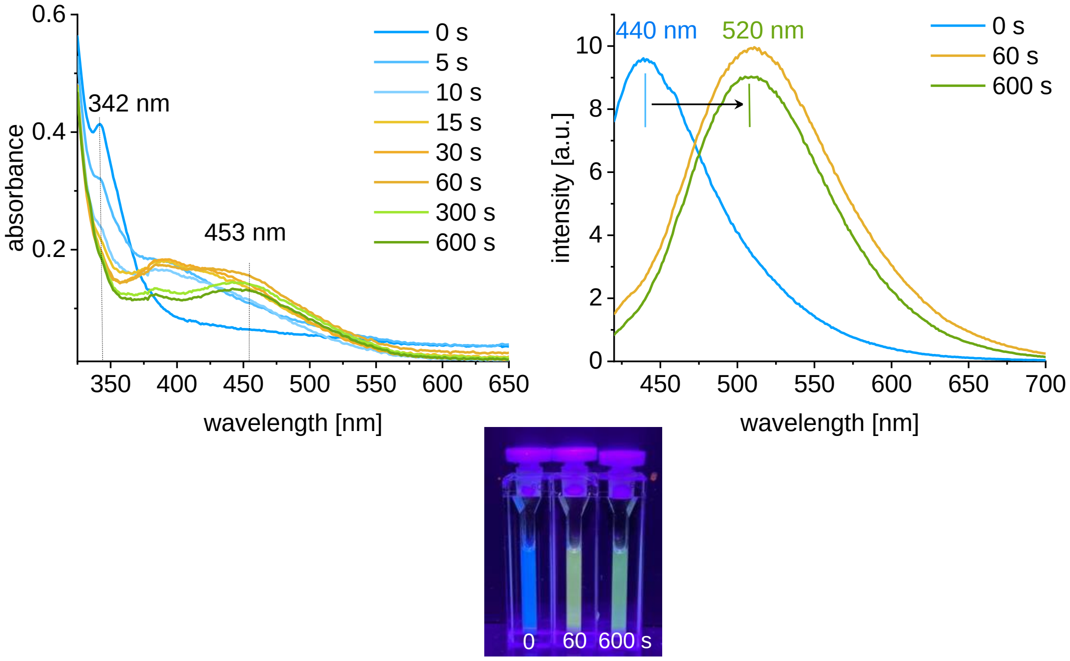

Figure 32. Left: UV/Vis absorbance spectra of the photoclick reaction between **2** and **20** (VdU) to product **26**; right: emission spectra, with excitation wavelength of $\lambda_{exc}$ = 405 nm; bottom: cuvettes during the irradiation, showing the same fluorescence changes as determined with emission specta.

The same experiment was performed for tetrazole **6**, where in contrast to tetrazole **2**, a loss of absorbance occurs in the two maxima at λ = 376 nm and 402 nm during a reaction time of 100 min (Figure 33, left). Additionally, an isosbestic point is formed at λ = 450 nm. After the reaction is initiated, the new band at λ = 458 nm increases from 6 to 100 min. The emission of the reaction was measured at an excitation wavelength of λ = 480 nm, which is above the isosbestic point and therefore shows a fluorogenic product with a broad band at 560 nm (Figure 33, right) that increases with time. Furthermore, the emission colour shows slight changes from yellow (excitation at 405 nm) to green (excitation at 480 nm; Figure 33, bottom). It is evident that tetrazole **6** requires a longer reaction time because it must be irradiated for 100 min instead of tetrazole **2**, which requires only 10 min to achieve conversion. This might be due to the modification of the pyrene with the electron-donating dimethylamino group, which stabilizes the nitril imine as intermediate.[188]

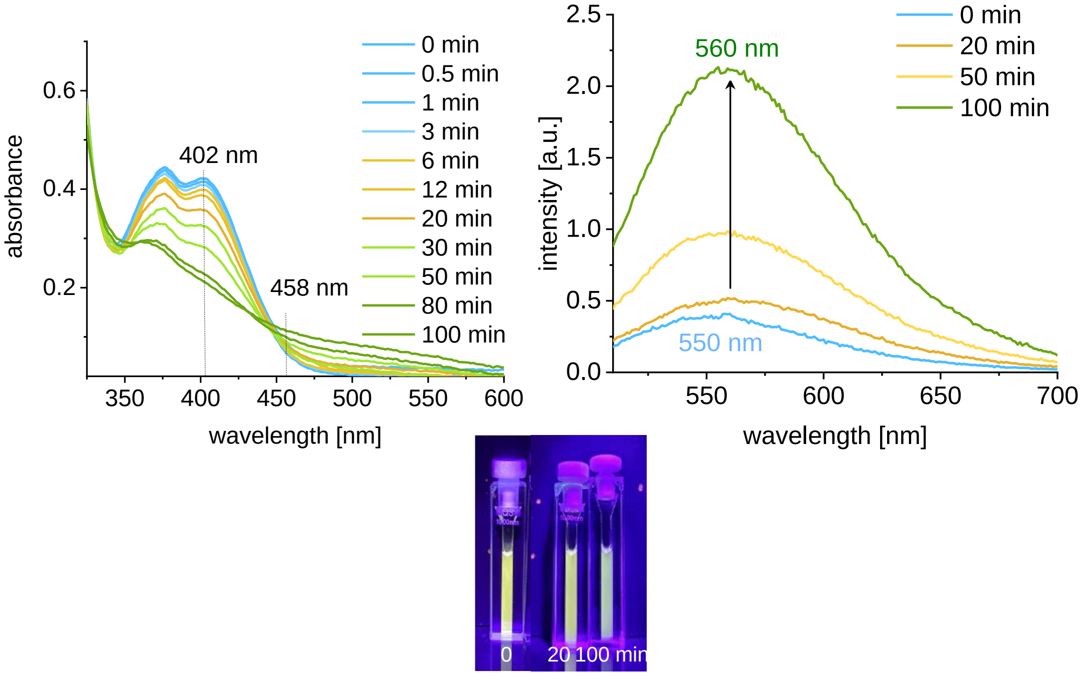

Figure 33. Left: UV/Vis absorbance spectra of the photoclick reaction between **6** and **20** to **32**. Right: emission spectra, with excitation wavelength of $\lambda_{exc}$ = 480 nm; bottom: cuvettes over the course of the irradiation.

The observable fluorescence changes between the reactants and products are a major advantage and greatly facilitate metabolic labelling and subsequent imaging experiments using a confocal microscope.

## 2.2 HPLC Kinetics vs UV/Vis Kinetics

To receive kinetic information about the photoreactivity of **2** and **6**, the above-described library **17-22** was used, as they cover a wide range of functional groups and their nucleoside analogues known in the literature, to undergo "*fast*" photoclick reactions.[189-190] It is important to note that the photoclick reaction consists of two successive steps, as explained in section II.1.3.

In the first step, light irradiation induces the irreversible cleavage of nitrogen, which can be observed in the UV/Vis spectra. In the second step, the highly reactive intermediate undergoes a 1,3-dipolar cycloaddition with the alkene or alkyne. The rate constant of the first step was calculated based on the decrease in absorbance in the characteristical band of the starting material. For **2**, this was determined at $\lambda_{max}$ = 342 nm, and for **6** at $\lambda_{max}$ = 402 nm.

Additionally, a tenfold excess of dienophile relative to the tetrazoles was used for the kinetics to yield pseudo-first-order kinetics, in accordance with the literature.[190] Practically, the values were calculated while taking the maximima from both tetrazoles and using the absorbance values to plot those against the irradiation time. This curve was exponentially fitted and the resulting constant $k$, divided by the concentration of the tetrazole gave the reaction constant.

Those rate constants for the photolysis of tetrazole **2** with **17-22**, when irradiated with a 405 nm LED, are in a similar range between $k_2 = 2730 \pm 130\ M^{-1}s^{-1}$ to $6800 \pm 700\ M^{-1}s^{-1}$ (Table 1) and as an example for **2** + **17** shown in Figure 34A. Similar results were observed for the click reactions with tetrazole **6** and **17-22**, irradiated with 405 nm LED as well, to compare directly. However, the results of the photolysis rates are significantly slower with $k_2$ in a range between $9 \pm 0.8\ M^{-1}s^{-1}$ to $30 \pm 3\ M^{-1}s^{-1}$ (Table 1). One example for determining the reaction constants is shown in Figure 34B. Herein it is obvious, that the exponential fit of the starting material decreasing is faster for tetrazole **2** than for tetrazole **6.**

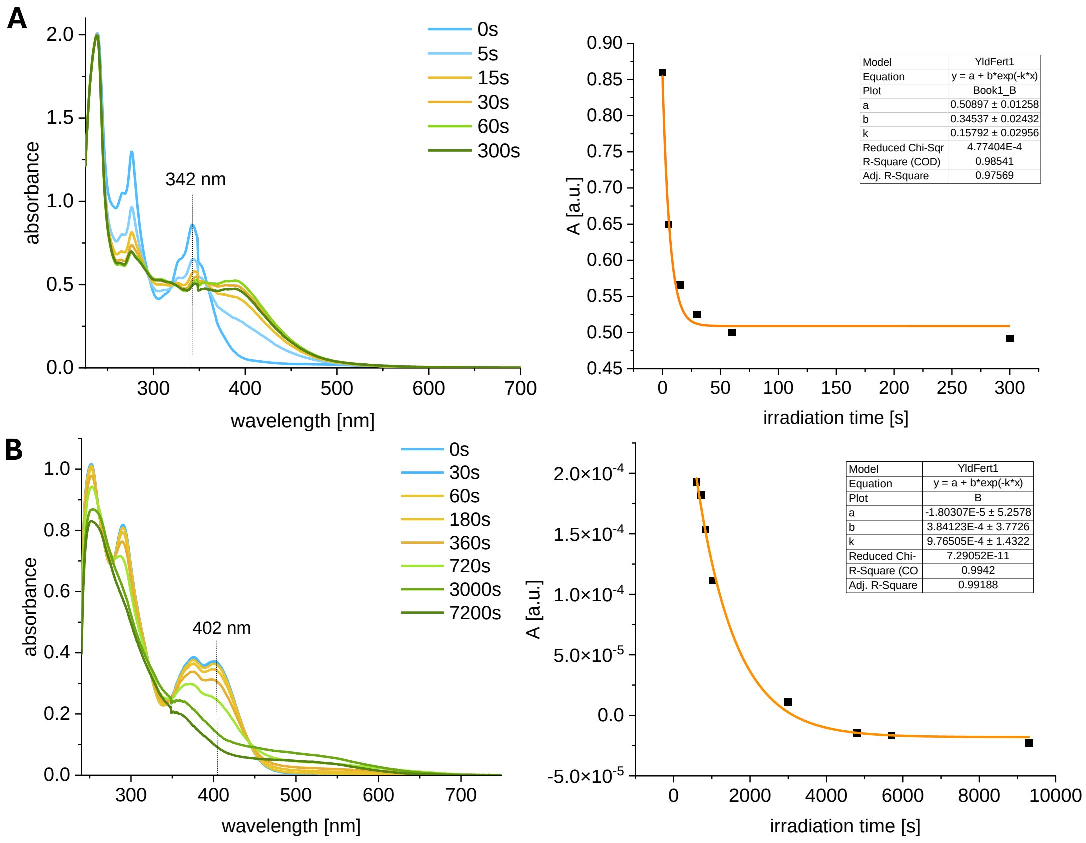

Figure 34. UV/Vis absorbance spectra and reaction constant calculations for the photolysis of tetrazoles. In A: **2** + **17**; B: **6** + **17**. Concentrations of the tetrazoles are 25 µM and the reactive counterpart **17** has a concentration of 250 µM.

The control experiments for this study involved irradiating the tetrazoles without a reaction partner. Similar values were obtained for the photolysis of compound **2** (3640 ± 250 $M^{-1}s^{-1}$) and for the photolysis of compound **6** (15 ± 1.6 $M^{-1}s^{-1}$).

Rate constants of the photolysis were verified by means of RP-HPLC analysis. This allowed to determine the product formation reaction constants of the photoclick reaction. Since kinetic investigations on the reaction of tetrazoles **2** and **6** and the modified nucleosides **20**-**22** using RP-HPLC were not feasible due to the solubility, functional group analogues (**17**-**19**) were employed. In the experiment a fourfold higher concentration of the two tetrazoles (c = 100 µM) and for the reaction partner (c = 1 mM) was used, because otherwise the reaction could not be followed due to low UV/Vis extinction. The chromatograms of the course of the reaction between **2** and **17** are shown as an example (Figure 35).

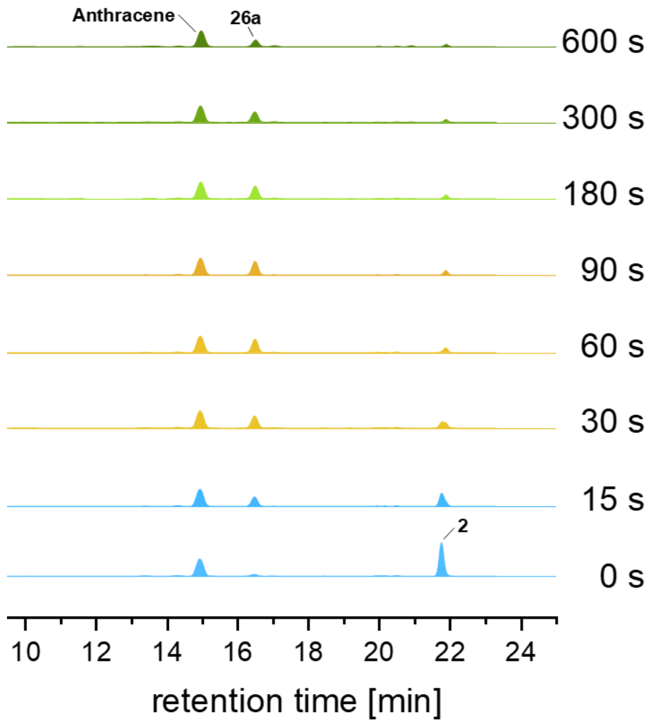

Figure 35. Reaction progress of the photoclick reaction between **2** and **17** to form **23** over 600 seconds. The concentration of compound **2** was c = 100 µM, while the concentration of compound **17** was c = 1 mM. Anthracene was used as internal standard for the reaction in a concentration of 1 mM. Acetonitrile was used as the solvent, and the reaction was irradiated with 405 nm LED. The spectrum above shows the reaction of compound **2** with **17**, with the progression of the reaction represented by the color gradient from light blue to dark green.

The first HPLC analysis was started before the irradiation to clearly identify the tetrazole and its reaction partner. In the chromatogram (Figure 35), the anthracence peak belongs to the internal standard (IS) and can be found at a retention time of 15 min. The IS is used to correct instrumental variations during analysis. The peak of tetrazole **2** is identified at 21 min. The tetrazole peak decreases significantly during the first-time interval of 15 s and has almost entirely vanished after 600 s of irradiation. Correspondingly, the peak at 17 min is assigned to the reaction product **23**. As the amount of tetrazole **2** decreases, the product peak increases, reaching its maximum after 600 s of irradiation. The assignments were further confirmed using ESI HR-MS.

By integrating the peak areas and plotting these values against the irradiation time, the reaction rate constants for both the photolysis and product formation were calculated from the HPLC analysis.

All reaction rate constants for the photoclick reaction of **2** and **6** including the photolysis as well as the product formation reaction that were determined using both of the above described methods are summarized in Table 1.

Table 1: Second order rate constants $k_2$ [$M^{-1}s^{-1}$] of the photoclick reactions between **2** and **6**, and their reactive counterparts **17-22** to products **23-25**.

| Alkene/ Alkyne | Tetrazole **2** | | Tetrazole **6** |
|---|---|---|---|
| | Photolysis $k_2$ [$M^{-1}s^{-1}$] | Product formation $k_2$ [$M^{-1}s^{-1}$] | Photolysis $k_2$ [$M^{-1}s^{-1}$] |
| - | 3640 ± 250[a] | - | 15 ± 1.6[a] |
| **17** | 6320 ± 950[a]<br>600 ± 25[b] | **23**: 650 ± 20[b] | 30 ± 3[a]<br>2.0 ± 1.1[b] |
| **18** | 2730 ± 130[a]<br>560 ± 170[b] | **24**: 540 ± 150[b] | 25 ± 3[a]<br>1.6 ± 1[b] |
| **19** | 4070 ± 190[a]<br>480 ± 110[b] | **25**: 680 ± 190[b] | 27 ± 4[a]<br>7.0 ± 0.8[b] |
| **20** | 5400 ± 500[a] | n.d.[c] | 9.0 ± 0.8[a] |
| **21** | 5000 ± 390[a] | n.d.[c] | 11 ± 0.8[a] |
| **22** | 6800 ± 700[a] | n.d.[c] | 15 ± 1[a] |

[a] Determined by means of UV/Vis absorption decease for with **2** or **6** (each 25 µM) and **17-22** (each 250 µM). [b]Determined by means of RP-HPLC analyses with **2** or **6** (each 100 µM) and **17-19** (each 1 mM). [c]Not determined due to insufficient HPLC separation.

The resulting second-order rate constants of the photolysis, which correspond to the decrease of starting material are generally lower in the HPLC experiments than those from the UV/Vis absorption analysis. For the photolysis of **2** in the presence of **17** the second-order rate constant results in $k_2 = 600 \pm 25$ $M^{-1}s^{-1}$ the presence of **18** $k_2 = 560 \pm 170$ $M^{-1}s^{-1}$ and in the presence of **19** $k_2 = 480 \pm 110$ $M^{-1}s^{-1}$. The values are an order of magnitude lower than those obtained from the UV/Vis kinetic calculations, which is probably due to light filtering effects caused by the higher concentrations of both the tetrazoles and their reactive counterparts **17-19**.

Those experiments, resulting in the product formation second-order rate constant of tetrazole **2** with **17** to product **23** is $k_2 = 650 \pm 20\ M^{-1}s^{-1}$, with **18** to product **24** is $k_2 = 540 \pm 150\ M^{-1}s^{-1}$ and with **19** to product **25** is $k_2 = 680 \pm 190\ M^{-1}s^{-1}$.

As explained at the beginning of the chapter, **17** and **18** as well as their nucleoside-analogue **21** and **22** are frequently used in click chemistry because of their highly strained structure and therefore high reactivity.[189-190] Nevertheless, the rate constants for the reactions with **2** and **6** for both of the highly stained counterparts (**17** and **18**) are not higher than the one for **16** without additional ringstrain. Therefore, rates of photoclick reactions with **2**, do not depend on the reactive counterpart and it does not significantly matter if the reactive counterpart is strained or not. This stands in contrast to known literature.[189-190]

The photolysis rate, within experimental error, appears to be comparable or even identical to the rate of product formation, not only for individual reactions but also when comparing different reactions for each tetrazole. This suggests that the kinetics are influenced by different factors such as light source, light intensity, and the internal filter effect of both the tetrazoles and their reactive counterparts, which was discussed in section II.1.3. The photolysis step determines the kinetics of the entire reaction. This is further supported by the significant difference in the values between the two tetrazoles **2** and **6**. The photolysis rate constants for **6** are two orders of magnitude lower than those for **2**. The difference in the structure of the molecules is the additional group introduced at the pyrene moiety of **6**. The lower values obtained for **6** support the previously made statement that the nitrile imine in **6** can be stabilized by the additional electron-donating groups, thereby slowing down the reaction.[188] This, in turn, is consistent with the final statement that the reaction rate is solely dependent on the first step.

As a result, for photoclick-labelling in cells, the simplest and smallest alkene-modified nucleoside, VdU **20**, can be applied as a reactive counterpart for metabolically modified DNA. It is important to highlight that the efficiency of the metabolic incorporation into the cells is highly dependent on the size of the modification in the modified 2'-deoxynucleoside used.[72] **20** has a similar size to natural thymidine, making it well-recognized by cellular enzymes for incorporation into DNA.[72, 191] Based on the kinetic studies of this work, there is no need to pursue the labelling of genomic DNA with modified nucleosides like **24** or **25**, which contain larger reactive groups as modifications.

# 3 *In cellulo* Experiments

Metabolic labelling was performed in different steps. Firstly, **20** was incubated and incorporated into the genomic DNA of the cell. Secondly, the cells get fixed. Thirdly, photoclick reaction with applying tetrazoles **2** and **6**, incubating and irradiating as well as the last step, the imaging was done. To prove that the photoclick reactions can be initiated in cells under visible light conditions, HeLa cells were incubated with compound **20** (c = 20 µM) for 48 h to ensure at least one cell division.

Following the metabolic incorporation of compound **20**, the cells were fixed with 4% paraformaldehyde (PFA) and the DNA was denatured using HCl. Cells were then incubated for 1 h with either 60 µM tetrazole **2** or 30 µM tetrazole **6** in acetonitrile, ensuring the absence of water in the system due to the bad water solubilty of the tetrazoles. The cells were subsequently irradiated with a 405 nm LED for 90 s (**2**) or 20 min (**6**). After irradiation, cells were washed twice with MeCN to thoroughly remove any unbound tetrazole.

Using a 405 nm laser setup, to excite the bound labelled product in cells, emission channels were set to 420 – 500 nm for both products, to compare them directly. The outcomes of these labelling experiments are presented in Figure 36. The success of the labelling reaction was confirmed by the fluorescence signal in rows A and C, which can be mainly found in the nucleus of the cell. To make sure, there is no unspecific binding or reaction in the cells, negative controls were performed without the initial incubation with **20**. In these control experiments, only diffuse and low-intensity fluorescence is visible, enabling a definite distinction between unspecifically (in the absence of newly built DNA, modified with **20**) and specifically (in the presence of newly built DNA, modified with **20**) reacted tetrazoles. The low unspecific fluorescence in the control experiments is probably due to photoreactions with other nucleophiles (amines, thiols etc.), see section II.1.3.

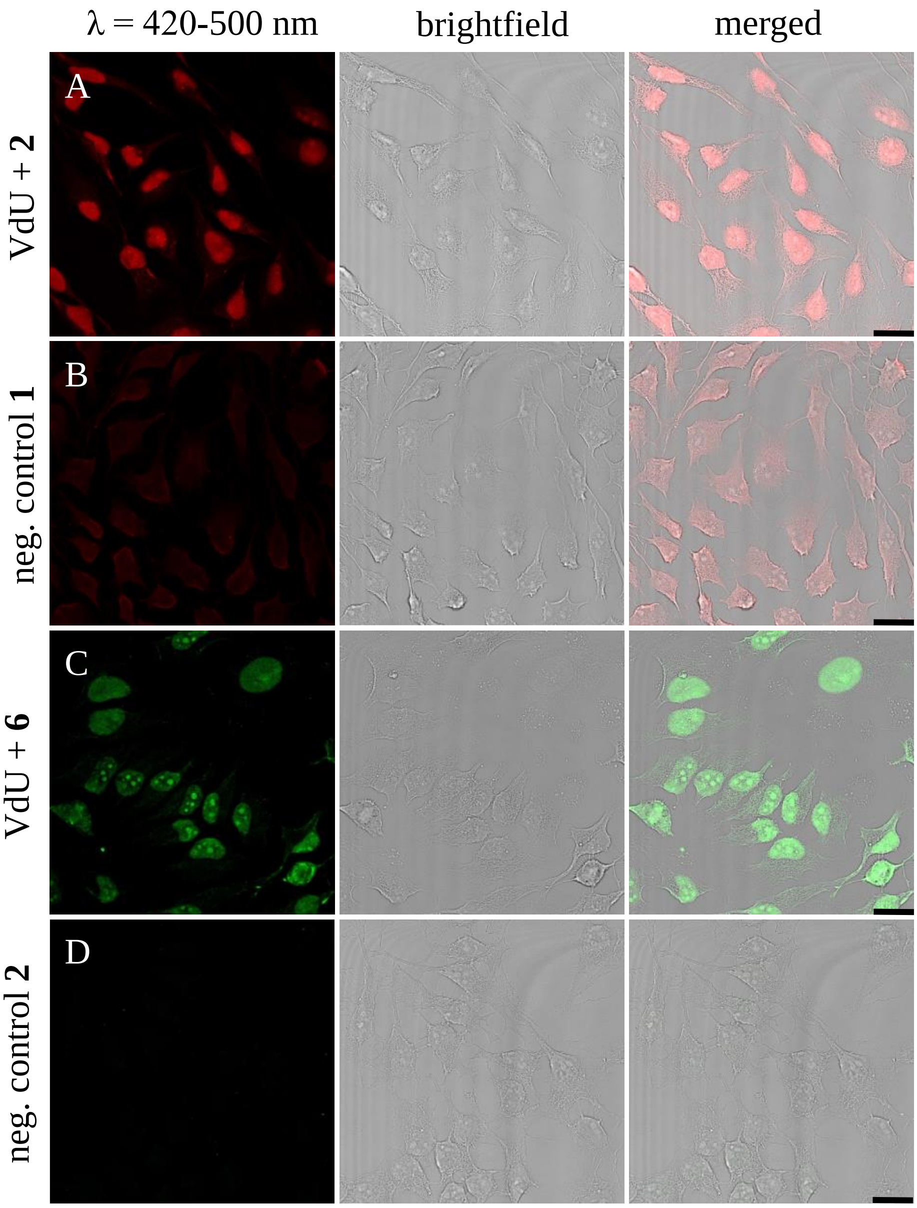

Figure 36. HeLa cells were metabolically incubated with **20** (20µM) for 48 h, fixed, denaturated with HCl, permeabilized with 0.5% Triton-X-100, treated with **2** (60 µM) or **6** (30 µM) and subsequently irradiated with 405 nm LED for 90 s (**2**) / 20 min (**6**). Imaging was performed using a confocal fluorescence microscope with $\lambda_{exc}$ = 405 nm laser at 10% intensity. The emission channel was set to 420-500 nm. Results are given with an additional brightfield and merged image. As negative controls **1** and **2**, cells were not incubated with **20** and therefore irradiated without reactive counterpart but afterwards treated equally to the other samples. A: VdU was incorporated and reacted with tetrazole **2**, resulting in red fluorescence in the nucleus of the cell. B represents the first negative control 1 for tetrazole **2**, where no intense fluorescence is obvious. C depicts the positive results from incubation with compound **20** followed by treatment with tetrazole **6**, resulting in green fluorescence. D, the negative control 2 for tetrazole **6**, shows incubation and activation of the tetrazole without VdU (**20**) incorporation. Different concentrations were used for technical reasons, to obtain the best cell images. Scale bar: 20 µm.

When performing a photoclick experiment using a 450 nm LED with an irradiation time of 20 min comparable labelling results were obtained with tetrazole **6**. Imaging was performed using a 405 nm laser at a confocal microscope to allow a better comparison of the results

(Figure 37). The images show the successful click reaction between **20** and **6**, with distinct labelling of the cell nucleus. In a magnified view of the cell image, it can be observed that not only the nucleus but also the nucleoli are distinctly labelled. In the negative control, no incubation with **20** was performed, and the cells were again irradiated following the incubation with tetrazole **6** (30 µM). Here, no specific staining in the nucleus or the nucleoli can be found. Comparing these images with literature, shows nucleoli staining as well.[192-193]

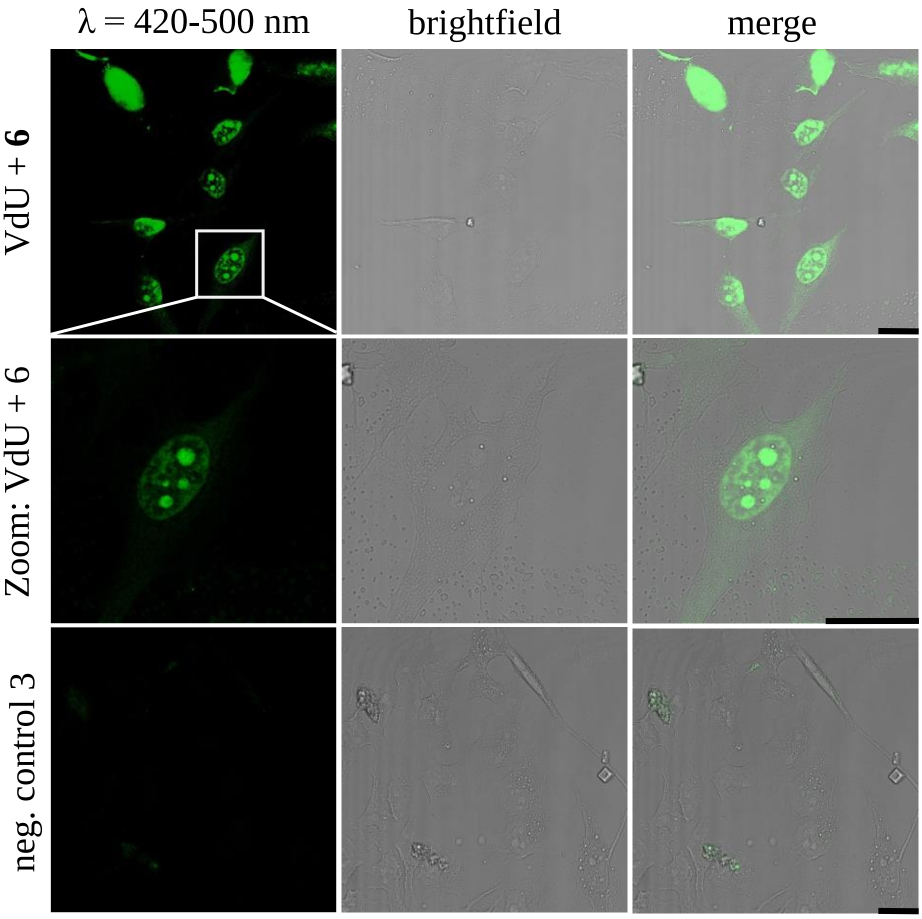

Figure 37. HeLa cells were incubated with **20** (20µM) for 48 h, fixed, denaturated with HCl, permeabilized with 0.5% Triton-X-100, treated with **6** (30 µM) and subsequently irradiated with 450 nm LED for 20 min (**6**). Imaging was performed using a confocal fluorescence microscope with a 405 nm laser at 10% intensity. The emission channel was set to 420-500 nm. Results are given with an additional brightfield and merged image. As negative control 3, cells were not incubated with **20** and therefore irradiated without reactive counterpart. Scale bar: 20 µm.

Additional costaining experiments with DRAQ5 as a DNA intercalating dye were performed to ensure the nuclear DNA was labelled by the photoclick procedure. Here a significant colocalization of both fluorescent signals was observed (Figure A 4 for **2** and Figure A 5 for **6**). These results allow the conclusion that newly built DNA was labelled with the photoclick reaction. Due to the required presence of MeCN when performing a labelling reaction with **2** or **6**, the method could so far only be applied as a proof-of-principle in fixed cells. Nevertheless, these results are important, because the application of the less harmful light with its spatiotemporal control bears a huge potential for future applications in living cells.

# 4 Conclusion and Outlook

In this chapter, a visible light-induced and fluorogenic photoclick reaction with spatiotemporal control for metabolic labelling DNA in fixed cells was developed. The synthesized tetrazoles **2** and **6** show a unique combination of optical properties of the pyrenyl moiety bound to the tetrazole. This modification not only shifts the photochemistry and irradiation wavelength of the system to the visible light but also provides the fluorescent readout for the labelling. The photoclick reaction of **2** and **6** to the corresponding pyrazoline and pyrazole induces a fluorescence colour change, which is a significant advantage for fluorescence imaging with a confocal microscope.

The determined reaction rate constants for the photolysis are in a range between $k_2$ = 2730 - 6800 $M^{-1}s^{-1}$ for **2** and $k_2$ = 9 - 30 $M^{-1}s^{-1}$ for **6**. The rate constants for the product formation step determined using RP-HPLC are in the range between $k_2$ = 540 - 680 $M^{-1}s^{-1}$ for **2**. Significantly, these rates do not depend on the type of alkene or alkyne that is used as a reaction partner. This is an advantage of the tetrazoles **2** and **6** because the smallest and simplest alkene-modified nucleoside VdU (**20**) can be used as a reactive counterpart in the DNA, which is advantageous for an application in vivo. Cellular enzymes tolerate smaller modifications better than bigger ones.

In the metabolic labelling experiments, HeLa cells were incubated with **20**, fixed and labelled using **2** and **6**. Both tetrazoles allow the activation of the tetrazoles for photoclick reaction with visible light 405 nm or 450 nm. Previous known literature for photoclick reactions in cells was triggered with UV light (350 nm). Additionally, the latter tetrazole was modified with a negatively charged coumarin.[194] These molecules induce electrostatic repulsion with the negatively charged backbone of DNA. The pyrene tetrazole conjugates developed in this chapter have intercalating properties into the DNA through the pyrene and therefore avoid the above-described electrostatic repulsion.

This method has huge potential as versatile tag that reacts rapidly. However, the labelling of fixed cells, like shown in this chapter is not the final aim of this work. In future experiments, living cells should be labelled.

The main challenge of this system is the low solubility of **2** and **6** in polar solvents, which prevents the reaction from occurring in aqueous environments and, consequently, in living systems. The criteria for conducting a photoclick reaction in living systems, as described above, involve two key aspects: the use of visible light as a trigger and the water solubility of the tetrazoles. One problem, while using UV light, has been resolved by the addition of a pyrene moiety thereby red-shifting the activation wavelength into the visible light range. However, future efforts must address the solubility of the tetrazoles in water and their limited cell permeability.

In previous experiments, the cells were permeabilized by Triton-X-100, to allow the tetrazole to enter. Structural modifications are necessary to enable tetrazoles to penetrate the cell membrane in live systems without permeabilization. These modifications should facilitate a specific pathway for cellular uptake, for instance by cell-penetrationg peptides.

Nevertheless, the shift to visible light with spatiotemporal control has the potential for future application in living cells. Additionally, it is possible to not only label specifically modified DNA but also use it as a more general tool for visualizing small molecules, proteins or RNA inside living cells.

# IV. Water Soluble Tetrazoles for Metabolic Labelling in Live Cells

The above described modification of the tetrazole with large aromatic systems at their 2-position led to a shift of the excitation wavelength to the visible light spectrum, enabled successful cell experiments in fixed cells using MeCN as a solvent. However, applying these tetrazoles in living cells remained challenging due to their insufficient water solubility. To overcome this, the aim of this chapter is to introduce the following modifications from Figure 38 at the 5-position of the tetrazole for successful photoclick reaction in live cells.

In comparison to its methylated derivative **2** (Figure 38), a carboxyl group modification **3** (Figure 38) generally provides better water solubility properties. The carboxylic group is deprotonated in aqueous solutions at physiological conditions, leading to a negative charge. However, this prevents the molecule from passing and penetrating the negatively charged cell membrane. Therefore, an amine **4** was further introduced (Figure 38) to increase the molecule’s affinity for the cell membrane and potentially facilitate its permeabilization across the membrane. As a final attempt to further increase water solubility, a hydrophilic polyethylene glycol **5** (PEG) moiety was conjugated into the molecule employing a similar synthesis protocol (Figure 38). This approach aims to investigate which functional groups enable the optimal uptake of tetrazoles in living systems, as well as to assess their potential toxicity when used in biological environments.

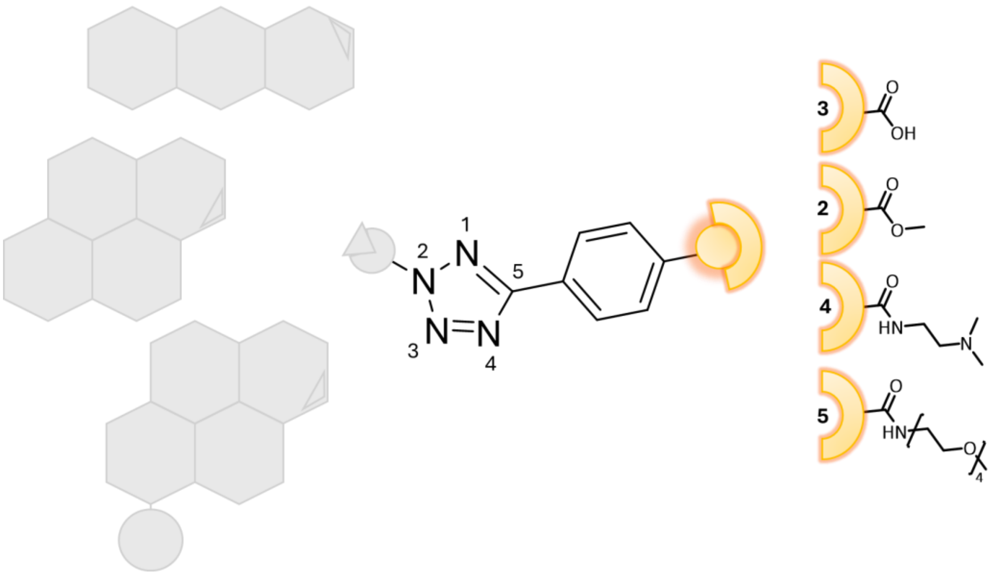

Figure 38.Overview of the core structure of the different used tetrazoles **2**-**5**. Modifications (orange coupling partner) in the 5-position were introduced in para position of a benzylic mojety.

# 1 Synthesis

As previously described in section III.1.1, tetrazoles **2** and **6** were synthesized as methyl-carboxyl ester. The tetrazoles **3**, **4**, and **5** shown in Figure 24 were synthesized to investigate the influence of their solubility on the permeability within the cell and on the photoclick reactivity.

To introduce the carboxyl group for tetrazoles **2** and **6**, the saponification reaction of tetrazoles **2** and **6** was first attempted. However, neither of the tetrazoles could be successfully saponified (Figure 39). Modifying the reaction parameters, using different bases like NaOH and LiOH as well as changing and mixing the solvents did not yield any success, requiring an alternative approach. Therefore, it was decided to synthesize the tetrazole **3** directly from a benzoic acid (Figure 40).

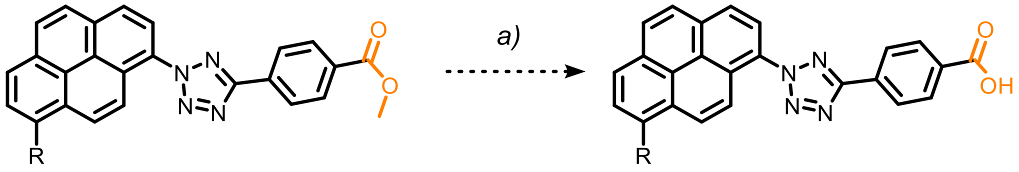

tetrazole 2: R = H
tetrazole 6: R = $NMe_2$

Figure 39. Overview of the base-catalyzed ester hydrolysis of the estergroup on tetrazole **2** and tetrazole **6**. The group to be hydrolyzed is highlighted in orange. a) NaOH, THF / $H_2O$, r. t., 24 h.

The benzoic acid can be introduced directly into the synthesis. During the hydrazole formation, prior to the final tetrazole formation, a hydrazide of 4-formylbenzoate (**37**) was prepared instead of a hydrazide of methyl-4-formylbenzoate (**16**) to maintain the modularity of the tetrazoles for as long as possible. This reaction was successfully carried out for tetrazole **2**, yielding tetrazole **3** in a yield of 38%. Using aminopyrenyl-modified tetrazole **6** as starting material, no product could be isolated employing this synthesis route.

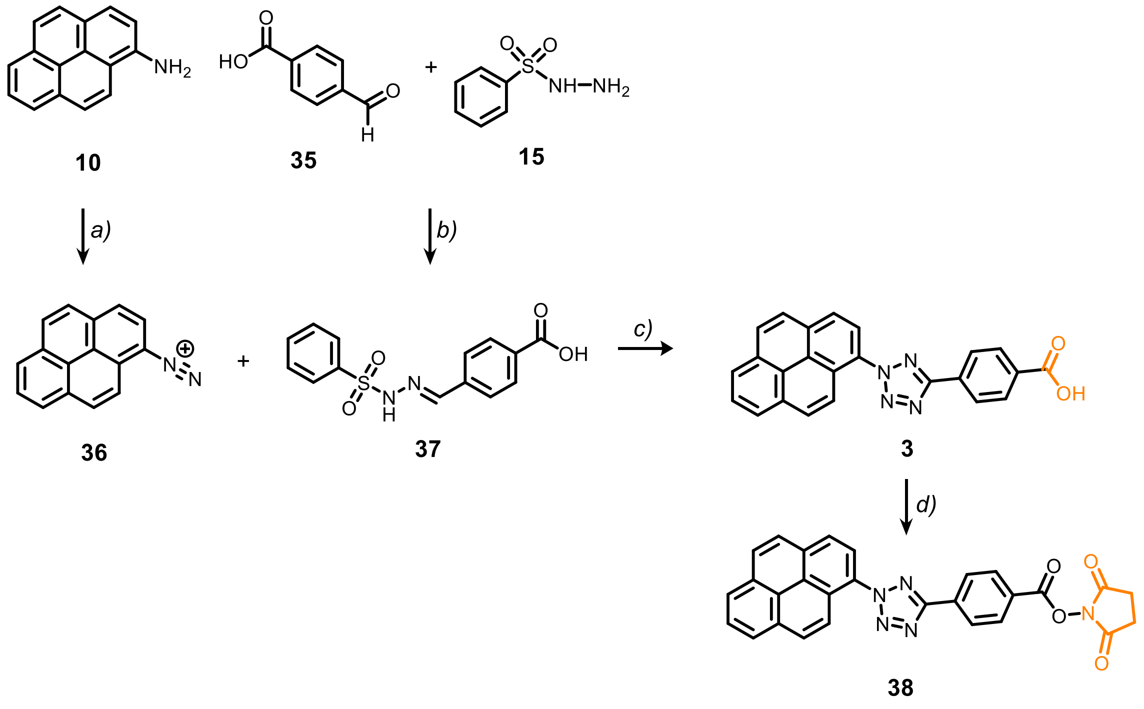

Figure 40.Synthesis of tetrazole **3**, from **14** to **35** and therefore receiving tetrazole **3** instead of **2**. a) sodium nitrate, HCl, EtOH/$H_2O$, 0 °C, 20 min; b) EtOH, 45 °C, 1 h, 95%; c) hyrazone (**37**), pyridine, 0 °C to r. t., over night, 38%; d) NHS, EDC-HCl, DMF, r. t., 20 h, 89%.

Tetrazole **3** was converted into the active ester **38**, enabling an amide coupling and serving as a platform for introducing the desired modifications. To obtain a positively charged tetrazole under physiological conditions and thus enable a comparison with tetrazole **3**, which is expected to be negatively charged in aqueous environments, tetrazole **38**[1] was reacted with *N,N'*-Dimehtylethylenediamine Figure 41a) to form tetrazole **4**[2]. In addition, a PEG-amine[3] was coupled to tetrazole **3**, resulting in **5**, which should be way more hydrophilic than the dimethyleneamine due to the long hydrophilic chain, making it suitable for applications in cellular environments.

---

[1] Synthesized as part of the Master thesis by L. Rieger, Karlsruhe Insitute of Technology (KIT), 2021.
[2] Synthesized as part of the Master thesis by L. Rieger, Karlsruhe Insitute of Technology (KIT), 2021.
[3] Synthesized by Dr. Philipp Bohn, Karlsruhe Insitute of Technology (KIT).

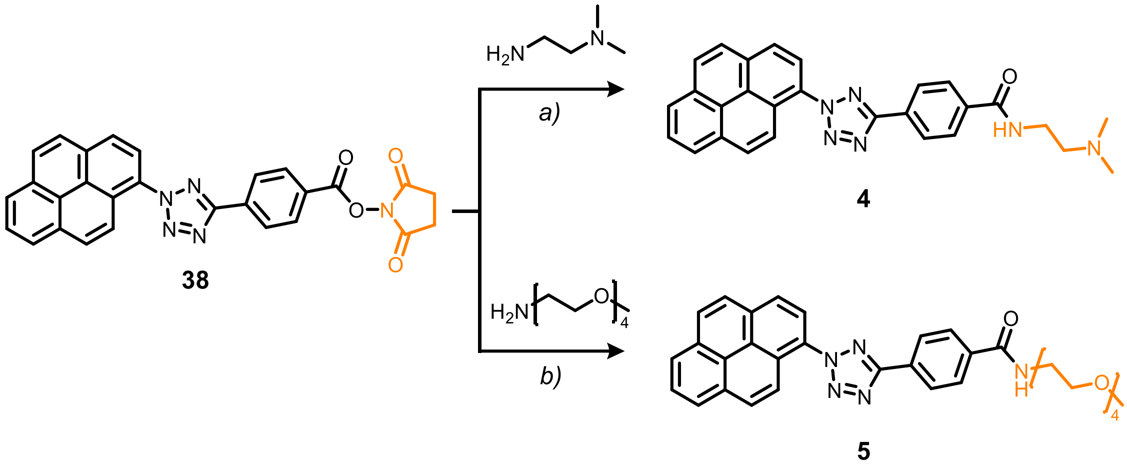

Figure 41. Synthetic strategy to receive the modified tetrazoles **4** and **5**. a) $Et_3N$, DMF, r. t., 20 h, 20%.b) $Et_3N$, DMF, r. t., 20 h, 20%.

These four synthesized tetrazoles **2**-**5** were further investigated regarding their solubility and reactivity in acetonitrile, a mixture of acetonitrile and water, as well as water only. The photolysis was followed by UV/Vis spectroscopy and used to compare the molecules **2** to **5** in the following chapter.

## 2 UV/Vis Experiments

As previously demonstrated in section III.2.1, the light irradiation experiments were conducted using the same LED (405 nm with 30 mW) and identical concentrations (c = 25 µM). Since the different tetrazoles **2-5** (Figure 42) are based on the pyrene-tetrazole framework, similar kinetics for the photolysis were expected. Therefore, a time interval of 0–600 s of irradiation was chosen for the experiments.

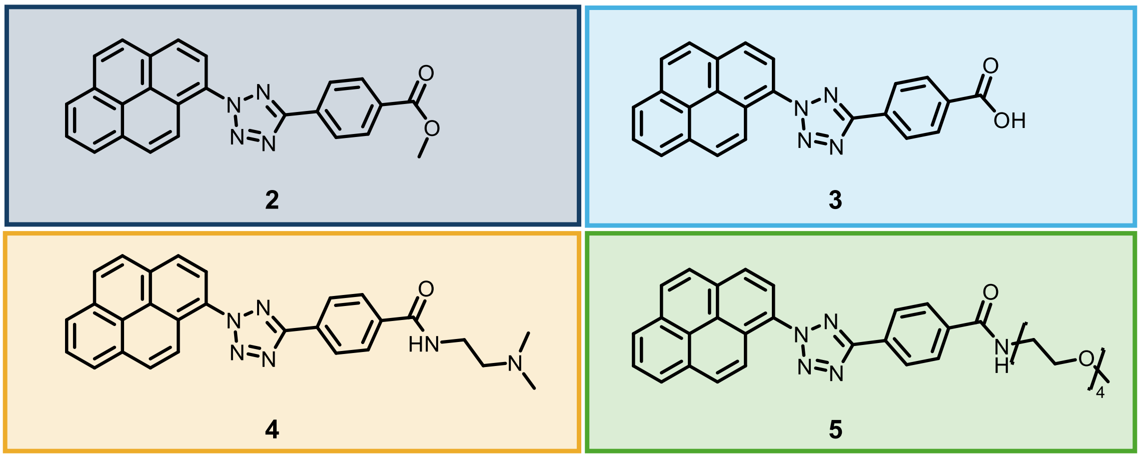

Figure 42. Synthesised tetrazoles **2-5** with different modifications that potentially enhance the water solubility.

In contrast to the previous chapter, herein the 5-position of the tetrazoles was modified, leading to the possibility to change the solvent from MeCN to a MeCN / $H_2O$ (1:1 v/v) mixture and $H_2O$ only. For better comparison of the herein synthesised tetrazoles with the above introduced ones, first experiments were carried out using MeCN.

For all following irradiation experiments, a stock solution (6.33 mM) of the investigated tetrazoles was prepared in DMSO and diluted in the respective solvent to adjust the desired concentration (25 µM) and keeping the DMSO percentage below 1%.

Subsequently, the tetrazoles were exposed to light from a 405 nm LED for a defined time interval after which UV/Vis absorption was measured before beginning the next irradiation time interval (Figure 43). This approach allows for precise monitoring of the photolysis of the tetrazole. Pre-irradiation, all tetrazoles show three distinctive absorbance maxima at $\lambda_1 = 240$ nm, $\lambda_2 = 290$ nm and $\lambda_3 = 343$ nm. After 10 s of irradiation, the absorbance maxima decrease, and an isosbestic point develops at $\lambda_1 = 375$ nm. The decrease of the absorption maximum can be explained by the decomposition of the compounds into the nitril imines (photolysis).With longer irradiation times, the main signal is shifting, namely, the local maximum at $\lambda_3$ = 343 nm is almost vanished. Further, a new absorbance maximum at λ = 453 nm, indicating sucessful and complete photolysis of the tetrazoles. The new modifications at the 2-position of the tetrazoles do not significantly alter the spectrum compared to the changes observed when substituting the 5-position.

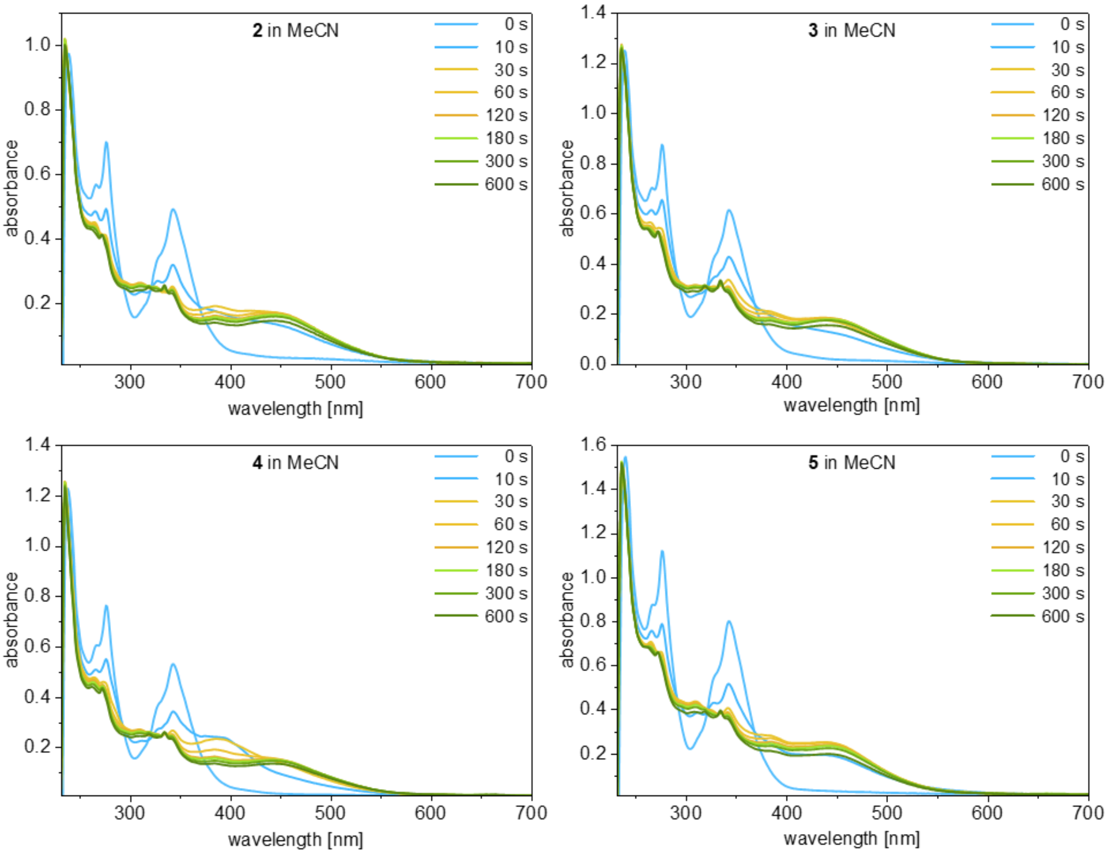

Figure 43. UV/Vis spectral analysis of the irradiation experiments of the tetrazoles **2**-**5** in MeCN in irradiation intervals up to 600 s with a 405 nm LED. Concentration was the same for all the tetrazoles with c = 25 µM.

On closer inspection, the UV/Vis absorbance spectra indicate that the photolysis is complete after 60 s of irradiation, when the newly appeared absorbance maximum at λ = 450 nm reaches its highest intensity. It was therefore decided for the following experiments to discuss only the tetrazoles before irradiation and after irradiation of 60 s for clarity.

Following experiments were conducted in either MeCN/$H_2O$ mixtures or water to investigate the photolysis of the tetrazoles in aqueous **2-5** solvents as premilinary experiments for further application *in cellulo* (Figure 44).

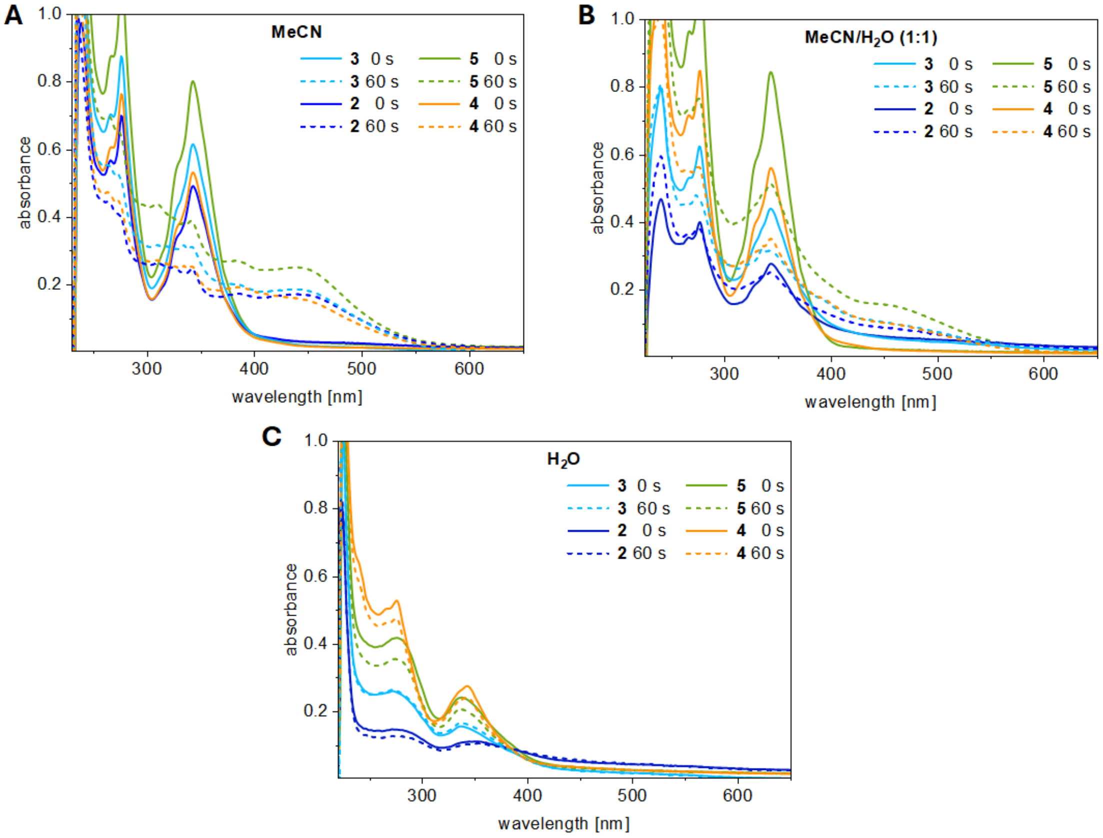

Figure 44. UV/Vis absorption spectra for tetrazoles **2-5** at concentrations of 25 µM in different solvent mixtures at two different time points of the reaction (bolt line 0 s, dashed line 60 s). A: MeCN; B: MeCN/$H_2O$ (1:1); C: $H_2O$. Tetrazole **2** is dark blue, **3** is light blue, **4** is orange and **5** is green.

The tetrazoles still exhibit their typical absorption in the range of 220-400 nm. However, the intensity differs, and the isosbestic point is not as well-defined as in Figure 43. Furthermore, the maximum at 342 nm appears to broaden slightly. Additionally, in the green curve of tetrazole **5**, a decrease in the minimum at 400 nm can be observed. These are all indicators of aggregates, because the solubility was diminished in these solvents. In tetrazole **2**, the change is the most distinct. In Figure 44A, there is a maximum at $\lambda$ = 342 nm with an intensity of about 0.5 and the isosbestic point is visible at $\lambda$ = 372 nm.

In the solvent mixture MeCN/$H_2O$, the maximum significantly decreases in intensity and becomes slightly broader. An isosbestic point is still visible, but the rise of a new product band above λ =400 nm is considerably weaker. Additionally, a slight increase in the baseline values above λ = 400 nm is observed, which also suggests that aggregation is occurring.

When comparing the spectra in MeCN and MeCN/$H_2O$ with the spectra in $H_2O$ (Figure 44A and B), a significant broadening of the peaks and an increase above λ = 400 nm in the baseline spectrum can be observed. Additionally, no isosbestic point is present, indicating that no photolysis is occurring. The excited state cannot initiate the release of $N_2$. In general, it can also be stated that Figure 44B clearly shows which molecule has the best water solubility. Thus, tetrazole **5** exhibits the highest intensity, followed by **4**, then tetrazole **3**, and finally the esterified tetrazole **2**. This poor water solubility of **2** is also clear in Figure 44C. As a summary, Figure 45 shows the different tetrazoles **2-5** from left to right, increasing water solubility.

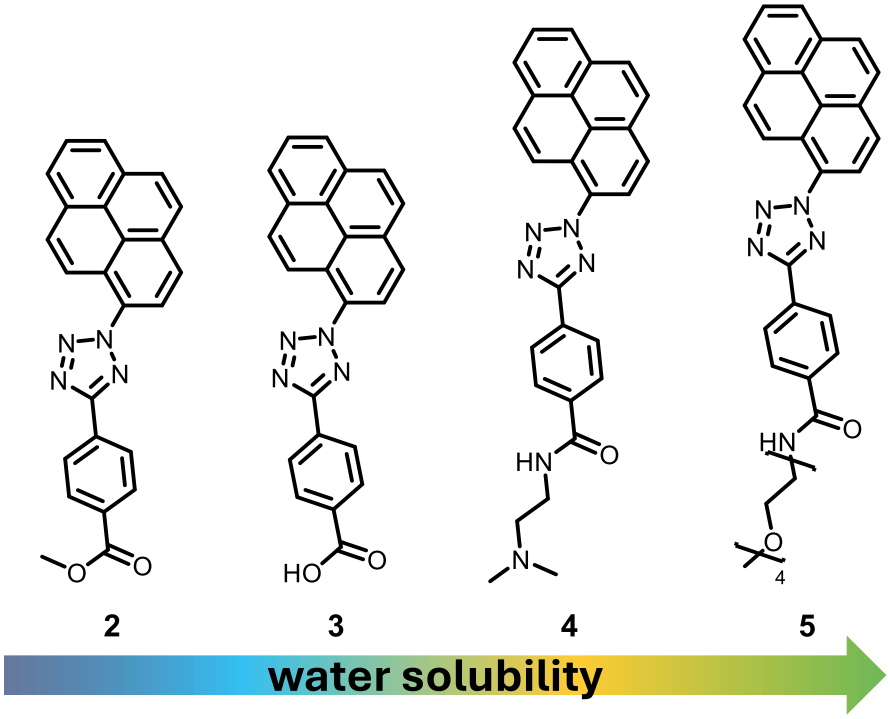

Figure 45. Relative solubility of tetrazoles **2-5** in water.

Additional experiments were conducted to investigate whether the solubility of the tetrazoles or the photochemistry itself is the problem of the photoclick reaction in water. Therefore, time resolved measurements were performed and only show the transient absorption of the singulet state ($S_1$) of the tetrazoles **2** + **3** whereas no spectroscopic signature of a triplet state ($T_1$) is present within 1 ns (Figure A 6) in MeCN. This suggests that the photochemistry itself might be the problem, most likely due to the altered energetic level or the population of the $T_1$ state by intersystem crossing (ISC).

# 3 MTT Tests

Beyond achieving visible light activation and enhanced water solubility, it is essential to investigate the cytotoxicity of tetrazoles **2**, **3**, **4** and **6** at specific concentrations to ensure their application in live cell studies.

To evaluate the cytotoxic effects of tetrazoles, an MTT assay (3-(4,5-dimethylthiazol-2-yl)-2,5-diphenyl tetrazolium bromide) was performed. This method involves treating cells with five concentrations of tetrazoles, spanning the concentration range used in the tetrazole cell experiments. Upon addition to the cells, the yellow, water-soluble MTT is reduced by cellular enzymes, producing purple, water-insoluble formazan crystals. Those crystals need to be solubilized and afterwards the formazan's absorbance, within its detection range, is measured photometrically using a plate reader (explained in the experimental section VIII.6.2) Comparing these readings to a negative control (cells treated only with MTT reagent) enables assessment of cell metabolic activity and, consequently, cell viability under specific conditions.[195]

HeLa cells (Figure 46A) and A549 cells (Figure 46B) were incubated with various concentrations of each tetrazole (10 µM, 20 µM, 30 µM, 60 µM, 80 µM) for 72 h. The tetrazoles were added directly to the cell medium, and the cells were subsequently treated with the MTT reagent. A solubilization step needed to be performed to receive the soluble formazan. The cell viability was then determined as a percentage relative to the control, depending on the tetrazole concentration, as presented in Figure 46.

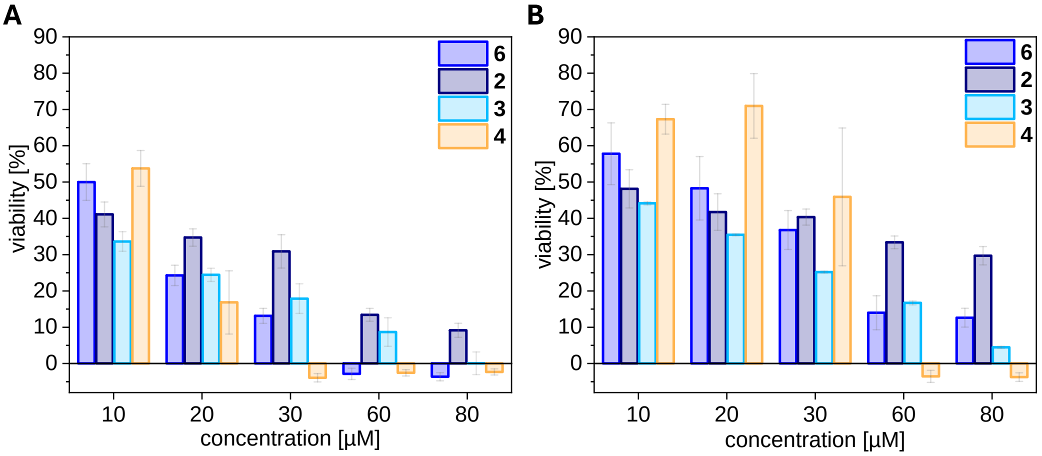

Figure 46. The viability of two different cell lines at various concentrations of tetrazoles **2**, **3, 4**, and **6**, was determined via the MTT assay. HeLa (A) and A549 (B) cells, cultured in DMEM, were incubated for 48 h with the respective compounds at their designated concentrations, followed by MTT treatment. Each concentration experiment was performed six times and the results represent values from biological duplicates.

Both HeLa and A549 cell viability were evaluated, as these cell lines will be used for click experiments in the subsequent chapters. A general observation from the MTT assays is that significantly higher levels of cell death occurred in HeLa cells (Figure 45A) compared to A549 cells (Figure 45B). This suggests that HeLa cells are more sensitive to the synthesized tetrazoles, displaying a greater degree of cell death in response to the tetrazole treatment across the tested concentrations. This difference in sensitivity is an important factor to consider in the following experiments.

The MTT assay results for tetrazoles **2**, **3**, **4**, and **6** indicate a clear correlation between water solubility and cell viability. The more water-soluble tetrazoles demonstrate reduced cell viability, indicating increased cytotoxicity as solubility and cell permeability are increased. This is particularly evident with tetrazole **4**, which, due to its assumed solubility and cell permeability, shows the highest toxicity even at a relatively low concentration of 30 µM. At the highest concentration tested (80 µM), only cells treated with tetrazole **2** exhibited any remaining viability, going along with the prediction that its lower water solubility limits its ability to penetrate the cell membrane effectively.

This trend is also seen in A549 cells (Figure 45B), although overall the cell viability in A549 is approximately 20% higher than in HeLa cells (Figure 45A), emphasizing HeLa cells' higher sensitivity to the tetrazole treatments.

Comparing tetrazoles **2** and **6** further confirms this trend. While neither has significant water-soluble modifications, tetrazole **6** should exhibit slightly greater solubility due to the addition of a dimethylamino group on the pyrene moiety, correlating with its lower cell viability compared to tetrazole **2**. This reinforces the pattern observed across all four compounds, linking increased hydrophilicity with enhanced cellular uptake and subsequent cell cytotoxicity.

In conclusion, it can be postulated that a short incubation period for tetrazoles in both HeLa and A549 cells is feasible. Since the MTT reagent was added after 72 h, concentrations can likely be effective after approximately 1 h of exposure. Tetrazoles **2** and **6**, which were previously applied to cells, were used at concentrations of 60 µM (for tetrazole **2**) and 30 µM (for tetrazole **6**). Tetrazole **2** can be applied in HeLa cells in concentrations up to 60 µM and in A549 cells up to 80 µM. In contrast, the concentration of tetrazole **6** should not exceed 20 µM in HeLa cells and 30 µM in A549 cells if the viability threshold is set at 25%.

Both MTT assays (conducted with HeLa and A549 cells) confirm the correlation between water solubility and cell toxicity: the more water-soluble the tetrazole, the better its cellular penetration, resulting in reduced cell viability.

## 4 *In cellulo* Experiments

After determinating the toxicity of the tetrazoles *in cellulo*, the results were transferred to live HeLa cells to investigate the bioorthogonal labelling of DNA employing a photoclick reaction that can be activated with visible light. Therefore, the concentrations (i.e. 30 µM for **6**, µM and 60 µM for **3**) were selected and evaluated for easier comparison with the labelling experiments described in the previous section (III.3).

To determine the differences between fixed cell experiments and live cell experiments, the first experiment was conducted following the previously established fixation protocol: VdU **20** was added to the cells and incubated for 48 h. Afterwards, one part of the experiment was to determine if the cell fixation, employing 4% paraformaldehyde (PFA), followed by permeabilization with 0.5% Triton-X-100 and washing with PBS leads to the same results as the fixation with additional steps, used in section III.3. In accordance with this reaction in water, compared to MeCN, the click reaction also needs to be followed in live cells.

Herefore no fixation was performed and the tetrazole solution was added to the OptiMEM used in the cell experiments. Tetrazole **3** was chosen for the experiments, due to its water solubility and cytotoxicity between **2** and **4**. Additionally, it is important to keep short irradiation times for the experiment with live cells.

In Figure 47, **20** was added to the cells, seeded in µ-slides and incubated for 48 h. Following incubation with tetrazole **3** and irradiation at λ = 405 nm for row A and row C. All rows were washed with OptiMEM (for rows A and B) or PBS (for rows C and D). For the images in row A and B, cells were kept in the incubator to perform live cell imaging For rows C and D fixation was applied. For nuclear costaining, DRAQ5 was used, with an excitation wavelength of $\lambda_{exc}$ = 636 nm.

In row A, live cells were irradiated for 2 min, while row B was kept in the dark (protocol, given in section VIII.6.4). Rows C and D were fixed as previously described (short protocol, explained in section VIII.6.5) and incubated with tetrazole **3**; row C was irradiated for 2 min, whereas row D remained in the dark.

Strong fluorescence staining of the cell nucleus was expected in the irradiated images (rows A and C), consistent with the results obtained in section III.3, whereas no fluorescence staining of the cell nuclei was expected for the samples that were kept in the dark (rows B and D) as no nitrile imine is generated and therefore no labelling reaction with the VdU takes place.

However, none of the photoclick experiments (rows A1-A4) showed any fluorescence staining upon irradiation with a 405 nm LED and when excited in its respective excitation range ($\lambda_{exc}$ = 405 nm; $\lambda_{em}$ = 420-490 nm).The only fluorescence observed is the yellow emission from the DRAQ5 dye in rows A2-D2, which is the costaining of the cell nucleus. The rows for labelling newly replicated DNA remain dark in all four images. For row B and C we expect the images to be dark, but for rows A and C, the tetrazole was activated and should therefore bind the incorporated **20**.

Thus, it can be concluded that the photoclick reaction is inhibited by the aqueous environments and, consequently, is not effective in biological systems. This is consistent with the spectroscopic investigations *in vitro*.

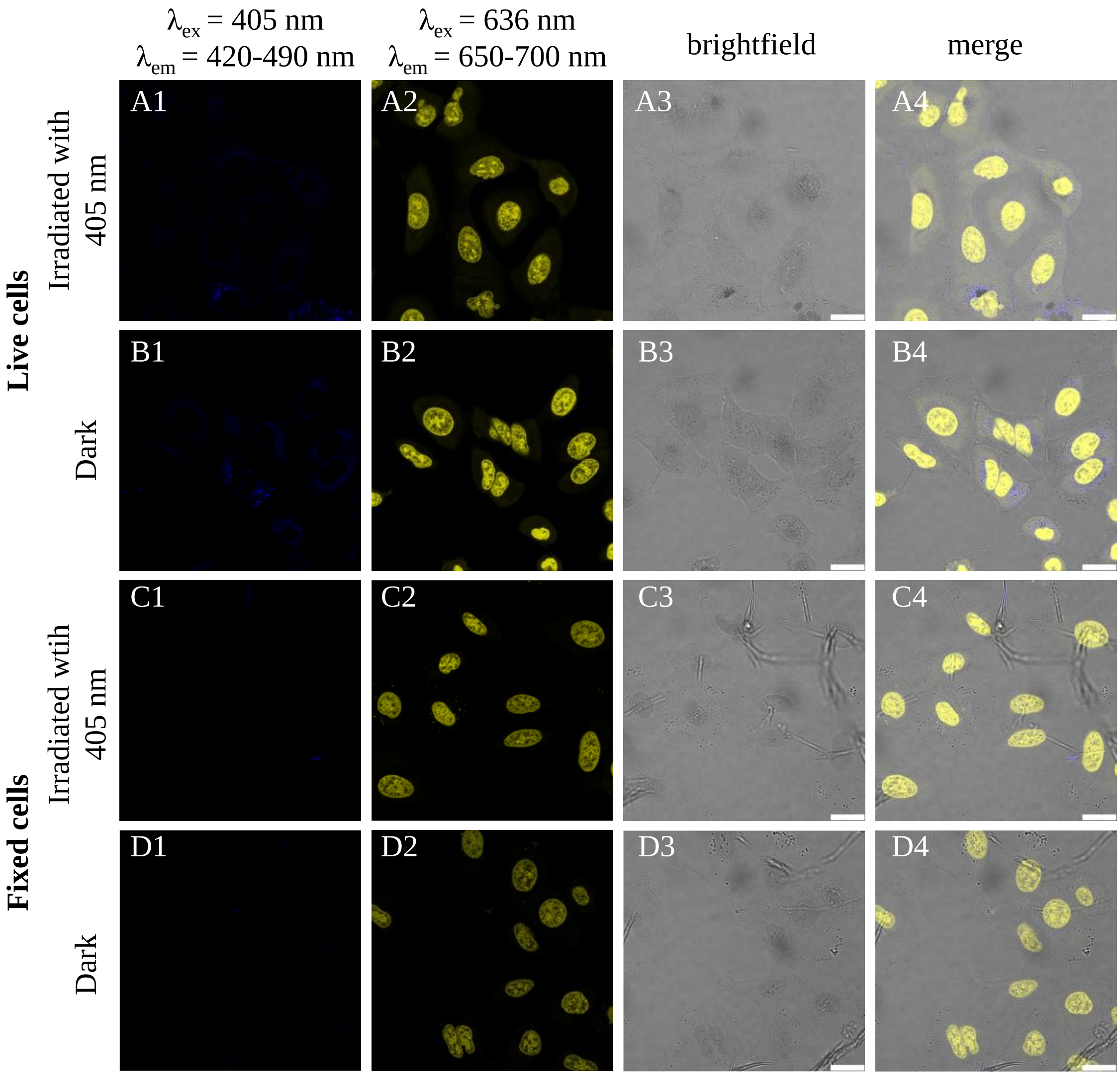

Figure 47. HeLa cells, incubated with **20** (20µM) for 48 h rows A and B show live cell experiments with incubation of **3** in a concentration of 60 µM. Row A was irradiated for 2 min with 405 nm LED and B was kept in the dark; rows C and D. C was irradiated with 405 nm and D was kept in the dark; in A2-D2 costaining of DRAQ5 is shown in yellow; A3-D3 shows the brightfield image and A4-D4 shows the merge of the emission channels with the brightfield; scale bar: 20 µm.

# 5 Conclusion and Outlook

In this chapter, the established concept of photoclick labelling in cells (discussed in chapter III) was extended to living systems. It has been demonstrated that tetrazoles can be irradiated and activated using visible light above $\lambda = 400$ nm. The goal was to modify tetrazoles **2** and **6** to increase their water solubility and improve cellular uptake without requiring cell permeabilization and fixation. Due to insufficient solubility of the modular system by modification of tetrazole **6**, only tetrazole **2** was modified, and compounds **2**, **3**, **4**, and **5** were evaluated through UV/Vis absorbance, while compounds **2**, **3**, **4**, and **6** were tested using MTT assays. In the UV/Vis absorbance experiments, several solvents were explored beyond MeCN, including MeCN-water mixtures and water, to better simulate the aqueous environment of living systems and monitor the reactivity of the modified tetrazoles.

The UV/Vis spectra reveal a correlation between solubility and the kinetics of the photoclick reaction. In MeCN, all tetrazoles from **2** to **5** can be successfully photolyzed. In water, however, the spectral changes are minimal: there is only a slight decrease in their maximum aborption. The 1:1 solvent mixture (MeCN/$H_2O$) provided insights into the water solubility in the following order: tetrazole **5**, **4**, **3**, and **2**. This suggested, the formation of aggregates as solubility decreases. These observations indicate that while the synthesis of more water-soluble tetrazoles was successful, the photoclick reaction does not perform effectively in water despite their increased solubility. A plausible explanation relates to the photochemistry of the system, which might be highly solvent-dependent. Based on the absorption measurements of tetrazole **2** in different solvents and subsequent cellular experiments, it appears that the population of the photoactive triplet state is less occupied in water compared to MeCN (Figure A 6).

MTT tests were conducted with all synthesized tetrazoles to investigate the toxicity of the light-responsive unit and anticipate their use in cellular systems, such as live HeLa cells in a water/MeCN mixture. The concentrations tested ranged from 10 µM to 80 µM. Results indicated that even at the lowest concentrations, tetrazoles led to a maximum of 50% viability in HeLa cells. In contrast, A549 cells exhibited higher stability and up to

75% viability with tetrazole **4** at the same concentrations. However, it is important to note that the tetrazoles were incubated at 10–80 µM for 72 h in the MTT assays, while they remain on the cells for just over an hour during the actual photoclick experiments, making direct correlation of results challenging.

In the *in cellulo* experiments conducted with a concentration of 60 µM of **3**, a maximum cell viability of 15% (HeLa) and 25% (A549) was observed. This suggests that by limiting the incubation time to a maximum of 2 h, it should be possible to perform the photoclick reaction while keeping the cytotoxic effects of the tetrazoles to a minimum. Regarding permeability, it is evident that as the tetrazoles become more water-soluble, they also become increasingly toxic to the cells, likely due to the better cellular uptake, irrespective of the cell line. Consequently, the modular modifications improve permeability, thus fulfilling the primary criterion of enhanced water solubility.

As already investigated through the UV/Vis spectra, no photoclick reaction occured in aqueous environments, further evidenced by the in cellulo experiments with tetrazole **3**. Here, no fluorescence of the nucleus was imaged after the irradiation of the tetrazoles.

This lack of fluorescence was consistent in both fixed cells (without HCl denaturation) and live cells. Interestingly, the cells appeared quite live even when incubated with the tetrazole for more than 1 h. There were no visible signs of cell death, suggesting that the toxicity may not be as high as initially thought based on the MTT test results.

In conclusion, the water-soluble tetrazoles synthesized in this work are not suitable for use in photoclick reactions to metabolically label DNA in live cells effectively. The primary challenges are the limitations of the photoclick reaction itself and the associated photochemistry. Although successful photoclick experiments in PBS/MeCN or even PBS have been reported in the literature, these rely on UV light, making them unsuitable for *in vivo* applications.[194] A potential solution could be the synthtesis of additional tetrazoles, using different chromophores.

Within all bioorthogonal labelling methods, only the photoclick reaction provides critical control of both time and position, enabling the on-demand and remote visualisation of biological processes in highly dynamic living systems. Besides offering the opportunity to visualise cellular processes, bioorthogonal reactions are also used for the development and improvement of the targeting of chemotherapeutics as many anti-cancer pharmaceuticals aim to inhibit the nucleic acid synthesis of cells to suppress the growth of the tumour tissue. As already discussed in the theoretical section (II.3.2), various techniques are used to label and investigate anti-cancer drugs with so-called photoactivatable chemotherapeutics being the most commonly used and most successful ones. A method was developed and applied in collaboration with the *Bonnet* research group, focusing on the visualisation of photoactivatable chemotherapeutics to determine their localization, mode of action and therapeutic effect.

The following chapter combines the light-induced activation of an anti-cancer pharmaceutical with the CuAAC with the labelling of replicated DNA through IEDDA, resulting in a dual labelling method to monitor the inhibition of a cell replication by the photoactivated chemotherapeutic agent. The combination of IEDDA as labelling method was selected due to its suitability in fixed cells and its potential application in living systems, offering valuable insights into the integration of click chemistry into cancer research.

# V. Visualizing the Invisible: Imaging Ruthenium-based PACT Agents in Fixed Cells

The clinical success of photodynamic therapy (PDT) and photodynamic diagnosis (PDD) has heightened interest in cancer treatment. While light therapy offers the advantage of localized drug activation, potentially reducing side effects, it also has some drawbacks. A primary concern is the production of reactive oxygen species (ROS), which, while beneficial in shrinking tumors,[155] can also harm non-cancerous cells at high concentrations. ROS generation leads to oxidative stress in proteins, lipids, and DNA, affecting not only cancer cells but also healthy surrounding tissues, resulting in necrosis.[156] Additionally, most PDT compounds require oxygen to exert their therapeutic effects, limiting their efficacy in hypoxic tumor environments, where they remain largely inactive.[196-197]

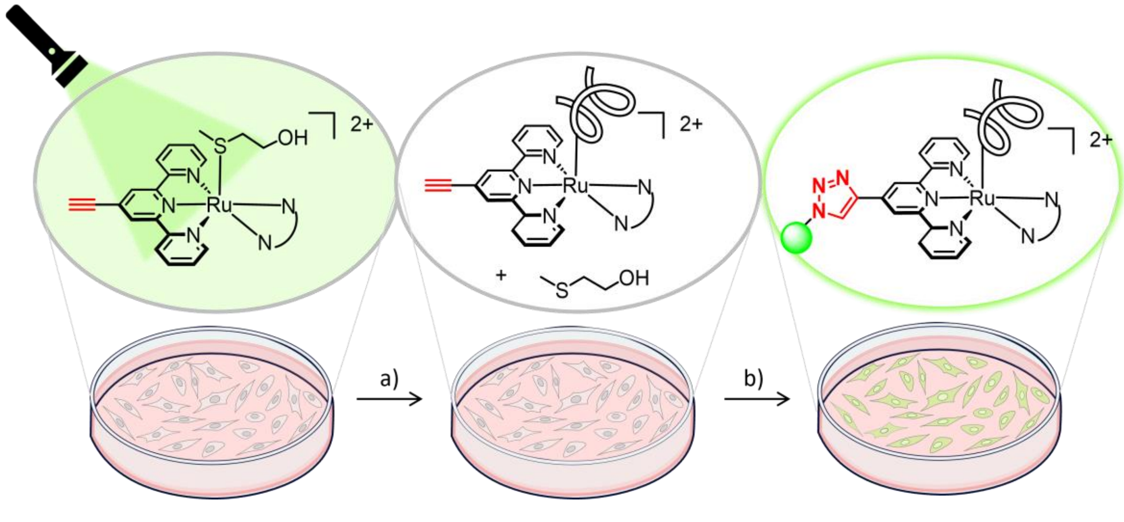

Figure 48. Overview of PACT treatment combined with CuAAC; a) activated incubation; b) fixation and CuAAC.

Photoactivated chemotherapy (PACT)[198] offers a promising approach for achieving precise temporal and spatial control in environments lacking oxygen, minimizing the risk of reactive oxygen species (ROS) in non-cancerous tissue. In PACT, a biologically active inhibitor is attached to a photocage (see section II.3) rendering both molecules biologically inactive until activation.[47, 156] Ruthenium (polypyridine) complexes are particularly suitable for photocaging small molecules. Upon exposure to light at a specific wavelength, the inhibitor is released from the photocage or metal complex, enabling one or both molecules to bind to their respective targets (Figure 48).[199] Like photodynamic therapy (PDT) agents, PACT compounds can have systemic toxicity, but the chemotherapeutic agent is activated solely in areas exposed to light, ensuring localized toxicity. Unlike PDT, PACT agents do not require oxygen for activation, allowing their use in hypoxic tumors. However, a limitation of PACT compared to PDT is that most PACT agents are not emissive, complicating analysis of their pathways and mechanisms using conventional methods such as microscopic imaging.[167]

Consequently, this chapter of the thesis presents a methodology to render the invisible visible. Bioorthogonal chemistry, specifically CuAAC, is utilized to achieve this goal. Previously reported PACT agents were functionalized with an alkyne, the smallest possible functional group, without altering their photochemical and photophysical properties.[8, 167] Additionally, the biological activity of the compound was evaluated and compared to the parent compound. Following cell fixation, the CuAAC reaction was applied to visualize the complex under various conditions. This study further examined how location and enrichment patterns varied with different incubation and light exposure times. Finally, the specific organelle localization was determined using immunofluorescence costaining experiments.

# 1 Synthesis of PACT Agents

In order to functionalize the synthesized PACT agents suitable for biorthogonal reaction three key factors were considered: First, it was essential to determine whether the functionalization was ‘minimal’, ensuring it would not affect the photochemical or biological properties of the PACT agent. Second, the use of click chemistry of azide-functionalized dyes can be evaluated in fixed cells while comparing across different fixation time points. Finally, the localization of the PACT agents must be able to be tracked through colocalization experiments.

With this knowledge in mind, the PACT compounds [**2**]($(PF_6)_2$) and [**4**]($(PF_6)_2$), shown in Figure 49, were synthesized according to the synthetic route developed for the non-toxic analogue [Ru(HCC-tpy)(bpy)(Hmte)]$(PF_6)_2$ (where HCC = alkyne group, tpy = 2,2’:6’2’’-terpyridine, bpy = 2,2’-bipyridine and Hmte = 2-(methylthio)ethanol).[47] Shortly, the terminal alkene was protected with a *tert*-butyldimethylsilyl (TBDMS) group during all steps of the synthesis of the ruthenium PACT complex. Such protection prevents the reaction between the terminal alkyne and the metal centre, which would result in the formation of undesired polymerization side products that are difficult to remove. TBDMS was selectively removed at the final step of the synthetic procedure using an excess of potassium fluoride, to afford the complexes as brown reddish salts in moderate to high yield ([**2**]$(PF_6)_2$: 62%; [**4**]$(PF_6)_2$: 83%). $^1$H-NMR spectroscopy in acetone-$d_6$ confirmed successful deprotection and the formation of the free alkyne.[167] Given the low water solubility of [**2**]$(PF_6)_2$, the $PF_6^-$ counter ions were exchanged with an ion-exchange protocol using n-butylammonium chloride ($Bu_4NCl$), against $Cl^-$ by yielding [**2**]$Cl_2$ in quantitative yields (synthetic procedure is shown in section VIII.4.2). All final products (Figure 49) were characterized by $^1$H-NMR, $^{13}$C-NMR spectroscopy and ESI/HR mass spectrometry.[167]

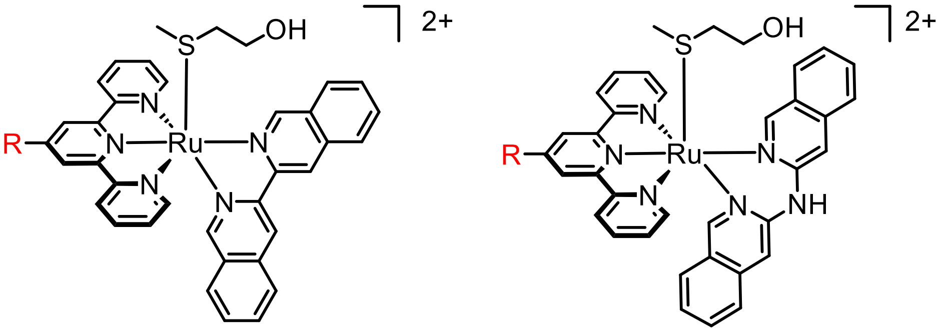

R= H [**1**]$^{2+}$
R= CCH [**2**]$^{2+}$

R= H [**3**]$^{2+}$
R= CCH [**4**]$^{2+}$

Figure 49. Ruthenium-based PACT agents. Compound [**1**]$^{2+}$ and [**3**]$^{2+}$ are unmodified, compound [**2**]$^{2+}$ and [**4**]$^{2+}$ are modified with an alkyne.

Comparison of the X-ray structure of the compounds with ([**2**]$(PF_6)_2$ and [**4**]$(PF_6)_2$) and without functionalization ([**1**]$(PF_6)_2$ and [**3**]$(PF_6)_2$) as well as DFT calculations for the four compounds show, that there is no significant effect on the bond lengths and overall geometry of the ground-state complexes due to the modification. [167]

# 2 Photochemical Analysis

The first step in investigating the photochemistry of PACT agents involves analyzing the compound by UV/Vis spectroscopy in aqueous solutions. As illustrated in Figure 50, it was evident that both [**2**]$^{2+}$ and [**4**]$^{2+}$ exhibit a $^{1}$MLCT absorption band at 470 and 485 nm, respectively. Alkyne functionalization, when compared to the non-functionalized analogues [**1**]$^{2+}$ and [**3**]$^{2+}$, resulted in a bathochromic shift of the $^{1}$MLCT absorption.

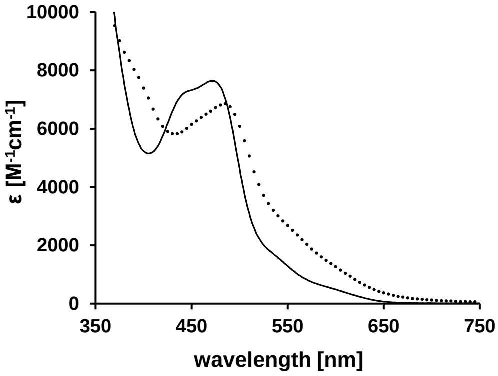

Figure 50. Molar extinction coefficient of aqueous solutions of [**2**]$\mathrm{Cl}_2$ (—) and [**4**]$(\mathrm{PF}_6)_2$ (···).

The photoreactivity of [**2**]$^{2+}$ and [**4**]$^{2+}$ was investigated by irradiation of solutions of the complexes in water with a green LED (517 nm) at 37 °C and followed by UV/Vis spectroscopy (Figure 51).

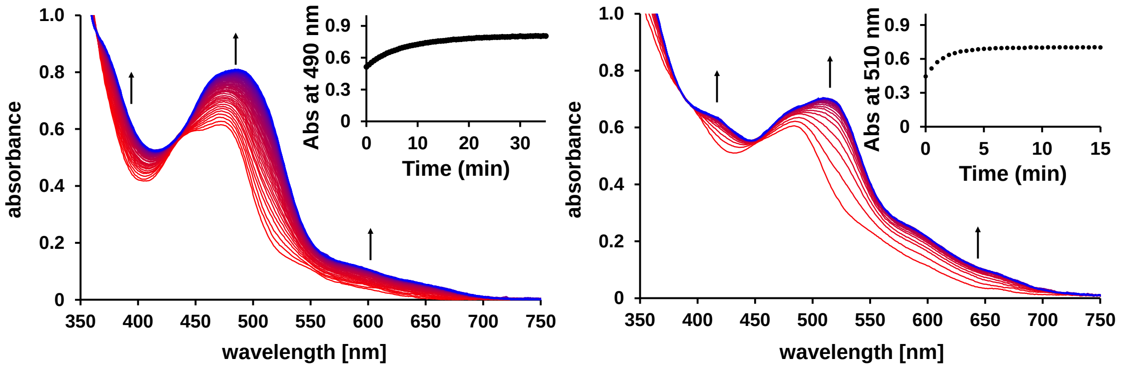

Figure 51. UV/Vis absorption spectra of an aqueous solution of [**2**]$\mathrm{Cl}_2$ (left) and [**4**]$(\mathrm{PF}_6)_2$ (right) upon green light irradiation. Conditions: $T$ = 37 °C, light source: $\lambda = 517$ nm, $\Delta\lambda_{1/2} = 23$ nm, 5.2 mW, photon flux $\Phi_{517} = 5.3\cdot10^{-8}$ and $5.2\cdot10^{-8}$ mol · s$^{-1}$, V = 3 mL, under air atmosphere. Inset: Time evolution of absorbance at wavelength 490 nm for [**2**]$\mathrm{Cl}_2$ and 510 nm for [**4**]$(\mathrm{PF}_6)_2$, colour coding is from red to blue which is the end point.

Upon irradiation, each complex exhibited a bathochromic shift in its absorption maximum, indicative of the release of the thioether ligand to form the corresponding aqua complex.[167, 200-202]

As previously demonstrated and published by *Busemann et al.*,[167] the photosubstitution properties such as reaction quantum yields, are optimal, thereby enabling the agents [**2**]$^{2+}$ and [**4**]$^{2+}$ to be utilized in PACT. The obtained values are comparable to those reported for complexes [**1**]$^{2+}$ and [**3**]$^{2+}$.[8, 167] These similarities allow for the postulation of good photosubstitution agents.

These results confirmed that the alkyne functionalization did not alter the photochemical properties compared to its parent compounds. Before *in vitro* testing, the thermal stability in the cell-cultural medium (OptiMEM complete) (conditions: dark at 37 °C for 24 h) (Figure A 7), showed that the complex remains intact and might be a good PACT candidate.

With these results in hand, the potential PACT candidates were evaluated towards their ability to be (photo)cytotoxic. This is defined as its capacity to become toxic following the application of an external trigger. The following chapter comprises the procedures and the comparison of the respective biological tests.

# 3 *In vitro* Evaluation of PACT Agents

To gain information regarding the PACT agents when utilized within cells, cytotoxicity assays were performed and [**2**]$Cl_2$ and [**4**]$(PF_6)_2$ were evaluated under normoxic conditions (21% $O_2$) in human lung carcinoma (A549) cell line. By the established protocol,[203] complexes were incubated for 24 h in the dark at various concentrations before green light activation (520 nm, 38 J/cm$^2$, 30 min[203]). At the same time, an additional plate equipped with A549 cells and the complexes at the same concentrations were kept in the dark. Then, both plates were further incubated for an additional 48 h[203] before measuring the relative cell proliferation with a sulforhodamine B (SRB) end-point assay. The dose-response curves are illustrated in Figure A 8. The effective concentrations that inhibit 50% cell growth in comparison to the untreated control ($EC_{50}$ values) and the photo indices (PI) (Quotient of $EC_{50,\ light}$ by $EC_{50,\ dark}$) are presented in Table 2.[167] With this information, a high PI value reaches a significant difference in activity between dark and light conditions. Low PI values would explain, that there are only minimal differences in activity between dark and light conditions.

In the absence of light the cytotoxicity of [**2**]$Cl_2$ was found to be comparable to that of its non-functionalized analogue [**1**]$(PF_6)_2$ ($EC_{50}$ = 66 vs. 79 µM), while [**4**]$(PF_6)_2$ was twice as toxic as [**3**]$(PF_6)_2$ ($EC_{50}$ = 29 vs. 62 µM). Upon green light activation, both [**2**]$Cl_2$ and [**4**]$(PF_6)_2$ became more cytotoxic compared to kept in the dark, with similar $EC_{50}$ values ([**2**]$Cl_2$: $EC_{50}$ = 5 µM and [**4**]$(PF_6)_2$: $EC_{50}$ = 7 µM, respectively). It is noteworthy that while both i-Hdiqa (di(isoquinolin-3-yl)amine)-based complexes exhibit a PI value of 4, the alkyne functionalization of the i-biq (3,3'-biisoquinoline) complex led to a threefold increase in PI, raising it from 4 to 12. This indicates that the alkyne group exerts differing effects on the $EC_{50}$ values of the two complexes.

In conclusion, it can be stated that the alkyne functionalization in [**2**]$Cl_2$ and [**4**]$(PF_6)_2$ resulted in enhanced cytotoxicity compared to their non-functionalized counterparts [**1**]$(PF_6)_2$ and [**3**]$(PF_6)_2$ both in the absence of light and after light activation

Table 2. Cytotoxycity ($EC_{50}$ with 95% confidence interval in µM)[a)] and cellular uptake (CU with mean deviation in nmol Ru/mg cell protein)[b)] of [**1**]$(PF_6)_2$ – [**4**] $(PF_6)_2$ in lung cancer cells (A549) under normoxic conditions (21% $O_2$).

| | [**1**](PF6)$_2$ | | [2]$Cl_2$ | | [**3**](PF6)$_2$ | | [**4**](PF6)$_2$ | |
|---|---|---|---|---|---|---|---|---|
| R | H | | CCH | | H | | CCH | |
| $EC_{50,\ \mathrm{dark}}$ | 79.7 | $^{+6.1}_{-5.7}$ | 66.0 | $^{+12.4}_{-9.9}$ | 62.1 | $^{+16.4}_{-13.8}$ | 29.4 | $^{+2.7}_{-2.4}$ |
| $EC_{50,\ \mathrm{light}}$ | 20.6 | $^{+3.0}_{-2.6}$ | 5.3 | $^{+1.4}_{-1.1}$ | 13.8 | $^{+4.3}_{-3.6}$ | 7.0 | $^{+1.5}_{-1.3}$ |
| PI[c)] | 3.9 | | 12.5 | | 4.5 | | 4.2 | |
| CU | 0.32 ± 0.14 | | 0.73 ± 0.12 | | 0.69 ± 0.16 | | 1.19 ± 0.20 | |

a) The (photo)cytotoxicity experiments were performed in biological and technical triplicates; b) Cell uptake upon incubation for 24 h with 30 µM drug. Results are averaged over three independent experiments; c) the photo index (PI) is defined as $EC_{50}$, dark/$EC_{50}$, light.

Checking the $EC_{50}$ values, it is essential to consider the cellular uptake, which is also illustrated in Table 2. The concentration of ruthenium in nmol per mg cell protein was measured by high-resolution continuum source atomic absorption spectrometry (HRCS AAS) after incubating the drug at 25 µM for 24 h in the dark. The results indicate that the alkyne-functionalized complexes [**2**]$Cl_2$ and [**4**]$(PF_6)_2$ are taken up by cells at double the rate of their non-functionalized analogues [**1**]$(PF_6)_2$ and [**3**]$(PF_6)_2$ (Table 2).[8, 167] In the case of [**4**]$(PF_6)_2$, this increased uptake correlated with a halving of the $EC_{50}$ value. The complexes were observed to persist under both dark and light conditions following activation. Similarly, for the other complex [**2**]$Cl_2$ the same phenomenon was observed. Doubling the amount of ruthenium accumulated into the cells before irradiation had little effect on the dark cytotoxicity while comparing after light activation, the $EC_{50}$ value was fourth as high as that of [**1**]$(PF_6)_2$. In conclusion, the functionalized complexes demonstrate a higher cellular uptake, which correlates with enhanced cell toxicity. This is likely attributed to the increased lipophilicity, which may result from the small CCH substituent.

# 4 *In cellulo* Labelling of PACT Agents

Considering these results, further tests that shed light on the mode of action have been performed to clarify the cellular distribution and localization of the molecules. For this purpose, the additional alkyne group on the compound was employed to perform a CuAAC based click reaction, as illustrated in Figure 52. Therefore, CuAAC was performed to click the alkyne on the complex with the azide linked to the fluorophore AlexaFluor™ 488-azide.

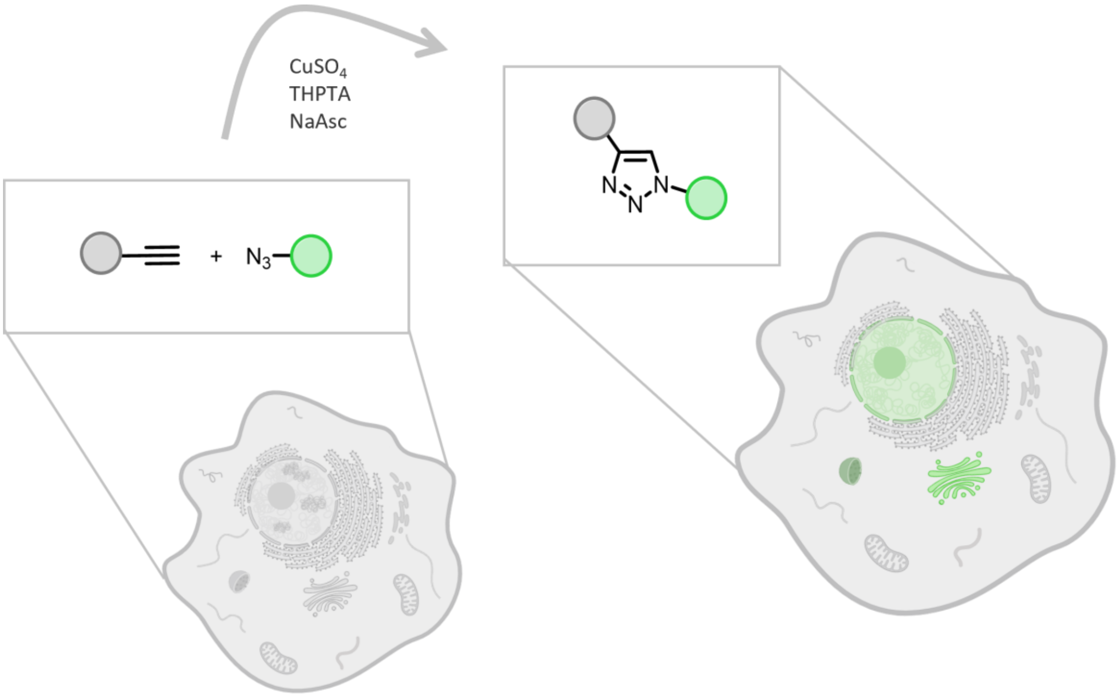

Figure 52. Overview of CuAAC between Ru-complex (grey circle) modified with an alkyne, with an azide that is bound to AlexaFluor™ 488. The reaction gets catalyzed with $CuSO_4$, which is reduced with NaAsc and stabilized with THPTA. After the reaction, on the right side of the image, a triazole is built and the fluorescence becomes visible in the specific targets.

For this objective, the cells were seeded, treated with the complexes [**2**]$Cl_2$ and [**4**]$(PF_6)_2$, incubated at concentrations ranging from 5 to 25 µM, activated by 1 h irradiation with $\lambda$ = 520 nm (76 J/cm$^2$) and 1 h incubation time, and immediately fixed. Then, the cells were labelled in accordance with a modified protocol from *DeRose* and coworkers.[181] Finally, immunofluorescence costaining was used to identify the specific targets of the complexes, with the samples being analyzed *via* confocal microscopy.

Figure 53 displays the images obtained from the confocal microscope when cells were incubated at various concentrations (5, 10, 15, 20, and 25 µM). The focus was on ensuring that the settings on the confocal microscope were optimized for obtaining the most intense fluorescence for the fluorescence pattern outside the nucleus on one side. The images demonstrate that the most notable outcomes for both compounds were observed at a concentration of 25 µM. (Images for compound [**4**]($(PF_6)_2$ Figure 53, [**2**]$Cl_2$ Figure 54).

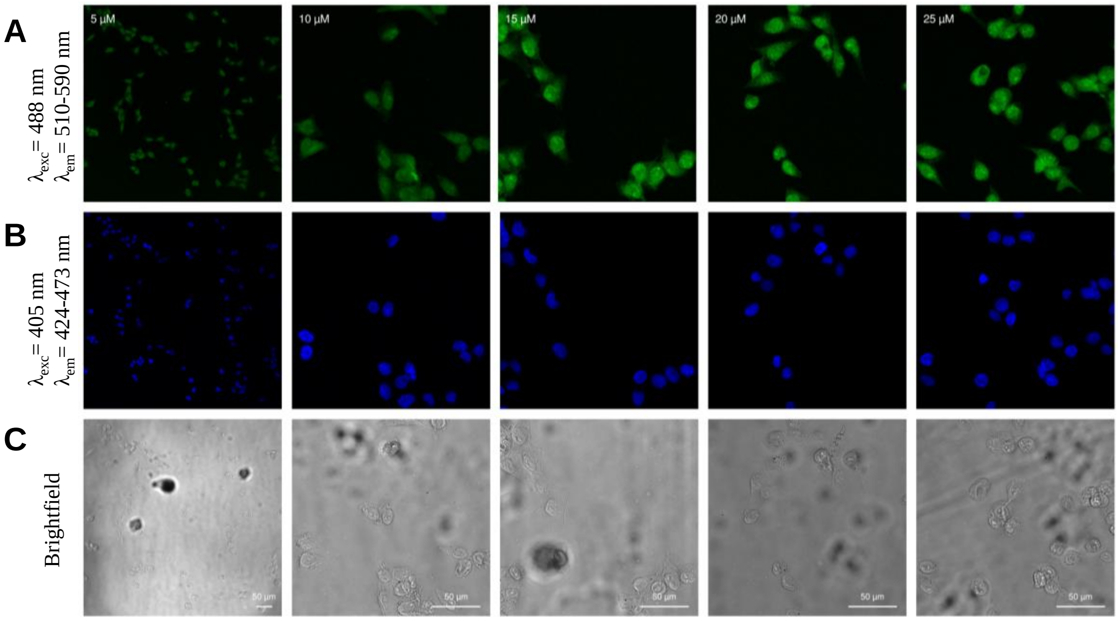

Figure 53. Concentration experiments of [**4**]$(PF_6)_2$ in different concentrations of 5 µM, 10 µM, 15 µM, 20 µM and 25 µM with 1h irradiation with λ = 520 nm (76 $J/cm^2$) with 1 h incubation time. Afterwards, fixation with PFA 4%, permeabilization with 0.5% Triton-X-100 and the CuAAC reaction was performed. Confocal microscopy is used for imaging and the different emission channels are used as follows: A: CuAAC excitation with 488 nm, emission from 510-590 nm. B: Hoechst excitation with 405 nm, emission from 424-473 nm.

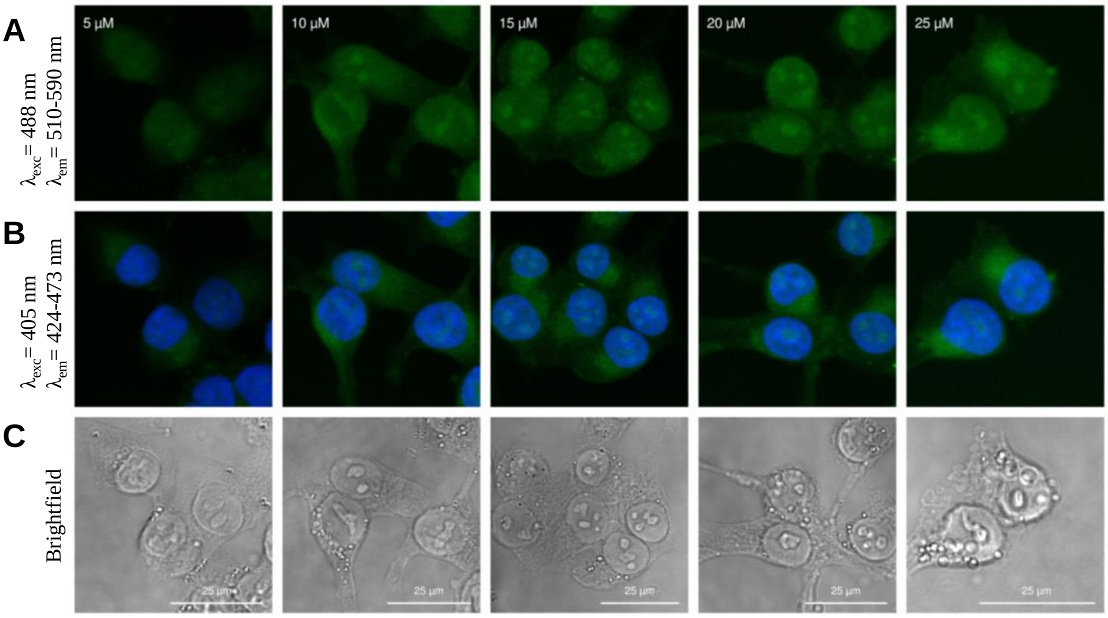

Figure 54. Concentration experiments of [**2**]$Cl_2$ in different concentrations of 5 µM, 10 µM, 15 µM, 20 µM and 25 µM with 1h irradiation with λ = 520 nm (76 J/cm$^2$) with 1 h incubation time. Afterwards, fixation with PFA 4%, permeabilization with 0.5% Triton-X-100 and the CuAAC reaction was performed. Confocal microscopy is used for imaging and the different emission channels are used as follows: A: CuAAC excitation with 488 nm, emission from 510-590 nm. B: Hoechst excitation with 405 nm, emission from 424-473 nm.

Although the best results were observed when 25 µM was administered to the cells, special attention had to be paid to the cytotoxicity of the compounds. In previous experiments, the $EC_{50}$ values were found to be 5 or 7 µM respectively (see Table 2), and the incubation time was reduced from 24 to 1 h after light activation. This step was required to ensure that a comparable amount of cells remained viable to perform the confocal studies. Under these conditions, the cells exhibited signs of stress and could be imaged with early indications of apoptosis, such as blebbing around the cells.

After confirming that the cells remained imageable following activation at 25 µM, the CuAAC setup was tested in the initial cell experiments. Control experiments validated this as a suitable method for visualizing the complexes. In the top row of Figure 55, images A and C, show cells that were not treated with the complex [**4**]$(PF_6)_2$ while images B and D depict treated cells. All four images were exposed to λ = 520 nm for 1 h (76 J/cm$^2$). In images C and D, copper was omitted, and, as expected, no fluorescence was observed under these conditions. Among the four images, Figure 55B displays the strongest fluorescence signal.

The intense green fluorescence is predominantly located outside the nucleus, with much lower intensity is observed within the nucleus. The fluorescence observed in the cytoplasm is mainly concentrated on one side of the nucleus for [**4**]($PF_6$)$_2$. The same results were obtained for [**2**]$Cl_2$ and are presented in the supporting information, alongside the concentration studies in Figure 53 and Figure 54. As expected, the fluorescence intensity in the images is considerably weaker for complex [**2**]$Cl_2$, which may be attributed to a lower cellular uptake compared to complex [**4**]($PF_6$)$_2$. In the absence of the copper catalyst, as shown in Figure 55C and D, no fluorescence signal was detected, indicating minimal background fluorescence. This demonstrates that CuAAC is an effective method, as fluorescence is visible in the presence of Cu(I), but remains absent without it.

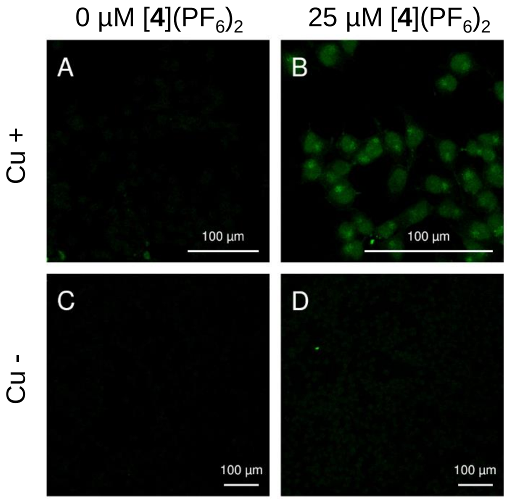

Figure 55: Control experiment for the CuAAC experiment. Cellular imaging of PACT agents modified with an alkyne handle using CuAAC click post-functionalization of a fluorophore in fixed cells. Cells were either not treated (A, C) or treated (B, D) with 25 µM [**4**]($PF_6$)$_2$ and irradiated with $\lambda$ = 520 nm for 1h (76 J/cm$^2$). In C and D copper was omitted (see details in the SI). Scale bar: 100 µm.

These results indicate that the alkyne moiety on the complexes allows [**2**]$Cl_2$ and [**4**]($PF_6$)$_2$ to be labelled with an AlexaFluor$^{TM}$ 488 azide in fixed cells. This approach forms the basis for the identification of intracellular targets and visualization of the trajectory of previously undetectable PACT agents.

In the next step, further investigations were carried out by costaining the different cell compartments in the cytoplasm and the nucleus using indirect immunofluorescence protocols.[204] In addition to localization experiments in which specific organelles were stained, experiments were performed in which the irradiation and incubation times were varied before fixation. The different conditions used in these experiments are listed in Table 3.

Table 3. Different conditions for the imaging experiments, while changing irradiation time from 60 min to 30 min and incubation times from 60 min to 0 min.

| Different conditions | Irradiation Time [min] | Incubation Time [min] |
|---|---|---|
| 1. | 60 | 60 |
| 2. | 60 | 0 |
| 3. | 30 | 60 |

First, the specific targets of the complexes will be identified and quantified through immunofluorescence experiments. The next section will examine the movement of the complex under different conditions to determine whether it relocates to a different organelle depending on irradiation or incubation time. This analysis will distinguish between two main cellular regions: the nucleus and the cytoplasm of the cell.

## 4.1 Costaining Experiments

To explore potential targets for comparison in antibody costaining experiments, hydrophobic organelles such as mitochondria, the endoplasmic reticulum (ER), lysosomes, and the Golgi apparatus were evaluated for costaining with antibodies. The Golgi apparatus, which is crucial for intracellular trafficking, is responsible for processing and packaging proteins that are subsequently transported to lysosomes. Within the lysosomes, these proteins play an essential role in degrading and recycling of cellular components.[205] The Golgi apparatus has previously been identified as a potential target for other Ru-polypyridyl complexes.[206-207] This close connection between the Golgi apparatus and the lysosomes is crucial for normal cellular metabolism and the maintenance of cellular functions. Accordingly, these two organelles were selected for detailed analysis in combination in detail.

Generally, the cells incubated with the respective ruthenium-based compound and labelled with CuAAC, provided the basis for further labelling of the different organelles. To minimize non-specific binding of proteins or antibodies, bovine serum albumin (BSA) was added as a blocking agent to enhance the specificity of antibody-antigen interactions. The primary antibody (prim AB), which targets a specific organelle, was then applied to the fixed and blocked cells. Before proceeding with the secondary antibody (sec AB), it is essential to perform a thorough washing step, to remove any unbound antibodies. The sec AB, which is conjugated with a fluorophore, was then applied to visualise the organelles using confocal microscopy.

The cell nucleus was stained with Hoechst dye to reveal nuclear structures. Three different lasers and corresponding emission channels were used for imaging. In all the images obtained from the confocal microscopy experiments presented in this chapter, the same lasers and channels were consistently applied.

Table 4. Different excitation and emission channel wavelengths for the three dyes from Hoechst for the nucleus, AlexaFluor 488 for the ruthenium-complex and the secondary AB for ER, mitochondria, Golgi apparatus and lysosomes.

| | $\lambda_{exc}$ [nm] | $\lambda_{em}$ [nm] |
|---|---|---|
| Hoechst | 405 | 424-473 |
| AlexaFluor™ 488 | 488 | 510-590 |
| Secondary AB | 638 | 670-720 |

Each experiment included a control plate that was kept in the dark and a plate that was exposed to green light (520 nm). The samples were irradiated for 30 min (38 J/cm²) and incubated for an additional 60 min. The images are organized as follows: a) the fluorescence of [**2**]$Cl_2$ / [**4**]$(PF_6)_2$ post-labeled with AlexaFluor$^{TM}$ 488 azide was measured in the green channel, and b) the specific organelle costaining was measured in the red channel. In Figure 56, Hoechst dye is used as a marker for nuclear staining, exhibiting an overlap between the green and blue emission channels. Images on the left represent the unactivated, so-called "dark" sample, while the images on the right depicts the activated sample. Similar to the fluorescence signal in Figure 55 the green fluorescence in Figure 56 represents a) the complex while b) red/orange fluorescence displays the respective stained organelle (ER or mitochondria) and c) the blue fluorescence of the nucleus of the cell.

As seen in Figure 56b), no overlap of the red fluorescence in the images of the ER and mitochondria was observed, therefore the ER and mitochondria can be excluded as targets for compound [**4**]($PF_6$)$_2$.

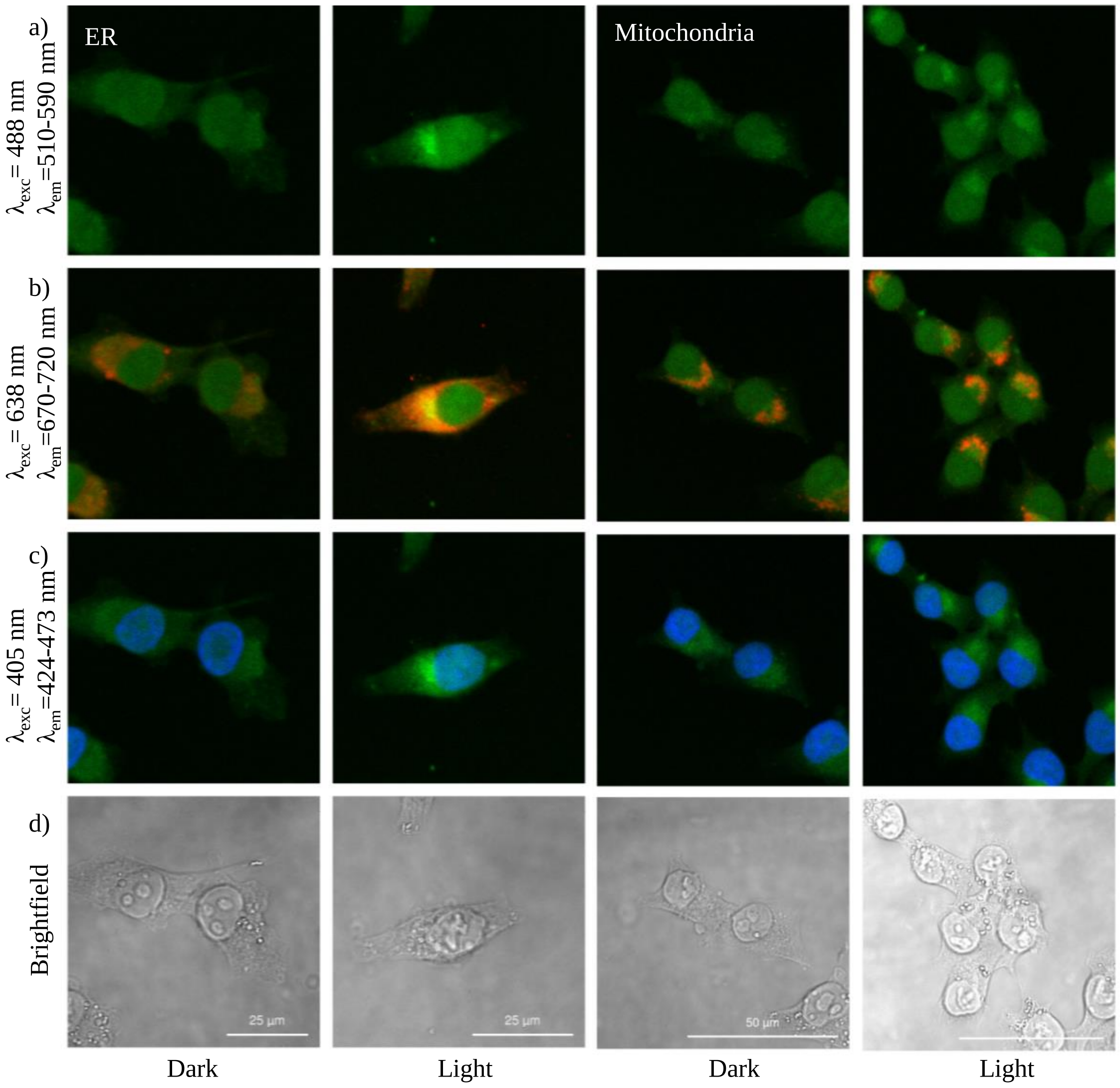

Figure 56. Costaining of ER (left) and mitochondria (right) of A549 cells treated with compound [**4**]($PF_6$)$_2$ for 24 h and activated by green light (right) for 30 min ($\lambda$ = 520 nm, 38 J/cm$^2$) or kept in the dark (left) and incubated for 1 h. From top to bottom three fluorescence channels are shown: a) $\lambda_{exc}$ = 488 nm, $\lambda_{em}$ = 520-590 nm, (Cu-click + [**4**]($PF_6$)$_2$), b) $\lambda_{exc}$ = 638 nm and $\lambda_{em}$ = 670-720 nm (costaining of the organelle), c) $\lambda_{exc}$ = 405 nm and $\lambda_{em}$ = 424-473 nm (Hoechst). The last row shows brightfield images of the cells. In b), the overlap between green fluorescence from the clicked Ru compound and the red fluorescence of the organelle results in orange colour.

The lysosomes and Golgi apparatus presented a more complex scenario in comparison. For lysosomal costaining, an antibody targeting lysosomal-associated membrane protein 1 (LAMP1), a commonly used marker for lysosome localization, was utilized.[208] LAMP1 is located on lysosomal membranes, and is essential for cellular digestion and waste removal. Its use in costaining provides valuable insights into the function and dynamics of biomolecules within the cell. For the Golgi apparatus, the Golgi-matrix protein (GM130) was employed as a marker, as it is a peripheral membrane protein specifically localized to the cis-Golgi network. Like LAMP1, GM130 is a reliable marker for identifying the structure and organization of the Golgi apparatus.[209-210]

As previously mentioned, in row a), the green fluorescence in the images is confined to one side of the nucleus within the cytoplasm. In the emission channel b) which shows the costaining of the Golgi apparatus and lysosomes, the organelles display specific fluorescence in the same location as [**4**]($(PF_6)_2$. This overlap of red and green emission results in orange fluorescent dots Figure 57b). Additionally, the green fluorescence is not limited to the cytoplasm but is also present in the nucleus, as shown in row c) of Figure 57.

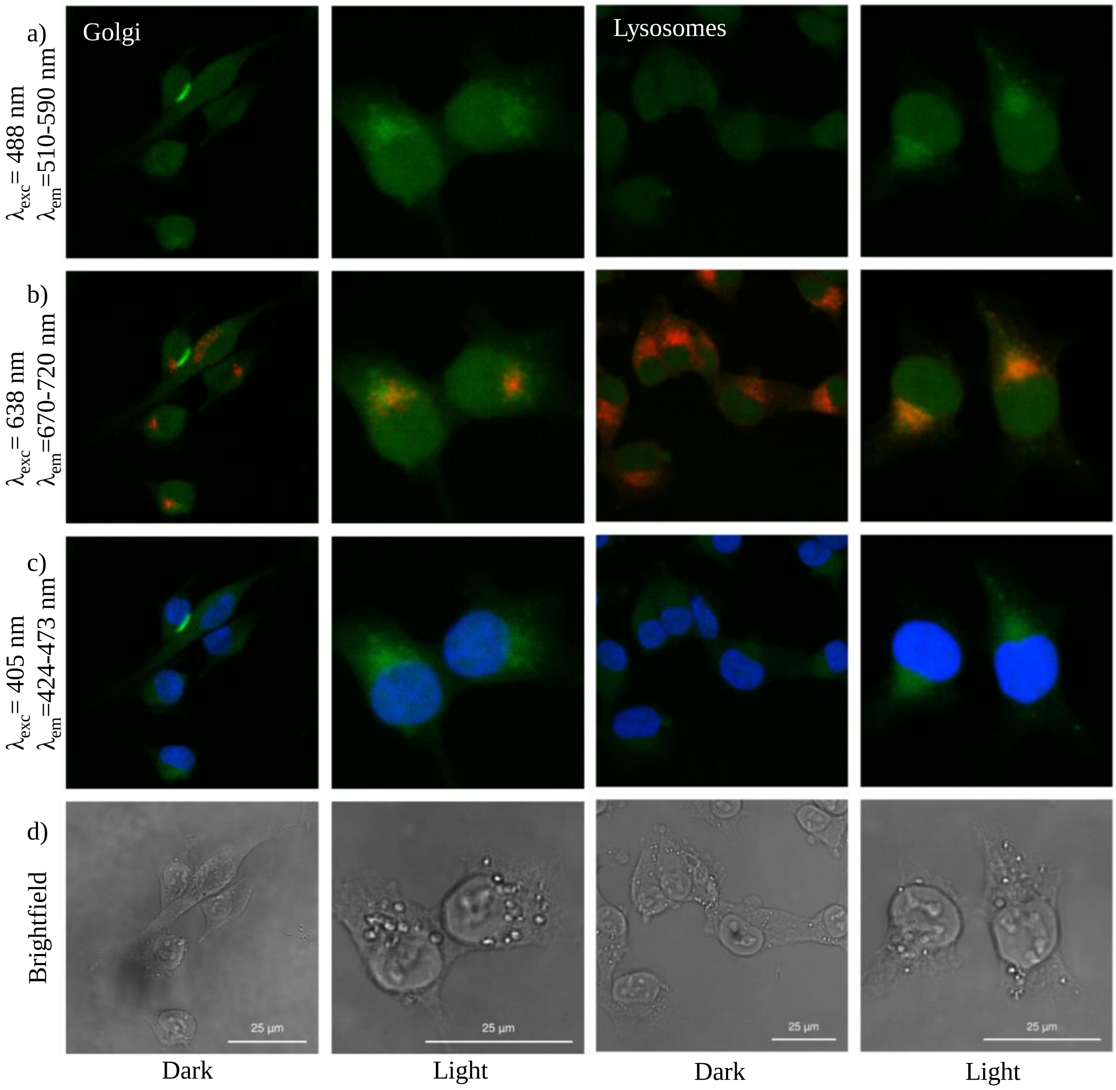

Figure 57. Costaining of lysosomes (left) and Golgi apparatus (right) of A549 cells treated with compound [**4**]($(PF_6)_2$) for 24 h and activated by green light (right) for 30 min ($\lambda$ = 520 nm, 38 J/cm$^2$) or kept in the dark (left) and incubated for 1 h. From top to bottom three fluorescence channels are shown: a) $\lambda_{exc}$= 488 nm, $\lambda_{em}$ = 520-590 nm, (Cu-click + [**4**]($(PF_6)_2$)), b) $\lambda_{exc}$ = 638 nm and $\lambda_{em}$ = 670-720 nm (costaining of the organelle), c) $\lambda_{exc}$ = 405 nm and $\lambda_{em}$ = 424-473 nm (Hoechst). The last row shows brightfield images of the cells. In b), the overlap between green fluorescence from the clicked Ru compound and the red fluorescence of the organelle results in an orange colour.

The intensity of the AlexaFluor™ 488 fluorescence increased (Figure 57a) upon light activation of [**4**]($(PF_6)_2$) indicating an increased presence of the complex. These data align with the results obtained from the cellular uptake studies. It appears that the aqua-Ru complex is more likely to pass through the cell membrane than the non-activated prodrug. Similar results have been observed for the unalkynated complexes [**1**]($(PF_6)_2$) and [**3**]($(PF_6)_2$) in SH-SY5Y cells.[211] Additionally, the costaining experiments indicate that the PACT agents accumulate primarily in the lysosomes and Golgi apparatus, with a small amount also present in the nucleus of the cell. Complex [**2**]$Cl_2$ was investigated using the same conditions as for [**4**]$(PF_6)_2$. Herein, a less intensive fluorescence signal was monitored (Figure 58) due to the lower cellular uptake of the complex (see cellular uptake studies with AAS).

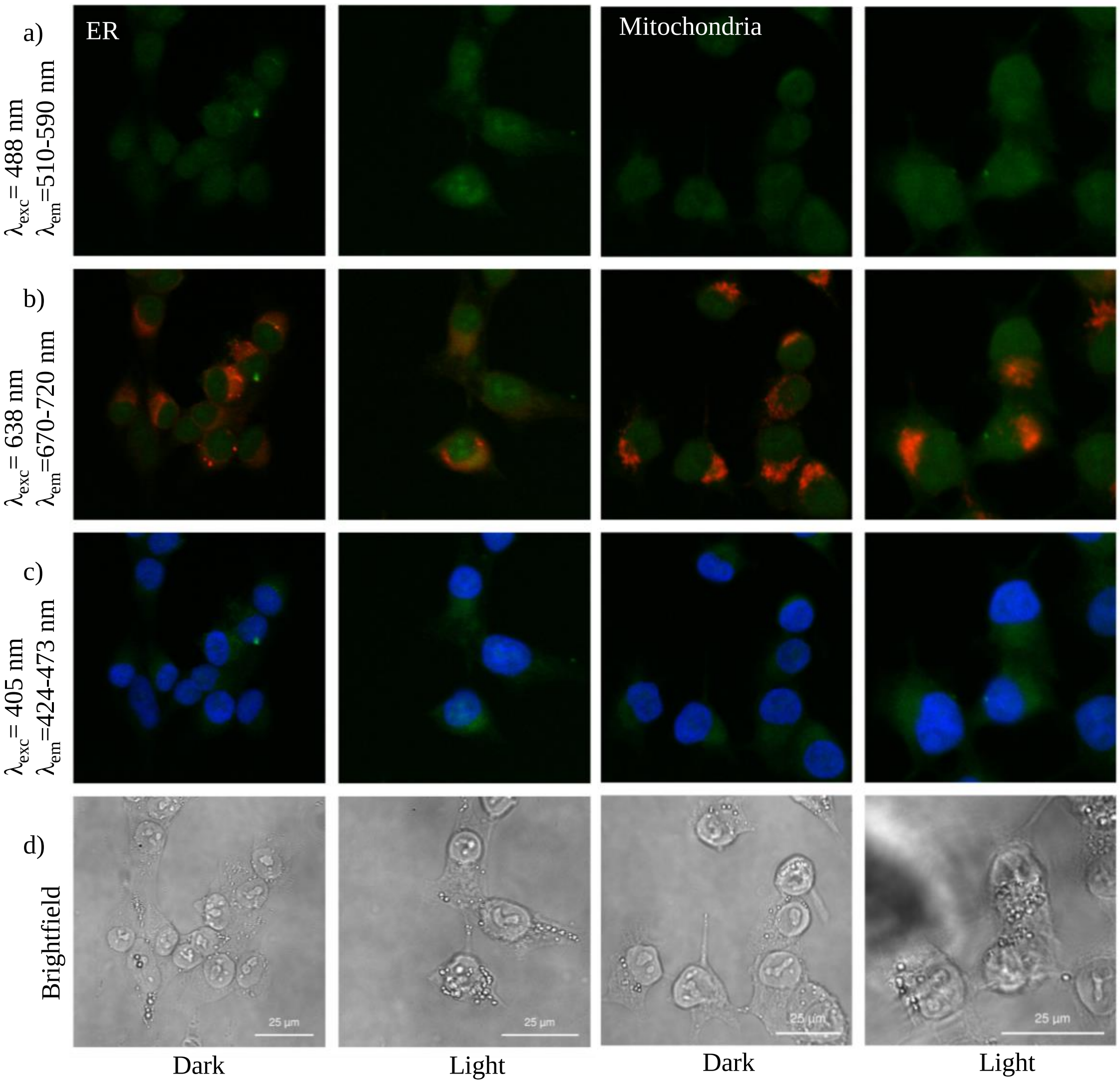

Figure 58. Costaining of ER (left) and mitochondria (right) of A549 cells treated with compound [**2**]$Cl_2$ for 24 h and activated by green light (right) for 30 min ($\lambda$ = 520 nm, 38 J/cm$^2$) or kept in the dark (left) and incubated for 1 h. From top to bottom three fluorescence channelss are shown: a) $\lambda_{exc}$ = 488 nm, $\lambda_{em}$ = 520-590 nm, (Cu-click + [**2**]$Cl_2$), b) $\lambda_{exc}$ = 638 nm and $\lambda_{em}$ = 670-720 nm (costaining of the organelle), c) $\lambda_{exc}$ = 405 nm and $\lambda_{em}$ = 424-473 nm (Hoechst). The last row shows bright-field images of the cells. In b), the overlap between green fluorescence from the clicked Ru-compound and the red fluorescence of the organelle results in orange colour.

Despite the weak signal, colocalization of the various organelles could be recognized. Different to [**4**]$(PF_6)_2$, complex [**2**]$Cl_2$ appears to overlap with the mitochondrial costaining (Figure 58b, light row). No overlap with the ER was observed.

While conducting the experiments under the specified conditions of 30 min of irradiation and 60 min of incubation prior to cell fixation, the costaining for the lysosomes and the Golgi apparatus is illustrated in Figure 59. As demonstrated for complex [**4**]($PF_6$)$_2$, both the Golgi apparatus and the lysosomes overlap with the fluorescence in emission channel a).

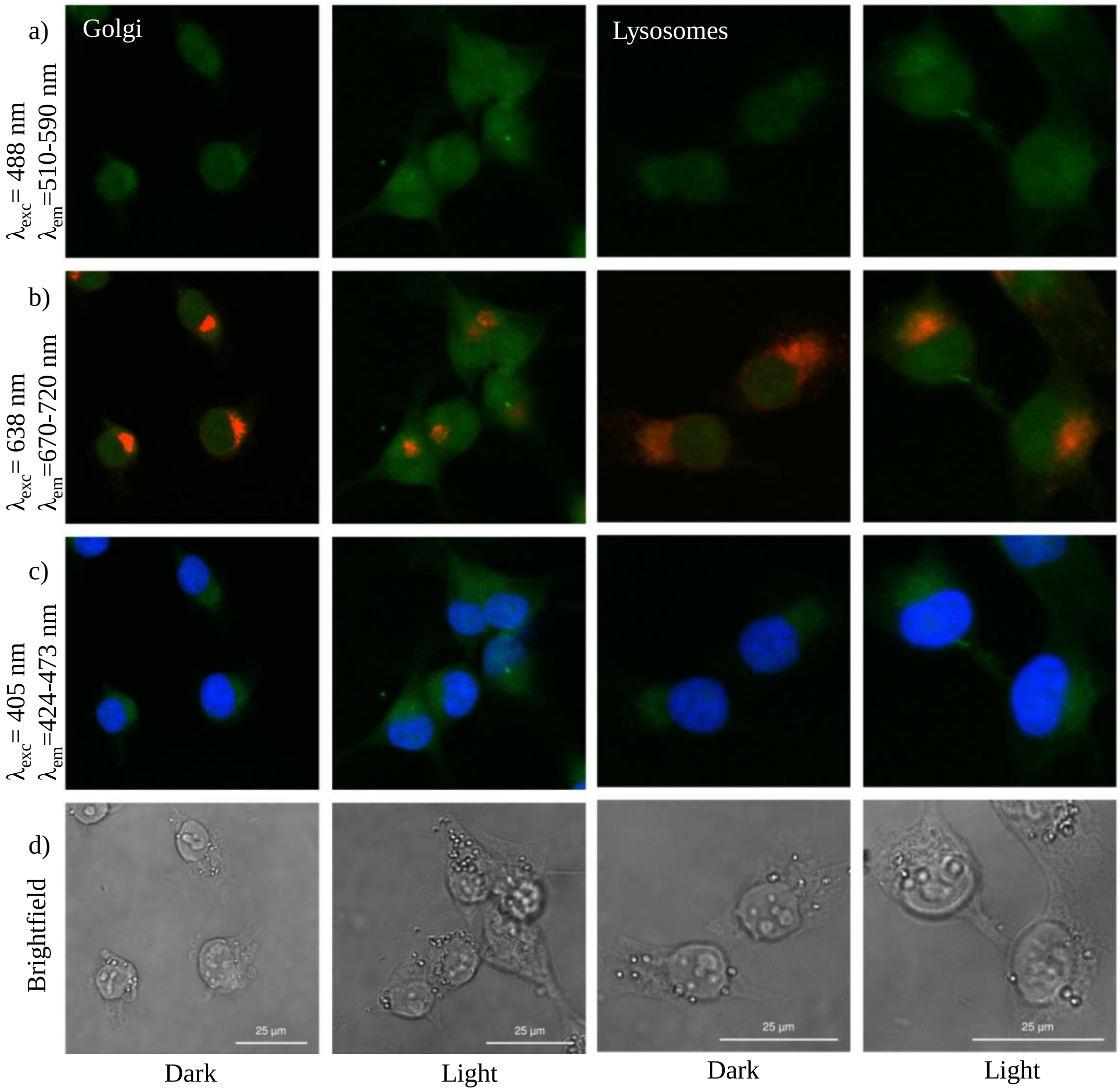

Figure 59. Costaining of lysosomes (left) and Golgi apparatus (right) of A549 cells treated with compound [**2**]$Cl_2$ for 24 h and activated by green light (right) for 30 min ($\lambda$ = 520 nm, 38 J/cm$^2$) or kept in the dark (left) and incubated for 1 h. From top to bottom three fluorescence channels are shown: a) $\lambda_{exc}$= 488 nm, $\lambda_{em}$= 520-590 nm, (Cu-click + [**2**]$Cl_2$), b) $\lambda_{exc}$ = 638 nm and $\lambda_{em}$ = 670-720 nm (costaining of the organelle), c) $\lambda_{exc}$ = 405 nm and $\lambda_{em}$ = 424-473 nm (Hoechst). The last row shows brightfield images of the cells. In b), the overlap between green fluorescence from the clicked Ru-compound and the red fluorescence of the organelle results in orange colour.

Based on the obtained information, it can be concluded that using costaining immunofluorescence methods, complexes [**2**]$Cl_2$ and [**4**]$(PF_6)_2$ are present within the cytoplasm and nucleus. In both complexes, the target locations were limited to the Golgi apparatus, lysosomes, and nucleus, while complex [**2**]$Cl_2$, also involved the mitochondria. To further confirm the fluorescence observed in the images, the next chapter will focus on the quantification of the images.

## 4.2 Image Quantification

After identifying the presence of certain compartments within the cell, further experiments were conducted to gain a deeper understanding of the intracellular movement of the PACT agents. For this purpose, a series of experiments were performed, varying the light exposures and incubation times. First, a comparison was made between a 60 min irradiation period with no incubation time, followed by immediate fixation and imaging after light activation, and a control group that underwent no irradiation and was incubated for 60 min. Second, the irradiation time was held constant, while the incubation time was extended from 30 to 60 min. Third, the irradiation time was reduced to 30 min instead of 60 min, while the incubation time after activation remained 60 min.

This chapter tracked the intracellular movement of the PACT agents. Accordingly, cell experiments were conducted, and the resulting images were quantified. Unlike in previous experiments the use of Pearson's coefficient[212] was not suitable for the quantification due to the widespread fluorescence after cellular uptake overlapping with organelle-targeted emission. This overlap produced excessively high Pearson coefficients, potentially leading to false positives for organelle localization. Hence, only the quantified analysis is presented in this chapter and the images can be found in the appendix (Figure A 11-Figure A 16).

The problem was addressed using an alternative approach, specifically the CellProfiler program[213] in collaboration with *Sam Davidse* from the Leiden University (LACDR). This method involves segmenting cells into nuclear and cytoplasmic compartments. The AlexaFluor$^{TM}$ 488 signal was quantified in the two distinct compartments, and a ratio between the cytoplasmic and nuclear signals was calculated. This single-cell approach enables the quantification of the localization of the tagged complex through costaining of various organelles. Tracking the overlap between high-intensity regions allows for an assessment of the extent to which the complex of interest colocalizes with these organelles. Figure 60A illustrates the fluorescence ratio between cytoplasmic and nuclear signals when the incubation time was set to 60 min followed by 30- or 60-min irradiation, respectively (38 J/cm² vs. 72 J/cm²). With an irradiation time of 30 min, the majority of the fluorescence is observed in the cell nucleus. After an additional 30 min of irradiation, there is a clear shift in the fluorescence of the complex towards the cytoplasm.

These ratios indicate a reduction in emission within the nucleus as the irradiation time is extended from 30 to 60 min. Based on these observations, it appears that the complex relocates to different cellular compartments as the irradiation time is prolonged. Reducing the incubation time from 60 min to 0 min, showed no significant change in the fluorescence of [**4**]($PF_6$)$_2$ (shown in Figure A 9). Nevertheless, reducing the irradiation time to 30 min altered the fluorescence pattern in the cell compared to 60 min of irradiation.

In Figure 60B and Figure 60C a single-cell approach is presented, to gain further insights into the colocalization of the complexes through costaining experiments that dye various organelles within cells. As previously stated, the Pearson correlation coefficient was not applicable for these experiments. Thus, the overlap of the organelle emission channel with more than 50% of the emission channel of the complex at $\lambda_{em}$ = 520-590 nm was compared. The AlexaFluor™ 488 channel demonstrated the most significant overlap with the Golgi apparatus and lysosomes which is in accordance with our previous results from section 4.1

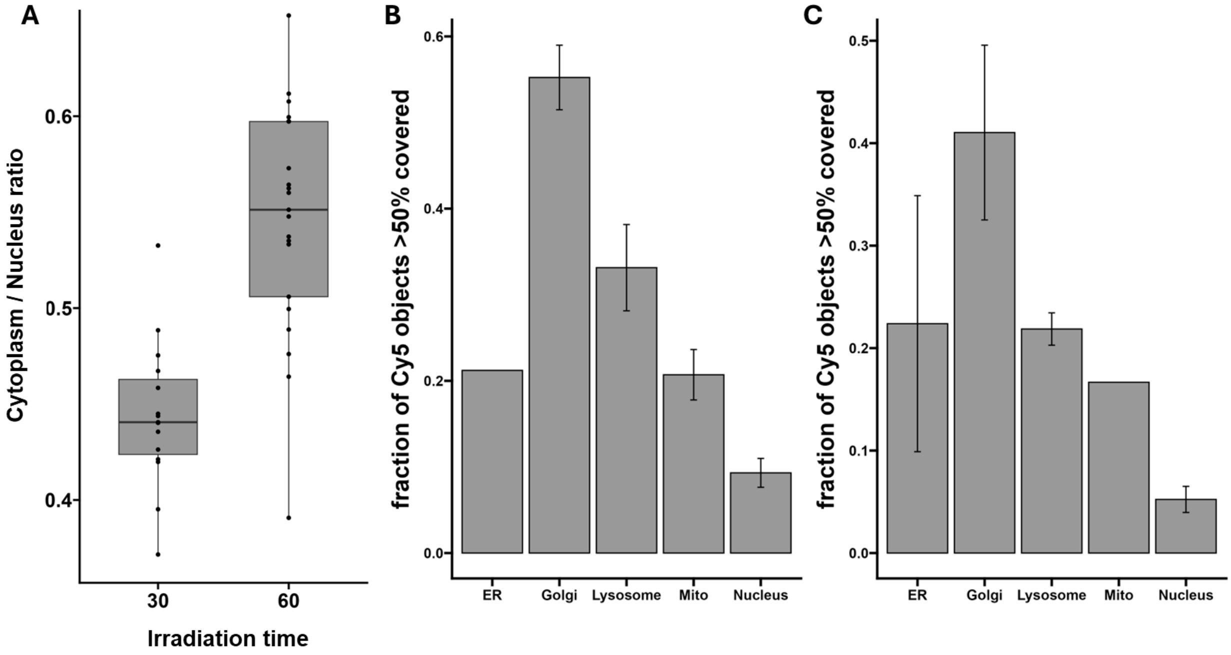

Figure 60. A: Quantified fluorescence ratio between the cytoplasmic and nuclear signals while using [**4**]$(PF_6)_2$ after 60 min of incubation time after the irradiation times of 30 or 60 min. B + C: localization of the post-labelled complex through staining of various organelles. B with 30 min irradiation, 60 min incubation and C with 60 min irradiation and 60 min incubation.

Graphs for the colocalizing experiments for [**2**]$Cl_2$ are provided in Figure A 10. The images used for the image quantification are shown in the appendix Figure A 11-Figure A 16.

## 4.3 DNA Interaction Studies with pUC 19

Given the confirmed presence of the complexes in the nucleus, DNA-binding studies were performed in collaboration with *Dr. Regeni* from the *Bonnet* working group, using a protocol that is used in the group, to assess the DNA as potential target as well as their ability to induce DNA cleavage upon irradiation.[214-215] The pUC19 plasmid DNA was incubated with increasing concentrations of the ruthenium complexes, then either exposed to light or kept in the dark. The binding/cleaving ability was futher analyzed using gel electrophoresis. The complex concentrations ranged from 0.25% to 11% in the whole suspension. It was hypothesized that higher complex concentrations would cause a shift in DNA band migration, with bands moving towards approximately 3000 base pairs (bp), indicative of DNA unwinding due to complex binding. A migration shift from 2000 bp to 3000 bp was observed for both complexes at a concentration of 1.25% (Figure 61). These results suggest that the complexes interact with DNA, potentially explaining the nuclear fluorescence observed in cells, where DNA is localized.

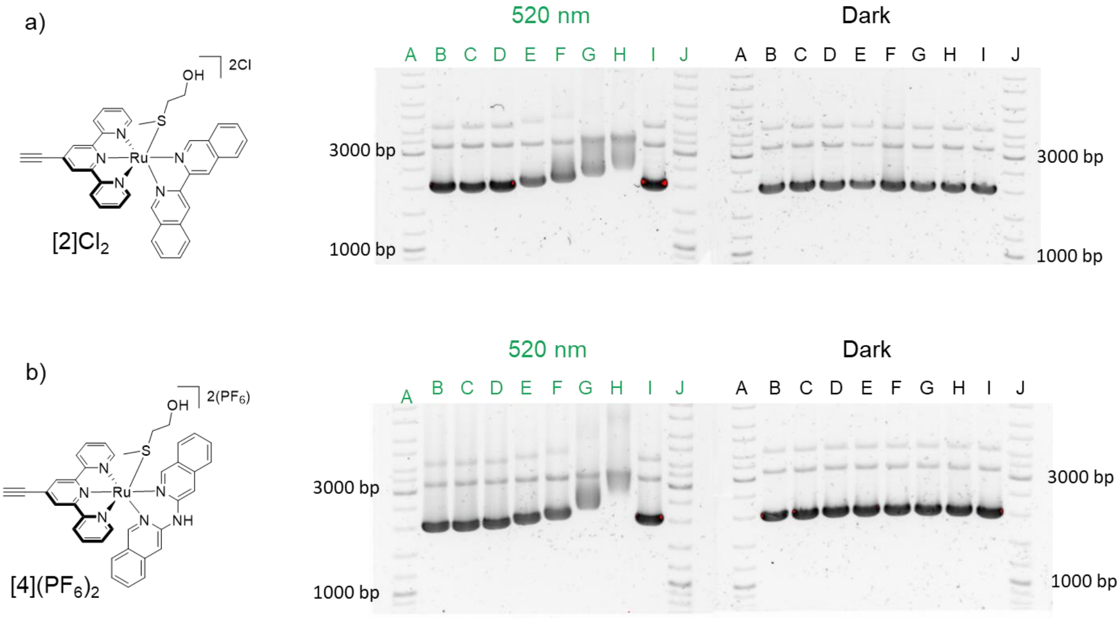

Figure 61. Agarose gel showing the difference of binding of a) [**2**]Cl$_2$ and b) [**4**](PF$_6$)$_2$ to pUC19 upon light irradiation (green lables, 520 nm) and in the dark (black lables, Dark). Sample composition: A λ MW marker, B cisplatin, C DNA control, D 400:1 BP:MC, E 400:5 BP:MC, F 400:10 BP:MC, G 400:25 BP:MC, H 400:50 BP:MC, I DMSO control, J λ MW marker.

# 5 Conclusion and Outlook

This chapter discusses two novel ruthenium-based PACT agents modified with alkyne groups, enabling their traceability through bioorthogonal click chemistry and providing an excellent example of this technique's application. The photosubstitutable ligand serves as a non-toxic protective group, while the ruthenium center contributes to cytotoxicity. The alkyne group, as the reactive site, enables post-treatment with AlexaFluor™ 488-azide for use in CuAAC.

Despite the addition of the small alkyne functional group, the X-ray structure and photosubstitution properties of the complexes remained largely unchanged compared to their unfunctionalized counterparts. This finding indicates that the free alkyne moiety is suitable for minimal functionalization in this class of complexes. The alkyne-functionalized complexes allowed for visualization of light-dependent activation; the non-activated prodrug showed limited cellular membrane penetration and was removed before imaging. Using CuAAC for post-treatment enabled visualization of these otherwise non-emissive compounds. Immunofluorescence analysis revealed the localization of the complexes in cancer cells across five organelles: the endoplasmic reticulum (ER), mitochondria, lysosomes, the Golgi apparatus, and the nucleus. The compounds primarily accumulated in the Golgi apparatus and lysosomes, with a slight fluorescence increase noted in the nucleus. Subsequent pUC19 DNA experiments confirmed interactions between the PACT agents and DNA, suggesting that the action mechanism for these ruthenium-based PACT agents may involve multiple target sites within the nucleus, Golgi apparatus, and lysosomes.

Given the limitations of *in vitro* experiments compared to living organisms, it is essential to develop an alternative system for monitoring DNA replication while treating cells with chemotherapeutic agents. To address this, the subsequent chapter employs a dual labelling approach, allowing for the determination of the duration of DNA replication over a specified time interval.

# VI. Dual Labelling: CuAAC Labelling of PACT Agents and Metabolic Labelling of Newly Built DNA

The initial challenge of visualizing the PACT agents was addressed in the previous chapter by modifying the PACT agents and subsequently employing CuAAC in fixed cells. The target organelles were then identified using the well-established technique of immunostaining.

For scientists, *in vitro* experiments, such as the DNA intercalation assay with pUC19, often prove to be insufficient and difficult to interpret, when extrapolated to *in cellulo* experiments. While these results provide initial insights and may support existing hypotheses, claims of DNA intercalation remain speculative without further validation in a cellular context. Additional experiments, such as extended gel electrophoresis or the use of ethidium bromide as a DNA intercalating dye, could be employed to stain DNA in cells. However, ethidium bromide only confirms intercalation if the chemotherapeutic agent competes for the same binding site, resulting in a decrease in fluorescence.

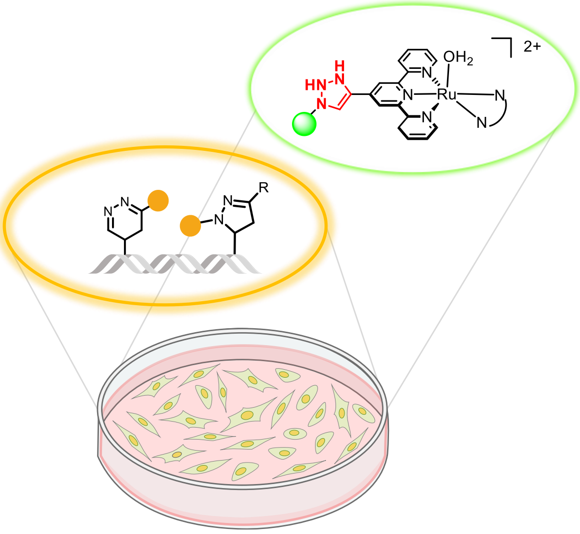

Figure 62. Combination of two bioorthogonal reactions. One is labelling the PACT agent (from the previous chapter), the other bioorthogonal reaction is labelling the metabolically incorporated modified nucleoside with IEDDA or photoclick reaction.

Furthermore, this approach labels all cellular DNA, complicating the interpretation of specific molecular interactions.

To address these challenges, the final chapter of this work aims to selectively label newly replicated DNA formed during the treatment or incubation period with PACT agents. A novel dual-labelling strategy, illustrated in Figure 62, is employed to achieve this. This method involves introducing a modified nucleoside into cells at the moment the chemotherapeutic agent is activated. As the cells attempt replication, they incorporate the modified nucleotide into their DNA, although replication may be disrupted at specific stages. In this approach, the CuAAC reaction is combined with another bioorthogonal reaction targeting the metabolically incorporated nucleoside. This dual-labelling strategy seeks to identify the critical time window during which DNA synthesis is impeded, providing insights into the disruptions caused by the chemotherapeutic agent.

# 1 Photoclick vs. IEDDA

In general, both the photoclick reaction and IEDDA can be combined with CuAAC for dual labelling applications. Photoclick chemistry, in particular, offers considerable potential for dual labelling, as it does not react with primary alkynes, while CuAAC remains unreactive toward alkenes, such as VdU (**20**). Additionally, the photoclick reaction requires an external trigger, allowing for precise control over the reaction. Theoretically, orthogonality should be preserved in both combinations, enabling selective and independent labelling of distinct biomolecules within the same cell, as illustrated in Figure 63.

When selecting specific click reactions, it is crucial to consider additional complexities, such as spatiotemporal control and the required fixation method. In the previous chapter, the CuAAC labelling of PACT agents utilized a fixation protocol without HCl denaturation, which involved fixation with 4% paraformaldehyde (PFA), permeabilization with 0.5% Triton-X-100, and thorough washing steps with water. In contrast, the photoclick reaction described in chapter III necessitates significantly more steps, including $NH_4Cl$ and glycine neutralization, HCl denaturation, washing, and imaging in MeCN. It is essential to evaluate whether these additional steps are necessary to achieve the desired outcome or if an alternative labelling approach could be employed.

The photoclick reaction using tetrazoles **1-6**, synthesized earlier in this work, did not yield conclusive results. This may be attributed to issues with the PACT agents in MeCN and the challenges of combining two photoactivatable methods. To address the problem outlined in the introduction, the IEDDA reaction, which employs two-factor tetrazines (discussed in section II.1.2), presents a relevant alternative for labelling newly synthesized DNA. As illustrated in Figure 63, this approach offers a potentially simpler and more efficient strategy. A careful assessment is necessary to determine the feasibility of combining these methods for the specific research objectives.

At the point of DNA labelling in the experiment, the cells are fixed, effectively halting all biological processes. In the experiment described in the previous chapter, the critical period of interest spans from the activation of the Ru compounds to the fixation of the cells. During this timeframe, all cellular processes must proceed with precise spatial and temporal control. However, once fixation occurs, the cells are no longer alive, and time point is effectively 'frozen'. This allows the incorporated nucleoside to be labelled by adding tetrazine without the need for an additional trigger, as the fixation process preserves the cells, removing any further temporal constraints for the labelling.

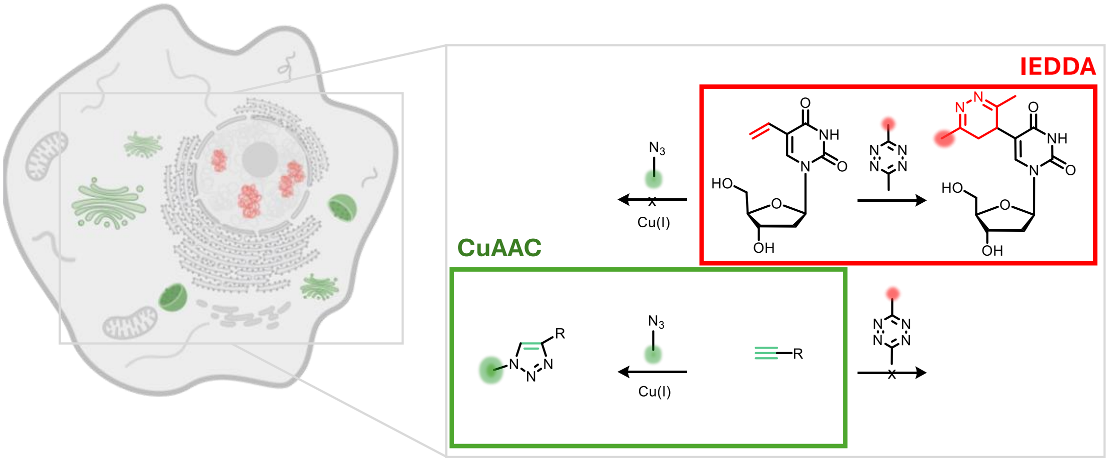

Figure 63. Examplary overview over dual labelling while using IEDDA and CuAAC. CuAAC (in green) can be used to label the Ru-complex as PACT agent and IEDDA (red) to label the incubated VdU (**20**) in the newly replicated DNA of the cell.

# 2 *In cellulo* Experiments

In general, *in cellulo* experiments were initiated, building upon the extensive focus on CuAAC labelling of the PACT agent in the previous chapter. For the IEDDA experiments, a protocol established by the *Wagenknecht* lab was employed, as previously used within the group.[9, 84] In the experiments described in this chapter, tetrazine **I** and the PACT agent [**4**]($PF_6$)$_2$ were utilized, as shown in Figure 64.

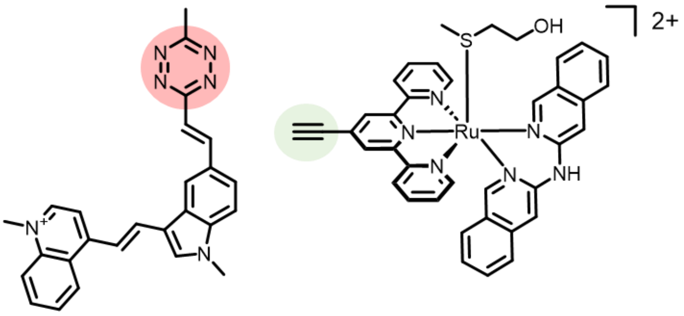

**I**

[**4**]($PF_6$)$_2$

Figure 64. Used compounds for IEDDA: **I** (c = 1 µM) and for PACT/CuAAC: [**4**]($PF_6$)$_2$ (c = 5 and 10 µM).

The A549 lung carcinoma cell line was chosen for these experiments because it has been extensively tested with PACT reagents and demonstrated the comparable performance of the IEDDA method in A549 cells. The cell-based experiments were designed to optimize reagent concentrations, assess orthogonality, and monitor the timing of cell fixation to determine the precise timeframe during which DNA replication remains active and when it is stopped.

## 2.1 Orthogonality

To establish a basis for the experiments and to determine the feasibility of labelling, the previously used concentration of chemotherapeutic agents was employed. The modified nucleoside **20** was added 24 h after the cells were incubated in an 18-well µ-slide (*IBIDI*), alongside the PACT agents.

The complexes were activated after an additional 24 h, and the cells were fixed 1 h after the conclusion of the light activation. Subsequently, two possible approaches could be taken for the continuation of the experiments: the CuAAC reaction could be performed first, followed by the IEDDA reaction, or the order could be reversed. Theoretically, both methods should yield comparable results. However, it is important to note that the CuAAC protocol involves extensive washing steps, whereas the IEDDA protocol, as outlined by *Wagenknecht et al*., requires only a 6 h incubation with tetrazine **I** followed by Hoechst staining for nuclear costaining.[9, 72, 134]

For the following cell images, the microscope settings, specifically the excitation wavelength ($\lambda_{exc}$) and emission channel wavelength ($\lambda_{em}$), were kept constant, as described in detail in section VIII.6.9. The complex was exposed to a 520 nm LED irradiation for 30 min (36 J/cm$^2$)in each experiment.

In Figure 65, rows A and B depict the experiment in which CuAAC was performed first, followed by IEDDA, while rows C and D represent the reverse order. In rows A and C of column 1, no fluorescence is observed, which aligns with the expectations; the complex is not activated by light, and therefore, it is not taken up by the cells and cannot bind to a specific target.

Conversely, in rows C and D of column 1, green fluorescence is visible, indicating that the complex has been activated and successfully bound to the target. Column 2 displays red fluorescence in all rows, as expected, due to the intense fluorescence of the metabolically incorporated nucleoside **20** after more than 12 h of incubation, resulting in a stained nucleus. Notably, there is no significant difference in fluorescence intensity between rows B and D in both the CuAAC and IEDDA columns, demonstrating that the order of the reactions does not influence the outcomes.

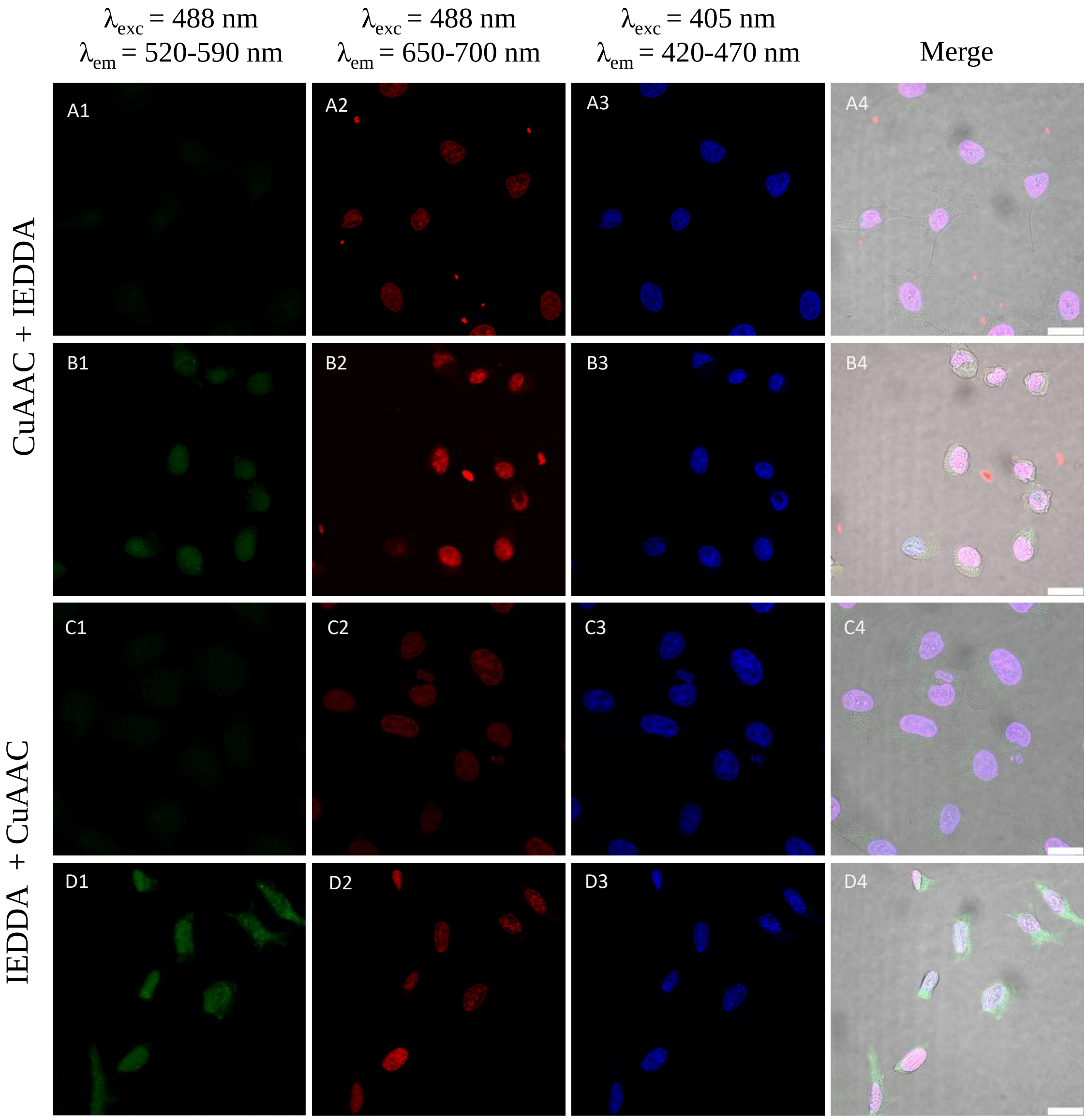

Figure 65. Dual Labelling overview for the orthogonality of CuAAC and IEDDA.; all rows were treated with VdU (**20**) (250 µM) and PACT agent [**4**]($(PF_6)_2$) (25 µM); A and B were treated with CuAAC before IEDDA and C and D *vice versa*.; row A and C were not activated with light, B and C were activated. Column 1 is the emission channel for the CuAAC reaction, column 2 for the IEDDA, column 3 for the Hoechst nucleus staining and 4 for the merge between all those emission channels.

Additionally, it became evident that CuAAC, even when the cells appear largely non-functional, exhibits a distinct reaction compared to IEDDA, as their fluorescence does not completely overlap, as shown in column 4. This indicates a different labelling pattern between the two reactions and confirms the feasibility of dual labelling with CuAAC and IEDDA in this context. To gain a deeper understanding of the effect of the PACT agent on DNA replication, further time- and concentration-dependent experiments will need to be conducted, as outlined in the following chapter.

## 2.2 Concentration and Time Dependency Experiments

While temporally tracking the incorporation of VdU (**20**) under the influence of PACT reagents it is necessary to reduce their concentration without compromising the labelling for microscopy. To achieve this, the protocol was slightly adjusted.

To ensure that only the DNA synthesized under the influence of the PACT agent is labelled, VdU (**20**) must be added at the moment [**4**]$(PF_6)_2$ is activated, allowing it to enter the cell and bind to its targets. Accordingly, the cells are incubated in 18-well µ-slides (IBIDI) for 24 h, after which [**4**]$(PF_6)$ is added and incubated for an additional 24 h. Following this incubation, VdU (**20**) is introduced, and the PACT compound is exposed to light for 30 minutes with a 520 nm LED and 36 $J/cm^2$. To monitor the effects on the cells over an extended period, the concentrations of the compound were reduced to 5 µM and 10 µM.

The first shown experiment belongs to the 5 µM concentration of [**4**]$(PF_6)_2$ (Figure 66). The images captured at time intervals before 6 h are provided in the appendix (Figure A 17 and Figure A 18). These did not exhibit any fluorescence apart from the Hoechst channel. In column 1, a low intensity of green fluorescence is observable, indicating that [**4**]$(PF_6)_2$ was labelled as described in the previous chapter. In column 2, the intensity of the red fluorescence representing the IEDDA product increases from 6 to 8 hours, followed by a decline at 24 hours. Figure A 19 demonstrates a positive metabolic labelling result for VdU (**20**) after 24 hours with tetrazine **I**, showing intense fluorescence using the same settings as those applied to the images below.

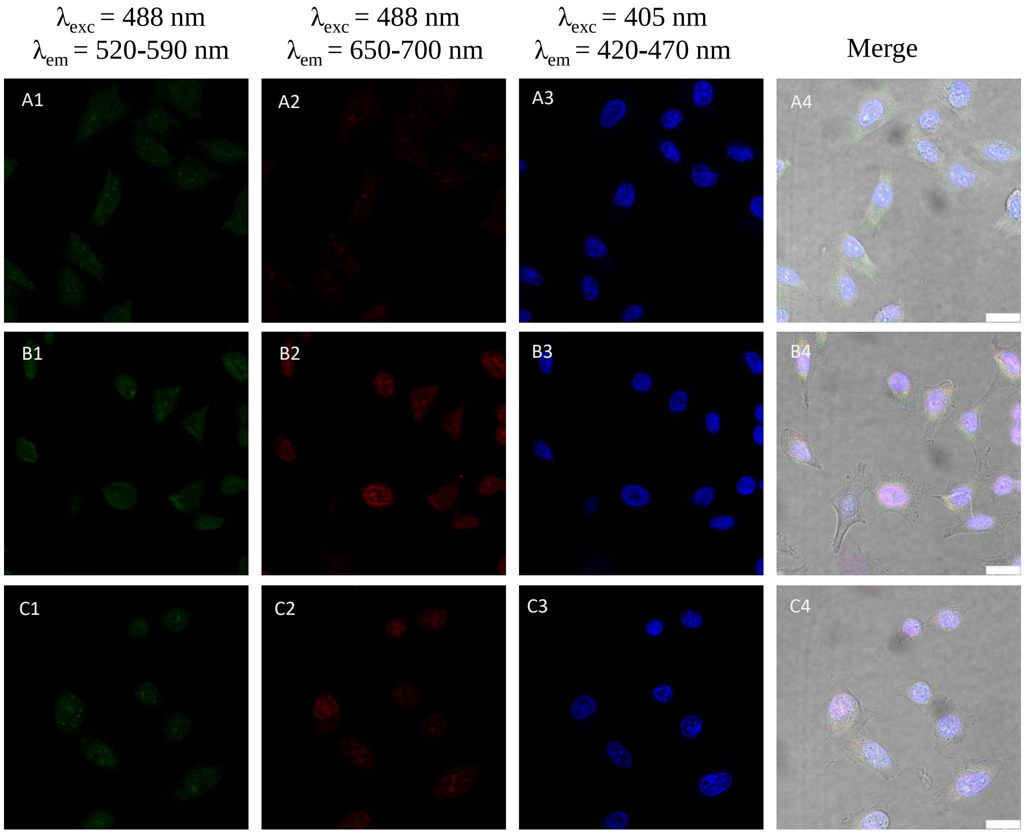

Figure 66. Dual labelling of CuAAC and IEDDA in [**4**]$(PF_6)_2$ concentration of 5 µM. Column 1 belongs to the CuAAC emission channel, 2 belongs to the IEDDA emission channel, 3 belongs to the Hoechst emission channel and 4 is merge of the different emission channels. Row A belongs to 6 h incubation, row B to 8 h incubation and row C to 24 h of incubation before fixation.

The second experiment, where the concentration was increased to 10 µM demonstrates the same effect (Figure 67). Following the same image layout, a more intense green fluorescence is observed in column 1, which was expected given the higher concentration of the PACT agent. In column 2, there is still an increase in signal from 6 to 8 h; however, the overall red fluorescence from the IEDDA reaction between tetrazine and VdU (**20**) in the newly synthesized DNA is lower. This reduced red fluorescence intensity suggests that the PACT agent is influencing the DNA replication as indicated by the stronger green fluorescence observed between 6 and 8 h. Theoretically, during this critical period of replication, DNA replication may be inhibited, resulting in decreased intensity in column 2 as less DNA is available for replication compared to the lower concentration of 5 µM of the PACT compound.

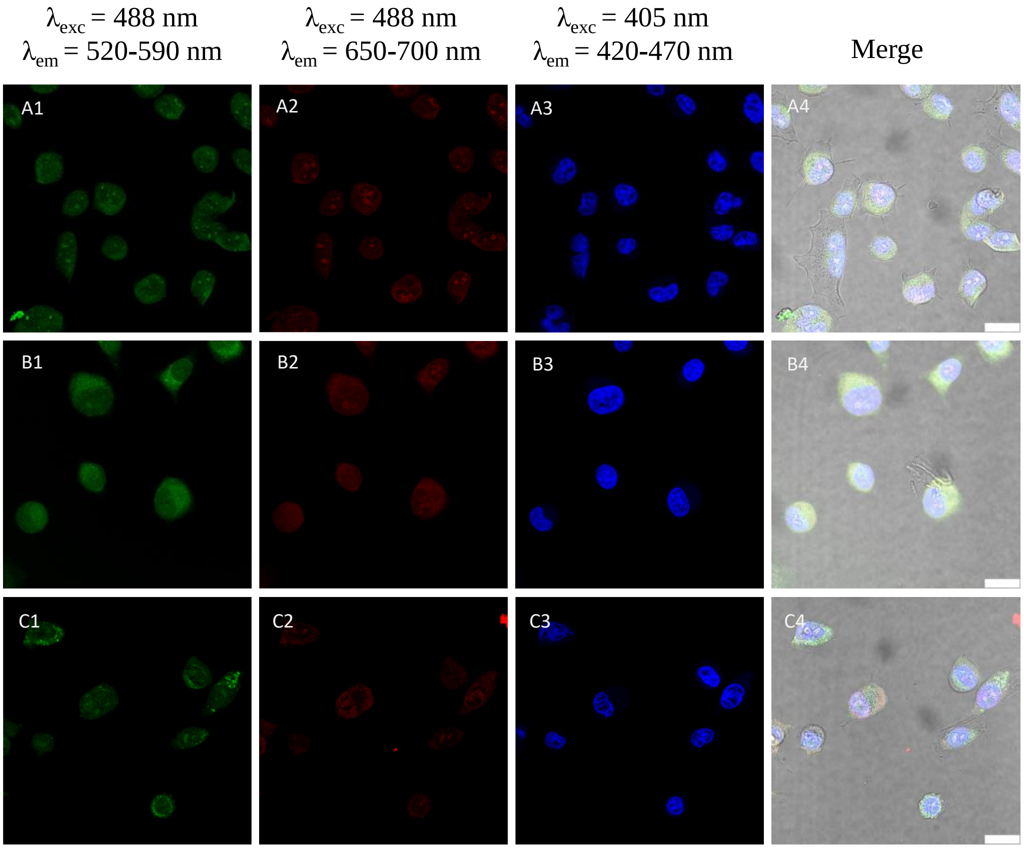

Figure 67. Dual labelling of CuAAC and IEDDA in [**4**]($PF_6$)$_2$ concentration 10 µM. Column 1 belongs to the CuAAC emission channel, 2 belongs to the IEDDA emission channel, 3 belongs to the Hoechst emission channel and 4 is merge of the different emission channels. Row A belongs to 6 h incubation, row B to 8 h incubation and row C to 24 h of incubation before fixation.

In this chapter, a new method combining photoactivatable chemotherapeutics with CuAAC for the visualization of [**4**]($PF_6$)$_2$ and IEDDA for detecting changes in newly synthesized DNA was employed. The red fluorescence observed in column 2 of Figure 65, which indicates newly replicated DNA after 24 h, is significantly stronger in the absence of direct chemotherapeutic influence compared to subsequent Figure 66 and Figure 67. This clearly shows that DNA replication is inhibited by the influence of the chemotherapeutic agent.

Expanding the experiment to include varying concentrations and time-dependencies illustrates that at a concentration of 5 µM of the PACT agent, confocal microscopy detected almost no fluorescence from the chemotherapeutic agent. However, at 10 µM, the fluorescence became clearly visible. Regarding time dependence, as expected, DNA replication begins after a few hours (6 – 10 h), and fluorescence became evident at that point. Under the influence of 5 µM of the PACT agent, the red fluorescence of the newly replicated DNA is more prominent (Figure 66) than with 10 µM of the PACT agent (Figure 67). This observation suggests a correlation between higher concentrations of [**4**]$(PF_6)_2$ and increased inhibition of DNA replication. Thus, as more PACT agent is introduced, its localization within the nucleus increases, leading to a more effective inhibition of DNA replication

# 3 Conclusion

The dual labelling method described above opens many doors for gaining more information in diagnostics with chemotherapeutics. However, a current limitation of this method is the inability to monitor in real-time where the chemotherapeutic agent is located, how quickly it diffuses into the cell, and the exact pathway it follows to bind to a specific target within the cell. Ideally, the chemotherapeutic agent should be emissive before being introduced to the cell.

Another approach would be to modify the PACT agent so that the chemotherapeutic can be labelled *via* a different bioorthogonal reaction. This would prevent any alteration in the uptake of the chemotherapeutic. However, the photochemical properties of the PACT agent may change due to the addition of a slightly larger group.

However, the ability to use dual labelling to track the pathway of PACT agents in nucleic acids, even in fixed cells, offers significant advantages. This approach could potentially be extended to target specific proteins, RNA, and other biomolecules as well.

In general, two photoactivatable methods were applied in cells in the previous chapters. Here, a bioorthogonal labelling method for DNA with spatial and temporal control was investigated, and the proof of principle was clearly demonstrated. The photoclick reaction was applied in fixed cells, but it still needs further development to be used in living cells.

Subsequently, work was done based on an alternative photochemical activation of a reaction. This involved the photoactivated release of a ligand from a ruthenium-based chemotherapeutic complex. A method was developed, also derived from the repertoire of bioorthogonal labelling techniques, specifically the CuAAC. This approach enabled the visualization of the previously non-emissive complex, allowing to identify specific targets within the cell. Additionally, the cell's DNA was included through the use of a costaining method.

To precisely track the effects of the chemotherapeutic agent on DNA, an initial attempt was made to follow DNA replication under the influence of the chemotherapeutic agent using the photoclick reaction. However, due to the use of MeCN as the reaction solvent, successful labelling could not be achieved, as the Ru complexes do not exhibit effective ligand release in MeCN. Consequently, to address the issue of DNA labelling, the IEDDA reaction was employed and used for dual labelling. It was clearly demonstrated that DNA replication was significantly impaired and stopped using the PACT agent.

# VII. Conclusion and Outlook

This work extensively explored the potential of externally-triggered reactions, particularly photoclick chemistry, to achieve precise temporal and spatial control over chemical modifications in cells. Building on the concept of visualizing biological processes through the controlled reactivity of the photoclick reaction, we demonstrated both the promise and challenges of light-controlled bioorthogonal methods. Although click chemistry is a widely used tool in biomedicine, advancing these techniques for application in aqueous solution and living cells remains challenging.

Using two photoactivatable approaches, a DNA labelling technique in fixed cells was developed in this thesis. This method was further expanded by a new synthetic route for water-soluble tetrazoles. However, these tetrazoles proved incompatible with living cells due to photochemical limitations. In addition, using an alternative photochemical activation with ruthenium-based chemotherapeutics, we combined bioorthogonal labelling techniques, to achieve target-specific visualization of the non-emissive complex and tracking DNA replication under chemotherapeutic influence.

Overall, this work lays the foundation for new diagnostic methods by establishing practical applications for DNA labelling with temporal and spatial control, although further refinement is needed for full *in vivo* compatibility.

# VIII. Experimental Section

## 1 Materials and Methods

The solvents and reagents used were comercially purchased at *ABCR, ACROS Organics, ALFA Aesar, BLD Pharm, Carl Roth, Chem Supply, CombiBlocks, Jena Bioscience, Merck, Sigma Aldrich, ThermoFisher Scientific* and *VWR.* Unless specifically noted, all solvents and reagents were used for synthesis without further purification. As written in section 8.2, some reactions were performed under dry inert atmosphere. The anhydrous solvents were purchased at *ACROS Organics* and stored over molecular sieves and under inert gas. Solvents used for reactions were either in *pro analysis* (p.a.) or HPLC grade purity. For HPLC separations, only high-purity organic solvents (HPLC grade) were used. Water for the HPLC separation was filtered and deionized using a *Merck* Millipore Q8 system. While performing reactions under inert conditions, the glassware was heated three times with a heat gun, dried in high vacuum ($10^{-3}$ mbar), followed by flooding with argon (99.999% purity). Liquids were transferred using V2A stainless steel needles and plastic syringes. Reactions without a specified temperature were conducted at room temperature (r. t.). For lower temperatures, cooling mixtures were used in Dewar vessels. For 0 °C ice/water mixture and -15 °C NaCl in ice/water was applied. The solvents used were removed at 40 °C under reduced pressure. To perform reactions under exclusion of light, either brown glassware was used, or the reaction flask were covered with aluminum foil.

### Chromatography

Flash Chromatography

Silica gel (pore size 60 Å, particle size 40-63 µM) was used as stationary phase and was purchased from *Sigma Aldrich.* The crude product was either dissolved in the solvent system or loaded onto silica gel before purification and protected with a thin layer of seasand (pure, cleaned with HCl) purchased from *Bernd Kraft Laborchemikalien*. Pressure was applied to the column using an air pump.

### Thin-Layer Chromatography (TLC)

For reaction controls, thin-layer chromatography with silica gel 60 $F_{254}$ coated aluminum plates by *Merck* was used. For detection, either $\lambda$ = 254 nm (fluorescence deletion) or $\lambda$ = 366 nm (fluorescence excitation) was used. The plates were stained with either 5 % $H_2SO_4$ in MeOH or 0.5% Ninhydrin in Butan-1-ol (spray reagent).

### HPLC-Chromatography

HPLC separation was performed on a *ThermoFisher Scientific* UltiMate™ 3000 system. For following the bioorthogonal reaction in vitro and the purification, a *Phenomenex*, Luna® 5 µm C18(2), 100 Å, (250 x 2 mm). To follow the reaction progress, all analytic runs were performed with a 10.0 µL injection volume at 40 °C, using a flow rate of 0.20 mL $min^{-1}$. Elution of the product was executed through using the eluents and gradient in Table 5.

Table 5: Gradient in mobile phase for the HPLC-analysis following the bioorthogonal photoclick reaction.

| **time [min]** | **% MeCN in $H_2O$** |
|---|---|
| 0.00 | 65 |
| 15.00 | 100 |
| 25.00 | 100 |
| 40.00 | 65 |

## Spectroscopy

### NMR Spectroscopy

NMR spectroscopic data was recorded using the following spectrometer hardware: *Bruker Avance Neo* $^1$H-NMR (400 MHz), $^{13}$C-NMR (101 MHz). 5-10 mg of the compound was dissolved in approx. 500 µL deuterated solvent ($CDCl_3$, DMSO). Chemical shifts of the $^1$H- and $^{13}$C-NMR spectra are reported in parts per million (ppm) relative to the solvent as an internal standard and was converted to the TMS reference system.

| | |
|---|---|
| $CDCl_3$ | $^1$H: $\delta$ = 7.26 ppm; $^{13}$C: $\delta$ = 77.16 ppm |
| DMSO-$d_6$ | $^1$H: $\delta$ = 2.50 ppm; $^{13}$C: $\delta$ = 39.52 ppm |

$^{13}$C-NMR spectroscopy was recorded while applying broadband $^1$H-decoupling. Coupling constants (*J*) are given in Hertz (Hz) and the multiplicity of signals are reported as follows: s (singlet), d (doublet), t (triplet), q (quadruplet), m (multiplet), dd (doublet of doublets), dt (doublet of triplets), td (triplet of doublets), tt (triplet of triplets) and tq (triplet of quadruplets). 2D technique experiments as COSY, HSQC and HMBC were used to determine the structures of the molecules.

UV/Vis Spectroscopy

UV/Vis absorbance spectra were either recorded on a *Varian* Cary100 Scan UV/Vis spectrometer or a Cary3500 Multicell UV/Vis spectrometer with Peltier element from *Agilent*. The samples were prepared using 1 cm quartz glass cuvettes (*Starna*) with a volume of 1 mL at 25 °C. To determine the extinction coefficients, different concentrations were measured and applied to Beer-Lambert’s law.

Fluorescence Spectroscopy

Fluorescence spectroscopic measurements in the UV and visible light spectrum were performed using a *Fluoromax-4* fluorescence spectrometer equipped with a Peltier element from *Horiba Scientific* (formerly *Jobin-Yvon*) at 20 °C. The fluorescence signal was corrected by subtracting the spectrum of the solvent to account for background interference. The spectrometer was calibrated using the Raman scatter of water as a reference to ensure accurate wavelength measurements.

### Mass Spectroscopy

Mass spectrometric analyses were performed by the Analytical Department of the Institute of Organic Chemistry at the Karlsruhe Institute of Technology (KIT), using an electron impact ionization on a *Q Exactive Plus Orbitrap* mass spectrometer from *Thermo Scientific*. The signals were recorded as mass-to-charge ratios (*m/z*), and the molecular ions were represented using the following notation $[M]^+$. In the case of protonated or sodium adduct forms, the ions were denoted as $[M+H]^+$ and $[M+Na]^+$, respectively.

LC-MS

LC-MS analyses were conducted using an *UltiMate 3000 Dionex* system coupled with an *LTQ Orbitrap Elite ESI* mass analyzer (*Thermo Scientific*). The same gradients and eluents as for the HPLC runs were used (see section 5.4).

# 2 Irradiation Setups

## 2.1 KIT

The LEDs used in the irradiation setup in Karlsruhe were purchased from *Roithner Laser Technik GmbH* (405 nm: 5P4FCA, 450 nm: LED450-03 and 505-B5B-433-B505, Figure 68 below). The setup shown in Figure 68 was designed and manufactured by the Uiniversity of Regensburg and the workshop of the Insitute for Physical Chemistry at KIT. A Lauda Alpha R8-thermostat was used either to cool the system (*in vitro* experiments, 20 °C) or to warm the samples (cell experiments, 36 °C). *In vitro* experiments were performed, employing a distance of 10 mm between the LED and the bottom of the vial, in cell experiments, the distance was increased to 35 mm between the LED and the bottom of the 8- or 18-well µ-slide.

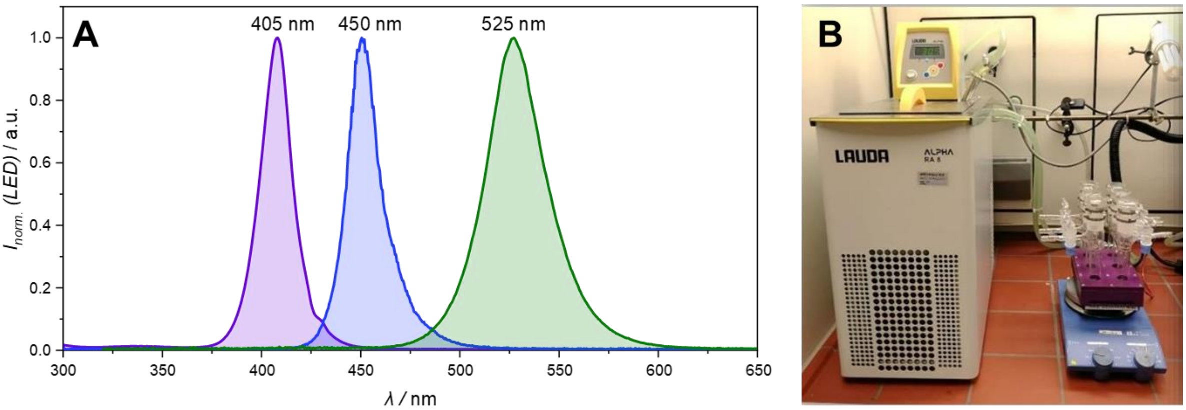

Figure 68: A: Emission spectra of the used LEDs (405 nm, 30 mW; 450 nm, 20 mW; 525 nm, 40 mW). B: Customized irradiation setup with thermostat, stirrer and customized sample holder for schlenk vials.

## 2.2 Leiden University

The cell-irradiation system consisted of a Ditabis thermostat (980923001) fitted with two flat-bottomed micro-plate thermoblocks (800010600) and a 96-LED array fitted to a standard 96-well plate. The 520 nm LED (OVL-3324), fans (40 mm, 24 VDC, 9714839), and power supply (EA-PS 2042-06B) were obtained from *Farnell*. See *Hopkins et al.* for a full description.[203]

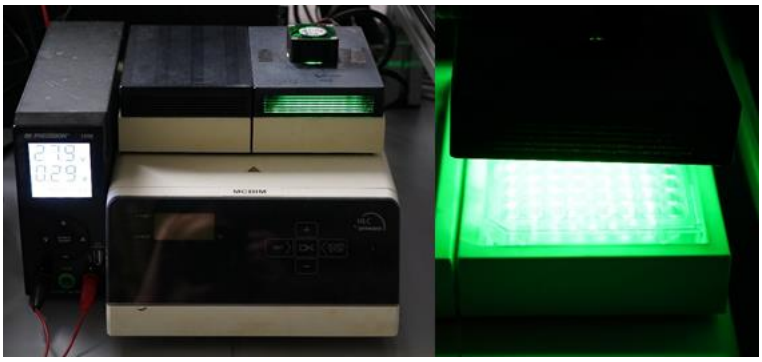

Figure 69: A: Customized irradiation setup with power supply, thermostat, LED plate from top with 96-LEDs made from Leiden University workshop. B: 96-well LED array fitted to a standard 96-well plate.

# 3 Cell Laboratory

Confocal Laser Microscopy

KIT:

Confocal Laser Microscopy was performed using a *Leica DMI8, TCS SP8 microscope* with a *HC PL APO 63x/1.40 OIL CS2* objective. Image acquisition was conducted at a resultion of 512 x 512 pixels and 8-bit depth using LAS X 3.5.7.23225 software. Leica X office 1.4.6.28422 was used to analyze the images. **6** was shown in green, **2** in red, Hoechst in blue, DRAQ5 in yellow and tetrazine **I** in red. The fluorescence channel of AlexaFluor™ 488 was always shown in green.

Leiden University:

Confocal imaging was performed on an *Eclipse Ti2-C2+ Nikon* confocal microscope using the 40x water (Apo LWD 40x/1.15 WI λS DIC N2) objective Lasers used: 405 nm for Hoechst 33342 (ex./em. 360/460 nm), 488 nm for [**2**]$^{2+}$ and [**4**]$^{2+}$ labeled with AlexaFluor™ 488 (ex./em. 495⁄519 nm), and 640 nm for AlexaFluor™ 647 (ex./em. 651/667 nm). The settings for image acquisition (laser power and PMT gain) were identical for all conditions. The images were processed using NIS-Elements AR software version 5.02.02, Fiji Image J software and Omero 5.6. The setting during image processing were identical for each condition. Hoechst, AlexaFluor™ 488 and AlexaFluor™ 647 were shown in blue, green and red.

Microplatereader

To evaluate the MTT-tests, a *LARIOstar plus* Plate Reader from *BMG-Labtech* was used. The absorption of the individual samples was determined at 570 nm.

# 4 Synthetic Procedures

## 4.1 Metabolic Labelling with Tetrazoles

Compound **3**, **4** and **38** were synthesized in the masterthesis in the *Wagenknecht* group by *L. Rieger*.[216] Compound **22** was synthesized by *E. List*,[101] *B. Pfeuffer* synthesized compounds **19** and **21**.[101]

Schemes of the different reactions to tetrazoles **1**, **3**, **2** and **6**

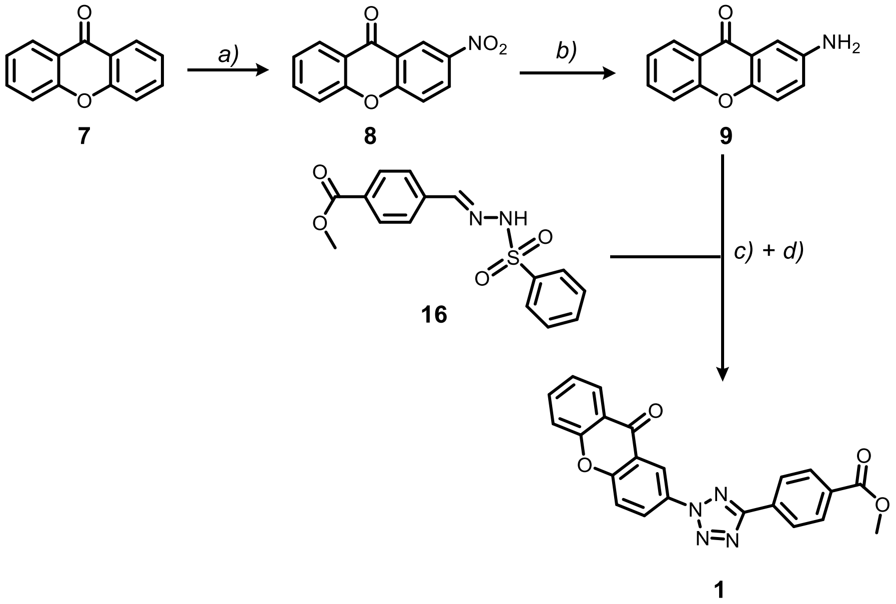

Scheme 1. Synthesis of **1.** a) $H_2SO_4/HNO_3$, $H_2SO_4$, 0 °C, 1.5 h; b) SnCl2·2 H2O, EtOH, 85 °C, 10 h, 12% over both reactions c) sodium nitrate, HCl, EtOH/H2O, 0 °C, 20 min; d) diazoniumsalt, hyrazone (**16**), pyridine, -30 °C to r. t., over night.

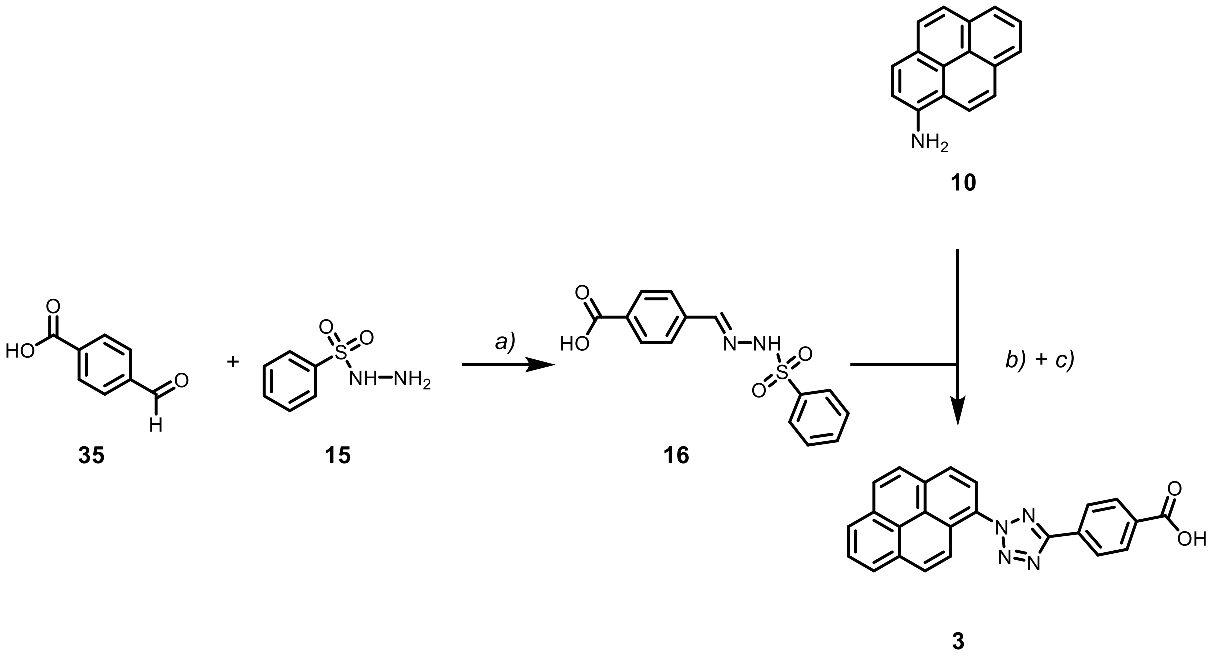

Scheme 2. Synthesis of **3**. a) EtOH, 45 °C, 60 min; 92%; b) $NaBF_4$, $HBF_4$ (50%), -10 °C, 30 min; c) hydrazone, pyridine, 0 °C, 2 h, 38%.

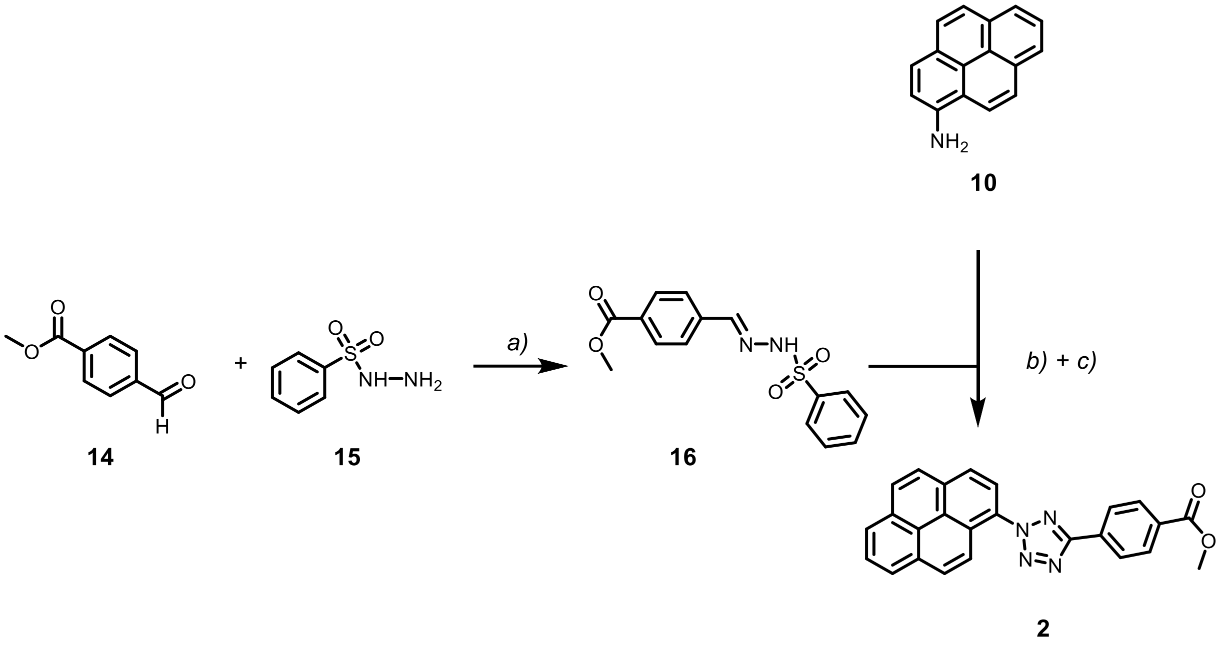

Scheme 3. Synthesis of **2**. Conditions: a) EtOH, 45 °C, 60 min; 95%; b) $NaBF_4$, $HBF_4$ (50%), -10 °C, 30 min; c) hydrazone, pyridine, 0 °C, 10 h, 31%.

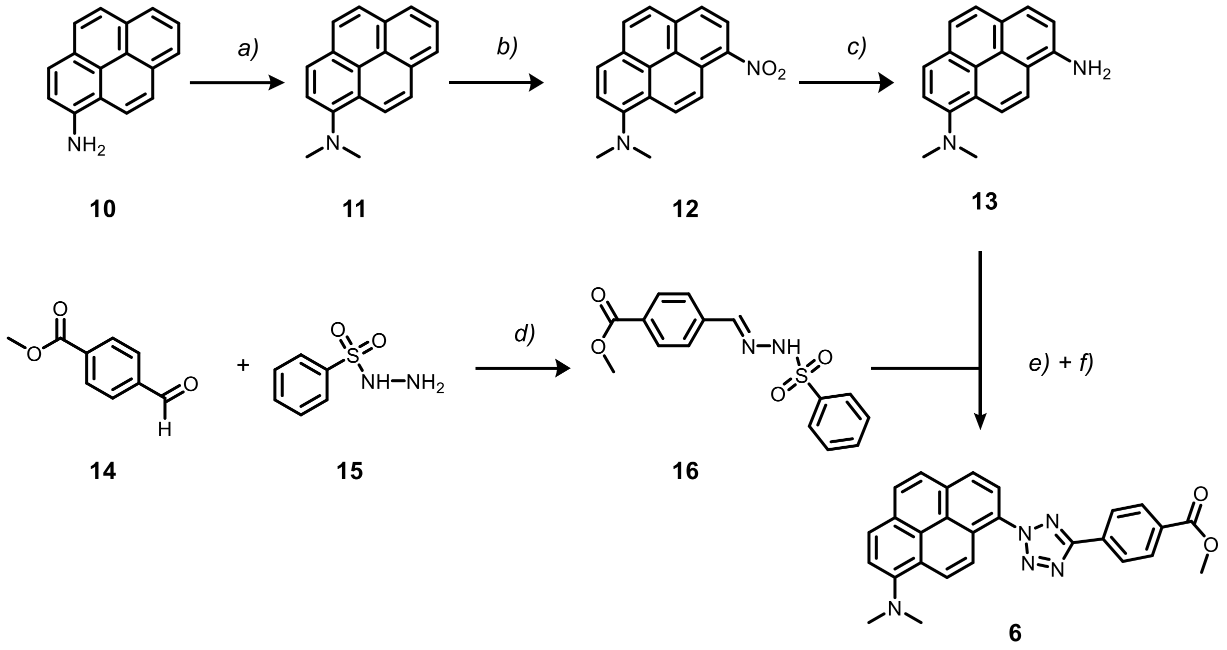

Scheme 4. Synthesis of **2**. Conditions: a) MeI, $K_2CO_3$, DMF, 120 °C, 2 h, 90%; b) $HNO_3$, AcOH, $Ac_2O$, r. t., 3 h, 51%; c) $H_2$, Pd/C, EtOAc, r. t., 30 min, 91%; d) EtOH, 45 °C, 60 min; 95%; e) HCl, $NaNO_2$, THF, EtOH/$H_2O$, 0 °C, 10 min; f) hydrazone, pyridine, 0 °C, 10 h, 13%.

## Synthesis of tetrazoles **4** and **5** out of tetrazole **3**

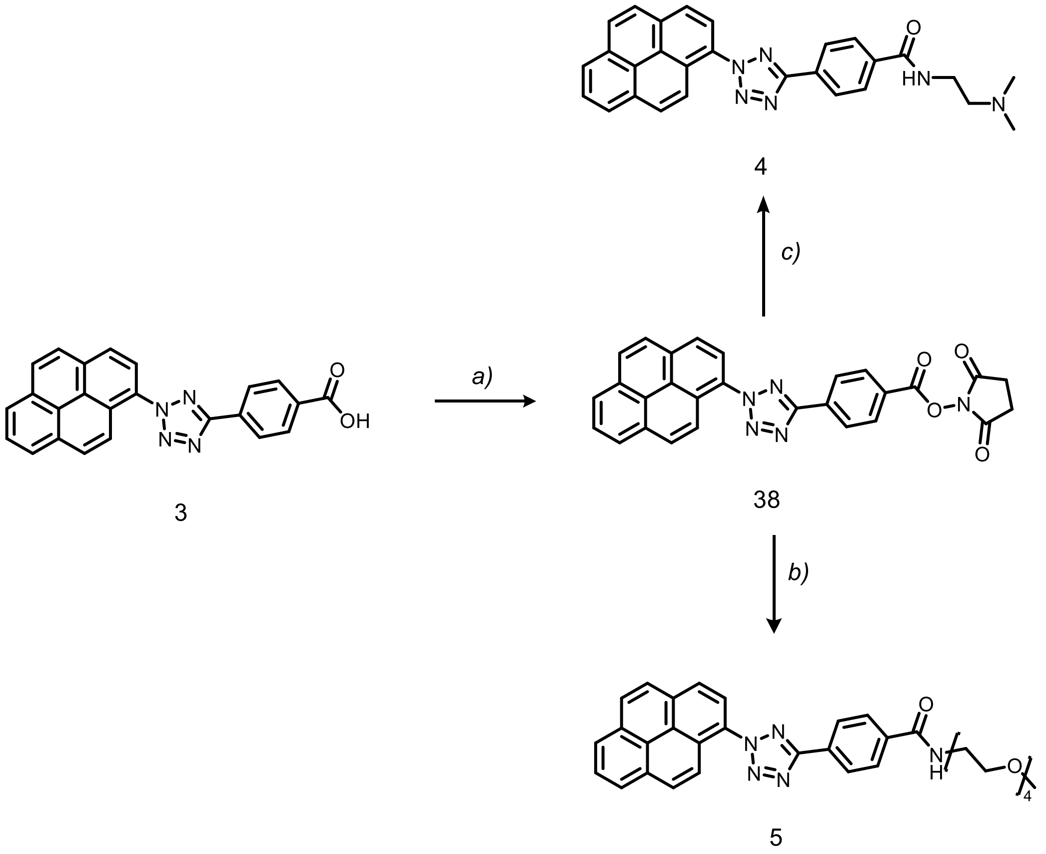

Scheme 5: Synthesis of water soluble tetrazoles. Conditions: a) NHS, EDC·HCl, DMF, 25 °C, 20h, 88%; b) PEG-200-Amin, $Et_3N$, DMF, 25 °C, 20h, 20%; c) Dimethylethane-1,2-diamine, $Et_3N$, DMF, 25 °C, 20 h, 20%.

Compund **8**

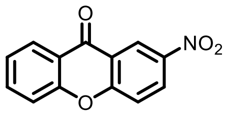

$C_{13}H_7NO_4$

241.04 g mol$^{-1}$

2.50 g of xanthone **7** (12.8 mmol, 1.0 equiv.) were dissolved in 7 mL of concentrated sulfuric acid and cooled to –15 °C. In a second flask, nitrating acid was prepared from 270 µL of fuming nitric acid (0.40 g, 6.38 mmol, 0.5 equiv.) and 1.50 mL of concentrated sulfuric acid (2.75 g, 28.1 mmol, 2.2 equiv.). The nitrating acid was added dropwise to the xanthone solution, ensuring the temperature of the flask remained below 5 °C. The reaction mixture was then stirred at 0 °C for 1.5 hours. After completion, the reaction mixture was poured onto ice, and the resulting precipitate was filtered. The solid was washed with cold water until the wash solution reached a neutral pH of 7. The crude product obtained was used directly in subsequent reactions without further purification, as described in the relevant literature.[186]

Compund **9**

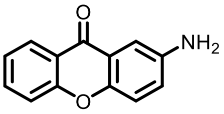

$C_{13}H_9NO_2$
211.06 g mol$^{-1}$

**9** was synthesized similarly to literature.[186] 3.00 g of **8** (12.0 mmol, 1.00 equiv.) was dissolved in EtOH and 8.43 mg $SnCl_2 \cdot 2H_2O$ (37 mmol, 3.00 equiv.) was added and stirred over night at 85 °C. The reaction mixture was cooled down and the solvent was removed under reduced pressure. 50 mL of a saturated $NaHCO_3$ solution was added to the obtained solid, stirred for 5 minutes, and then filtered. To extract the product from the solid mixture, 100 mL acetone was added, followed by incubation in an ultrasound bath for 2 minutes. The mixture was filtered to remove insoluble tin salts, and the solvent was removed under reduced pressure. The crude product was purified by column chromatography (*n*-Hex / EtOAc, 5:1), yielding 155 mg (12%) of a yellow oil. The spectroscopoic data is in agreement with literature.[186]

**$^1$H-NMR** (400 MHz, DMSO) $\delta$ (ppm) = 8.16 (dd, *J* = 8.0, 1.7 Hz, Aryl-H), 7.81 (ddd, *J* = 8.7, 7.0, 1.8 Hz, Aryl-H), 7.60 (dd, *J* = 8.6, 0.9 Hz, aryl-H), 7.45 – 7.37 (m, 2H, Aryl-H), 7.28 (d, *J* = 2.9 Hz, Aryl-H), 7.15 (dd, *J* = 8.9, 2.9 Hz, aryl-H), 5.46 (s, 2H, $NH_2$).

Compound **1**

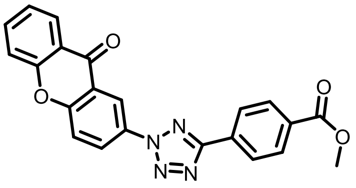

$C_{22}H_{14}N_4O_4$
398.10 g mol$^{-1}$

190 mg of compound **9** (0.890 mmol, 1.00 equiv.) were dissolved in 5 mL of 80% ethanol/water and cooled to 0 °C. Slowly, 300 µL concentrated HCl solution (0.164 mg, 4.50 mmol, 5.00 equiv.) was added dropwise. To this solution, 76 µg of $NaNO_2$ (1.10 mmol, 1.20 equiv.), dissolved in 1 mL of water was slowly added, ensuring the temperature did not exceed 5 °C. In a second flask, 425 mg of **16** (1.34 mmol, 1.50 equiv.) were dissolved in 7 mL pyridine and cooled to -40 °C. The diazonium salt solution was slowly added to this mixture. After stirring for 30 minutes, the ice bath was removed, and stirring continued for three hours.

The product precipitated from the reaction mixture, was filtered, and washed with water, yielding 207 mg (60%) as an orange solid.

**$^1$H-NMR** (400 MHz, $CDCl_3$) $\delta$ (ppm) = 9.12 (d, $J$ = 2.7 Hz, Aryl-H), 8.59 (dd, $J$ = 9.1, 2.7 Hz, Aryl-H), 8.37 (dd, $J$ = 9.2, 7.3 Hz, 3H, Aryl-H), 8.21 (d, $J$ = 8.3 Hz, 2H, Aryl-H), 8.05 – 7.94 (m, Aryl-H), 7.87 – 7.70 (m, 2H, Aryl-H), 7.56 (d, $J$ = 8.4 Hz, Aryl-H), 7.47 (d, $J$ = 7.6 Hz, Aryl-H), 3.97 (s, 3H, $CH_3$).

**$^{13}$C-NMR** (101 MHz, $CDCl_3$) $\delta$ (ppm) = 145.99, 135.55, 130.29, 129.93, 129.14, 127.92, 127.17, 127.06, 126.94, 126.04, 124.74, 120.09, 118.17, 117.98, 52.38.

**ESI-HRMS** *m/z*: calculated [M]$^+$: 398.1015; measured [M+H]$^+$: 399.10829.

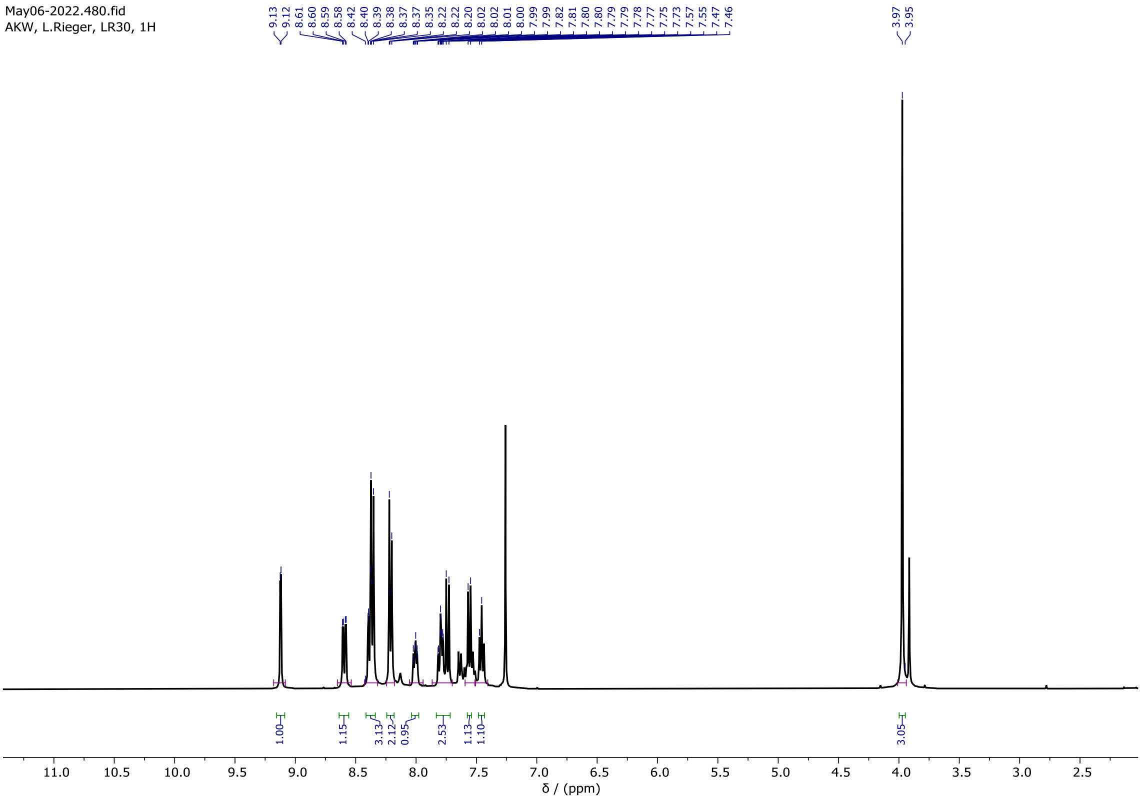

Figure 70: $^{1}$H-NMR spectrum of **1** (CDCl$_3$, 400 MHz).

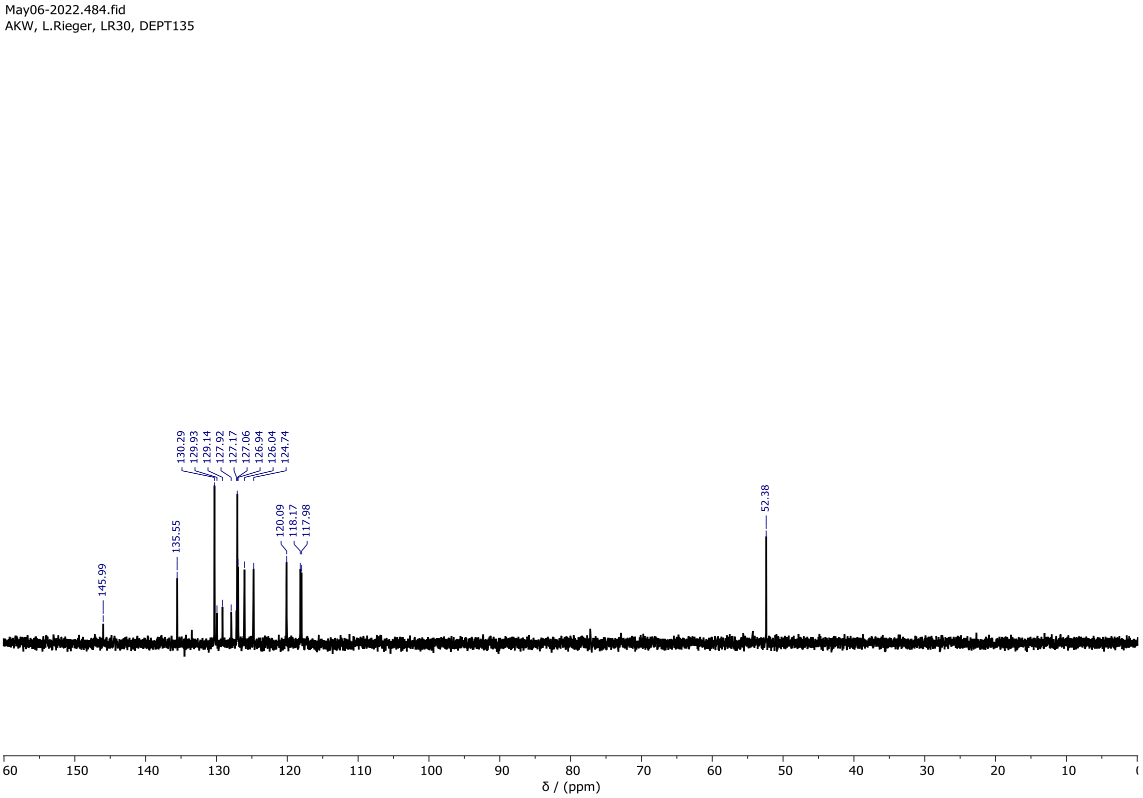

Figure 71: $^{13}$C-NMR spectrum of **1** (CDCl$_3$, 101 MHz).

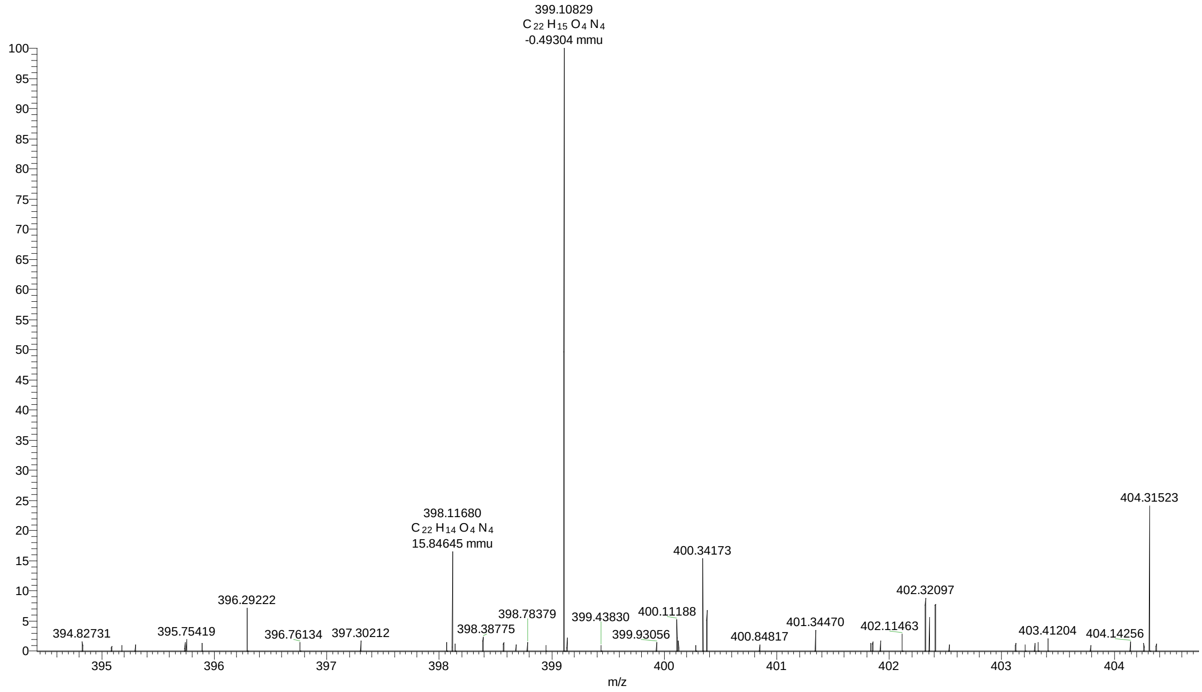

Figure 72: ESI-HRMS m/z: calculated [M] +: 398.1015; measured [M+H]+: 399.10829.

Compound **11**

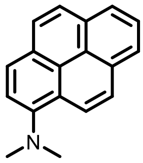

$C_{18}H_{15}N$
245.12 g mol$^{-1}$

Compound **11** was synthesized similarly to literature.[121] 2.00 g pyrene-1-amine (**24**) (9.21 mmol, 1.00 equiv.) and 6.37 g $K_2CO_3$ (46.1 mmol, 5.00 equiv.) were combined in a round bottom flask under argon. 12 mL dry DMF and 2.90 mL iodomethane (6.54 g, 46.1 mmol, 5.00 equiv.) were added dropwise over 10 min, while stirring the reaction solution. The flask was equipped with a balloon filled with argon und heated to 125 °C for 5 min and cooled down to r. t. Excessive iodomethane was quenched with 12 mL MeOH and the reaction was stirred for another 10 min at r. t. 250 ml EtOAc were added, followed by extraction of the mixture three times with 300 ml water. The combined organic layer was dried over $MgSO_{4,}$ and the solvent evaporated under reduced pressure. The product has been isolated as a brown oil and was used without further purification (2.17 g, 96%). The spectroscopic data is in agreement with literature.[121]

**$^1$H-NMR** (400 MHz, $CDCl_3$) $\delta$ (ppm) = 8.49 (d, $J$ = 9.2 Hz, 1H, Aryl-H), 8.16 – 8.08 (m, 5H, Aryl-H 8.01 – 7.92 (m, 3H, Aryl-H), 7.76 (d, $J$ = 8.3 Hz, 1H, Aryl-H), 3.08 (s, 6H, 2x$CH_3$).

Compound **12**

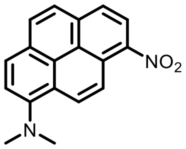

$C_{18}H_{14}N_2O_2$
290.10 g mol$^{-1}$

Compound **12** was synthesized according to literature[121] 3.81 g **11** (15.5 mmol, 1.00 equiv.) was dissolved in 200 mL acetic acid and 60 mL acetic anhydride. While stirring, $HNO_3$ (1.43 mL, 65%, 2.15 g, 34.2 mmol, 2.20 equiv.) in 10 mL acetic acid was added dropwise over 1 h to the reaction solution. Additional 0.143 mL $HNO_3$ (0.250 g, 3.42 mmol, 0.220 equiv.) was added dropwise to the solution. After 3 h, the reaction mixture got dark red. The solution was quenched with 150 mL $H_2O$ and extracted 4x with 200 mL DCM. The organic layer was washed twice with 300 mL water, dried over $MgSO_4$ and evaporated under reduced pressure. The product was adsorbed onto silica and purified by column chromatography (*n*-Hex / EtOAc gradient 25:1-10:1). The product was obtained as a dark red powder (2.34 g, 52%). Spectroscopic data is in agreement with literature.[121]

**$^1$H-NMR** (400 MHz, $CDCl_3$) $\delta$ (ppm) = 8.93 (d, *J* = 9.7 Hz, 1H, Aryl-H), 8.70 – 8.61 (m, 2H), 8.23 (dd, *J* = 8.4, 1.5 Hz, 1H, Aryl-H), 8.15 – 8.10 (m, 1H, Aryl-H), 8.04 (d, *J* = 8.5 Hz, 1H, Aryl-H), 7.92 (d, *J* = 8.9 Hz, 1H, Aryl-H), 7.79 – 7.73 (m, 1H, Aryl-H), 3.14(d, *J* = 1.3 Hz, 6H, 2x$CH_3$).

Compound **13**

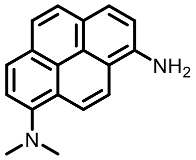

$C_{18}H_{16}N_2$
260.13 g mol$^{-1}$

Compound **13** was synthesized according to literature.[121] 200 mg of compound **12** (0.69 mmol, 1.00 equiv.) was dissolved in 50 mL EtOAc and 44 mg Pd/C (0.41 mmol, 0.6 equiv.) was added. $H_2$ (approx. 3 L balloon) was bubbled through the suspension for 1 h 30 min. The crude product was filtered over celite, and the solvent was removed under reduced pressure. The product was purified by column chromatography in *n*-Hex / EtOAc (99:1 to 4:1) and 149 mg of the product (83%) obtained as brown oil. The spectroscopic data is in agreement with literature.[121]

**$^1$H-NMR** (400 MHz, $CDCl_3$) $\delta$ (ppm) = 8.39 (d, $J$ = 9.5 Hz, 1H, Aryl-H), 8.00 (d, $J$ = 8.3 Hz, 1H, Aryl H), 7.94 (dd, $J$ = 16.9, 8.8 Hz, 2H, Aryl-H), 7.77 (t, $J$ = 11.3 Hz, 2H, Aryl-H), 7.70 (d, $J$ = 8.3 Hz, 2H, Aryl-H), 4.43 (s, 2H, NH), 3.04 (s, 6H, 2x$CH_3$).

Compound **6**

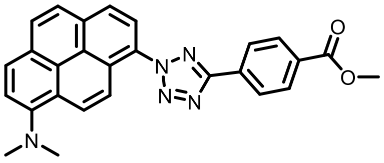

$C_{27}H_{21}N_5O_2$
447.16 g mol$^{-1}$

**6** was synthesized similarly to literature.[121] 300 mg **13** (1.15 mmol, 1.00 equiv.) was dissolved in a mixture of EtOH/$H_2O$ (3 mL each) and 130 µL HCl (4.14 mmol, 3.60 equiv.) and cooled to -10 °C in an ice/salt mixture. After 20 min, a solution of 95 mg $NaNO_2$ (1.38 mmol, 1.20 equiv.) in 1 mL $H_2O$ was cooled to 0 °C and added dropwise while stirring. The solution turned from yellow to dark blue and was continuously stirred for 10 min. Concomitantly, a solution of 622 mg **16** (1.96 mmol, 1.70 equiv.) in 5 mL pyridine was prepared and cooled to -10 °C. Subsequently, the blue solution, the diazonium salt, was added to the pyridine solution at -10 °C. The round bottom flask was covered with an argon balloon and allowed to warm to r. t. overnight. Afterwards the solution was poured onto 100 mL of 1 M HCl and further stirred for 1 h. 200 mL DCM were added, and the reaction mixture extracted 3x with 150 mL water. Afterwards the organic layer was washed with 100 mL 1 M HCl and water until the aqueous solution reached a pH of 7. The organic layer was dried over $MgSO_4$, and the solvent evaporated under reduced pressure. The product was purified via column chromatography in *n*-Hex / EtOAc (10:1). 66 mg of the product (13%) is obtained as yellow powder. The spectroscopic data is in agreement with literature.[121]

**$^1$H-NMR** (400 MHz, DMSO) $\delta$ (ppm) = 8.55 (d, $J$ = 9.6 Hz, 1H, Aryl-H), 8.48 – 8.37 (m, 5H, Aryl-H), 8.29 (d, $J$ = 9.0 Hz, 1H, Aryl-H), 8.25 – 8.20 (m, 2H, Aryl-H), 8.16 (d, $J$ = 8.9 Hz, 1H, Aryl-H), 8.12 (d, $J$ = 9.6 Hz, 1H, Aryl-H), 7.95 – 7.90 (m, 1H, Aryl-H), 3.93 (s, 3H, $CH_3$), 3.04 (s, 6H, 2x$CH_3$).

Compound **16**

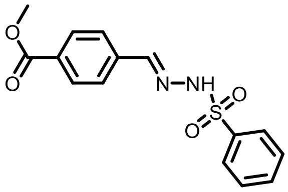

$C_{15}H_{14}N_2O_4S$
318.06 g mol$^{-1}$

Compound **16** was synthesized according to literature.[217] 1.90 g benzenesulfohydrazide (**15**) (11.0 mmol, 1.00 equiv.) was dissolved in 30 mL EtOH. Concomitantly, 1.70 g methyl-4-formylbenzoate (**14**) (11.0 mmol, 1.00 equiv.) was dissolved in 10 mL EtOH at 55 °C and transferred to the solution with benzenesulfohydrazide. The mixture was stirred at 40 °C for 1 h. The reaction mixture was poured on ice and diluted with 30 mL water. Subsequently, the product was filtered and washed two times with 50 mL cooled (0 °C) EtOH. The product was obtained as white powder (3.25 g, 95%). The spectroscopic data is in agreement with literature.[217]

**$^1$H-NMR** (400 MHz, DMSO) $\delta$ (ppm) = 11.81 (s, 1H, NH), 8.00-7.84 (m, 5H, Aryl-H), 7.77-7.51 (m, 5H, Aryl-H), 3.84 (s, 3H, $CH_3$).

Compound **2**

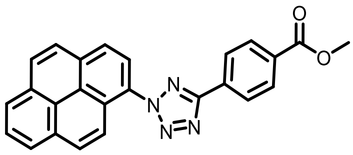

$C_{25}H_{16}N_4O_2$
404.13 g mol$^{-1}$

1.00 g amino-1-pyrene (**10**) (4.60 mmol, 1.00 equiv.) was dissolved in 120 mL THF and cooled with an ice / water mixture to -10 °C. 4.04 g $NaBF_4$ (36.8 mmol, 8.00 equiv.), 40 mL 50% $HBF_4$ and 7.50 mL $H_2O$ was added to the solution. After 20 min of stirring the aqueous solution, a solution of 381 mg $NaNO_2$ (1.42 mmol, 1.20 equiv.) in 1 mL $H_2O$ was cooled to -10 °C with an ice/water mixture and added dropwise while stirring for 2 h. A colour change from yellow to brown was observed. The product was filtered and added to a solution of 1.67 g **16** (5.23 mmol, 1.20 equiv.) in 25 mL pyridine at -20 °C. The reaction mixture was stirred for 1 h. Afterwards the mixture was poured into a mixture of 250 mL $H_2O$ and 50 mL concentrated HCl. The resulting solid was filtered and washed with 70 mL EtOH. The product was obtained as 558 mg (31%) dark red solid.[101][1]

**$^1$H-NMR** (400 MHz, $CDCl_3$) $\delta$ (ppm) = 8.45 (d, $J$ = 8.1 Hz, 2H, Aryl-H), 8.39 (dd, $J$ = 8.8, 4.6 Hz, 2H, Aryl-H), 8.34 – 8.28 (m, 3H, Aryl-H), 8.27 – 8.20 (dd, $J$ = 8.6, 5.2 Hz, 4H, Aryl-H), 8.17 (d, $J$ = 8.9 Hz, 1H, Aryl-H), 8.12 (t, $J$ = 7.6 Hz, 1H, Aryl-H), 3.99 (s, 3H, $CH_3$).

**$^{13}$C-NMR** (101 MHz, $CDCl_3$) $\delta$ (ppm) = 166.57, 164.56, 132.84, 131.94, 131.34, 131.15, 130.60, 130.34, 130.14, 130.09, 129.42, 127.10, 127.02, 126.92, 126.74, 126.35, 125.17, 125.05, 124.82, 124.12, 122.76, 121.43, 52.39.

**ESI-HRMS** *m/z*: calculated $[M]^+$: 404.1273; measured $[M]^+$: 404.1428.

---

[1] Spectroscopic data is already published and available in: “Metabolic labelling of DNA in cells by means of the “photoclick” reaction triggered by visible light”, L. Rieger, B. Pfeuffer and H.-A. Wagenknecht, *RSC Chem. Biol.*, **2023**, 4, 1037-1042; DOI: 10.1039/D3CB00150D

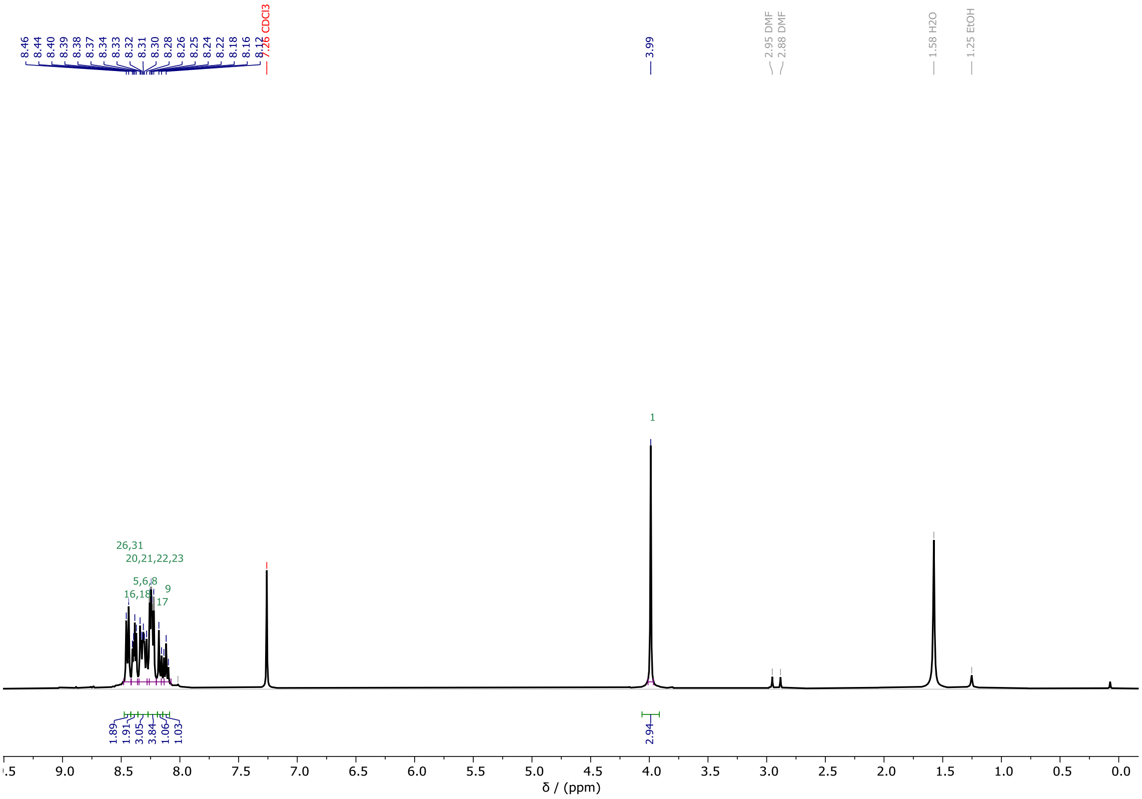

Figure 73: $^1$H-NMR spectrum of **2** ($CDCl_3$, 400 MHz).

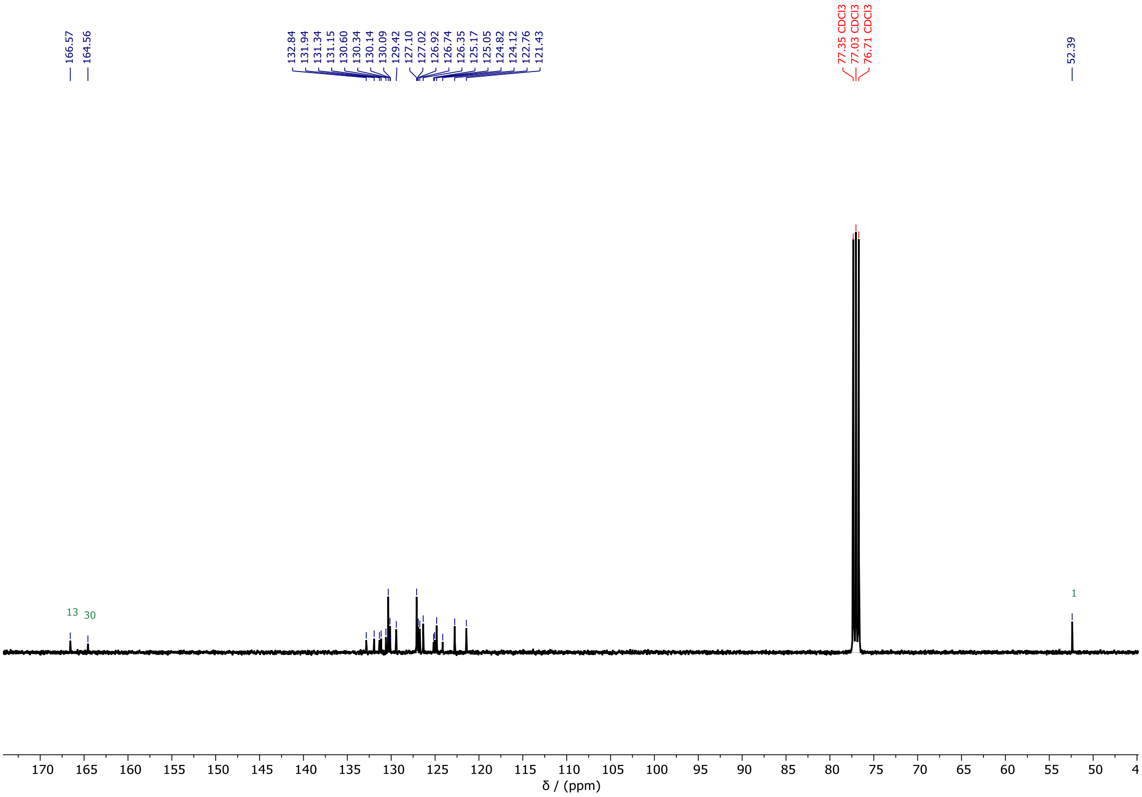

Figure 74: $^{13}$C-NMR spectrum of **2** ($CDCl_3$, 101 MHz).

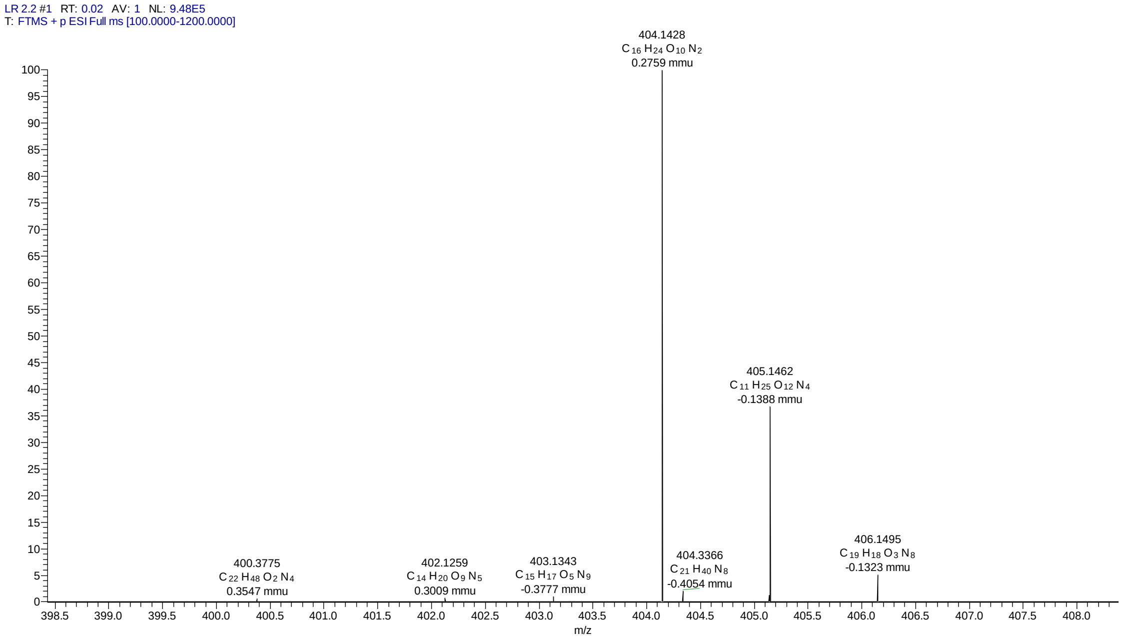

Figure 75: ESI-HRMS *m/z*: calculated $[M]^+$: 404.1273; measured $[M]^+$: 404.1428.

Compound **5**

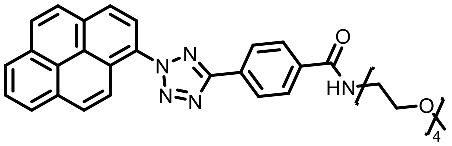

$C_{33}H_{33}N_5O_5$
579.66 g mol$^{-1}$

Compound **38** (40.0 mg, 82.1 µmol, 1.00 equiv.) was dissolved in 4 mL DMF. 25.5 mg PEG-200-amine (25.4 µL, 123 µmol, 1.50 equiv.) was added to the solution. $Et_3N$ (12.5 mg, 17.1 µL, 123 µmol, 1.50 equiv.) was added to the reaction solution after 5 min. The mixture was stirred for 19 h at 25 °C. The solvent was removed under reduced pressure and the crude product was purified *via* column chromatography in *n*-Hex / EtOAc (4:1). 9 mg compound **23** was obtained as light brown solid (15.5 µmol, 18%).

**$^1$H-NMR** (400 MHz, $CDCl_3$) $\delta$ (ppm) = 8.45 – 8.05 (m, 13H, Aryl-H), 7.46 (s, 1H, Aryl-H), 3.75 – 3.64 (m, 11H, Alkyl-H), 3.64 – 3.61 (m, 2H, Alkyl-H), 3.55 – 3.52 (m, 2H, Alkyl-H), 3.34 (s, 3H, $CH_3$).

**$^{13}$C-NMR** (101 MHz, $CDCl_3$) $\delta$ (ppm) = 167.01, 164.84, 136.67, 132.95, 131.29, 130.75, 130.28, 130.24, 129.97, 129.53, 128.16, 127.30, 127.16, 127.04, 126.85, 126.47, 125.32, 125.20, 124.96, 124.28, 122.91, 121.61, 72.01, 70.69, 70.59, 70.36, 70.12, 59.12, 40.13.

**ESI-HRMS** *m/z*: calculated $[M]^+$: 579.2482; measured $[M+H]^+$: 580.2558.

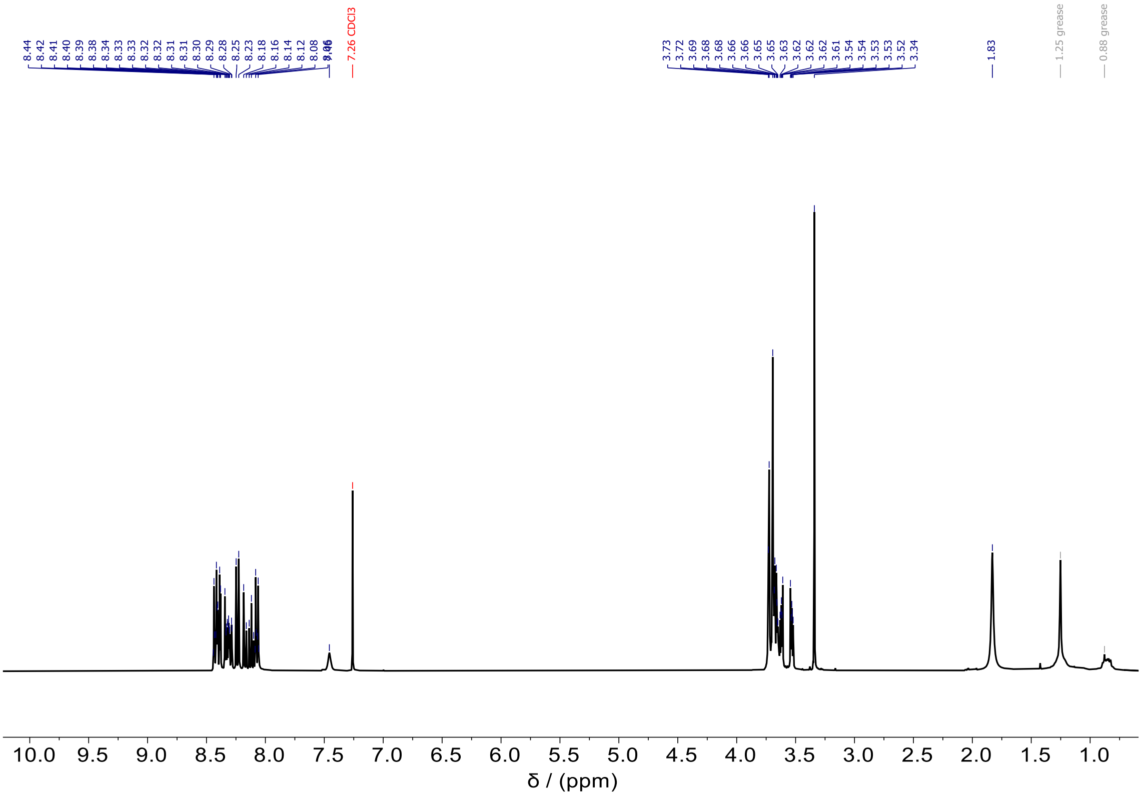

Figure 76: $^{1}$H-NMR spectrum of **5** ($CDCl_3$, 400 MHz).

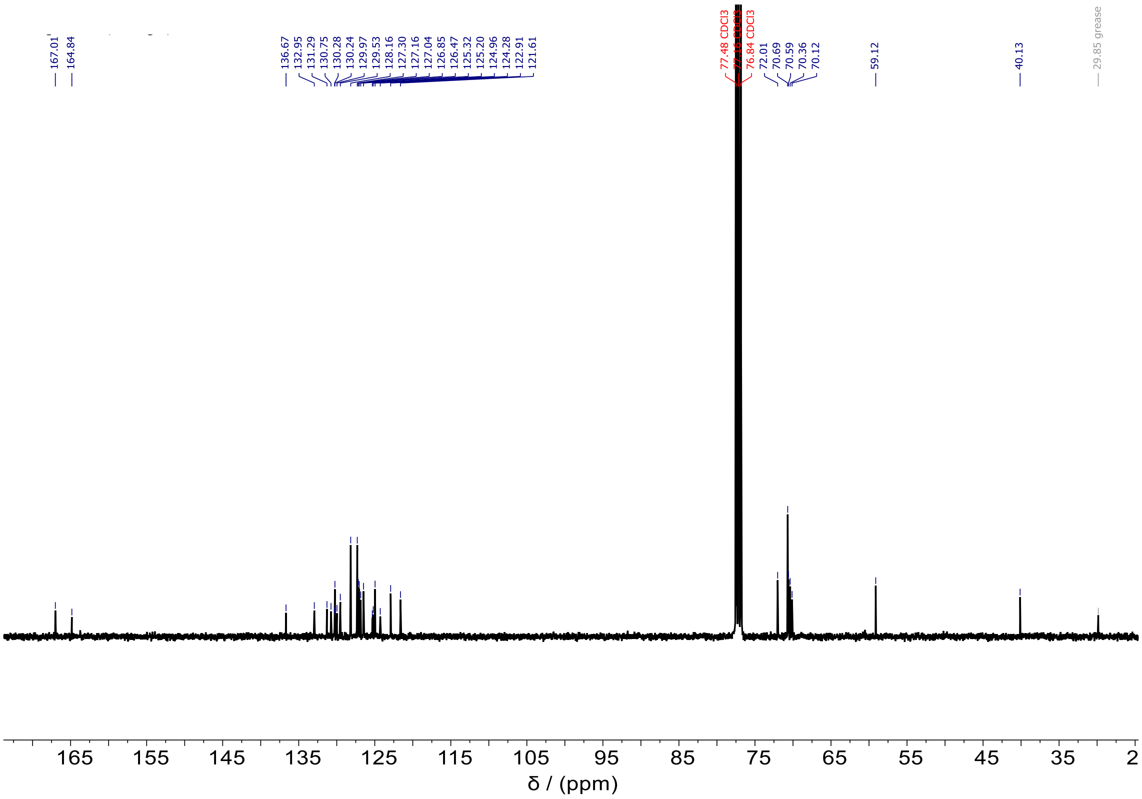

Figure 77: $^{13}$C-NMR spectrum of **5** ($CDCl_3$, 101 MHz).

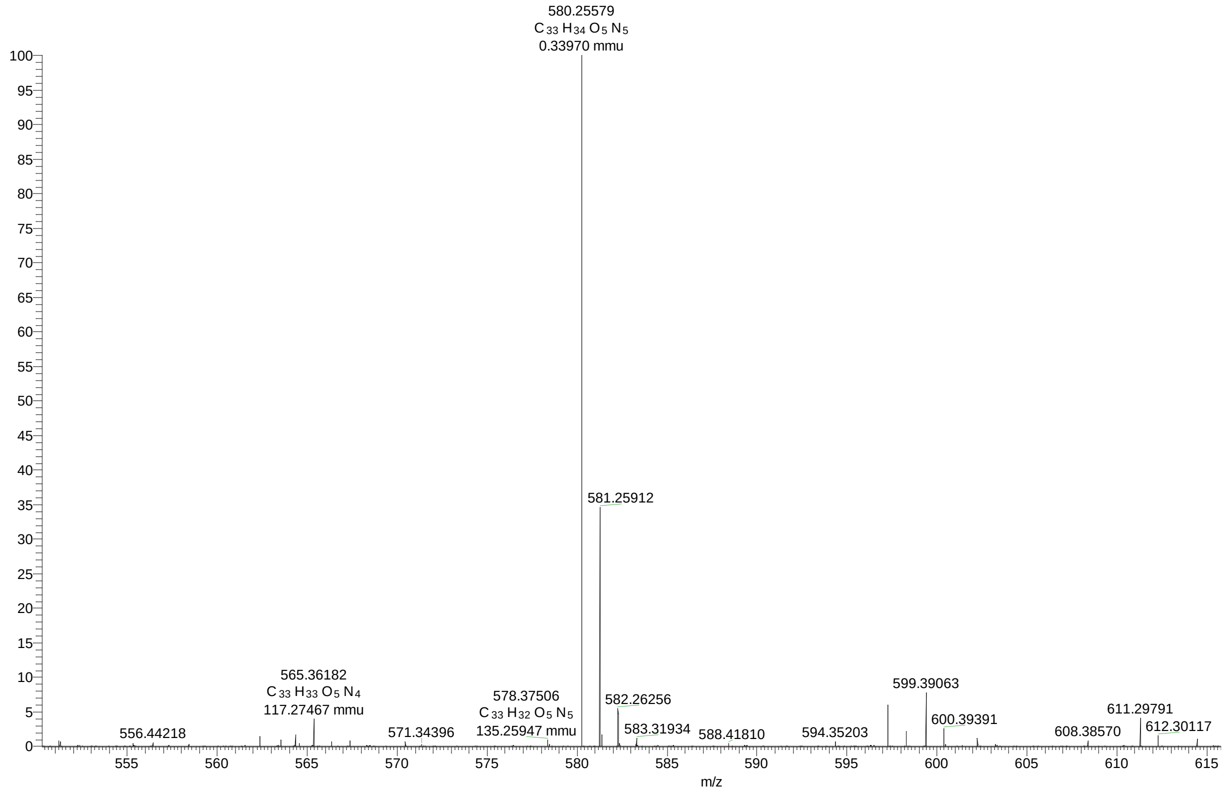

Figure 78: ESI-HRMS *m/z*: calculated [M] $^+$: 579.2482; measured [M+H]$^+$: 580.2558.

Compound **40**

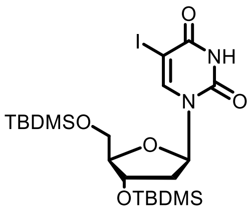

$C_{21}H_{39}IN_2O_5Si_2$
582.63 g mol$^{-1}$

2.00 g 5-Iod-2‘-desoxyuridin **39** (5.65 mmol, 1.00 equiv.) was dissolved in 50 mL dry DMF and 1.86 g TBDMS-Cl (12.1 mmol, 2.20 equiv.) and 1.52 g imidazole (22.2 mmol, 4.00 equiv.) were added and the reaction mixture stirred for 19 h at r. t. The reaction mixture was extracted with DCM (2 x 150 mL) and washed twice with 200 mL water. The organic layer was dried over $Na_2SO_4$, filtered and the solvent removed under reduced pressure. Column chromatography (DCM / MeOH 20:1) delivered 3.10 g of product **40** (5.32 mmol, 97%) of a white foam. The spectroscopic data is in agreement with literature.[218]

**$^1$H-NMR** (400 MHz, DMSO-$d_6$) $\delta$ (ppm) = 11.72 (s, 1H, NH), 7.96 (s, 1H, $H_{Aryl}$), 6.08 (dd, $J$ = 7.5, 6.0 Hz, 1H, 1‘-H), 4.35 (dt, $J$ = 6.0, 3.0 Hz, 1H, 4‘-H), 3.85 – 3.68 (m, 3H, 3’-H, 5‘-H), 2.25 – 2.07 (m, 2H,2‘-H), 0.89 (d, $J$ = 13.5 Hz, 18H, $CH_3$), 0.11-0.08 (d, $J$ = 1.6 Hz, 12H).

Compound **41**

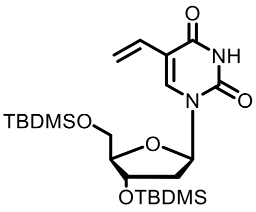

$C_{23}H_{42}N_2O_5Si_2$
482.77 g mol$^{-1}$

77 mg of palladium acetate (0.343 mmol, 0.10 equiv.), 0.179 g triphenylphosphine (0.686 mmol, 0.20 equiv.), and 3.60 mL triethylamine (26.4 mmol, 7.70 equiv.) were dissolved in approx. 6 mL DMF until a red coloration was observed. Simultaneously, in a separate flask, 2.00 g of **40** (3.43 mmol, 1.00 equiv.) and 16.9 mL of vinyl acetate (183 mmol, 53.2 equiv.) were dissolved in approximately 50 mL of dry DMF and stirred at 80 °C. The catalyst (red solution) was added to the dissolved **40** and stirred at 80 °C for 24 h. The reaction mixture was diluted with 400 mL water and 300 mL EtOAc. The combined organic phases were dried over $MgSO_4$**,** and the solvent was removed under reduced pressure. The crude product was purified by column chromatography *n*-Hex / EtOAc (4:1). Product **41** was isolated as a light-yellow solid with a yield of 877 mg (1.51 mmol, 53%). The spectroscopic data is in agreement with literature.[218]

$^1$**H-NMR** (400 MHz, DMSO-$d_6$) $\delta$ (ppm) = 11.47 (s, 1H, NH), 7.66 (s, 1H, Aryl H), 6.35 (dd, *J*=17.6, 11.5 Hz, 1H, CH), 6.13 (dd, *J* = 7.6, 6.1 Hz, 1H, 1‘-H), 5.98 (dd, *J* = 17.6, 2.2 Hz, 1H, Vinyl-$CH_2$), 5.15 (dd, *J* = 11.5, 2.2 Hz, 1H, Vinyl-$CH_2$), 4.45-4.31 (m, 1H, 4‘-H), 3.88-3.64 (m, 3H, 3‘-H, 5‘-H), 2.29 (s, 1H, 2‘-H), 2.12 (ddd, *J* = 13.4, 6.2, 3.1 Hz, 1H, 2‘-H), 0.87 (d, *J* = 3.0 Hz, 18H, TBDMS-t-Butyl), 0.07 (d, *J* = 10.9 Hz, 12H, TBDMS-$CH_3$).

Compound **20**

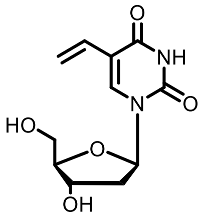

$C_{11}H_{14}N_{2}O_{5}$
254.24 g mol$^{-1}$

Under argon atmosphere 0.877 g of **41** (1.82 mmol, 1.00 equiv.) was dissolved in 10 mL anhydrous THF. 2.93 mL $Et_3N\cdot 3HF$ (3.34 g, 18.2 mmol, 10.0 equiv.) was slowly added to the reaction solution. The reaction was stirred for 16 h at r. t. The solvent was removed under reduced pressure prior to purification of the compound via column chromatography (DCM/MeOH 10:1). 521 mg of the desired product **20** (2.05 mmol, 99%) was obtained as a beige/brown foam. The spectroscopic data is in agreement with literature.[219]

**$^{1}$H-NMR** (400 MHz, acetonitrile-$d_3$) $\delta$ (ppm) = 8.16 (s, 1H), 6.41 (dd, $J$ = 17.7, 11.5 Hz, 1H), 6.12 (t, $J$ = 6.0 Hz, 1H), 5.94 (dd, $J$ = 17.7, 1.9 Hz, 1H), 5.45 (s, 2H), 5.13 (dd, $J$ = 11.4, 1.9 Hz, 1H), 4.44 (td, $J$ = 6.0, 4.4 Hz, 1H), 3.80 (dt, $J$ = 9.9, 3.6 Hz, 2H), 3.77–3.68 (m, 1H), 3.07 (q, $J$ = 7.3 Hz, 24H, $CH_2$), 2.31–2.09 (m, 2H), 1.25 (t, $J$ = 7.3 Hz, 37H, $CH_3$).

## 4.2 Visualizing the Invisible: Imaging of Ruthenium-based PACT Agents in Fixed Cancer Cells

Ruthenium-based metal complexes used in this work were synthesized and published in the PhD thesis of *Anja Busemann* at Leiden University under supervision of *Sylvestre Bonnet* in 2016. Anyhow a short overview over the used compounds will be shown below.

The ligand *i*-biq was synthesized according to literature;[220] *i*-Hdiqa, [**1**]($PF_6$)$_2$, and [**3**]($PF_6$)$_2$ followed a procedure by *Busemann et al.*[8] and [Ru(HCC-tpy)(bpy)(Hmte)]($PF_6$)$_2$ as described previously by the *Bonnet* group.[47] The following Scheme 6 is the designed synthetic route for the project with the additional alkyne group.[167]

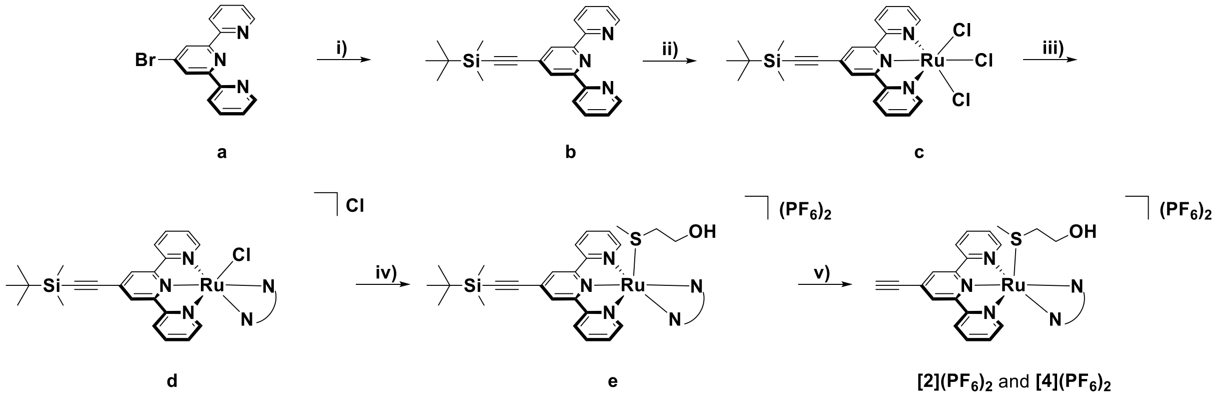

Scheme 6. Reaction scheme of the stepwise synthesis of [**2**]($PF_6$)$_2$ and [**4**]($PF_6$)$_2$. Conditions: i) CuI, $Pd(PPh_3)_2Cl_2$, TBDMS-ethyne, $Et_3N$, 80 °C, $N_2$, 7 h, 95%; ii) $RuCl_3$, EtOH, 80 °C, 16 h, 75%; iii) LiCl, $Et_3N$, EtOH/$H_2O$ 3:1), 60 °C, i-biq (overnight, 73%) or i-Hdiqa (5 h, 71%); (iv) Hmte, $H_2O$, 60 °C, $N_2$, 16 h, aq. $KPF_6$; 93 and 95%, respectively; v) KF, MeOH, 30 °C, 16 h, aq. $KPF_6$; 82 and 83%, respectively.

The final molecules were used for the work in chapter V and are shown in Figure 49.

## 4.3 Dual Labelling

The tetrazoles used in this chapter were synthesized as described in chapter 4.1. The tetrazines used in this chapter were synthesized by *Philipp Geng* in his PhD thesis at Karlsruhe Institute of Technology (KIT), 2023.[84]

# 5 General Click Experiment Procedures

## 5.1 Photoclick

The photoclick-reaction in Chapter II was monitored using UV/Vis spectrometry, fluorescence spectroscopy and RP-HPLC. The tetrazoles were used as 6.33 mM concentrated stock solutions in DMSO and the volumes required for the reaction were added to the reaction solvent (MeCN). For tetrazole **2** a concentration of 60 µM and for **6** a concentration of 30 µM was used. In addition, the nucleosides and the functional groups with which the reaction was carried out were prepared in 10 mM stock solutions and the used volumes are: 250 µM or 1 mM in cuvette experiments and 20 µM *in cellulo*. For this purpose, quartz glass cuvettes were used, which all had a layer thickness of 1 cm and contained a total volume of 1000 µL.

## 5.2 *In vitro* Photoclick Experiments

To obtain kinetic information about the photoinduced reaction of **2** and **6**, the photoclick reaction must be carefully studied. It is not a single step reaction but has two steps to be followed. The first step is the light-induced one, which is the photolysis of the tetrazole to form the nitril imine. This highly reactive intermediate reacts with the alkene or alkyne in the second step. Therefore, it must also be separated in the kinetic information whether the following kinetic information belongs to the photolysis or to the product being formed. Therefore, UV/Vis and HPLC kinetics were measured as described in the following chapter. UV/Vis kinetics were measured to receive the photolysis rate of the tetrazole. Product formation was followed *via* HPLC.

## 5.3 UV/Vis Kinetics

The determination of the second-order rate constant was firstly based on the absorbance decrease in both spectra (tetrazoles **2** and **6** in different time intervals) which correlates to the photolysis of the tetrazoles. As control, tetrazoles **2** and **6** were irradiated in quartz glass cuvettes in 25 µM concentration in different time intervals. For tetrazole **2**, the intervals were: 5 s, 10 s, 15 s, 30 s, 60 s, 300 s and 600 s. For tetrazole **6** the intervals were set to: 0.5 min, 1 min, 3 min, 6 min, 12 min, 20 min, 30 min, 50 min, 80 min and 100 min, after each interval for both tetrazoles the absorbance was measured. The same experiment was performed with the reactive counterpart. Here, a tenfold access of the reactive counterpart was applied (250 µM) and irradiated in the same intervals.

### 5.4 HPLC Kinetics with Functional Groups of the Reaction Partner

The received rate constants for the photolysis were validated employing RP-HPLC analysis in fourfold higher concentrations of the tetrazoles (100 µM **1** or **2**) while keeping the tenfold excess of the reactive counterpart (1mM). Additionally, an internal standard (anthracene in 25 µM) was added to the reaction solutions before injecting into the RP-HPLC to compensate instrumental irregularities and to determine the reaction kinetics *via* comparison of the ratio of the peak integrals of the starting material (photolysis) and product formation and the internal standard.RP-HPLC methods also allow to determine the rate constants for the product formation. Photolysis rate constants were calculated corresponding to the loss of starting material in the HPLC analysis. Product formation reaction rates were calculated with integrating the new peak in the HPLC spectrum.

## 6 Cell Experiments

Cell experiments were conducted under sterile conditions using a SafeMate 1.2 sterile bench from *Bioair*. Before use, all materials, equipment, and protective gloves were disinfected with an 80% ethanol solution in water. Consumables (e.g. pipette tips, Eppendorf tubes etc.) that were not sterile packaged were autoclaved before usage.

### 6.1 Cell Culture

KIT:

Wild type HeLa-cells and A549 cells were used for this work. They were incubated in an incubator from *Binder* at 37 °C, 5% $CO_2$ and humidity of 90% and cultured in Dulbecco’s Modified Eagle Medium (DMEM; [+] 4,5 g/l D-Glucose, L-Glutamin, [+] Pyruvat, GIBCO™) containing phenol red, supplemented with 10% fetal calf serum (FCS *Gibco™*), 1% penicillin / streptomycin (P/S).

Leiden University:

A549 cells were cultured in Dulbecco's Modified Eagle Medium containing phenol red, supplemented with 9.0% v/v FCS, 0.2% v/v P/S and 0.9% v/v Glutamine (GM) (called DMEM complete) and incubated at 37 ºC at 21% $CO_2$ in 75 $cm^2$ T-flasks. Fresh cells were passaged at least twice after being thawed and splitted once a week at 80-90% confluency.

## 6.2 MTT-Test

In a 96-well plate, $1 \cdot 10^4$ HeLa or A549 cells per well, cultured in DMEM complete, were seeded. The cells were incubated for 24 hours at 37 °C, 5% $CO_2$, and 90% humidity. Subsequently, the medium was removed, and DMEM containing the desired concentration of each compound was added to the samples. Six replicates were prepared for each concentration. The positive control was treated with 15 µL of 10% Triton-X-100 in PBS. The samples were incubated again for 72 hours at 37 °C, 5% $CO_2$, and 90% humidity. After the incubation period, 15 µL MTT reagent was added, and the samples were kept in the incubator for an additional two hours, followed by the addition of 100 µL of lysis buffer (solubilization buffer). After another 24 hours at 37 °C, 5% $CO_2$, and 90% humidity, the absorption of each well at 570 nm was determined using a plate reader. The obtained values of the same concentration were averaged, and the standard deviation was calculated. For the analysis, the absorption of the positive control was subtracted from the absorption of the samples, and the samples were normalized to the absorption of the negative control. The resulting values represent the relative viability of the cells in percentage.

## 6.3 Metabolic Labelling with Photoclick in Fixed Cells in MeCN

For metabolic labelling experiments, $1 \cdot 10^4$ cells/well were transferred into an 8-well µ-slide (*IBIDI*, Ibitreat) and incubated with nucleoside **20** (20 µM, stock solution in

DMSO) in DMEM with a final volume of 200 µL/well for 48 h. Cells were fixed with 4% paraformaldehyde in PBS for 10 min. Afterwards fixing was stopped with 50 mM glycine and 50 mM $NH_4Cl$ in PBS for 5 min and washed twice with PBS. Hereupon, the cells were washed with 0.2% Triton-X-100 in PBS for 5 min, followed by denaturation of the cells with 2 M HCl for 30 min at r. t. Cells were washed once with PBS and neutralized with 0.1 M Borax solution ($Na_2B_4O_7 \cdot 10H_2O$) for 10 min and washed twice with PBS. Then, **6** (30 µM, stock solution in DMSO) or **2** (60 µM, stock solution in DMSO) in MeCN was applied onto cells and incubated for 1 h at r. t. Accordingly, the µ-slide was photoirradiated with a 405 or 450 nm LED for 5 min (**2**) or 30 min (**6**) at 25 °C and afterwards washed with MeCN three times if not described otherwise. After irradiation, the fixed cells were imaged *via* confocal fluorescence microscopy using DRAQ5 in 10 µM as costaining for the nucleus with the excitation wavelengths and emission channels as shown in Table 6.

Table 6. Summary of the excitation wavelengths and the emission channels of the used dyes in metabolic labelling with photoclick in MeCN.

| | $\lambda_{ex}$ [nm] | $\lambda_{em}$ [nm] | *Laser Power* [%] |
|---|---|---|---|
| **2** | 405 | 420 – 500 | 10 |
| **6** | 405 | 420 – 500 | 10 |
| DRAQ5 | 636 | 650 – 700 | 5 |

## 6.4 Metabolic Labelling with Photoclick in Fixed Cells in OptiMEM

For metabolic labelling experiments, $1 \cdot 10^4$ cells/well were transferred into an 8-well µ-slide (*IBIDI*, Ibitreat) and incubated with nucleoside **20** (20 µM, stock solution in DMSO) in OptiMEM with a final volume of 200 µL/well for 48 h. Cells were fixed with 4% paraformaldehyde in PBS for 10 min. PFA was aspirated and 0.5% Triton-X-100 in PBS (200 µL) for 5 min was added. Hereafter, cells were washed with PBS. Subsequently, tetrazoles **2** and **6** were added into OptiMEM and incubated for 1 h. Accordingly, the µ-slide was irradiated with a 405 LED for 5 min (**2**) or 30 min (**6**) at 25 °C and washed once with PBS. After aspirating PBS, 10 µM DRAQ5 was added in OptiMEM and after

5 min incubation time at 37 °C imaging was performed using confocal microscopy (as described in section 3) with the excitation and emission channels, shown in Table 7.

Table 7. Summary of the excitation wavelengths and the emission channels of the used dyes in metabolic labelling with photoclick in OptiMEM.

| | $\lambda_{ex}$ [nm] | $\lambda_{em}$ [nm] | *Laser Power* [%] |
|---|---|---|---|
| **2** | 405 | 420 – 500 | 10 |
| **6** | 405 | 420 – 500 | 10 |
| DRAQ5 | 636 | 650 – 700 | 5 |

## 6.5 Metabolic Labelling with Photoclick in Live Cells in OptiMEM

For metabolic labelling experiments, $1\cdot10^4$ cells/well were transferred into an 8-well µ-slide (*IBIDI*, Ibitreat) and incubated with nucleoside **20** (20 µM, stock solution in DMSO) in OptiMEM with a final volume of 200 µL/well for 48 h. After 48 h OptiMEM was aspirated and tetrazole **3** in 60 µM concentration was added in OptiMEM and incubated for 1 h. Subsequently, the µ-slide was irradiated for 2 min with a 405 nm LED. The cells were washed with OptiMEM and DRAQ5 in OptiMEM was added, prior to 5 min incubation at 37 °C and subsequent imaging with confocal microscopy. The excitation wavelengths and emission channels are shown in Table 8.

Table 8. Summary of the excitation wavelengths and the emission channels of the used dyes in metabolic labelling with photoclick in OptiMEM in live cells.

| | $\lambda_{ex}$ [nm] | $\lambda_{em}$ [nm] | *Laser Power* [%] |
|---|---|---|---|
| **3** | 405 | 420 – 500 | 10 |
| DRAQ5 | 636 | 650 – 700 | 5 |

## 6.6 Metabolic Labelling with IEDDA in Fixed Cells in OptiMEM

For metabolic labelling experiments, $1\cdot10^4$ cells/well were transferred into an 8-well µ-slide (IBIDI, Ibitreat) and incubated with nucleoside **20** (20 µM, stock solution in DMSO) in OptiMEM with a final volume of 200 µL/well for 48 h. Cells were fixed with

4% PFA in PBS for 10 min. PFA was aspirated and 0.5% Triton-X-100 in PBS (200 µL) was added. Hereafter, cells were washed with PBS. For the IEDDA, tetrazine **I** in a concentration of 1 µM in OptiMEM was given onto the cells and incubated for 6 h. followed by immediate confocal microscopy without any additional washing steps.

Table 9. Summary of the excitation wavelength and the emission channel of the used dyes in metabolic labelling with photoclick in OptiMEM in fixed cells.

| | $\lambda_{ex}$ [nm] | $\lambda_{em}$ [nm] | *Laser Power* [%] |
|---|---|---|---|
| **I** | 488 | 650 - 700 | 10 |
| Hoechst 33342 | 405 | 415 – 460 | 10 |

## 6.7 Complex Labelling with CuAAC

A549 cells were seeded at t = 0 h in 96-well plates at a density of $5 \cdot 10^3$ cells/well (100 µL) in OptiMEM complete and incubated for 24 h at 37 °C and 21% $CO_2$. At t = 24 h, the cells were treated with aliquots (100 µL) of either [**2**]$Cl_2$ (50 µM) or [**4**]$(PF_6)_2$ (50 µM) and incubated for another 24 h. At t = 48 h, the plate was irradiated under air atmosphere using the cell-irradiation system (520 nm, 1 h, 76 J/cm$^2$) and further incubated. At t = 25 h, 1 h after irradiation, the wells were washed twice with 1x PBS (100 µL) and fixed with 4% PFA in PBS (100 µL) for 20 min. Then, PFA was aspirated, and 0.5% Triton-X-100 in PBS (100 µL) was added for 20 min. After aspiration, the wells were washed twice with BSA 3% (100 µL) for 10 min.

Hereafter, the 3% BSA solution was removed, and the click cocktail in PBS was added. For the click reaction the amount of reaction solutions was the following: 33 µL of 3 mM $CuSO_4 \cdot 5\ H_2O$ in 15 mM THPTA or 33 µL of 15 mM THPTA for Cu-free controls, 33 µL of 15 µM AlexaFluor$^{TM}$ 488-azide and 33 µL of 83 mM sodium ascorbate. Sodium ascorbate was given into the click solution as last ingredient, shortly before performing the reaction. The click mixture was kept at r. t. in dark for 1 h. Thereafter, the mixture was aspirated, and the wells were washed with 3% BSA in PBS for 10 min, PBS, 0.5% Triton-X-100, and finally PBS. Depending whether the immunostaining is included in the procedure or not it is carried out after the click reaction. If not, immediately Hoechst was added and the cells were imaged.

Materials: Black 96-well Screenstar plates (Product number #655866, *Greiner Bio-One*, Frickenhausen, Germany) were used for immunostaining; copper sulfate, sodium ascorbate, Triton-X-100, tris(3-hydroxypropyl-triazolylmethyl)amine (THPTA), phosphate buffered saline (PBS), and bovine serum albumin (BSA) were purchased from *Sigma Aldrich*; paraformaldehyde (PFA 16%) from *Alfa Aesar*; and AlexaFluor™ 488 Azide (A10266) from *Invitrogen* (*Thermo Fisher Scientific*).

## 6.8 Immunofluorescence Costaining

The costaining was performed in dim light after the complex labelling with CuAAC. Wells were washed twice with blocking buffer (5% BSA in PBS with 0.3% Triton-X-100 to block unspecific binding) for 1 h. After blocking, the primary antibodies were diluted in dilution buffer (1% BSA / 0.3% Triton-X-100 buffer in PBS). Blocking solution was aspirated and the solution of primary antibody was added and incubated overnight (lysosomes staining: LAMP1 in 1:300; Golgi apparatus staining: GM130 1:3200; ER staining: P4HB 1:1000; mitochondria staining: ATP5A 1:1000). After incubation, the wells were rinsed three times with PBS, 0.1% Triton-X-100 for 5 min. The secondary antibody was diluted in 0.1% Triton-X-100 in PBS for 1 h in dark (for lysosomes and Golgi apparatus anti-rabbit in 1:2000; ER and mitochondria anti-mouse in 1:2000 dilution). The wells were rinsed with 0.1% Triton-X-100 in PBS. After aspiration, nuclear costaining (NucBlue$^{TM}$, 1 drop/2 mL, 100 µL) was added and incubated for 1 h at r. t., followed by immediate confocal microscopy without any additional washing steps.

Materials: GM130 (D6B1) XP Rabbit mAb, LAMP1 (D2D11) XP Rabbit mAb, Anti rabbit IgG (H+L) F(ab‘) 2 Fragment AlexaFluor$^{TM}$ 647 Conjugate and Anti mouse IgG (H+L) F(ab‘) 2 Fragment AlexaFluor$^{TM}$ 647 Conjugate was purchased from *Cell Signaling – Bioké*. Anti-P4HB [RL90] Mouse (ab2792) and Anti-ATP5A antibody [15H4C4] Mouse (ab14748) was purchased from *Abcam*. NucBlue$^{TM}$ from *Invitrogen* (R37605).

Table 10. Summary of the excitation wavelength and the emission channel of the used dyes in immunofluorescence in OptiMEM in fixed cells.

| | $\lambda_{ex}$ [nm] | $\lambda_{em}$ [nm] | *Laser Power* [%] |
|---|---|---|---|
| AlexaFluor 488 azide | 488 | 510-590 | 3.10 |
| AlexaFluor 647 Conjugate | 638 | 670 - 720 | 0.72 |
| Hoechst 33342 | 405 | 415 – 460 | 3 |

## 6.9 Dual Labelling with CuAAC and IEDDA

A549 cells were seeded at t = 0 h in 18-well µ-slides at a density of $5 \cdot 10^3$ cells/well (100 µL) in OptiMEM complete and incubated for 24 h at 37 °C and 5% $CO_2$. At t = 24 h, the cells were treated with aliquots (100 µL) of [**4**]$(PF_6)_2$ (25 µM) and incubated for another 24 h. At t = 48 h, the plate was irradiated under air atmosphere using the irradiation setup from KIT with 33 mW for 30 min and was further incubated. At different incubation times after irradiation (1 h, 4 h, 6 h, 8 h and 24 h), the wells were washed with 1x PBS (100 µL) and fixed with 4% PFA in PBS (100 µL) for 20 min. Then, PFA was aspirated, and 0.5% Triton-X-100 in PBS (100 µL) was added for 20 min. After aspiration, the wells were washed twice with BSA 3% (100 µL) for 10 min.

Hereafter, the 3% BSA solution was removed, and the click mixture in PBS was added. For the click reaction the amount of reaction solutions was the following: 33 µL of 3 mM $CuSO_4$ x 5 $H_2O$ in 15 mM THPTA or 33 µL of only 15 mM THPTA for Cu-free controls, 33 µL of 15 µM AlexaFluor$^{TM}$ 488 azide, and 33 µL of 83 mM sodium ascorbate. Sodium ascorbate was given into the click cocktail, shortly before performing the reaction. The click mixture was kept at room temperature in dark for 1 h. Thereafter, the mixture was aspirated, and the wells were washed with 3% BSA in PBS for 10 min, PBS, 0.5% Triton-X-100, and finally PBS. Additionally, tetrazine **I** in a concentration of 1 µM was added for the second biothogonal labelling step, the IEDDA reaction and incubated of 6 h. Afterwards, the different wells were washed with PBS and Hoechst was added for staining of the nucleus, following by imaging with confocal microscope in different excitation, laser power and emission channels, shown in Table 11.

Table 11. Summary of the excitation wavelength and the emission channel of the used dyes in dual labelling with IEDDA in OptiMEM in fixed cells.

| | $\lambda_{ex}$ [nm] | $\lambda_{em}$ [nm] | *Laser Power* [%] |
|---|---|---|---|
| AlexaFluor 488-azide | 488 | 500-550 | 10 |
| **I** | 488 | 650 - 700 | 10 |
| Hoechst 33342 | 405 | 415 – 460 | 10 |

# IX. References

[1] G. J. Sabongi, *Chemical triggering: reactions of potential utility in industrial processes*, Springer Science & Business Media, **2012**.

[2] M. Peplow, *Nat. Biotechnol.* **2023**, *41*, 883-885.

[3] A. H. van Onzen, R. M. Versteegen, F. J. Hoeben, I. A. Filot, R. Rossin, T. Zhu, J. Wu, P. J. Hudson, H. M. Janssen, W. Ten Hoeve, *J. Am. Chem. Soc.* **2020**, *142*, 10955-10963.

[4] B. Liu, W. Ten Hoeve, R. M. Versteegen, R. Rossin, L. H. J. Kleijn, M. S. Robillard, *Chem. Eur. J.* **2023**, *29*, e202300755.

[5] Y. Chen, L. Bai, P. Zhang, H. Zhao, Q. Zhou, *Molecules* **2021**, *26*, 5679.

[6] J. A. Prescher, C. R. Bertozzi, *Nature Chem. Biol.* **2005**, *1*, 13-21.

[7] D. J. Vocadlo, H. C. Hang, E.-J. Kim, J. A. Hanover, C. R. Bertozzi, *Proc. Natl. Acad. Sci. U.S.A.* **2003**, *100*, 9116-9121.

[8] A. Busemann, I. Flaspohler, X. Q. Zhou, C. Schmidt, S. K. Goetzfried, V. H. S. van Rixel, I. Ott, M. A. Siegler, S. Bonnet, *J. Biol. Inorg. Chem.* **2021**, *26*, 667-674.

[9] P. Geng, E. List, F. Rönicke, H.-A. Wagenknecht, *Chem. Eur. J.* **2022**, *2022*, e202203156.

[10] E. M. Sletten, C. R. Bertozzi, *Angew. Chem. Int. Ed.* **2009**, *48*, 6974-6998.

[11] Y. Tian, Q. Lin, *ACS Chem. Biol.* **2019**, *14*, 2489-2496.

[12] V. Rigolot, C. Biot, C. Lion, *Angew. Chem. Int. Ed.* **2021**, *60*, 23084-23105.

[13] R. K. V. Lim, Q. Lin, *Chem. Commun.* **2010**, *46*, 1589-1600.

[14] D. M. Patterson, L. A. Nazarova, J. A. Prescher, *ACS Chem. Biol.* **2014**, *9*, 592-605.

[15] K. Krell, D. Harijan, D. Ganz, L. Doll, H. A. Wagenknecht, *Bioconjugate Chem.* **2020**, *31*, 990-1011.

[16] B. Cheng, Q. Tang, C. Zhang, X. Chen, *Annu. Rev. Anal. Chem.* **2021**, *14*, 363-387.

[17] H. Staudinger, J. Meyer, *Helv. Chim. Acta* **1919**, *2*, 635-646.

[18] R. N. Day, M. W. Davidson, *Chem. Soc. Rev.* **2009**, *38*, 2887-2921.

[19] K. Lang, J. W. Chin, *ACS Chem. Biol.* **2014**, *9*, 16-20.

[20] Z. Li, L. Qian, L. Li, J. C. Bernhammer, H. V. Huynh, J. S. Lee, S. Q. Yao, *Angew. Chem. Int. Ed.* **2016**, *55*, 2002-2006.

[21] B. D. Fairbanks, L. J. Macdougall, S. Mavila, J. Sinha, B. E. Kirkpatrick, K. S. Anseth, C. N. Bowman, *Chem. Rev.* **2021**, *121*, 6915-6990.

[22] N. Z. Fantoni, A. H. El-Sagheer, T. Brown, *Chem. Rev.* **2021**, *121*, 7122-7154.

[23] E. Saxon, C. R. Bertozzi, *Science* **2000**, *287*, 2007-2010.

[24] S. J. Luchansky, S. Argade, B. K. Hayes, C. R. Bertozzi, *Biochem.* **2004**, *43*, 12358-12366.

[25] V. V. Rostovtsev, L. G. Green, V. V. Fokin, K. B. Sharpless, *Angew. Chem. Int. Ed.* **2002**, *114*, 2708-2711.

[26] C. W. Tornøe, C. Christensen, M. Meldal, *J. Org. Chem.* **2002**, *67*, 3057-3064.

[27] R. Huisgen, L. Möbius, G. Müller, H. Stangl, G. Szeimies, J. M. Vernon, *Chem. Ber.* **1965**, *98*, 3992-4013.

[28] X. Wang, W. X. Wang, *Environ. Sci. Technol.* **2021**, *55*, 14772-14781.

[29] N. J. Agard, J. A. Prescher, C. R. Bertozzi, *J. Am. Chem. Soc.* **2004**, *126*, 15046-15047.

[30] J. M. Baskin, J. A. Prescher, S. T. Laughlin, N. J. Agard, P. V. Chang, I. A. Miller, A. Lo, J. A. Codelli, C. R. Bertozzi, *Proc. Natl. Acad. Sci. U.S.A.* **2007**, *104*, 16793-16797.

[31] A. T. Blomquist, L. H. Liu, *J. Am. Chem. Soc.* **1953**, *75*, 2153-2154.

[32] G. Wittig, A. Krebs, *Chem. Ber.* **2006**, *94*, 3260-3275.

[33] G. de Almeida, E. M. Sletten, H. Nakamura, K. K. Palaniappan, C. R. Bertozzi, *Angew. Chem. Int. Ed.* **2012**, *51*, 2443-2447.

[34] L. Li, Z. Zhang, *Molecules* **2016**, *21*, 1393.

[35] T. R. C. Qian Wang, Robert Hilgraf, Valery V. Fokin,* K. Barry Sharpless,* and M. G. Finn*, *J. Am. Chem. Soc.* **2003**, *125*, 3192-3193.

[36] H. C. Kolb, M. G. Finn, K. B. Sharpless, *Angew. Chem. Int. Ed.* **2001**, *40*, 2004-2021.

[37] J. E. Hein, V. V. Fokin, *Chem. Soc. Rev.* **2010**, *39*, 1302-1315.

[38] M. M. a. C. W. Tornøe, *Chem. Rev.* **2008**, *108*, 2952-3015.

[39] E. Haldon, M. C. Nicasio, P. J. Perez, *Org. Biomol. Chem.* **2015**, *13*, 9528-9550.

[40] H. C. Kolb, K. B. Sharpless, *Drug. Discov. Today* **2003**, *8*, 1128-1137.

[41] J. F. Lutz, G. Nanotechnology for Life Science Research, *Angew. Chem. Int. Ed.* **2007**, *46*, 1018-1025.

[42] P. M. Gramlich, C. T. Wirges, A. Manetto, T. Carell, *Angew. Chem. Int. Ed.* **2008**, *47*, 8350-8358.

[43] H. Jiang, T. Zheng, A. Lopez-Aguilar, L. Feng, F. Kopp, F. L. Marlow, P. Wu, *Bioconjugate Chem.* **2014**, *25*, 698-706.

[44] C. Uttamapinant, A. Tangpeerachaikul, S. Grecian, S. Clarke, U. Singh, P. Slade, K. R. Gee, A. Y. Ting, *Angew. Chem. Int. Ed.* **2012**, *51*, 5852-5856.

[45] C. F. Ancajas, T. J. Ricks, M. D. Best, *Chem. Phys. Lipids* **2020**, *232*, 104971.

[46] N. J. Farrer, D. M. Griffith, *Curr. Opin. Chem. Biol.* **2020**, *55*, 59-68.

[47] A. Busemann, C. Araman, I. Flaspohler, A. Pratesi, X. Q. Zhou, V. H. S. van Rixel, M. A. Siegler, L. Messori, S. I. van Kasteren, S. Bonnet, *Inorg. Chem.* **2020**, *59*, 7710-7720.

[48] V. Hong, N. F. Steinmetz, M. Manchester, M. Finn, *Bioconjugate Chem.* **2010**, *21*, 1912-1916.

[49] S. Li, L. Wang, F. Yu, Z. Zhu, D. Shobaki, H. Chen, M. Wang, J. Wang, G. Qin, U. J. Erasquin, L. Ren, Y. Wang, C. Cai, *Chem. Sci.* **2017**, *8*, 2107-2114.

[50] D. C. Kennedy, C. S. McKay, M. C. Legault, D. C. Danielson, J. A. Blake, A. F. Pegoraro, A. Stolow, Z. Mester, J. P. Pezacki, *J. Am. Chem. Soc.* **2011**, *133*, 17993-18001.

[51] T.-W. Yu, D. Anderson, *Mutat. Res.* **1997**, *379*, 201-210.

[52] D. C. Kennedy, C. S. McKay, M. C. Legault, D. C. Danielson, J. A. Blake, A. F. Pegoraro, A. Stolow, Z. Mester, J. P. Pezacki, *J. Am. Chem. Soc.* **2011**, *133*, 17993-18001.

[53] E. Stelmashook, N. Isaev, E. Genrikhs, G. Amelkina, L. Khaspekov, V. Skrebitsky, S. Illarioshkin, *Biochemistry (Mosc)* **2014**, *79*, 391-396.

[54] S. I. Presolski, V. P. Hong, M. G. Finn, *Curr. Protoc. Chem. Biol.* **2011**, *3*, 153-162.

[55] V. Hong, S. I. Presolski, C. Ma, M. G. Finn, *Angew. Chem. Int. Ed.* **2009**, *48*, 9879-9883.

[56] J. A. Codelli, J. M. Baskin, N. J. Agard, C. R. Bertozzi, *J. Am. Chem. Soc.* **2008**, *130*, 11486-11493.

[57] X. Ning, J. Guo, M. A. Wolfert, G. J. Boons, *Angew. Chem. Int. Ed.* **2008**, *47*, 2253-2255.

[58] J. Dommerholt, F. Rutjes, F. L. van Delft, *Top. Curr. Chem.* **2016**, *374*, 16.

[59] J. C. Jewett, E. M. Sletten, C. R. Bertozzi, *J. Am. Chem. Soc.* **2010**, *132*, 3688-3690.

[60] J. Dommerholt, S. Schmidt, R. Temming, L. J. Hendriks, F. P. Rutjes, J. C. van Hest, D. J. Lefeber, P. Friedl, F. L. van Delft, *Angew. Chem. Int. Ed.* **2010**, *49*, 9422-9425.

[61] I. Nikic, J. H. Kang, G. E. Girona, I. V. Aramburu, E. A. Lemke, *Nat. Protoc.* **2015**, *10*, 780-791.

[62] X. Ren, A. H. El-Sagheer, T. Brown, *Nucleic Acids Res.* **2016**, *44*, e79.

[63] J. M. Fehr, N. Myrthil, A. L. Garrison, T. W. Price, S. A. Lopez, R. Jasti, *Chem. Sci.* **2023**, *14*, 2839-2848.

[64] N. K. Devaraj, R. Weissleder, S. A. Hilderbrand, *Bioconjugate Chem.* **2008**, *19*, 2297-2299.

[65] M. L. Blackman, M. Royzen, J. M. Fox, *J. Am. Chem. Soc.* **2008**, *130*, 13518-13519.

[66] O. Diels, K. Alder, *Liebigs Ann. Chem.* **1928**, *460*, 98-122.

[67] J. Sauer, *Angew. Chem. Int. Ed.* **2003**, *6*, 16-33.

[68] J. G. Martin, R. K. Hill, *Chem. Rev.* **1961**, *61*, 537-562.

[69] B. L. Oliveira, Z. Guo, G. J. L. Bernardes, *Chem. Soc. Rev.* **2017**, *46*, 4895-4950.

[70] J. Sauer, R. Sustmann, *Angew. Chem. Int. Ed.* **1980**, *19*, 779-807.

[71] K. Lang, L. Davis, J. Torres-Kolbus, C. Chou, A. Deiters, J. W. Chin, *Nat. Chem.* **2012**, *4*, 298-304.

[72] D. Ganz, P. Geng, H. A. Wagenknecht, *ACS Chem. Biol.* **2023**, *18*, 1054-1059.

[73] H. Frisch, D. E. Marschner, A. S. Goldmann, C. Barner-Kowollik, *Angew. Chem. Int. Ed.* **2018**, *57*, 2036-2045.

[74] D. Wang, W. Chen, Y. Zheng, C. Dai, K. Wang, B. Ke, B. Wang, *Org. Biomol. Chem.* **2014**, *12*, 3950-3955.

[75] A. Darko, S. Wallace, O. Dmitrenko, M. M. Machovina, R. A. Mehl, J. W. Chin, J. M. Fox, *Chem. Sci.* **2014**, *5*, 3770-3776.

[76] Y. J. Lee, Y. Kurra, Y. Yang, J. Torres-Kolbus, A. Deiters, W. R. Liu, *Chem. Commun.* **2014**, *50*, 13085-13088.

[77] M. Handula, K. T. Chen, Y. Seimbille, *Molecules* **2021**, *26*, 4640.

[78] M. R. Karver, R. Weissleder, S. A. Hilderbrand, *Bioconjugate Chem.* **2011**, *22*, 2263-2270.

[79] B. Pinto-Pacheco, W. P. Carbery, S. Khan, D. B. Turner, D. Buccella, *Angew. Chem. Int. Ed.* **2020**, *59*, 22140-22149.

[80] A. Wieczorek, P. Werther, J. Euchner, R. Wombacher, *Chem. Sci.* **2017**, *8*, 1506-1510.

[81] H. Wu, N. K. Devaraj, *Acc. Chem. Res.* **2018**, *51*, 1249-1259.

[82] S. K. Choi, J. Kim, E. Kim, *Molecules* **2021**, *26*, 1868.

[83] G. B. Cserep, A. Herner, P. Kele, *Methods Appl. Fluoresc.* **2015**, *3*, 042001.

[84] B. Pfeuffer, P. Geng, H. A. Wagenknecht, *ChemBioChem* **2024**, *25*, e202300739.

[85] G. S. Kumar, Q. Lin, *Chem. Rev.* **2021**, *121*, 6991-7031.

[86] Y. Fu, N. A. Simeth, W. Szymanski, B. L. Feringa, *Nat. Rev. Chem.* **2024**.

[87] H. Zhang, M. Fang, Q. Lin, *Top. Curr. Chem.* **2024**, *382*, 1.

[88] M. A. Tasdelen, Y. Yagci, *Tetrahedron Lett.* **2010**, *51*, 6945-6947.

[89] B. Sandmann, B. Happ, J. Vitz, M. D. Hager, P. Burtscher, N. Moszner, U. S. Schubert, *Polym. Chem.* **2013**, *4*.

[90] P. Klan, T. Solomek, C. G. Bochet, A. Blanc, R. Givens, M. Rubina, V. Popik, A. Kostikov, J. Wirz, *Chem. Rev.* **2013**, *113*, 119-191.

[91] D. H. Rich, S. K. Gurwara, *Chem. Commun.* **1973**, 610-611.

[92] M. Hauf, F. Richter, T. Schneider, T. Faidt, B. M. Martins, T. Baumann, P. Durkin, H. Dobbek, K. Jacobs, A. Moglich, N. Budisa, *ChemBioChem* **2017**, *18*, 1819-1823.

[93] A. Schönberg, A. Mustafa, *J. Chem. Soc.* **1944**, 387-387.

[94] Y. Fu, K. Wu, G. Alachouzos, N. A. Simeth, T. Freese, M. Falkowski, W. Szymanski, H. Zhang, B. L. Feringa, *Adv. Funct. Mater.* **2023**, *33*.

[95] J. Li, H. Kong, L. Huang, B. Cheng, K. Qin, M. Zheng, Z. Yan, Y. Zhang, *J. Am. Chem. Soc.* **2018**, *140*, 14542-14546.

[96] J. S. Clovis, A. Eckell, R. Huisgen, R. Sustmann, *Chem. Ber.* **1967**, *100*, 60-70.

[97] M. Breugst, H. U. Reissig, *Angew. Chem. Int. Ed.* **2020**, *59*, 12293-12307.

[98] Y. Wang, C. I. Vera, Q. Lin, *Org. Lett.* **2007**, *9*, 4155-4158.

[99] W. Song, Y. Wang, J. Qu, Q. Lin, *J. Am. Chem. Soc.* **2008**, *130*, 9654-9655.

[100] W. Song, Y. Wang, J. Qu, M. M. Madden, Q. Lin, *Angew. Chem. Int. Ed.* **2008**, *47*, 2832-2835.

[101] L. Rieger, B. Pfeuffer, H.-A. Wagenknecht, *RSC Chem. Biol.* **2023**.

[102] W. Song, Y. Wang, J. Qu, M. M. Madden, Q. Lin, *Angew. Chem. Int. Ed.* **2008**, *120*, 2874-2877.

[103] Y. Wang, W. J. Hu, W. Song, R. K. V. Lim, Q. Lin, *Org. Lett.* **2008**, *10*, 3725-3728.

[104] P. An, Z. Yu, Q. Lin, *Chem. Commun.* **2013**, *49*, 9920-9922.

[105] Z. Yu, L. Y. Ho, Z. Wang, Q. Lin, *Bioorg. Med. Chem. Lett.* **2011**, *21*, 5033-5036.

[106] H. Zhang, M. Fang, Q. Lin, *Top. Curr. Chem.* **2023**, *382*, 1.

[107] X. S. Wang, Y. J. Lee, W. R. Liu, *Chem. Commun.* **2014**, *50*, 3176-3179.

[108] S. Jiang, X. Wu, H. Liu, J. Deng, X. Zhang, Z. Yao, Y. Zheng, B. Li, Z. Yu, *ChemPhotoChem* **2020**, *4*, 327-331.

[109] P. An, T. M. Lewandowski, T. G. Erbay, P. Liu, Q. Lin, *J. Am. Chem. Soc.* **2018**, *140*, 4860-4868.

[110] S. Zhao, J. Dai, M. Hu, C. Liu, R. Meng, X. Liu, C. Wang, T. Luo, *Chem. Commun.* **2016**, *52*, 4702-4705.

[111] Z. Yu, T. Y. Ohulchanskyy, P. An, P. N. Prasad, Q. Lin, *J. Am. Chem. Soc.* **2013**, *135*, 16766-16769.

[112] Z. Yu, L. Y. Ho, Q. Lin, *J. Am. Chem. Soc.* **2011**, *133*, 11912-11915.

[113] B. Lehmann, H.-A. Wagenknecht, *Org. Biomol. Chem.* **2018**, *16*, 7579-7582.

[114] K. Krell, H.-A. Wagenknecht, *Biomol.* **2020**, *10*, 480.

[115] H. A. Wagenknecht, *ChemPhysChem* **2013**, *14*, 3197-3198.

[116] A. N. Bashkatov, E. A. Genina, V. I. Kochubey, V. V. Tuchin, *J. Phys. D: Appl. Phys.* **2005**, *38*, 2543-2555.

[117] A. Hantzsch, A. Vagt, *Liebigs Ann. Chem.* **2006**, *314*, 339-369.

[118] S. Ito, Y. Tanaka, A. Kakehi, K.-i. Kondo, *Bull. Chem. Soc. Jpn* **1976**, *49*, 1920-1923.

[119] M. Ramanathan, Y. H. Wang, S. T. Liu, *Org. Lett.* **2015**, *17*, 5886-5889.

[120] P. Lederhose, K. N. Wust, C. Barner-Kowollik, J. P. Blinco, *Chem. Commun.* **2016**, *52*, 5928-5931.

[121] P. W. Kamm, J. P. Blinco, A. N. Unterreiner, C. Barner-Kowollik, *Chem. Commun.* **2021**, *57*, 3991-3994.

[122] F. M. K. Elekonawo, S. Lutje, G. M. Franssen, D. L. Bos, D. M. Goldenberg, O. C. Boerman, M. Rijpkema, *EJNMMI Res.* **2019**, *9*, 86.

[123] Y. Wang, J. Zhang, B. Han, L. Tan, W. Cai, Y. Li, Y. Su, Y. Yu, X. Wang, X. Duan, H. Wang, X. Shi, J. Wang, X. Yang, T. Liu, *Nat. Commun.* **2023**, *14*, 974.

[124] M. Kubeil, I. I. S. Martínez, M. Bachmann, K. Kopka, K. L. Tuck, H. Stephan, *Pharmaceuticals* **2022**, *15*.

[125] C. Simon, C. Lion, C. Spriet, F. Baldacci-Cresp, S. Hawkins, C. Biot, *Angew. Chem. Int. Ed.* **2018**, *57*, 16665-16671.

[126] R. M. Bednar, S. Jana, S. Kuppa, R. Franklin, J. Beckman, E. Antony, R. B. Cooley, R. A. Mehl, *ACS Chem. Biol.* **2021**, *16*, 2612-2622.

[127] W. Yi, P. Xiao, X. Liu, Z. Zhao, X. Sun, J. Wang, L. Zhou, G. Wang, H. Cao, D. Wang, Y. Li, *Signal Transduct. Target. Ther.* **2022**, *7*, 386.

[128] M. Smeenk, J. Agramunt, K. M. Bonger, *Curr. Opin. Chem. Biol.* **2021**, *60*, 79-88.

[129] F. Peschke, A. Taladriz-Sender, M. J. Andrews, A. J. B. Watson, G. A. Burley, *Angew. Chem. Int. Ed.* **2023**, *62*, e202313063.

[130] M. K. Narayanam, Y. Liang, K. N. Houk, J. M. Murphy, *Chem. Sci.* **2016**, *7*, 1257-1261.

[131] J. Schoch, M. Staudt, A. Samanta, M. Wiessler, A. Jaschke, *Bioconjugate Chem.* **2012**, *23*, 1382-1386.

[132] Y. Liang, J. L. Mackey, S. A. Lopez, F. Liu, K. N. Houk, *J. Am. Chem. Soc.* **2012**, *134*, 17904-17907.

[133] M. R. Karver, R. Weissleder, S. A. Hilderbrand, *Angew. Chem. Int. Ed.* **2012**, *51*, 920-922.

[134] N. Seul, D. Lamade, P. Stoychev, M. Mijic, R. T. Michenfelder, L. Rieger, P. Geng, H. A. Wagenknecht, *Angew. Chem. Int. Ed.* **2024**, *63*, e202403044.

[135] J. Yang, J. Seckute, C. M. Cole, N. K. Devaraj, *Angew. Chem. Int. Ed.* **2012**, *51*, 7476-7479.

[136] D. M. Patterson, L. A. Nazarova, B. Xie, D. N. Kamber, J. A. Prescher, *J. Am. Chem. Soc.* **2012**, *134*, 18638-18643.

[137] Z. Yu, Y. Pan, Z. Wang, J. Wang, Q. Lin, *Angew. Chem. Int. Ed.* **2012**, *51*, 10600-10604.

[138] F. Bray, M. Laversanne, H. Sung, J. Ferlay, R. L. Siegel, I. Soerjomataram, A. Jemal, *CA: Cancer J. Clin.* **2024**, *74*, 229-263.

[139] D. T. Debela, S. G. Muzazu, K. D. Heraro, M. T. Ndalama, B. W. Mesele, D. C. Haile, S. K. Kitui, T. Manyazewal, *SAGE Open Med.* **2021**, *9*, 20503121211034366.

[140] R. E. Nicoletto, C. M. Ofner, 3rd, *Cancer Chemother. Pharmacol.* **2022**, *89*, 285-311.

[141] J. Sharifi-Rad, C. Quispe, J. K. Patra, Y. D. Singh, M. K. Panda, G. Das, C. O. Adetunji, O. S. Michael, O. Sytar, L. Polito, J. Zivkovic, N. Cruz-Martins, M. Klimek-Szczykutowicz, H. Ekiert, M. I. Choudhary, S. A. Ayatollahi, B. Tynybekov, F. Kobarfard, A. C. Muntean, I. Grozea, S. D. Dastan, M. Butnariu, A. Szopa, D. Calina, *Oxid. Med. Cell. Longev.* **2021**, *2021*, 3687700.

[142] K. V. Huber, E. Salah, B. Radic, M. Gridling, J. M. Elkins, A. Stukalov, A. S. Jemth, C. Gokturk, K. Sanjiv, K. Stromberg, T. Pham, U. W. Berglund, J. Colinge, K. L. Bennett, J. I. Loizou, T. Helleday, S. Knapp, G. Superti-Furga, *Nature* **2014**, *508*, 222-227.

[143] S. Ghosh, *Bioorg. Chem.* **2019**, *88*, 102925.

[144] X. Li, J. Kim, J. Yoon, X. Chen, *Adv. Mater.* **2017**, *29*.

[145] E. Wiltshaw, *Platin. Met. Rev.* **1979**, *23*, 90-98.

[146] R. J. Browning, P. J. T. Reardon, M. Parhizkar, R. B. Pedley, M. Edirisinghe, J. C. Knowles, E. Stride, *ACS Nano.* **2017**, *11*, 8560-8578.

[147] A. M. Florea, D. Busselberg, *Cancers (Basel)* **2011**, *3*, 1351-1371.

[148] E. Alessio, L. Messori, *Molecules* **2019**, *24*.

[149] B. J. Park, P. Raha, J. Pankovich, M. Bazett, *Cancers (Basel)* **2022**, *15*.

[150] S. Monro, K. L. Colon, H. Yin, J. Roque, 3rd, P. Konda, S. Gujar, R. P. Thummel, L. Lilge, C. G. Cameron, S. A. McFarland, *Chem. Rev.* **2019**, *119*, 797-828.

[151] C. G. Hartinger, M. A. Jakupec, S. Zorbas-Seifried, M. Groessl, A. Egger, W. Berger, H. Zorbas, P. J. Dyson, B. K. Keppler, *Chem. Biodivers.* **2008**, *5*, 2140-2155.

[152] C. G. Hartinger, S. Zorbas-Seifried, M. A. Jakupec, B. Kynast, H. Zorbas, B. K. Keppler, *J. Inorg. Biochem.* **2006**, *100*, 891-904.

[153] Y. Arenas, S. Monro, G. Shi, A. Mandel, S. McFarland, L. Lilge, *Photodiagnosis Photodyn. Ther.* **2013**, *10*, 615-625.

[154] P. Agostinis, K. Berg, K. A. Cengel, T. H. Foster, A. W. Girotti, S. O. Gollnick, S. M. Hahn, M. R. Hamblin, A. Juzeniene, D. Kessel, M. Korbelik, J. Moan, P. Mroz, D. Nowis, J. Piette, B. C. Wilson, J. Golab, *CA: Cancer J. Clin.* **2011**, *61*, 250-281.

[155] S. Bonnet, *Dalton Trans.* **2018**, *47*, 10330-10343.

[156] S. Bonnet, *J. Am. Chem. Soc.* **2023**, *145*, 23397-23415.

[157] Y. Zhuang, K. Liu, Q. He, X. Gu, C. Jiang, J. Wu, *MedComm.* **2023**, *4*, e203.

[158] F. Borgia, R. Giuffrida, E. Caradonna, M. Vaccaro, F. Guarneri, S. P. Cannavo, *Biomedicines* **2018**, *6*.

[159] N. A. Kratochwil, Z. Guo, P. del Socorro Murdoch, J. A. Parkinson, P. J. Bednarski, P. J. Sadler, *J. Am. Chem. Soc.* **1998**, *120*, 8253-8254.

[160] L. Zayat, C. Calero, P. Alborés, L. Baraldo, R. Etchenique, *J. Am. Chem. Soc.* **2003**, *125*, 882-883.

[161] K. S. Lovejoy, S. J. Lippard, *Dalton Trans.* **2009**, 10651-10659.

[162] A. Juris, V. Balzani, F. Barigelletti, S. Campagna, P. Belser, A. v. von Zelewsky, *Coord. Chem. Rev.* **1988**, *84*, 85-277.

[163] C. R. Hecker, P. E. Fanwick, D. R. McMillin, *Inorg. Chem.* **1991**, *30*, 659-666.

[164] T. J. Meyer, *Pure Appl. Chem.* **1986**, *58*, 1193-1206.

[165] L. M. Loftus, J. J. Rack, C. Turro, *Chem. Commun.* **2020**, *56*, 4070-4073.

[166] T. N. Singh, C. Turro, *Inorg. Chem.* **2004**, *43*, 7260-7262.

[167] A. Busemann, Leiden University **2019**.

[168] E. P. van Geest, S. K. Gotzfried, D. M. Klein, N. Salitra, S. Popal, Y. Husiev, C. J. Van der Griend, X. Zhou, M. A. Siegler, G. F. Schneider, S. Bonnet, *Photochem. Photobiol.* **2023**, *99*, 777-786.

[169] C. Molenaar, J.-M. Teuben, R. J. Heetebrij, H. J. Tanke, J. Reedijk, *J. Biol. Inorg. Chem.* **2000**, *5*, 655-665.

[170] R. Safaei, K. Katano, B. J. Larson, G. Samimi, A. K. Holzer, W. Naerdemann, M. Tomioka, M. Goodman, S. B. Howell, *Clin. Cancer Res.* **2005**, *11*, 756-767.

[171] R. Safaei, B. J. Larson, T. C. Cheng, M. A. Gibson, S. Otani, W. Naerdemann, S. B. Howell, *Mol. Cancer Ther.* **2005**, *4*, 1595-1604.

[172] A. A. Nazarov, J. Risse, W. H. Ang, F. Schmitt, O. Zava, A. Ruggi, M. Groessl, R. Scopelitti, L. Juillerat-Jeanneret, C. G. Hartinger, P. J. Dyson, *Inorg. Chem.* **2012**, *51*, 3633-3639.

[173] A. Bahreman, J.-A. Cuello-Garibo, S. Bonnet, *Dalton Trans.* **2014**, *43*, 4494-4505.

[174] A. Luengo, I. Marzo, M. Reback, I. M. Daubit, V. Fernandez-Moreira, N. Metzler-Nolte, M. C. Gimeno, *Chem. Eur. J.* **2020**, *26*, 12158-12167.

[175] M. Zhou, Q. Li, R. Wang, *ChemMedChem* **2016**, *11*, 738-756.

[176] M. V. Babak, S. M. Meier, K. V. M. Huber, J. Reynisson, A. A. Legin, M. A. Jakupec, A. Roller, A. Stukalov, M. Gridling, K. L. Bennett, J. Colinge, W. Berger, P. J. Dyson, G. Superti-Furga, B. K. Keppler, C. G. Hartinger, *Chem. Sci.* **2015**, *6*, 2449-2456.

[177] J. D. White, M. F. Osborn, A. D. Moghaddam, L. E. Guzman, M. M. Haley, V. J. DeRose, *J. Am. Chem. Soc.* **2013**, *135*, 11680-11683.

[178] R. M. Cunningham, V. J. DeRose, *ACS Chem. Biol.* **2017**, *12*, 2737-2745.

[179] S. K. Fung, T. Zou, B. Cao, P.-Y. Lee, Y. M. E. Fung, D. Hu, C.-N. Lok, C.-M. Che, *Angew. Chem. Int. Ed.* **2017**, *129*, 3950-3954.

[180] S. Ding, X. Qiao, J. Suryadi, G. S. Marrs, G. L. Kucera, U. Bierbach, *Angew. Chem. Int. Ed.* **2013**, *52*, 3350-3354.

[181] R. Wirth, J. D. White, A. D. Moghaddam, A. L. Ginzburg, L. N. Zakharov, M. M. Haley, V. J. DeRose, *J. Am. Chem. Soc.* **2015**, *137*, 15169-15175.

[182] D. Hu, Y. Liu, Y.-T. Lai, K.-C. Tong, Y.-M. Fung, C.-N. Lok, C.-M. Che, *Angew. Chem. Int. Ed.* **2016**, *55*, 1387-1391.

[183] R. Masuma, S. Kashima, M. Kurasaki, T. Okuno, *J. Photochem. Photobiol. B* **2013**, *125*, 202-208.

[184] S. Arndt, H. A. Wagenknecht, *Angew. Chem. Int. Ed.* **2014**, *53*, 14580-14582.

[185] S. H. Szajnman, W. Yan, B. N. Bailey, R. Docampo, E. Elhalem, J. B. Rodriguez, *J. Med. Chem.* **2000**, *43*, 1826-1840.

[186] S. Arndt, Karlsruhe Insitute of Technology (KIT) **2016**.

[187] P. Kamm, Karlsruhe Institute of Technology (KIT) **2022**.

[188] G. Molteni, A. Ponti, *Molecules* **2017**, *22*.

[189] G. S. Kumar, S. Racioppi, E. Zurek, Q. Lin, *J. Am. Chem. Soc.* **2022**, *144*, 57-62.

[190] Z. Yu, Q. Lin, *J. Am. Chem. Soc.* **2014**, *136*, 4153-4156.

[191] J. I. H. Knaack, C. Meier, *ChemMedChem* **2024**, *19*, e202400160.

[192] A. Spampinato, E. Kuzmova, R. Pohl, V. Sykorova, M. Vrabel, T. Kraus, M. Hocek, *Bioconjugate Chem.* **2023**, *34*, 772-780.

[193] M. Kuba, P. Khoroshyy, M. Lepsik, E. Kuzmova, D. Kodr, T. Kraus, M. Hocek, *Angew. Chem. Int. Ed.* **2023**, e202307548.

[194] Y. Wu, G. Guo, J. Zheng, D. Xing, T. Zhang, *ACS Sens.* **2019**, *4*, 44-51.

[195] T. Mosmann, *J. Immunol. Methods* **1983**, *65*, 55-63.

[196] X. Li, L. Chen, M. Huang, S. Zeng, J. Zheng, S. Peng, Y. Wang, H. Cheng, S. Li, *Asian J. Pharm. Sci.* **2023**, *18*, 100775.

[197] L. N. Lameijer, D. Ernst, S. L. Hopkins, M. S. Meijer, S. H. C. Askes, S. E. Le Devedec, S. Bonnet, *Angew. Chem. Int. Ed.* **2017**, *56*, 11549-11553.

[198] S. Bonnet, *Dalton Trans.* **2018**, *47*, 10330-10343.

[199] J. A. Cuello-Garibo, M. S. Meijer, S. Bonnet, *Chem. Commun.* **2017**, *53*, 6768-6771.

[200] R. E. Goldbach, I. Rodriguez-Garcia, J. H. van Lenthe, M. A. Siegler, S. Bonnet, *Chem. Eur. J.* **2011**, *17*, 9924-9929.

[201] B. Siewert, M. Langerman, Y. Hontani, J. T. M. Kennis, V. H. S. van Rixel, B. Limburg, M. A. Siegler, V. Talens Saez, R. E. Kieltyka, S. Bonnet, *Chem. Commun.* **2017**, *53*, 11126-11129.

[202] L. N. Lameijer, T. G. Brevé, V. H. S. van Rixel, S. H. C. Askes, M. A. Siegler, S. Bonnet, *Chem. Eur. J.* **2018**, *24*, 2709-2717.

[203] S. Hopkins, B. Siewert, S. Askes, P. Veldhuizen, R. Zwier, M. Heger, S. Bonnet, *Photochem. Photobiol. Sci.* **2016**, *15*, 644-653.

[204] K. Im, S. Mareninov, M. F. P. Diaz, W. H. Yong, *An introduction to performing immunofluorescence staining*, Springer, **2019**.

[205] K. Cho, X. Wang, S. Nie, Z. Chen, D. M. Shin, *Clin. Cancer Res.* **2008**, *14*, 1310-1316.

[206] F. Zhao, W. Wang, W. Wu, *Dalton Trans.* **2021**, *50*, 3536-3541.

[207] L. Zhu, H. Liu, Y. Dou, Q. Luo, L. Gu, X. Liu, Q. Zhou, J. Han, F. Wang, *Int. J. Mol. Sci.* **2023**, *24*.

[208] E. J. Parkinson-Lawrence, C. J. Dean, M. Chang, J. J. Hopwood, P. J. Meikle, D. A. Brooks, *Cell. Immunol.* **2005**, *236*, 161-166.

[209] N. Nakamura, C. Rabouille, R. Watson, T. Nilsson, N. Hui, P. Slusarewicz, T. E. Kreis, G. Warren, *J. Cell Biol.* **1995**, *131*, 1715-1726.

[210] A. Kodani, C. Sütterlin, *Mol. Biol. Cell* **2008**, *19*, 745-753.

[211] S. K. Goetzfried, M. L. Hakkennes, A. Busemann, S. Bonnet, *ChemRxiv* **2024**.

[212] K. W. Dunn, M. M. Kamocka, J. H. McDonald, *Am. J. Physiol. Cell Physiol.* **2011**, *300*, C723-742.

[213] A. E. Carpenter, T. R. Jones, M. R. Lamprecht, C. Clarke, I. H. Kang, O. Friman, D. A. Guertin, J. H. Chang, R. A. Lindquist, J. Moffat, P. Golland, D. M. Sabatini, *Genome Biol.* **2006**, *7*, R100.

[214] A. N. Hidayatullah, E. Wachter, D. K. Heidary, S. Parkin, E. C. Glazer, *Inorg. Chem.* **2014**, *53*, 10030-10032.

[215] L. N. Lameijer, S. L. Hopkins, T. G. Breve, S. H. Askes, S. Bonnet, *Chem. Eur. J.* **2016**, *22*, 18484-18491.

[216] L. Rieger, Karlsruhe Institute of Technology (KIT) **2021**.

[217] L. Sun, J. Ding, W. Xing, Y. Gai, J. Sheng, D. Zeng, *Bioconjugate Chem.* **2016**, *27*, 1200-1204.

[218] H. Sugiyama, S. Matsuda, K. Kino, Q.-M. Zhang, S. Yonei, I. Saito, *Tetrahedron Lett.* **1996**, *37*, 9067-9070.

[219] S. Nakamura, S. Ogasawara, S. Matuda, I. Saito, K. Fujimoto, *Molecules* **2011**, *17*, 163-178.

[220] T. Funayama, M. Kato, H. Kosugi, M. Yagi, J. Higuchi, S. Yamauchi, *Bull. Chem. Soc. Jpn* **2000**, *73*, 1541-1550.

# X. Appendix

## 1 Metabolic Labelling of DNA by Means of the Photoclick Reaction Triggered with Visible Light

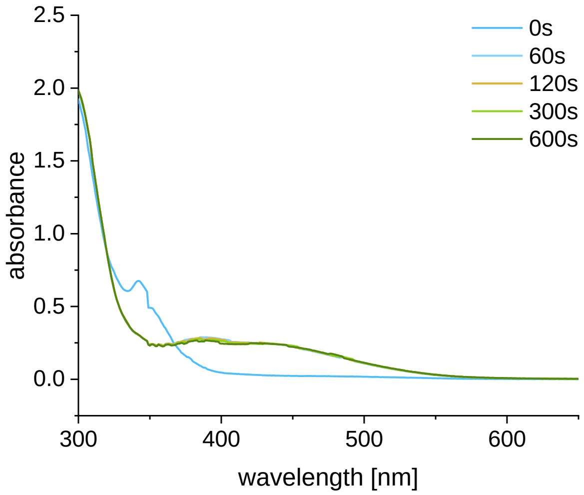

Figure A 1. Time-dependent UV/Vis absorbance of the photoclick reaction between **2** (25 µM) and **20** (250µM) in MeCN. The irradiation lasted until 60 s, but the reaction was followed until 600 s. Only the reaction to the pyrazoline is taking place. Therefore, it is concluded that the second reaction to form the pyrazole is light-induced as well.

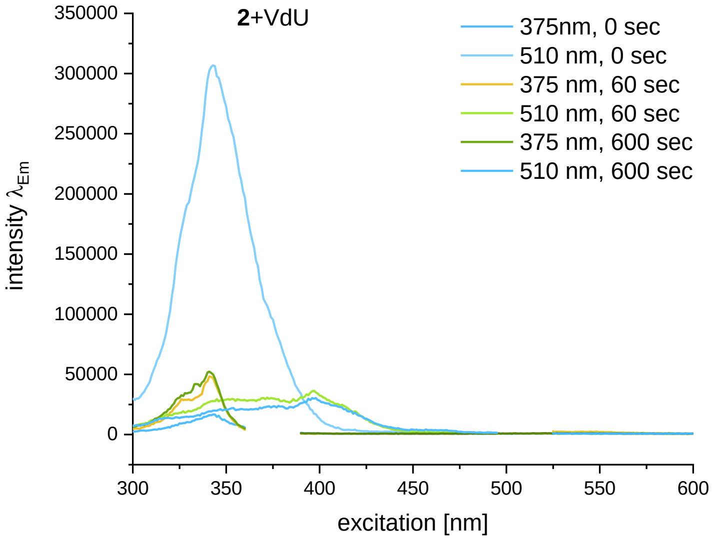

Figure A 2. Time-dependent excitation spectra of the photoclick reaction of **2** (25 µM) and **20** (250 µM) in MeCN, emission measured at 375 and 510 nm.

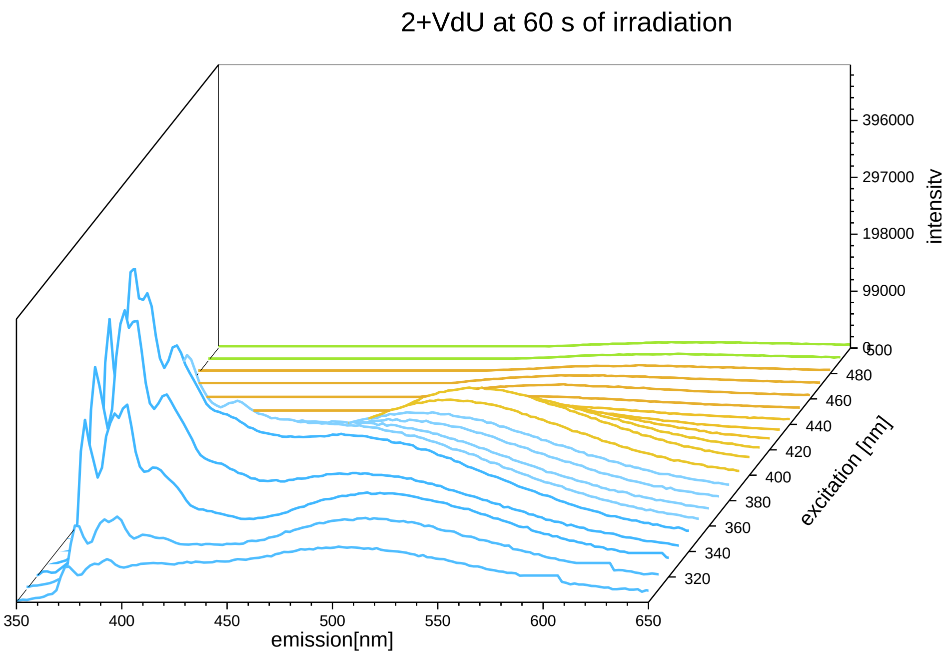

Figure A 3. 3D fluorescence after the “photoclick” reaction of **2** (25 µM) and **20** (250 µM) in MeCN.

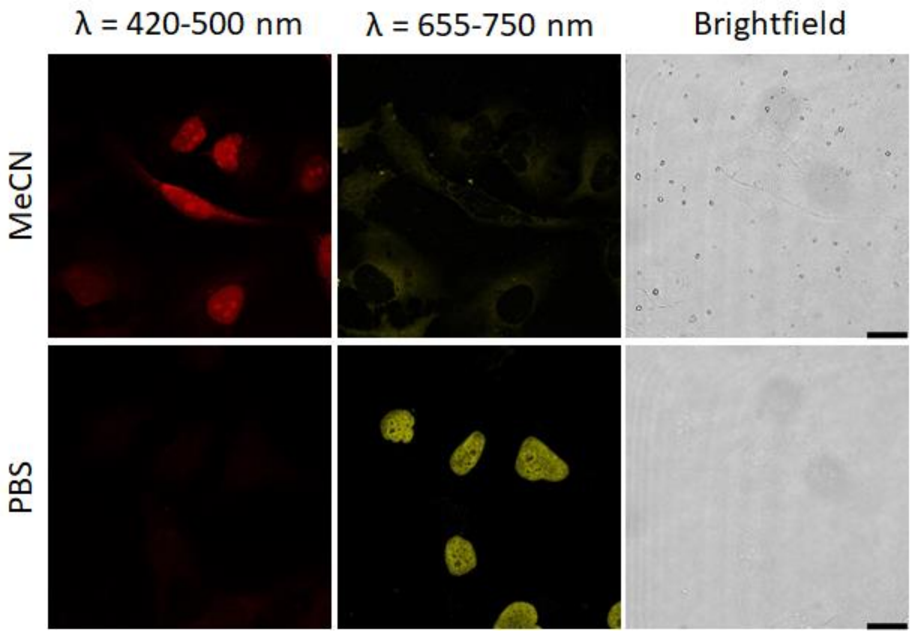

Figure A 4. Control staining experiments with **DRAQ5** (20 µM) that stains nuclear DNA in PBS and **2** (60 µM) staining the nuclear DNA in MeCN. Scale bar: 20 µm

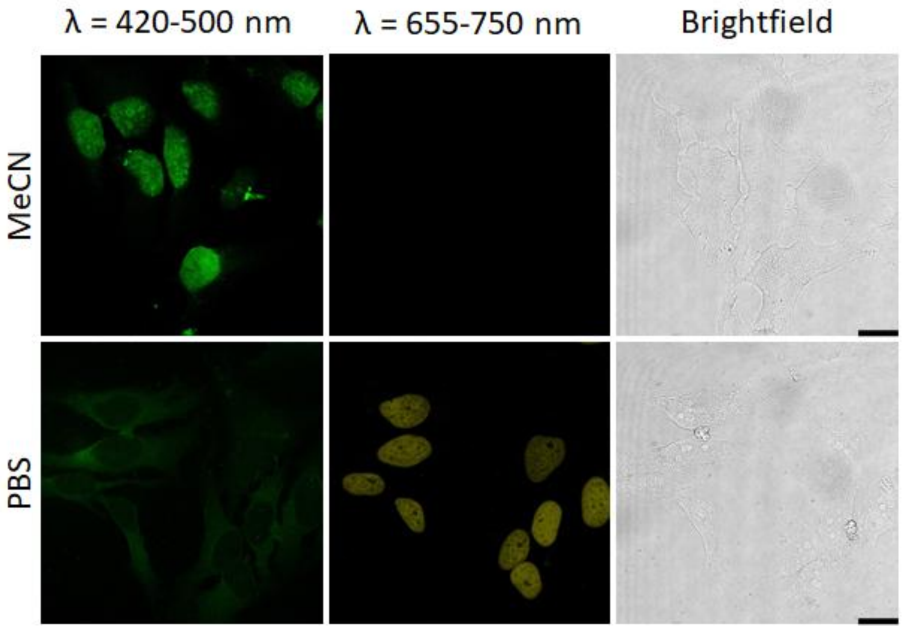

Figure A 5. Control staining experiments with **DRAQ5** (20 µM) that stains nuclear DNA in PBS and **6** (30 µM) staining the nuclear DNA in MeCN. Scale bar: 20 µm

## 2 Water Soluble Tetrazoles for Metabolic Labelling in Live Cells

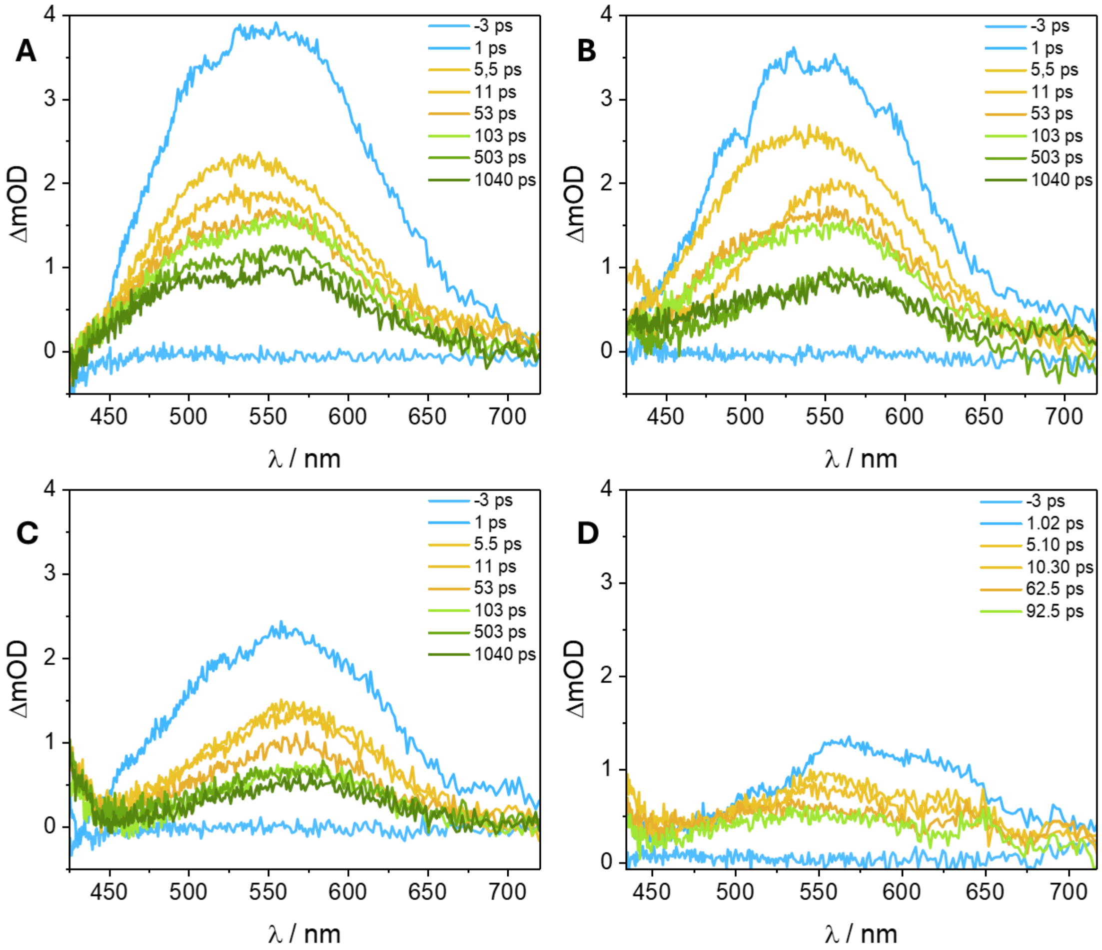

Figure A 6. Transient absorption of **3** in different solvent mixtures. A: 100% MeCN; B: 80% MeCN, 20% $H_2O$; C: 50% MeCN, 50% $H_2O$; D: 100% $H_2O$, excitation at 400 nm and E = 0.5 µJ. Monitored absorption changes at different time delays, lifetimes can be seen. Lifetime of the excited state is decreasing from **A** to **D**.

# 3 Visualizing the Invisible: Imaging Ruthenium-based PACT Agents in Fixed Cells

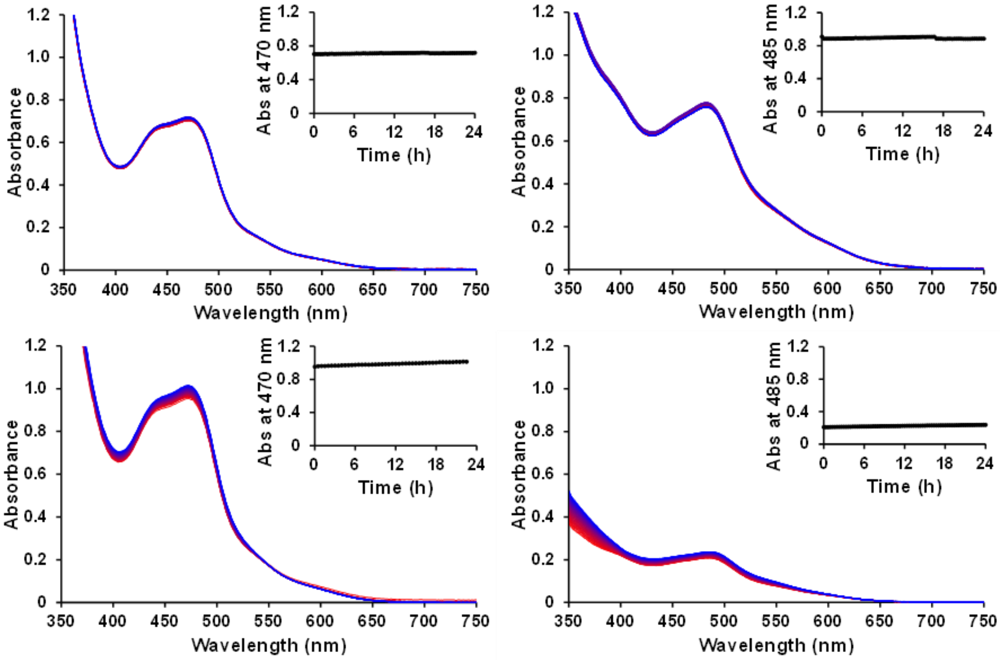

Figure A 7. Evolution of the UV/Vis spectra (region 350 – 750 nm) of a solution of a) [**2**]Cl$_2$ and b) [**4**](PF$_6$)$_2$ in water, and c) [**2**]Cl$_2$ and d) [**4**](PF$_6$)$_2$ in OptiMEM complete. T = 37 °C, t = 24 h, V = 3 mL, under air atmosphere and in the dark. Inset: Time evolution of absorbance at wavelength 470 nm for [**2**]Cl$_2$ and 485 nm for [**4**](PF$_6$)$_2$.

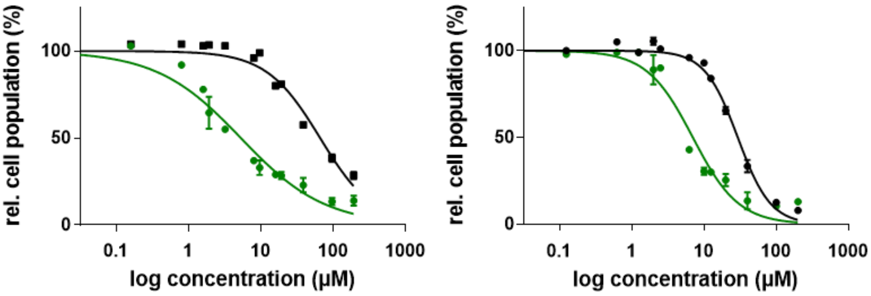

Figure A 8. Dose response curves for A549 cells under normoxic conditions treated with [**2**]Cl$_2$ (left) or [**4**](PF$_6$)$_2$ (right) and irradiated with green light (520 nm, 38 J/cm$^2$) 24 h after treatment (green line) or left in the dark (black line).

[**4**]($PF_6$)$_2$

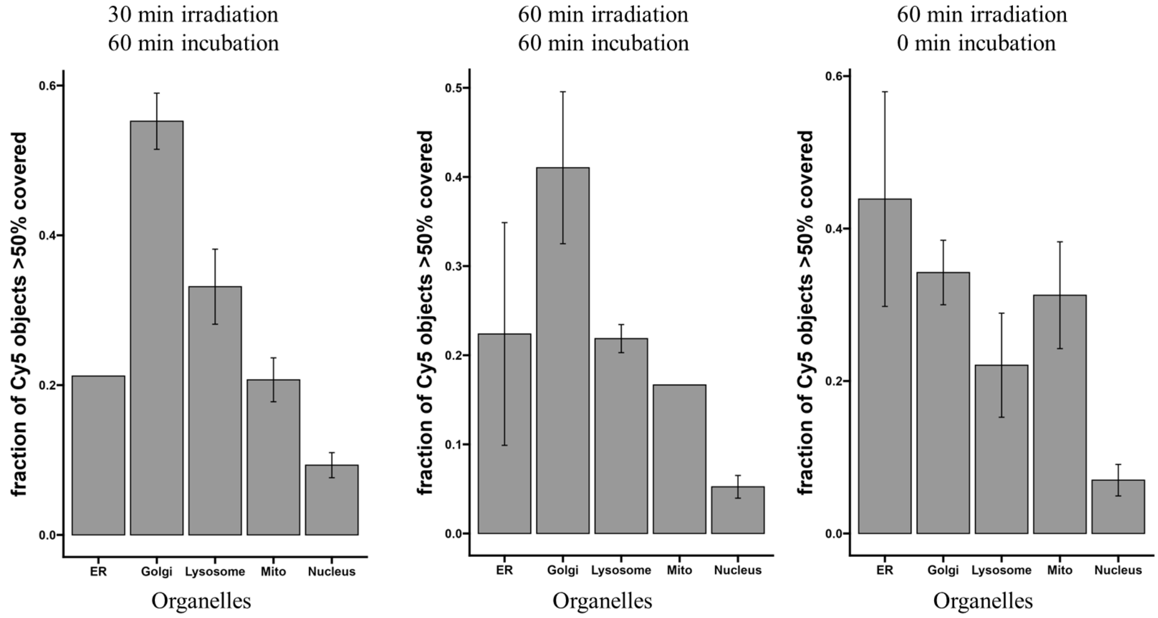

Figure A 9. Localization of the tagged complex [**4**]($PF_6$)$_2$ through staining of various organelles: ER, Golgi apparatus, lyososmes, mitochondria and nucleus of the cell. From left to right in the conditions: 1. 30 min irradiation, 60 min incubation, 2. 60 min irradiation, 60 min incubation, 3. 60 min irradiation, 0 min incubation.

[**2**]$Cl_2$

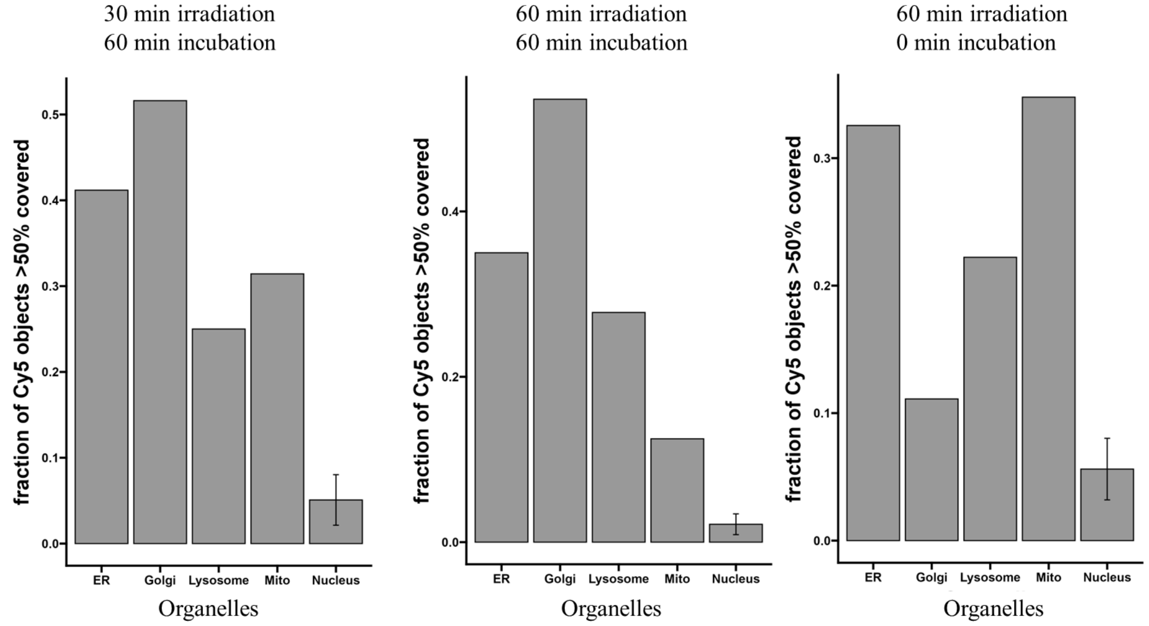

Figure A 10. Localization of the tagged complex [**2**]$Cl_2$ through staining of various organelles: ER, Golgi apparatus, lyososmes, mitochondria and nucleus of the cell. From left to right in the conditions: 1. 30 min irradiation, 60 min incubation, 2. 60 min irradiation, 0 min incubation.

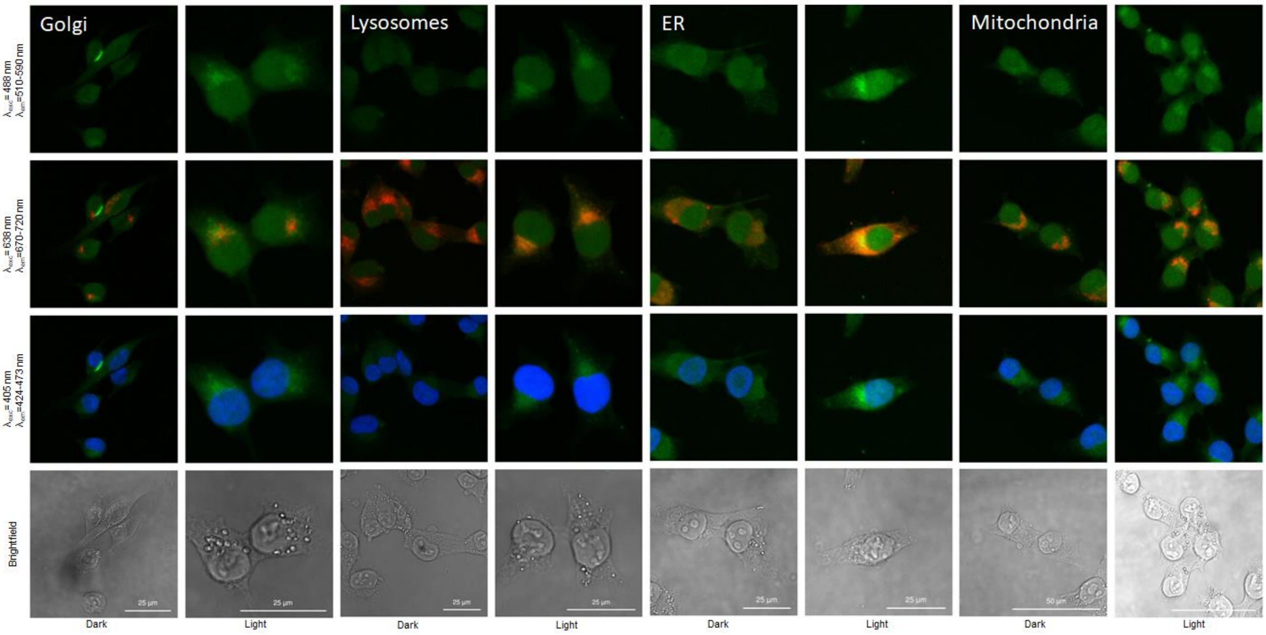

Figure A 11. [**4**]($(PF_6)_2$ in 25 µM concentration; treatment: 30 min irradiation (38 J/cm$^2$), 60 min incubation.

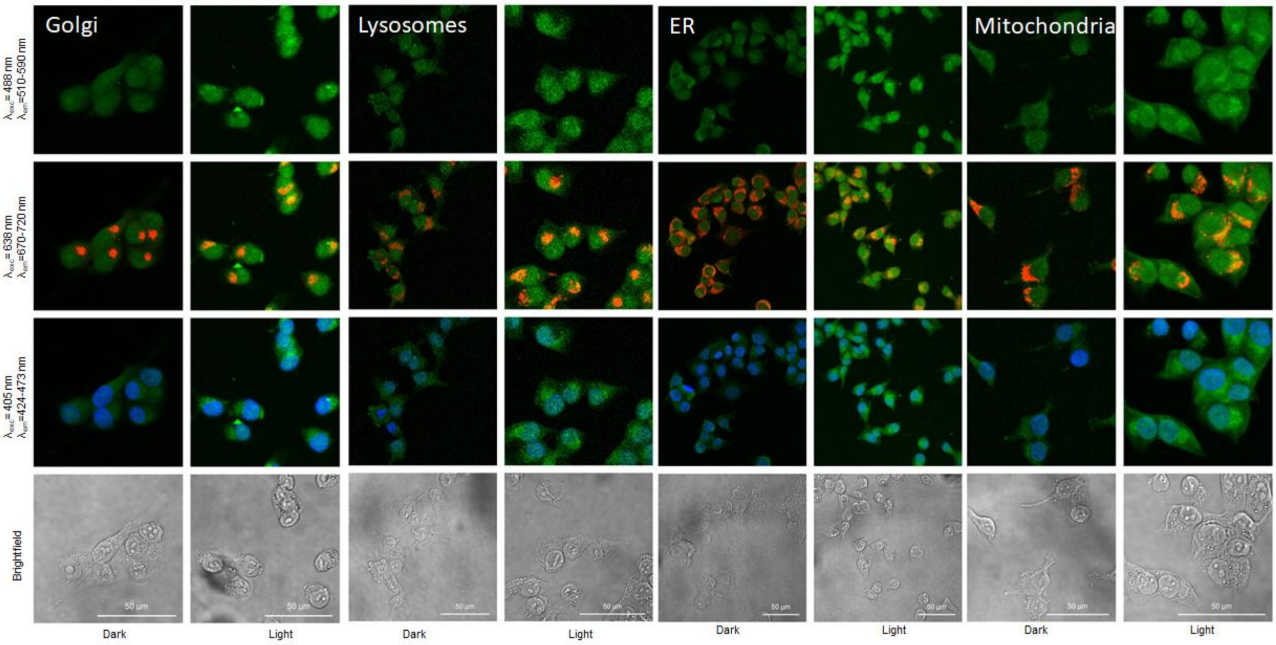

Figure A 12. [**4**]$(PF_6)_2$ in 25 µM concentration; treatment: 60 min irradiation (76 J/cm$^2$), 0 min incubation.

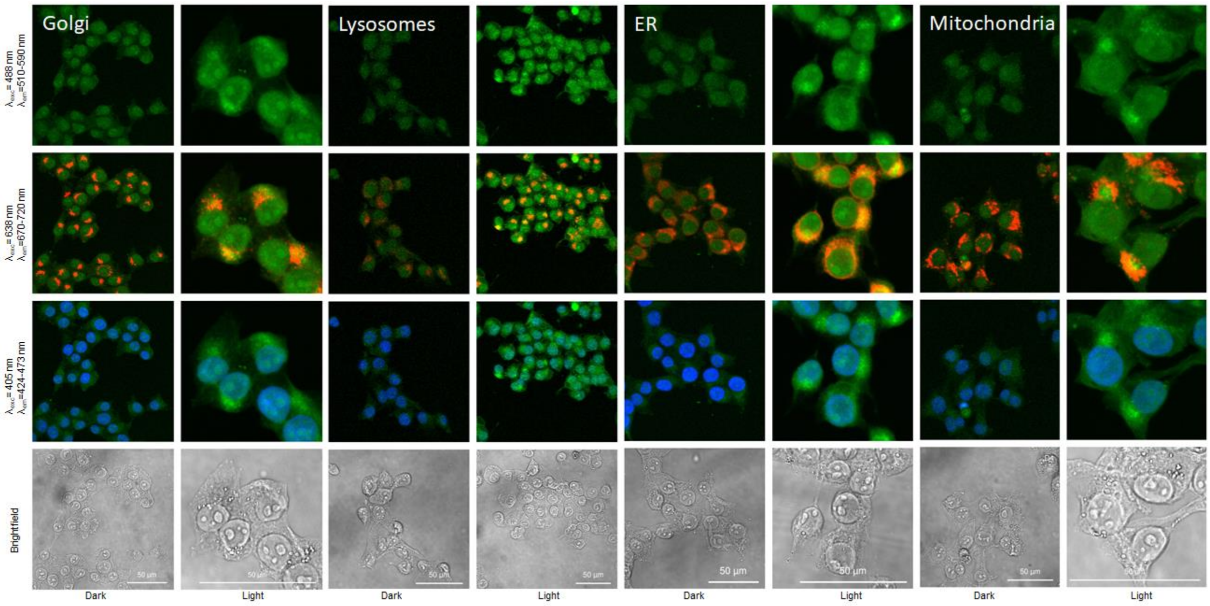

Figure A 13. [**4**]$(PF_6)_2$ in 25 µM concentration; treatment: 60 min irradiation (76 J/cm$^2$), 60 min incubation.

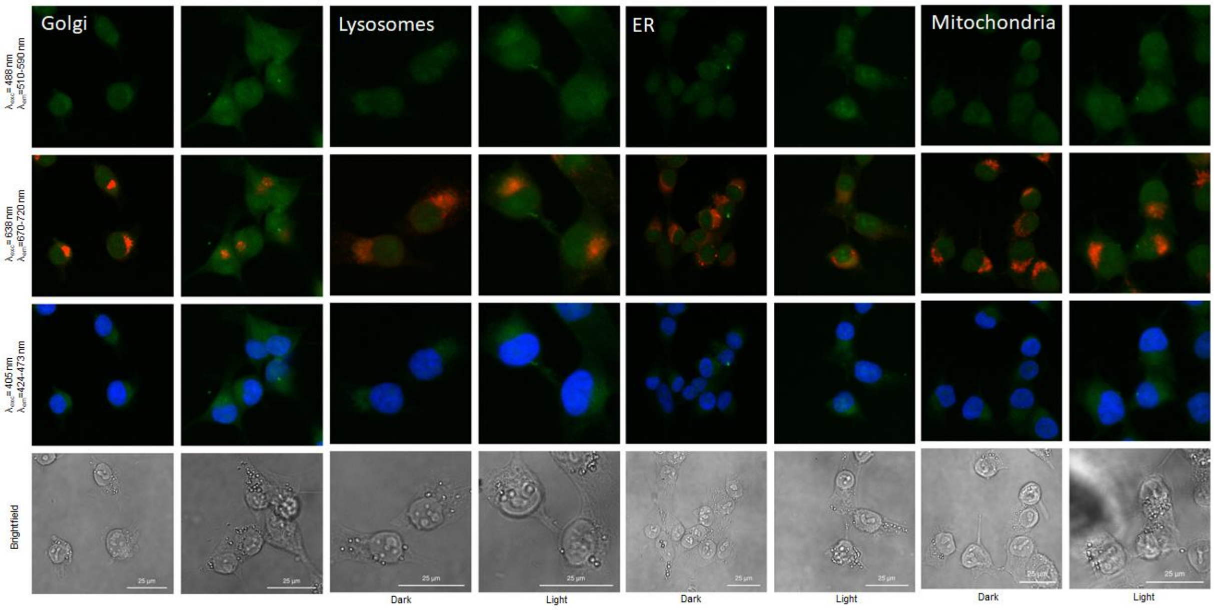

Figure A 14. [**2**]$Cl_2$ in 25 µM concentration; treatment: 30 min irradiation (38 J/cm$^2$), 60 min incubation.

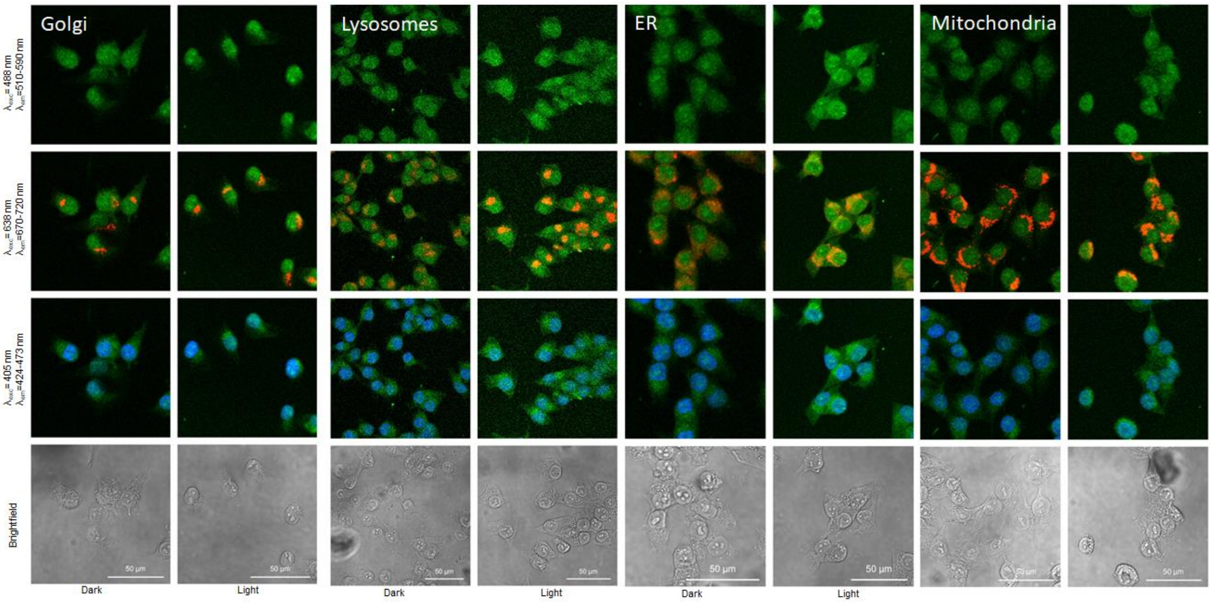

Figure A 15. [**2**]Cl$_2$ in 25 µM concentration; treatment: 60 min irradiation (76 J/cm$^2$), 0 min incubation.

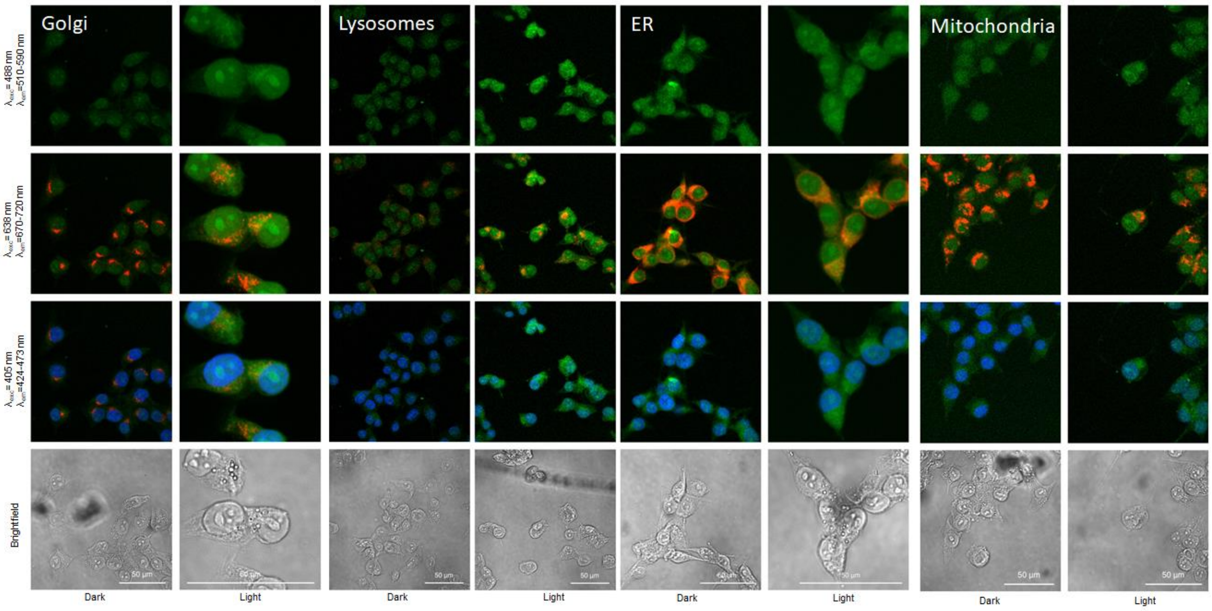

Figure A 16. [**2**]Cl$_2$ in 25 µM concentration; treatment: 60 min irradiation (76 J/cm$^2$), 60 min incubation.

# 4 Dual Labelling: CuAAC Labelling of PACT Agents and Metabolic Labelling of Newly Built DNA

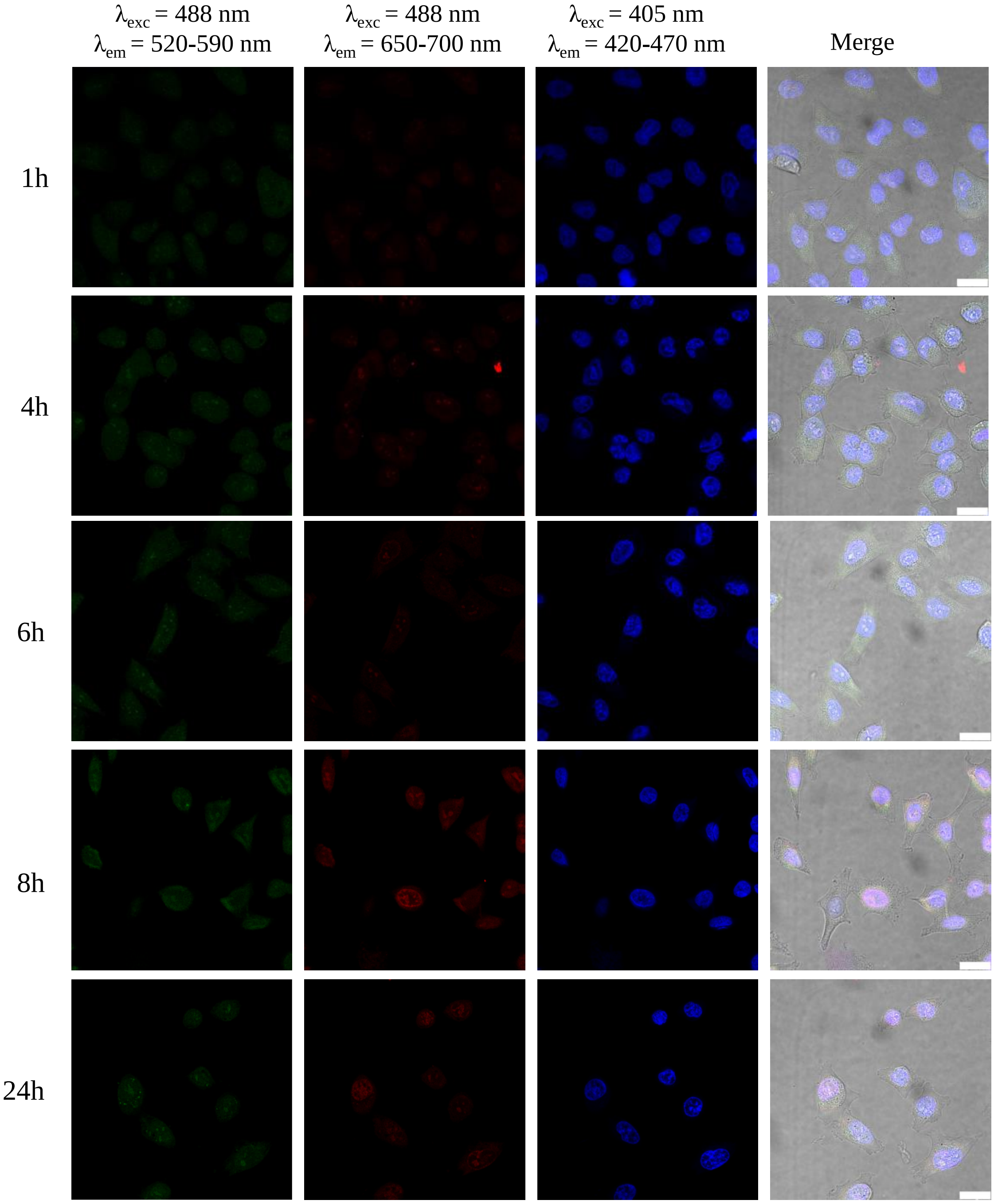

Figure A 17. Dual Labelling of CuAAC and IEDDA, [**4**]$(PF_6)_2$ concentration of 5 µM. Column 1 belongs to CuAAC emission channel, 2 belongs to IEDDA emission channel, 3 belongs to Hoechst emission channel and 4 is merge of the different emission channels. Rows belong to different incubation times before fixation of the cells. Scale bar: 20 µm.

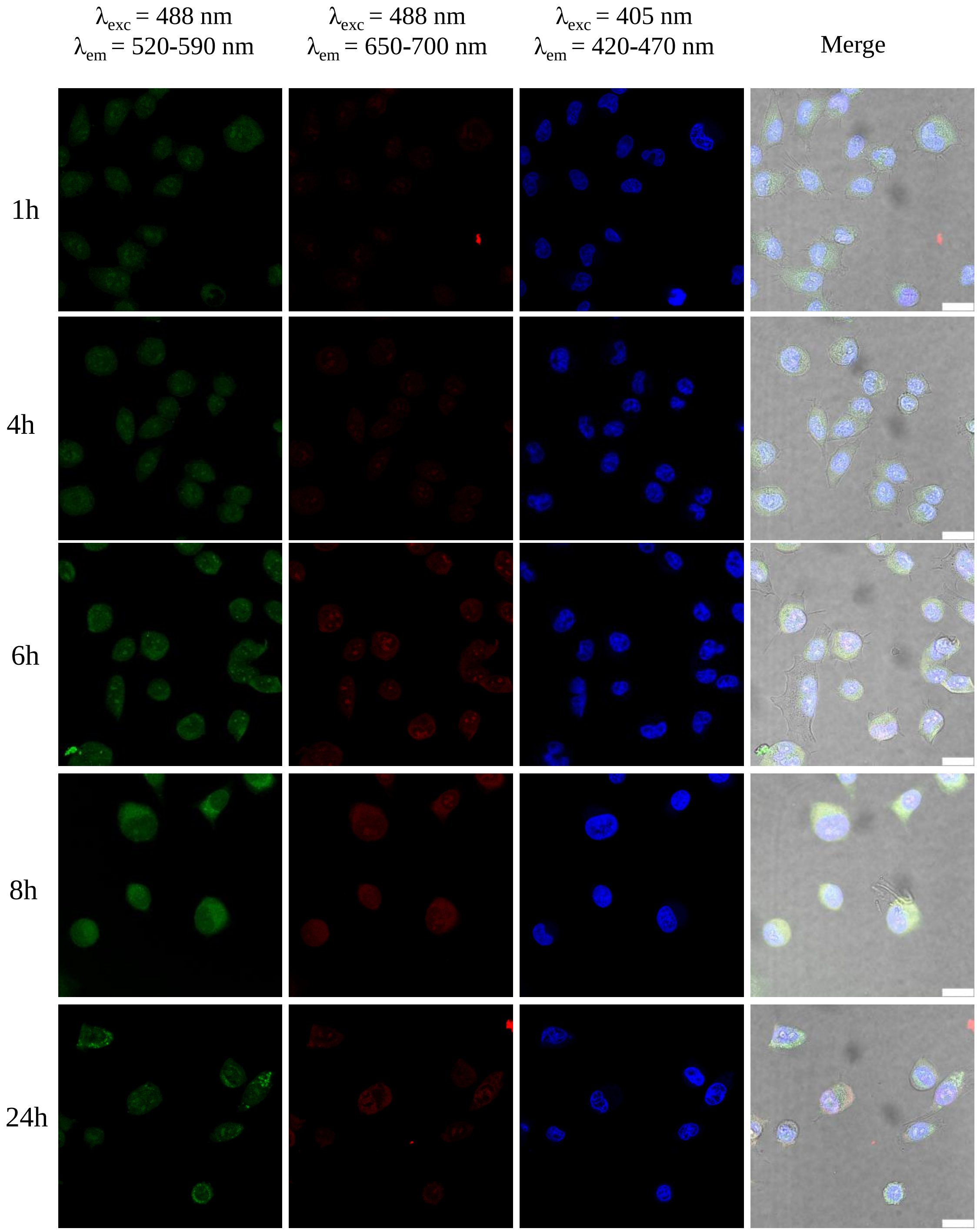

Figure A 18. Dual Labelling of CuAAC and IEDDA, [**4**]$(PF_6)_2$ concentration of 10 µM. Column 1 belongs to CuAAC emission channel, 2 belongs to IEDDA emission channel, 3 belongs to Hoechst emission channel and 4 is merge of the different emission channels. Rows belong to different incubation times before fixation of the cells. Scale bar: 20 µm.

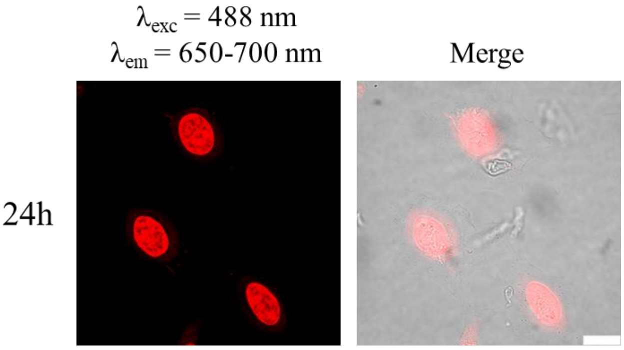

Figure A 19. Metabolic labelling of VdU (**20**) in 25 µM concentration with an incubation time of 24 h. Afterwards, fixation with PFA 4%, Triton-X-100 0.5% and BSA 3%. Labelling with **I** for 6 h incubation time. Scale bar: 20 µm.

# XI. Acknowledgments

Zuerst möchte ich mich bei allen bedanken, die mich im Rahmen meines Studiums und dieser Arbeit unterstützt haben.

Mein besonderer Dank gilt Prof. Dr. Hans-Achim Wagenknecht für das interessante Thema, die Unterstützung, den nötigen Freiraum und das Vertrauen. Bedanken möchte ich mich auch für die Möglichkeit, einen Teil meiner Dissertation in den Niederlanden durchführen zu können, für die Konferenzen in den USA, England und Deutschland und für die vielen Ratschläge. Danke auch für die gemeinsamen Feierabend-Aperolis, die zweimal in Obergurgl und die AK-Ausflügen.

I would also like to thank Sylvestre Bonnet for making the stay at Leiden University possible. Thank you for the opportunity to look into the world of chemotherapeutics, and for the support and encouraging conversations that made the rainy, dark winter in the Netherlands better so that I am thinking of moving back to the Netherlands!

Danke, dass Sie beide mich als Wissenschaftlerin geschätzt und gefordert habt und mich dadurch zu einer besseren Chemikerin und einer stärkeren Persönlichkeit gemacht haben.

Als nächstes möchte ich mich bei Prof. Ute Schepers für die Zweitkorrektur dieser Arbeit bedanken.

Zusätzlich möchte ich mich beim KHYS für die finanzielle Unterstützung während meines Auslandsaufenthaltes in den Niederlanden bedanken.

Ganz besonders möchte ich mich bei folgenden Personen bedanken:

- Dr. Andreas Rapp und Lara Hirsch, sowie dem gesamten Team der analytischen Abteilung des IOC für die Hilfe bei FAB, ESI und LC-MS Messungen bedanken, sowie die 24 h Bereitschaft, falls das NMR doch mal wieder ausfällt.
- Prof. Andreas-Neil Unterreiner, Jisu und Pascal für die transienten Absorptionsmessungen der Tetrazole.
- Annette Hochgesand für die vielen Bestellungen, die Versuche meine Tetrazole im MALDI zu messen und die vielen Gespräche.

- Claudia Sommer für die Hilfe bei allen organisatorischen Problemen, Dienstreiseanträgen oder das gemeinsame Buchen von Stadtmobil Autos für Obergurgl. Durch deine Positivität und dein Lachen, sowie die vielen Gespräche über dein Enkelkind und mein Patenkind, Urlaub oder auch welcher Sekt der Beste ist, hast du jeden noch so dunklen Tag etwas heller gemacht. Du bist ein großes Vorbild für uns alle!
- Ariane Baumgart, danke für die Hilfe bei bürokratischen Problemen. Danke, dass du zu uns in die Gruppe gekommen bist, für dein Engagement und deine Herzlichkeit, die mich vor allem am Ende sehr aufgemuntert hat.
- Meinen ehemaligen und aktuellen Kollegen aus dem Arbeitskreis Wagenknecht: Vielen Dank für die gemeinsame Zeit, die Hilfsbereitschaft bei allen möglichen Problemen, die Feierabend-Bierchen/Aperolis, die AK Ausflüge, die Frühstücke, Feiern und viele weitere Veranstaltungen. Es war mir ein Fest!
- Nicola, Rita, Eileen und Sina für das Korrekturlesen dieser Arbeit, sowie Mathis als Word-Profi und bei der Hilfe für das grandiose Bild für die Einleitung.
- Meinem Vertieferstudent Jérome Wagner, für deine Mithilfe an meinem Forschungsprojekt, deinen wilden Charakter und deine unermüdliche Säulaction.
- Allen Kollegen aus 203. Fabian Premium Weick, danke für die vielen schönen Gespräche, Kaffeepausen, Bierchen und Sonntag-Abend Burger im Oxford um die Ecke. Wir haben immer zusammengehalten und uns gegenseitig wieder aufgebaut, wenn es bitter nötig war. Danke, dass ich immer auf dich zählen kann, egal wo ich gerade bin. Sven Klehenz, Madeleine Giraud und Eileen List, wir kennen uns einfach schon 8 Jahre. Danke, dass wir zusammen durch dieses Studium gegangen sind und uns bis zum bitteren Ende nie im Stich gelassen haben. Danke an Sven (Klempner) Klehenz, ohne den meine Küche ein Schlachtfeld geworden wäre, die vielen Montag Abende im Zirkel, die Stunden die wir über Gott und die Welt diskutiert haben und natürlich für den besten Sonntagmittag ever, bei dem wir stundenlang in meinem Innenhof in der Sonne Aperol im Campingstuhl getrunken haben! Madeleine Giraud, danke für die vielen Gespräche in deiner alten Wohnung, die Ich bis heute nie vergessen habe. Danke, dass ich immer auf dich und deine Positivität zählen kann.

- Allen Kollegen aus 204: Maren Schrödter, danke, dass du immer ein offenes Ohr hast und wenn ich mal wieder durchdrehe in Gesprächen mit dir die Ruhe zurückbekomme, die du ausstrahlst. Danke auch für das unfassbar coole AK Wappen, dem Mitarbeiter des Monats und allen anderen kreativen Aktionen! Stephan Behling, danke für die Hilfe bei allen Fahrradproblemen, Radtouren, unsere Kleinanzeigen Aktionen und deine niemals nachlassenden Witze, die so schlecht sind, dass man schon wieder schmunzeln muss. Hör niemals damit auf, das zaubert ein Lächeln ins Gesicht. Lukas Frey, danke für deinen trockenen Humor und deine witzigen Blicke, falls etwas unerwartetes passiert oder wenn du dich konzentrierst. Andreas Schmidt für deine offene und ehrliche Art, die vielen Gespräche und deinen badischen Dialekt. Mathis für deinen ehrlichen Charakter, danke für deine Hilfsbereitschaft, deine witzigen Sprüche und deine wilden Geschichten. Danke auch für die vielen Tipps wo es gratis Essen gibt, wo es Angebote gibt oder wann man im Schlafanzug zu Ikea muss. Danke auch für die vielen Word- bzw Computer- Probleme die du für mich gelöst hast.
- Nicola Seul, danke, dass du immer für mich da bist. Danke, dass wir zusammen auf Vulkane wandern, aber auch entspannt am Strand liegen können. Danke, dass du mir durch deine Positivität und Ruhe oft zeigst, dass eine vermeintlich schlechte Situation gar nicht so schlimm ist.
- Meinen Laborkollegen aus 205: Bastian Pfeuffer, für die herzliche Aufnahme in 205, deine offene Art, unser Geheule über Muskelkater, die vielen witzigen Momente im Labor aber auch außerhalb. Danke für deine offene, liebe Art und die Umarmungen, wenn der Tag echt mal wieder aus dem Ruder gelaufen ist.
- Rita Michenfelder, danke dir für die unfassbar tolle Freundschaft, die sich in so kurzer Zeit entwickeln konnte. Danke, dass egal was mir auf dem Herzen liegt, ich immer damit zu dir kommen kann, egal wo auf der Welt du gerade bist. Danke, dass du mich genauso nimmst, wie ich bin und wir uns immer verstehen, auch wenn wir nicht einer Meinung sind! Danke, dass du mir jeden Tag morgens um 9 Uhr schon ein Lächeln ins Gesicht gezaubert und die Zeit im AKW deutlich schöner gemacht hast.

- Meinen Kollegen aus dem Erdgeschoss. Jan Kunzmann, danke für deine verpeilte, herzliche Art, die Bierchen und die Kaffeepausen. Danke, dass du uns ohne böse zu werden, Witze über deine Computerfähigkeiten und deine Handschrift machen lässt, das ist alles gut genauso wies ist. Simon Heckmeier und Sebastian Häcker, danke, dass ihr mich immer in eurem Labor aufgenommen habt, wenn ich mal wieder Zeit im Zelllabor totschlagen musste, danke, dass ihr mich zum Radfahren motiviert und wir über alles Mögliche diskutieren können. Simon, für deinen IT Support und eure offene und lustige Art, die mich zum Lachen bringt. Kerstin Müller danke ich, für die ehrlichen Gespräche, die Hilfe am Synthesizer und die leckeren Blätterteigschnecken die du immer mitbringst. Anna-Lena Roupp für die Motivation auf jeglichen Feiern noch nicht nach Hause zu gehen und die neusten Malle Hits die wir durch dich in unsere Malle Playlist aus 205 mitaufnehmen konnten.
- Meinen Freunden aus dem Studium, Jonas, Häcker, Jules und Luis. Danke, dass wir uns in der ersten Woche kennengelernt, uns durch das Studium und schlussendlich auch durch die Promotion geprügelt und uns nie im Stich gelassen haben.
- Eileen. Ich kann kaum in Worte fassen, für was ich dir alles danken möchte aus den letzten 8 Jahren. Ob von unserer ersten Woche gemeinsam in der O-Phase, unserem Campingurlaub, meinen Umzügen, dem Wochenende auf Malle, den unzähligen Abenden auf meinem Sofa mit unserem Lieblingsessen. Danke, dass ich das alles mit dir teilen kann. Danke, dass es dich gibt und wir in den letzten Jahren zu einem unzertrennlichen Duo geworden sind. Wir müssen nicht mal mehr reden, um uns zu verständigen. Du kannst einen schon morgens verlorenen Tag wieder zu einem Guten machen, wir können zusammen lachen und weinen (oder beides gleichzeitig) und ich kann zu jeder Sekunde Ich sein. Dich will ich nie mehr missen.
- Meine alten Mitbewohner aus der Ettlinger Straße, Linda und Tom. Danke, dass wir fünf Jahre jeden Sommer auf unserem Balkon Bowle getrunken haben, Corona zusammen mit Pamela Reif Workouts überstanden haben und ich immer mit welch wilder Story ich wieder ankam unterstützt wurde. Danke auch an Bego,

dass unsere Freundschaft so unkompliziert funktioniert, egal wo wir gerade wohnen und was wir gerade machen, wir verlieren uns nie aus den Augen und wenn wir uns treffen, bleibt alles wie immer.

- Meinen Freunden aus der Heimat. Melli, danke, dass wir seit dem Kindergarten befreundet sind und ich egal wie lange ich weg bin und wir uns nicht sehen, immer auf dich zählen kann. Danke, dass du mich aus meinem Chemie Alltag rausholst und danke auch, dass alles so unkompliziert ist. Caro, danke, dass du immer Verständnis für mich aufbringst, die Liebe zum Wandern und Skifahren mit mir teilst und ich mich durch deine ehrliche, liebevolle Art in deiner Gegenwart sehr wohl fühle. Danke, dass wir die letzten Jahre zusammen Silvester feiern und ich durch dich Berend kennenlernen durfte. Annaleah, danke, dass wir zusammen die Schulzeit überstanden und die Liebe für die Chemie gefunden haben. Danke, dass wir uns im Ausland gegenseitig besuchen und ich mich immer auf dich verlassen kann. Danke, dass wir immer zusammenhalten und ich euch immer in meinem Leben haben werde!
- Lieve Berend, bedankt dat je er altijd voor me bent om me na lange dagen weer tot rust te brengen en me de kalmte geeft die ik zelf soms mis. Bij jou kan ik mijn typisch Duitse, strakke organisatie even loslaten en leren meer van het leven te genieten. Bedankt dat je met me bergen en vulkanen beklimt, je liefde voor skiën met me deelt en samen met me de wereld verkent. We hebben zelfs samen genoten van de meest regenachtige winter in Nederland. Vooral de laatste maanden was je mijn rots in de branding. Je gaf me stabiliteit en zekerheid – ik kijk uit naar alles wat in het verschiet ligt.
- Meiner Familie, allen voran meinen Eltern Claudia und Rolf. Danke für euer Vertrauen, eure endlose Liebe und die Unterstützung. Egal was passiert, ich weiß ihr werdet immer alles stehen und liegen lassen, wenn ich euch brauche. Danke, dass ihr mir gezeigt habt, was wichtig ist und ihr mich zu der Frau gemacht habt, die ich heute bin. Ihr seid meine größten Vorbilder. Danke an meine Brüder Florian und Johannes, meine Schwägerin Conny und mein Patenkind Charlotte sowie Oma und Opa. Danke, dass wir immer zusammenhalten und ich bei euch immer Willkommen bin. Danke, dass ihr immer an mich glaubt.

# XII.Curriculum Vitae

| | |
|---|---|
| **Name** | Lisa Maria Rieger |
| **Languages** | German (native), English (proficient) |

**Education**

| | |
|---|---|
| *12/2021-12/2024* | **PhD** Candidate<br>Group of Prof. Dr. Hans-Achim Wagenknecht<br>Karlsruhe Institute of Technology, Germany |
| *10/2023-02/2024* | **PhD exchange**<br>Group of Prof. Dr. Sylvestre Bonnet<br>Leiden University, Netherlands |
| *04/2020-09/2021* | **Master** of Science, Chemistry<br>Karlsruhe Institute of Technology (KIT)<br>Final Grade: 1.2 |
| *09/2016-03/2020* | **Bachelor** of Science, Chemistry<br>Karlsruhe Institute of Technology (KIT)<br>Final Grade: 2.0 |
| *09/2008-07/2016* | General higher education entrance qualification (**Abitur**)<br>Scheffelgymnasium Bad Säckingen<br>Grade: 2.6 |

# 1 Publications

“Metabolic labelling of DNA in cells by means of the “photoclick” reaction triggered by visible light”, L. Rieger, B. Pfeuffer and H.-A. Wagenknecht, *RSC Chem. Biol.*, **2023**, 4, 1037-1042.

DOI: 10.1039/D3CB00150D

“Cyclopropenes as Chemical Reporters for Dual Bioorthogonal and Orthogonal Metabolic Labelling of DNA”, N. Seul, D. Lamade, P. Stoychev, M. Mijic, R. T. Michenfelder, **L. Rieger**, P. Geng and H.-A. Wagenknecht, *Angew. Chem. Int. Ed.*, **2024**, 63, e202403044.

DOI: 10.1002/anie.202403044

“Visualizing the invisible: Imaging of ruthenium-based PACT agents in fixed cancer cells”, Anja Busemann, [†a] **Lisa Rieger**, [†b] Rachael Cunningham, [c] Sylvia Le Dévédec,[d] Ingrid Flaspohler, Claudia Schmidt, [f] Xue-Quan Zhou, [a] Vincent van Rixel,[a] Maxime Siegler,[e] Ingo Ott,[f] Hans-Achim Wagenknecht, [b] Vicky DeRose*,[c] Sylvestre Bonnet*[a]

*Manuscript in preparation.*

# 2 Conferences and Oral Presentations

| | |
|---|---|
| *17/09/2024-20/09/2024* | **Poster Presentation with Poster Prize**<br>8th Cambridge Symposium on Nucleic Acids Chemistry and Biology<br>Queens College, Cambridge, UK |
| *14/09/2023-15/09/2023* | **Poster Presentation**<br>XI. Nukleinsäurechemie-Treffen 2023, DNG<br>Würzburg, Germany |
| *04/09/2023-06/09/2023* | **Talk** and **Poster Presentation**<br>Rethinking Chemistry<br>Wissenschaftsforum (WiFo), GDCh<br>Leipzig, Germany |
| *24/06/2023-30/06/2024* | **Poster Presentation**<br>Chemical Biology of Nucleosides and Nucleic Acid Towards Human Therapeutics Nucleosides, Nucleotides & Oligonucleotides<br>Gordon Research Conference<br>Newport, Rhode Island, United States (USA) |
| *29/06/2022-01/07/2022* | **Poster Presentation**<br>Biochemistry, GDCh<br>Münster, Germany |

## 3 Student Supervision

| | |
|---|---|
| *July 2024* | Supervision of „Vertieferpraktikum“ |
| *June 2024* | Supervision of „organisch-chemisches Fortgeschrittenen-Praktikum für Studierende der Chemie“ |
| *March 2024* | Supervision of „organisch-chemisches Grundpraktikum für Studierende der Chemie“ |
| *August 2023* | Supervision of „organisch-chemisches Fortgeschrittenen-Praktikum für Studierende der Chemie“ |
| *June 2023* | Supervision of „organisch-chemisches Fortgeschrittenen-Praktikum für Studierende der Chemie“ |
| *February 2023* | Supervision of „organisch-chemisches Fortgeschrittenen-Praktikum für Studierende der Chemie“ |
| *November 2022* | Supervision of „organisch-chemisches Grundpraktikum für Studierende der Chemie“ |
| *June 2022* | Supervision of „organisch-chemisches Fortgeschrittenen-Praktikum für Studierende der Chemie“ |

## 4 Grants

Research Travel Grant from the Karlsruhe House of Young Scientists to support 5 months of research stay at Leiden University in Leiden, Netherlands.